UNIVERSITÀ
DEGLI STUDI
DI PADOVA

Sede Amministrativa: Università degli Studi di Padova
Dipartimento di Ingegneria Industriale

SCUOLA DI DOTTORATO DI RICERCA IN: INGEGNERIA INDUSTRIALE
INDIRIZZO: Ingegneria Energetica
CICLO: XXV

# Aerodynamic Shape Optimization of the Helicopter Main Rotor Hub Beanie, Using Advanced Multi-Objective Evolutionary Algorithms

**Direttore della Scuola :** Ch.mo Prof. Paolo Colombo
**Coordinatore d’indirizzo:** Ch.mo Prof. Luisa Rossetto
**Supervisore**: Ch.mo Prof. Ernesto Benini

**Dottorando** : Lorenzo Dal Mas

# ABSTRACT

In this PhD thesis, a comprehensive aerodynamic characterization of the helicopter main rotor hub beanie is carried out. This component is involved in the reduction of the tail shake phenomenon which is a problem of great concern for the industrial manufactures, such as *AgustaWestland*, the helicopter company that has sponsored this research. The numerical model of three beanie geometries are created and validated against specific experimental data. Then, an extensive CFD test campaign was carried out to evaluate the aerodynamic performance of such a component at different operating conditions and in different configurations. In particular, the attention is focused on the analysis of both the beanie capabilities to downward deflect the oncoming flow, and the aerodynamic loads that act on this component. On the basis of these analyses, a series of new guidelines for the design and the certification of the beanie are gathered and submitted to *AgustaWestland*.

Moreover, the aerodynamic optimization of a specific beanie model, the AW101, is presented in this work. The final aim is the investigation of new hub cap geometries that manifest improved capabilities in the downward deflection of wake and low aerodynamic drag with respect to the original model. Amongst the different optimal solutions provided by the multi-objective optimization carried out using an advanced evolutionary algorithm, three new beanie geometries are selected and analysed via CFD to compare their aerodynamic performances to those of the original AW101 hub cap.

Finally, a new beanie concept-design, named HBM, is presented. The model was created in order to investigate the effects of a hollow structure on the beanie capabilities in the downward deflection of the wake. A parametric study is also carried out to highlight the effects of some specific geometrical parameters on the beanie performances. The results are encouraging, and the HBM model seems promising, though a more comprehensive numerical analysis will be required before the model can be used for real industrial purposes.

# ABSTRACT

Questa tesi di dottorato è finalizzata all'analisi aerodinamica completa e approfondita di un componente dell'elicottero, denominato *beanie*, che viene installato sulla parte superiore del rotore principale a copertura del mozzo. Tale componente è coinvolto nella riduzione del fenomeno del *tail shake* che risulta essere un problema di particolare interesse per i produttori di elicotteri come *AgustaWestland*, l'Azienda che ha finanziato questa ricerca. I modelli numerici di tre differenti geometrie di *beanie* sono stati creati e validati utilizzando specifici dati sperimentali. E' stata svolta una dettagliata campagna di test CFD al il fine di valutare le prestazione aerodinamiche di questi componenti in diverse condizioni di esercizio. In particolare, si è focalizzata l'attenzione sull'analisi sia delle capacità del *beanie* di deflettere il flusso verso il basso, sia sui carichi aerodinamici che agiscono su di esso. Sulla base dei risultati ottenuti, è stato possibile ottenere una serie di nuove linee guida per la progettazione e la certificazione di questo particolare componente aerodinamico, che andranno a sostituire l'attuale metodo applicato da *AgustaWestland*.

E' stata poi svolta la ottimizzazione aerodinamica di uno specifico modello di beanie, l'AW101, con lo scopo di investigare nuove geometrie di questo componente che presentassero migliori capacità di deflessione verso il basso della scia e contemporaneamente fossero caratterizzate da una minore resistenza aerodinamica. L'ottimizzazione multi-obiettivo è stata realizzata usando una specifica procedura che implementa al suo interno un algoritmo evolutivo avanzato. Tra tutte le possibili soluzioni "ottime" ottenute, ne sono state scelte tre e le loro prestazioni sono state poi confrontate con quelle del modello di beanie originale.

Infine è stato presentato un nuovo prototipo di *beanie,* denominato HBM. Il modello è stato creato con lo scopo di investigare gli effetti di una struttura cava sulle capacità del componente di deflettere verso il basso della scia. Oltre ad una analisi del modello base si è proceduto anche a uno studio parametrico per evidenziare gli effetti di alcune specifiche variabili geometriche sulle prestazioni aerodinamiche del *beanie*. I risultati sono incoraggianti e il modello HBM sembra avere delle caratteristiche promettenti, tuttavia è necessaria ancora un'analisi numerica dettagliata e approfondita prima che questo nuovo beanie possa essere impiegato in ambiente industriale.

# ACKNOWLEDGMENTS

The work presented in this PhD thesis was possible because of the support provided by a number of people to whom I owe a great deal of thanks. First and foremost, I would like to record my special gratitude to my tutor Prof. Ernesto Benini (of the University of Padova), and Rita Ponza (of HIT09 S.r.l). Their assistance and guidance in the technical aspects of this work was crucial to its completion. I would also like to express my gratitude to *AgustaWestland S.p.A*. for the sponsorship of this PhD activity. In particular, I would like to acknowledge Antonio Saporiti for the help and assistance during these three years. Finally, I want to thank my family and my friends for their support during this PhD research and throughout my life.

# CONTENTS

# LIST OF FIGURES

# LIST OF TABLES

# 1. INTRODUCTION

## 1.1 The tail shake phenomenon

Tail shake, also known as tail buffeting, is an interactional aerodynamic phenomenon clearly perceived by the helicopter pilots within the cockpit, that adversely affect the overall performance, occupants' comfort and handling qualities of the helicopter. It is caused by the interaction of the rotor hub wake with the tail boom and vertical tail. There are many factors that may contribute to excitation of the structure lower elastic modes, since the wake that impinges the helicopter tail is generated by different components, such as the main rotor hub, the engine intakes and exhaust, cowlings shapes and the rotor, as shown in Figure 1.1. Therefore, the aerodynamic design of each of these components may influence the tail shake phenomenon.

The shake response to the structure excitation is shaped on the first lateral bending mode, which is a two-node mode. This means in practice that the vibration is mostly felt in front of the forward node, i.e. on flight crew stations (Figure 1.1)[1]. The phenomenon is random and clearly unsteady, hence difficult to be predicted during a helicopter early design stage. The problem normally appears during the expensive wind tunnel test campaigns that are carried out before and after first flight tests, but due to the complexity of the interactional aerodynamics, it is possible that vibration problems might be encountered only during the flight ([2],[4],[5],[6],[7]).

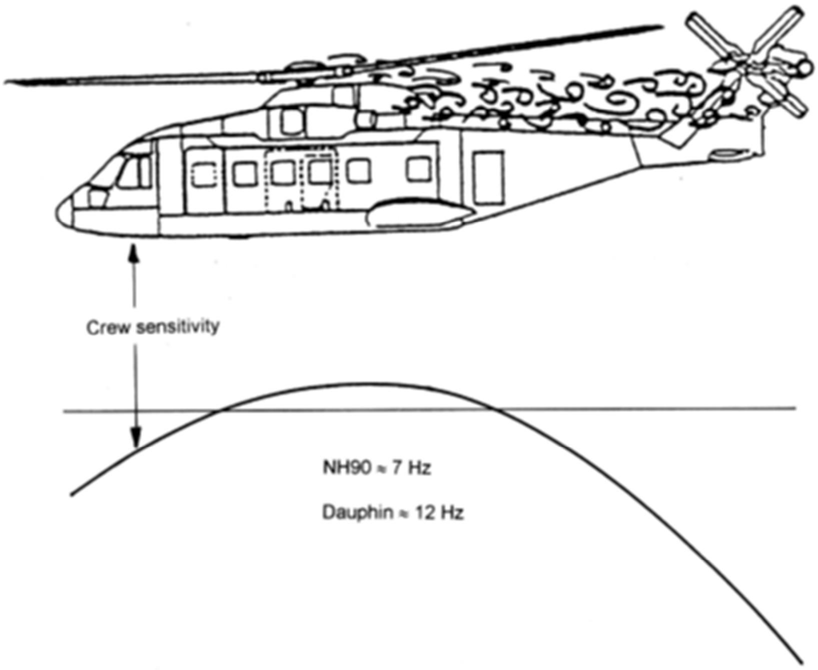

Figure 1.1: Wake/tail aerodynamic interaction and first lateral banding mode (2 nodes)[1].

Over the years, the manufactures have introduced on their helicopter models a series of different aerodynamic devices that aim at reducing the tail shake phenomenon, among which the most important are probably the blade fairing and the main hub fearing (or beanie). While the former reduces and modifies the wake characteristic of the blade hinges, the latter induces a downward deflection of the entire wake that generates form the main rotor hub system and also by part of the engine upper deck, with consequent positive effects on the tail shake.

Nowadays almost every helicopter is provided with a beanie, the geometrical characteristics of which may substantially vary from a helicopter model to another in order to maximize its performance. The beanie has become a component of great concern for the industrial manufacturers, since it can have remarkable dimensions, and because it contributes to the main rotor overall aerodynamic drag. Therefore, a correct design of this component is necessary in order to improve its capabilities in the deflection of the wake, while keeping the drag to a minimum at the same time.

## 1.2 The AgustaWestland objectives

The helicopter design and manufacturing companies, such as *AgustaWestland*, are showing an increasing interest in the tail shake phenomenon, and are developing new design methodologies, based on the modern computer codes, that are able to reduce the tail vibrations caused by the wakes that generate form the aerodynamic components located around the main rotor hub ([8],[9]).

This PhD activity, sponsored by *AgustaWestland*, is placed within the context of a wider project that aims at assessing the characteristics and the contribution to the tail shake of each wake that impinges the tail fin. In particular, the company is interested in the analysis and the aerodynamic characterization of three different beanie models that are mounted over the main rotor hub of the AW139, AW109, and AW101 helicopters, which are shown in Picture 1.1. In fact, these components are the most important aerodynamic devices involved in the reduction of the tail shake phenomenon. Therefore, the introduction of a validated and robust computer fluid dynamic procedure may be useful to better understand the beanie aerodynamic behaviour, and it may also help in the development of new procedures for the design and certification of such a component.

Finally, *AgustaWestland* aims also at investigating new beanie geometries with improved wake deflection capabilities and lowered impact on the helicopter overall aerodynamic drag, especially as far as the AW101 beanie is concerned. In fact, the design of this component has been based only on the company experience and wind tunnel tests, thus the implementation of advanced and powerful optimization methodologies, such as the one developed by the University of Padova, is strongly recommended.

**Picture 1.1: The AW139 (left), the AW109 (center), and the AW101 (right) beanie models.**

## 1.3 The thesis objectives and outline

In agreement with *AgustaWestland*, the objectives of the present research were:

I. The aerodynamic validation and aerodynamic characterization of three different types of beanie using a computational fluid dynamic (CFD) approach, to better understand the characteristics of this component wake and the way it interacts with the helicopter tail fin. Moreover, this activity is also addressed to the development of a new procedure for the determination of the beanie limit loads to be used as an alternative to the guidelines for the beanie structural design and certification that *AgustaWestland* has applied so far;
II. The aerodynamic optimization of the AW101 helicopter beanie by means of a computer based procedure implementing the advanced multi-objective evolutionary algorithm GeDEA [26], developed by the University of Padova.

The research activity was subdivided into five different parts:

1. the validation of the AW139 beanie numerical model;
2. the validation of the AW109 beanie numerical model;
3. the aerodynamic characterization of the AW101 beanie model;
4. the development of a new methodology for the evaluation of the beanie limit loads;
5. the aerodynamic optimization of the AW101 main rotor hub beanie.

At the end of each part, a detailed report was written and submitted to *AgustaWestland* for the final review and approval. This thesis summarizes the main results achieved during the entire research activity, though some details will be omitted due to industrial proprietary reasons. In particular, Chapter 2 discusses the validation of the AW139 and AW109 beanie numerical models and the aerodynamic characterization of the AW101 hub cap. Chapter 3 focuses on the determination of the beanie aerodynamic limit loads, and it presents the new guide-lines that are to be followed for the design an certification of this component. Chapter 4 deals with the aerodynamic optimization of the AW101 beanie, while Chapter 5 introduces a new beanie concept-design for future applications on the AW101 helicopter. Finally, Chapter 6 contains general conclusions about the work as well as a discussion of future work that should be done.

# 2. CFD VALIDATION AND AERODYNAMIC CHARACTERIZATION OF THREE DIFFERENT BEANIE MODELS

## *2.1 Introduction*

The validation and aerodynamic characterization of a beanie numerical model is the first required step towards the future optimization of this helicopter component. To this purpose, three different activities concerning the AW139, AW109 and AW101 main rotor hub caps were carried out during 2010 with the support of *AgustaWestland*. The main outcomes of these studies will be presented in this chapter.

The first analysis involved the AW139 beanie. The results of a series of wind tunnel test campaigns performed on this beanie model, were provided by *AgustaWestland* for the validation of the numerical model. A grid sensitivity analysis was carried out by comparing the results of the CFD simulations to the experimental data in terms of static pressure distribution over the beanie surfaces, of total pressure losses at the beanie wake, and of global aerodynamic beanie loads. The main outcomes of this activity were reported in [10].

This mesh sensitivity analysis made it possible to identify a series of grid parameters which allowed the achievement of a good match between the CFD results and the available experimental data. Therefore, the indication drawn in this activity, were followed for the set-up of the AW109 beanie numerical model, due the similarities between the AW139 and AW109 wind tunnel test campaigns. For this specific model, the comparison between numerical results and experimental data was possible only in terms of the distribution of the static pressure over the beanie surfaces, due to the lack of other experimental acquisitions. The outcomes of this activity were reported in [11].

Finally, the results drawn from the extensive numerical analyses of the AW139 and AW109 main rotor hub caps were followed for the numerical investigation of the flow field behaviour over the AW101 helicopter beanie, for which no experimental data was available. In this specific case, the CFD analysis was aimed at investigating the effects of the presence of the engine upper deck on the downward deflection induced by the beanie on the oncoming flow stream. In particular, the attention was focused on the characteristics of the wake at the tail fin location. The results of this investigation were reported in [12].

Form a practical point of view, the targets of these activities were accomplished by means of some commercial software that are normally used by *AgustaWestland*: CATIA V5® was used for the creation of the CAD model, and for the generation of the surface mesh of both the beanie and the virtual wind tunnel; the volume mesh was created by means of TGrid®; finally, ANSYS Fluent® was selected as the fluid dynamic solver.

## 2.2 The AW139 beanie CFD validation

The AW139 beanie CFD validation activity was performed using data measured during a wind tunnel test campaign carried out in early 2003 in the 4x4m$^2$ closed test section of "Politecnico di Milano" on the AW139 full-scale, non-rotating beanie, aimed at assessing the static pressure distribution over the component upper and lower surfaces for structural design purposes. Different incidence angles were investigated, in order for the attitudes' envelope needed for the certification to be fully covered by experiments. Moreover, the extensimetric apparatus installed between the beanie and the wind tunnel supporting system provided the values of the global forces acting on the component at the various tested conditions. Finally, a wake rake located downstream of the beanie was used to measure the total pressure coefficient distribution, in order to assess both the wake losses and the fluid flow behaviour behind the beanie, with particular regard to the downward deflection it induces on the oncoming flow stream. The drag rake was installed in a position corresponding to the beanie mid-section; thus the collected acquisitions were inevitably affected by the experimental apparatus. All the details of on the experimental test campaign were reported in [13] and [14].

A numerical model of the AW139 was created and simulated via CFD. The numerical results were then compared to the experimental data. Since the are several parameters that may influence a fluid dynamic simulation (for instance the superficial mesh type and size, the volumetric grid refinement, the type of the fluid dynamic solver etc.), it was important to identify the best configuration that allowed for the achievement of a good match with experimental results, while keeping the required computational resources to a reasonable level. To this purpose, different numerical models of the beanie at zero angle of attack were created changing a single feature at a time, and both simulated pressure coefficient distribution and total pressure losses in the wake were compared to the experimental acquisitions. Once the most suitable numerical model configuration was identified, CFD simulations at non-null attack angles of attack were carried out, and the lift, drag, and pitching moment polars were extracted, with the aim of evaluating the beanie attitude in terms of lift, to drag ratio at varying incidence.

### 2.2.1 The wind tunnel test campaign

The model used in the tests was the exact reconstruction of the full-scale AW139 hub fairing, which was mounted on a pylon equipped with a force transducer and installed in the “Politecnico di Milano” wind tunnel. A proper interface was created between the rotor hub and the extensimetric balance, in order to allow straightforward modification of the beanie angle of attack. In particular, the balance was positioned on a rotating bracket moved by the connecting rod hidden within the main structure. A wooden box connected to the bracket protected the instrumentation form the external flow. The beanie and the balance were connected by means of two flanges. All the cables were arranged to reduce their influence on the test results as much as possible.

Besides the global forces, also the static pressure coefficients were acquired in the wind tunnel tests, by means of a series of 81 static pressure taps distributed on both the upper and lower surfaces of the beanie over a 72° sector of the model. Therefore, the model had to be rotated around its axis to obtain the pressure data over different azimuth angles. Figure 2.1 depicts the location of the pressure sensors over the beanie surfaces. Moreover, the total pressure measurements were carried out by means of 47 probes organized in a vertical rake and positioned downstream of the beanie, in such a way that the probe number 29 was aligned to the top of the beanie when positioned at zero angle of attack (Figure 2.2). The drag rake was installed in a position corresponding to the beanie mid-section, and its position was held fixed during the whole test campaign.

A total amount of 90 tests were carried out to acquire the static pressure distribution over the beanie surfaces, aerodynamic coefficients acting on the beanie, and the total pressure measurements at the beanie wake rake. These runs were performed at different angle of attack (form $\alpha$=-24° to $\alpha$=30°) at the wind tunnel conditions reported in Table 2.1.

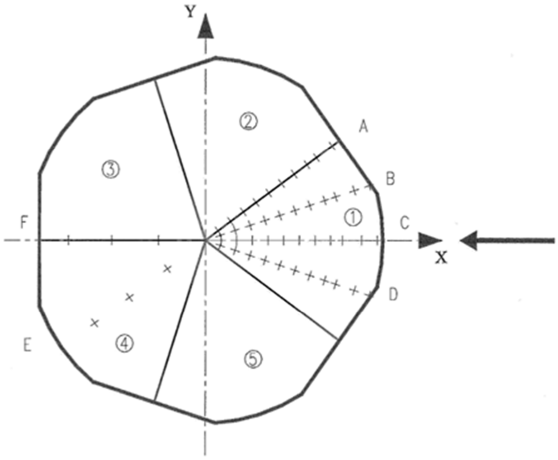

**Figure 2.1: Location of the pressure taps over the beanie upper surface.**

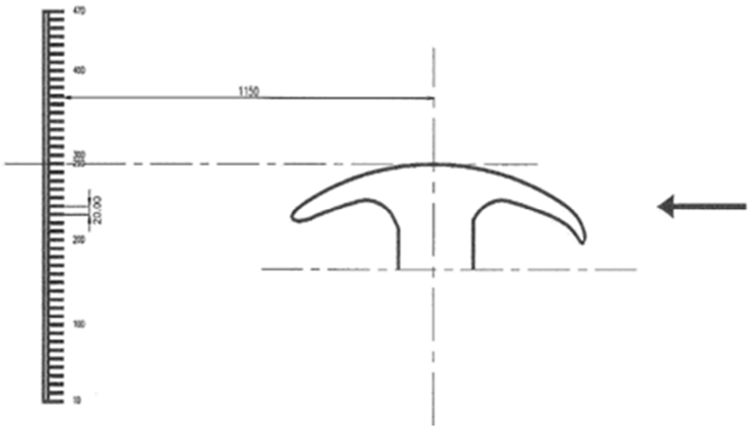

**Figure 2.2: Location of the total pressure rake.**

| | | |
|---|---|---|
| Air Flow Speed | 40 | m/s |
| Temperature | 20 | °C |
| Pressure | Ambient pressure | |

**Table 2.1: The wind tunnel test conditions.**

## 2.2.2 The numerical model.

As already mentioned, the beanie geometric model was created by means of CATIA V5®. The CAD model used for computations was derived from some simplifications of the real geometry tested in the wind tunnel, both because some geometrical data were missing, and because the representation of all the details characterizing the beanie, the balance and the supporting system might have negatively affected the quality of the final mesh. A comparison between the real tested model and the CAD one used in the simulations is shown in Figure 2.3

Only the upper portion of the supporting shaft was reproduced in the CAD model, since it was assumed that the remaining portion connected to the floor did not influence the tests. Consequently, the beanie CAD model resulted suspended within the wind tunnel, though at the same height of the real case.

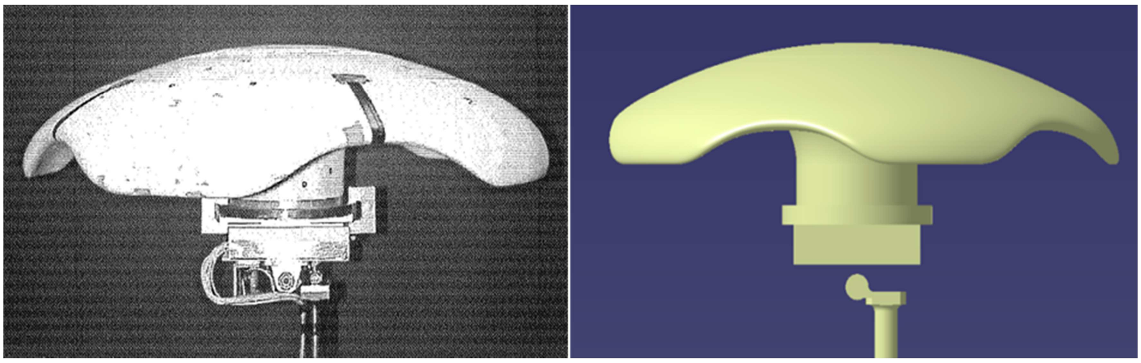

**Figure 2.3: Comparison between the real beanie, balance and retaining structure (on the left), and the CAD model (on the right).**

The superficial mesh over the AW139 beanie and its supporting system, as well as the bounding box representing the virtual wind tunnel, were generated using a specific tool within CATIA V5®. The selected parameters as quality indicators for the mesh were its skewness and aspect ratio. In fact, a maximum skewness value less than 0.75 is strongly recommended, in order for the mesh quality not to adversely affect the calculations.

In particular, two different superficial meshes, both with triangle based, linear type elements were created, in order to assess the sensitivity of the numerical results to the grid refinement:

- A grid with a whole of 60,000 elements, hereafter referred to as "*fine superficial mesh*";
- A grid with a whole of 160,000 elements, hereafter referred to as "*very fine superficial mesh*".

The different degrees of refinement can be appreciated by looking at Figure 2.4, which shows some views of the two superficial grids.

After creation of the superficial grids and control of their quality, some minor modifications were performed within TGrid® inserted of CATIA®, due to the higher flexibility of the former. Actually, within TGrid® some further improvements in the surface mesh quality indicators with respect to the those imported form CATIA® might be achieved. In the case of "*fine superficial mesh*", and the "*very fine superficial mesh*", both skewness and aspect ratio values were within the suggested ranges.

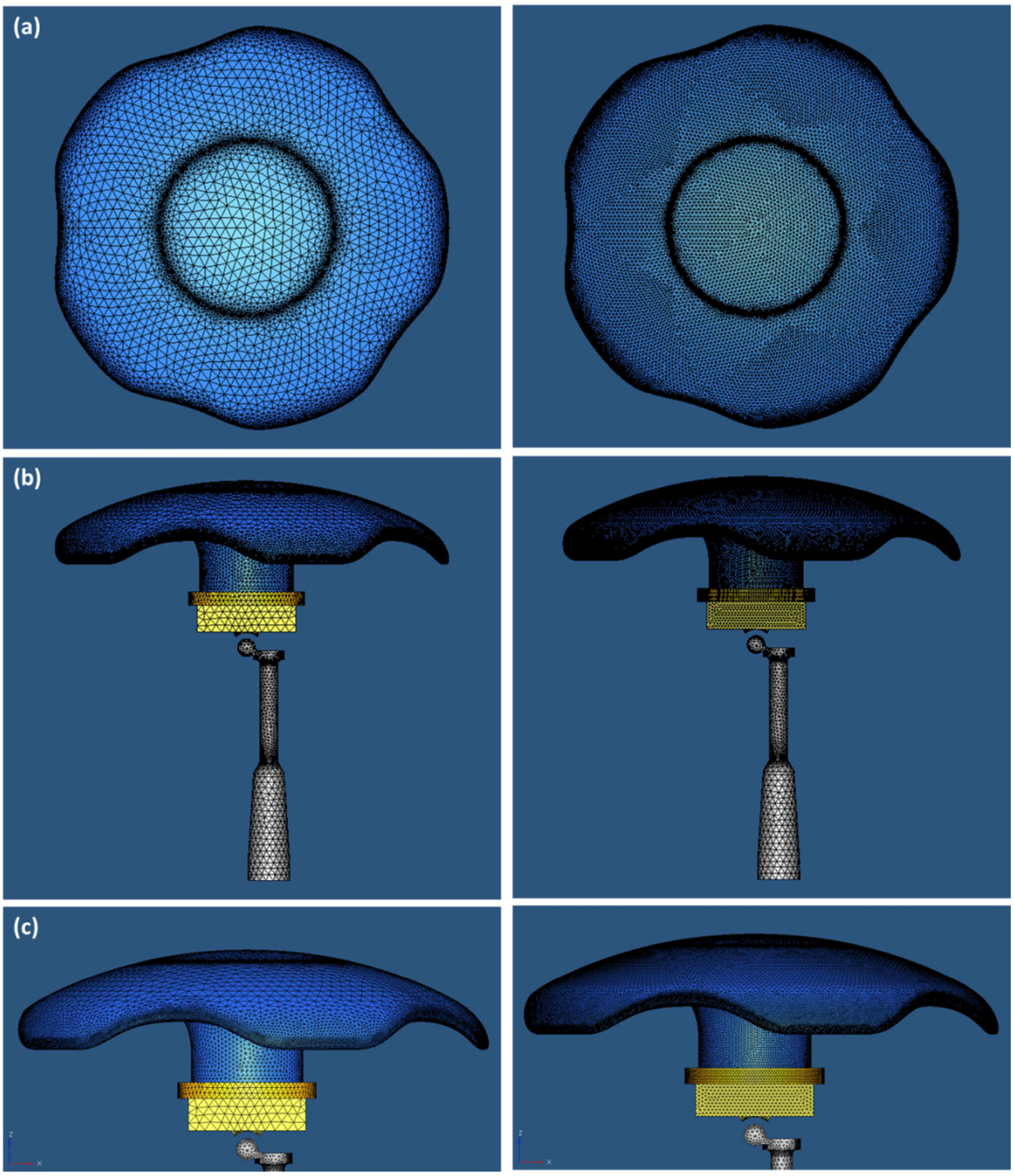

**Figure 2.4: "Fine superficial mesh" (on the left) and "Very fine superficial mesh" (on the right): top view of the beanie (a), side view of the beanie and supporting system (b) and close-up of the beanie view (c).**

As far as the bounding box is concerned, the same transversal section of the original wind tunnel (that is 4mx4m) was reproduced in the simulations, while three different longitudinal lengths were tested, with the aim of assessing the effects of the external volume dimensions on the CFD results. To this purpose, a trade-off needed to be achieved between the wind tunnel length and the subsequent number of elements in the grid. Actually, the longer the wind tunnel, the more realistic are the undisturbed flow conditions that have to be imposed over the inlet and outlet sections. As obvious, this implies an increasing number of elements, which needs to be kept to a reasonable levels due to computational resource limits.

Specifically, the three analysed cases were characterized by the following wind tunnel dimensions:

- 4x4x4 meters;
- 4x4x8 meters;
- 4x4x11.5 meters.

The three different wind tunnel configurations used in the CFD simulations are depicted in Figure 2.5. It is worth noting that the criteria used to refine the 4x4x11.5m mesh were slightly different from the others, as the number of elements would have grown beyond the limits imposed by a reasonable computational times, if the same criteria as the other two cases were adopted.

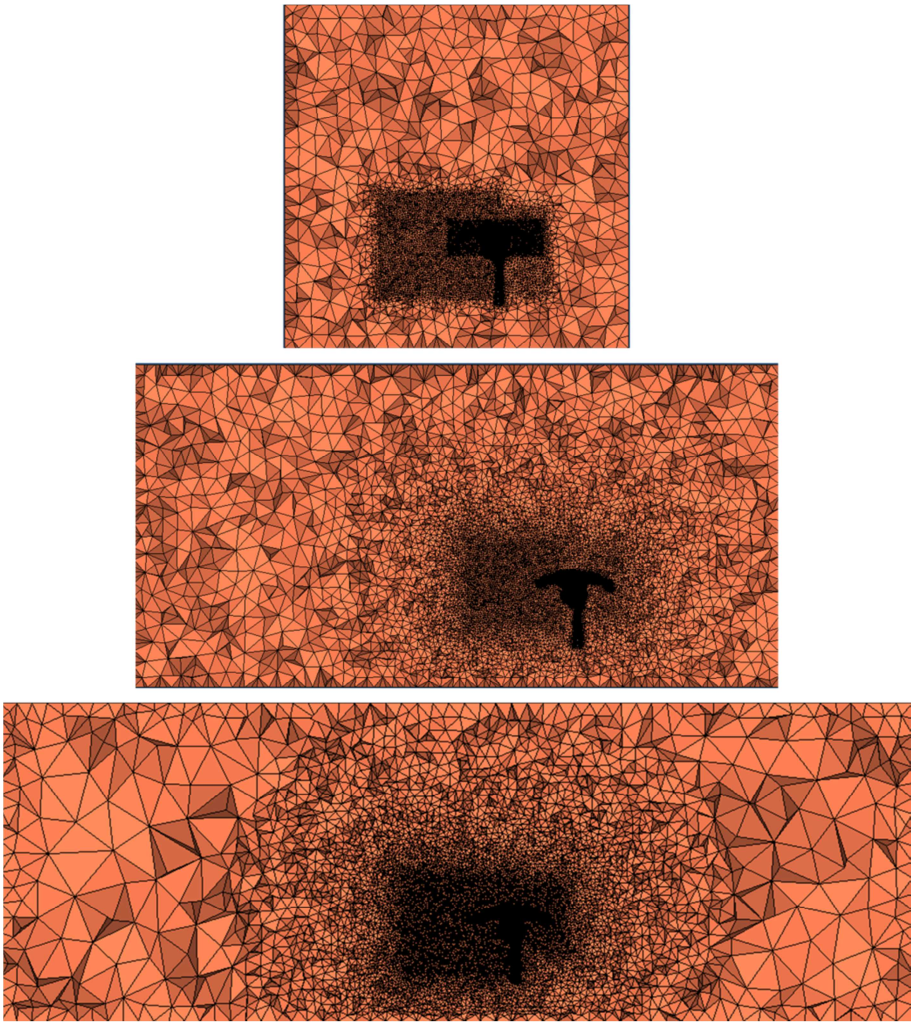

**Figure 2.5: Longitudinal section of the three volumetric meshes with different wind tunnel dimesions 4x4x4m (top), 4x4x8m (middle) , and 4x4x11.5 (bottom).**

Once the superficial grids were created, TGrid® was used for the generation of the volumetric meshes which were unstructured, with some structured elements over the beanie surfaces in order to better simulate the boundary layer. However, as the CFD calculations were carried out using conventional turbulence models, it was not necessary to create an extremely fine boundary layer. To this purpose, a specific set of first layer thickness, growth rate and number of layers was selected. The driving parameters were both the a low growth rate, which could lower the cell aspect-ratio of the boundary layer, and a total number of layers high enough to reach the total height which could correctly represent the physical boundary layer. Some of the previous guidelines are in juxtaposition one another: for example, a higher number of layer makes it possible to match the boundary layer but exaggeratedly increases the element number; a too low first height, without modification of the superficial mesh, brings the aspect-ratio to unacceptable levels; a too low growth rate, while being beneficiary to the aspect ratio, requires an increased number of layers etc. Actually, the selected set-up was shown to guarantee that for all the examined test cases the non-dimensional mesh thickness at the beanie surface $y+$ fell between 30 and 250, which is consistent with the discretization levels ($y^{+} = 30 \div 500$) suggested for the wall functions implemented in the conventional turbulence models to work properly.

Moreover, a proper volumetric grid refinement was necessary downstream of the beanie to the total pressure rake location in order to avoid numerical dissipation and correctly capture total pressure losses in the wake. As already mentioned, the mesh set up should be the result of a trade-off between the grid accuracy and its overall dimensions. To this purpose, grids with different degrees of refinement were generated in order to carry out a sensitivity study and identify the refinement level suitable to get a good correlation with experimental data in reasonable computing time. This particular study was carried out using only the 4x4x4m virtual wind tunnel and the “*very fine surface mesh*”. Three different volumetric grids, each characterized by an increased refinement level, were created:

- A volumetric grid with a whole of 1.5 million elements, hereafter referred to as “coarse volume mesh”;
- A volumetric grid with a whole of 2.7 million elements, hereafter referred to as “fine volume mesh”;
- A volumetric grid with a whole of 2.9 million elements, hereafter referred to as “very fine volume mesh”.

For each mesh, a box surrounding the beanie and extending downstream through the global domain to the total pressure rake was built, in which a local refinement could be specified. In this way, the numerical dissipation in the region of the beanie wake could be reduced, while keeping the overall number of elements to reasonable levels. Moreover, in the "*fine volume mesh*" and the "*very fine volume mesh*" a further inner box was generated near to the beanie, so as to make the transition from the boundary layer mesh to outer box more regular and gradual. This can be clearly appreciated in Figure 2.6, where a global longitudinal section of the three meshes is illustrated, while in Figure 2.7 a close-up near the beanie is reported for the three cases.

The comparison of simulation results with experimental data allowed verifying that the "*very fine volume mesh*" was the best choice for correlation with wind tunnel test acquisitions, so the same refinement criteria used to generate the "*very fine volume mesh*" were applied to create the volumetric grids with different wind tunnel dimensions. However, in order to reduce the total number of elements, rapidly growing up with the external volume dimensions, the inner box surrounding the beanie was removed, and an expansion law was given for the transition from boundary layer to the outer box.

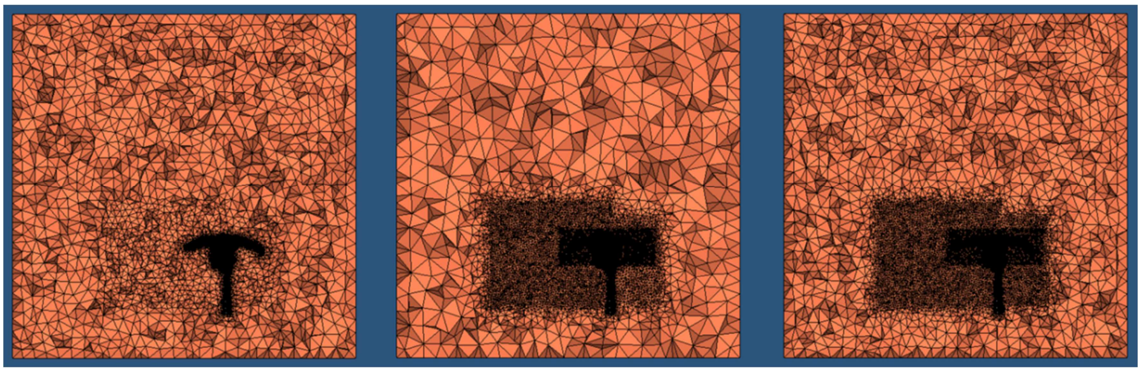

**Figure 2.6: Lonfitudinal section of the three gnerated different volumetric meshes: "Coarse Volume mesh" (left), "Fine Volume Mesh" (center), and "Very Fine Volumetric Mesh" (right).**

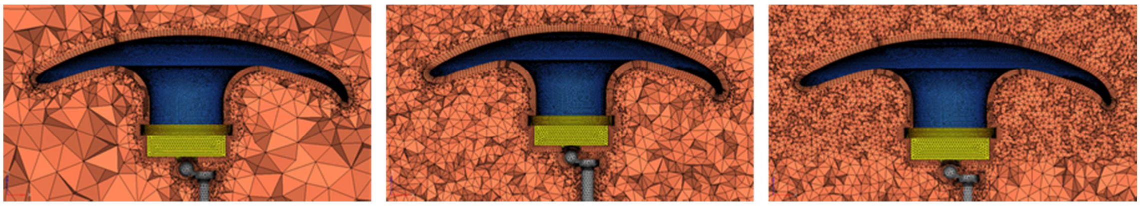

**Figure 2.7: Close-up near the beanie of three different volumetric meshes generated: "Coarse Volume mesh" (left), "Fine Volume Mesh" (center), and "Very Fine Volumetric Mesh" (right).**

### 2.2.3 The CFD simulations

CFD simulations were carried out using ANSYS Fluent® V12.0. A pressure-based type with absolute velocity formulation and steady approach was used for the numerical calculations. The k-ω SST turbulence model was selected for the simulation of the viscous effects. The air was treated as an ideal gas having constant specific heats, which automatically enabled the energy equation resolution. Fluid viscosity was modelled using the pre-defined three-coefficient Sutherland law.

The following boundary conditions were prescribed: a total pressure condition based on the experimental data was imposed on the wind tunnel inlet, while a static pressure was assigned on the outlet section. Total pressure and total temperature were calculated based on ps, T, and Ma which are the wind tunnel static pressure (i.e.101325 Pa), temperature (i.e. 293.16 K) and the Mach number at 40m/s and at 20°C respectively.

Regarding the turbulence specification method, a turbulence intensity of 5%, along with a hydraulic diameter equal to the beanie mean diameter were prescribed. All the beanie and supporting system surfaces were treated as hydraulically smooth and adiabatic, while a symmetry condition was used for the lateral surfaces of the wind tunnel box. The adopted boundary conditions for each test case are summarized in Table 2.2

| **Viscous Model** | k-ω SST | |
|---|---|---|
| **Fluid** | Air | Ideal Gas |
| | | Sutherland low for viscosity |
| **Boundary Conditions** | Pressure inlet | Gauge total pressure = 102291 Pa |
| | | Total temperature=292.94K |
| | Pressure Outlet | Gauge Pressure=101325Pa |
| | | Backflow total temperature=293.94 K |
| | Symmetry | All lateral surfaces |
| | Wall | Beanie and supporting system (No-slipping walls) |

**Table 2.2: CFD boundary condition settings**

As far as the solution algorithm is concerned, a SIMPLE scheme that solves the pressure and moment equations separately was adopted. The discretization scheme is gradually varied from the First Order Upwind to the Third Order MUSCL, passing through the Second order one, to improve the solution accuracy despite the increase of both the simulation time and the normalized RMS residuals. The under relaxation factors were left to their default values, unless the residuals were shown oscillate around a mean value, due for instance to high gradients in the fluid domain.

The solution was initialized by assessing the fluid values of the inlet section over the whole grid, in order for the iterative process to start from a reasonable solution, so that the convergence times could be reduced.

For each simulation, the convergence criterion was established when the normalized RMS residuals were less than $1 \cdot 10^{-5}$. Furthermore, some characteristic features of the flow field, such as the aerodynamic coefficients of the beanie were simultaneously monitored, in order to make sure they reached stabilized values at the end of the simulations.

The test plan of the numerical simulations was conceived as follows:

- **Step 1**: The two different beanie surface meshes ("*fine superficial mesh*" and "*very fine superficial mesh*") were compared in order to identify the best solution to be used in subsequent steps.
- **Step 2**: using the 4x4x4 m virtual wind tunnel, three volume meshes characterized by different refinement levels ("*coarse volume mesh*", "*fine volume mesh*", and "*very fine volume mesh*" respectively) were created to compare the numerical results with experimental data at the total pressure rake location.
- **Step 3**: Three wind tunnels with different longitudinal length and the same transversal section (4x4x4m, 4x4x8m, and 4x4x11.5m respectively) were analysed using the same boundary conditions to find the better compromise between mesh size and solution accuracy.
- **Step 4**: The accuracy of the First Order, Second Order and Third order discretization schemes was investigated by comparing the results obtained using the mesh that turns out to be the best choice among all the previously tested solutions.
- **Step 5**: the best mesh was then used for the simulations at angles of attack other than zero.

Among all the tested configuration, the final grid selected for the discretization order and tests and simulations at beanie different incidence angles was the 4x4x8m, with "*very fine superficial mesh*", as it was shown to match all the desired requirements in terms of:

- Reasonable required computational resources;
- Solution accuracy of the pressure distribution over the beanie surface;
- Good correlation with experimental data at the wake.

### 2.2.4 Results of the CFD test campaign

The results of the CFD simulations were compared to experimental acquisitions in terms of both pressure coefficient distribution over the beanie surfaces (along five azimuthal sections as depicted in Figure 2.8), and total pressure losses registered at the wake rake. Moreover, the experimental aerodynamic coefficients of the beanie at various angles of attack were compared to the respective CFD results.

All the data presented in the plots were normalized with respect to specific reference values due to industrial proprietary reasons.

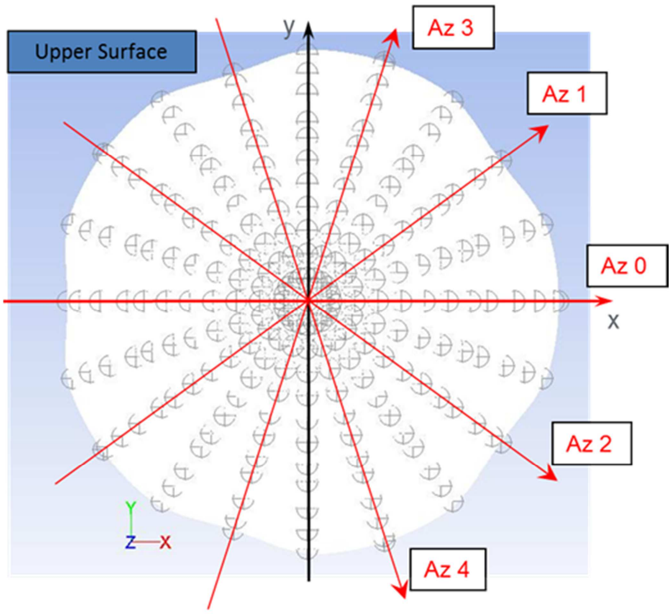

**Figure 2.8: Static pressure taps over the opper and lower surfaces of the beanie. Azimuthal section analysed during the validation process (in red).**

The **first step** aimed at understanding the effects of different beanie superficial meshes on the final CFD simulations. To this purpose, the results obtained using the "*fine superficial mesh*" and the "*very fine superficial mesh*" were compared to the experimental data in terms of static pressure distribution over the beanie upper and lower surface along five azimuthal sections. As apparent form Figure 2.9 and Figure 2.10, both the meshes gives good correlation to the wind tunnel test acquisitions over the upper surface, being the discrepancies within the range of presumable experimental uncertainty.

The differences between the two meshes were more evident at the beanie lower surface were the "*very fine superficial mesh*" gives slightly better results, especially over some azimuthal sections. Though the general trend was always captured even at this surfaces, the discrepancies between the CFD results and experimental data were more pronounced, in particular in the component fore portions, where a large flow separation region was observed and which seemed far from being captured in the simulations.

As far as the wake rake is concerned (Figure 2.11), the CFD total pressure coefficients did not satisfactorily match the experimental data, mainly because the mesh was too coarse in that particular region.

The outcomes of this fist analysis suggested that the finer mesh ("*very fine surface mesh*") was able to provide better results, in particular over the beanie lower surface, therefore this configurations was retained for the successive steps.

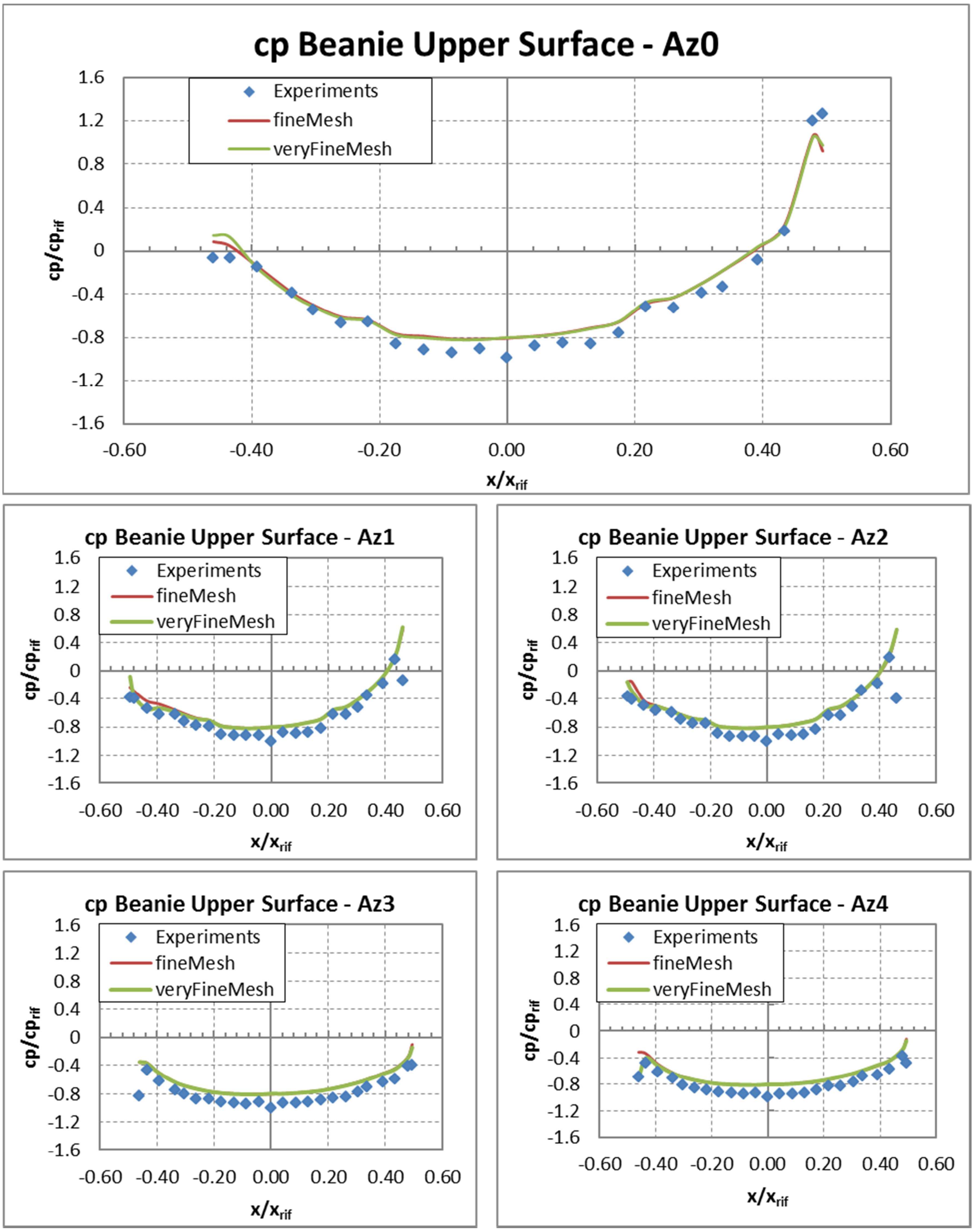

**Figure 2.9: STEP 1 – The non-dimensionalized static pressure coefficient over the beanie upper surface at different azimuthal angles.**

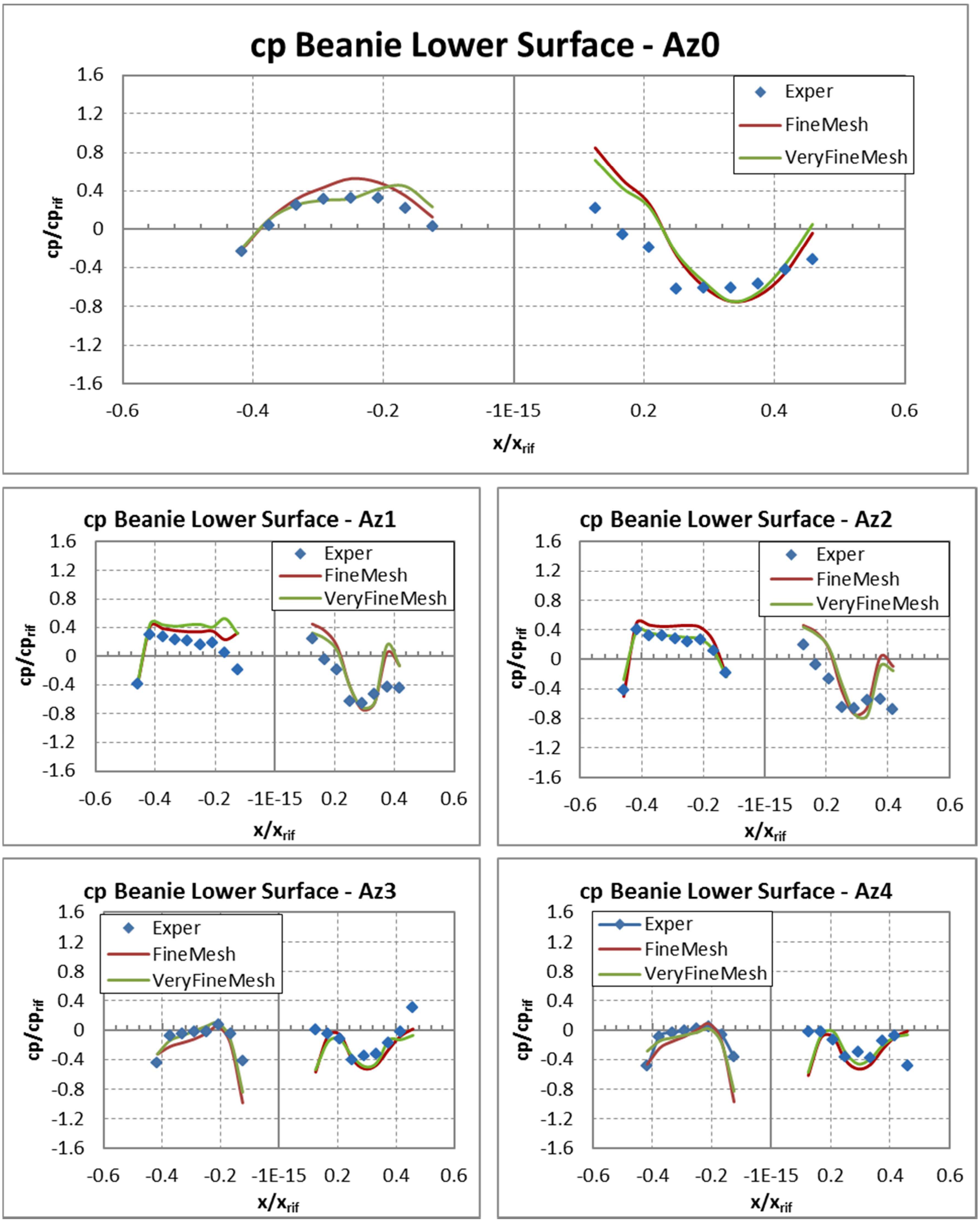

**Figure 2.10: STEP 1 – The non-dimensionalized static pressure coefficient over the beanie lower surface at different azimuthal angles.**

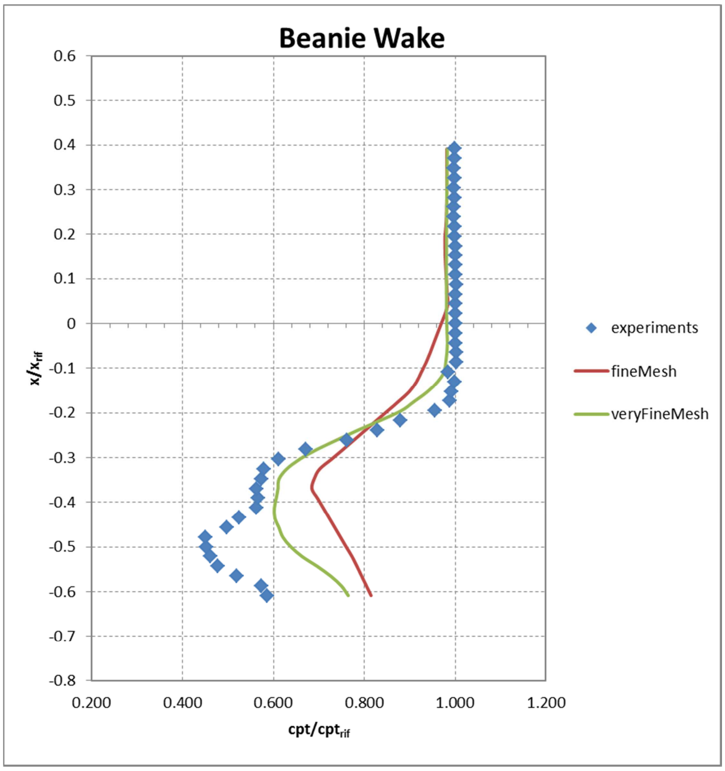

**Figure 2.11: STEP 1 – The non-dimensionalized total pressure coefficient distribution at the wake rake.**

The **second step** aimed at identifying the influence on the final CFD results of different refinement grades of the volume mesh. Figure 2.12 and Figure 2.13 depict the static pressure distribution over the beanie surfaces at different azimuthal angles compared to the experimental acquisitions. In particular, the refinement grade seemed not to influence the static pressure distribution over the beanie upper surface, as the curves were almost superimposed, while some improvements were observed at the lower surface. However, there were still evident discrepancies which were due to both the experimental uncertainty and CAD model simplification of the experimental apparatus, as is has already been explained in the previous paragraphs.

The effects of a good refinement were instead clear at the wake rake. Figure 2.14 shows the total pressure coefficient distribution at this zone. The finer meshes gave excellent agreement with the experimental data on the upper portion of the rake. Total pressure measurements at the lower part of the rake were strongly influenced by the wind tunnel experimental apparatus and by the beanie retaining structure. As these components were simplified in the CAD model, the lack of correlation was expected.

This analysis clearly showed that a grid refinement was required to avoid the numerical dissipation and correctly capture the wake characteristic downward of the beanie. Therefore, the criteria used for the creation of the "*very fine volume mesh*" were also applied during the following analysis, since they provided better results.

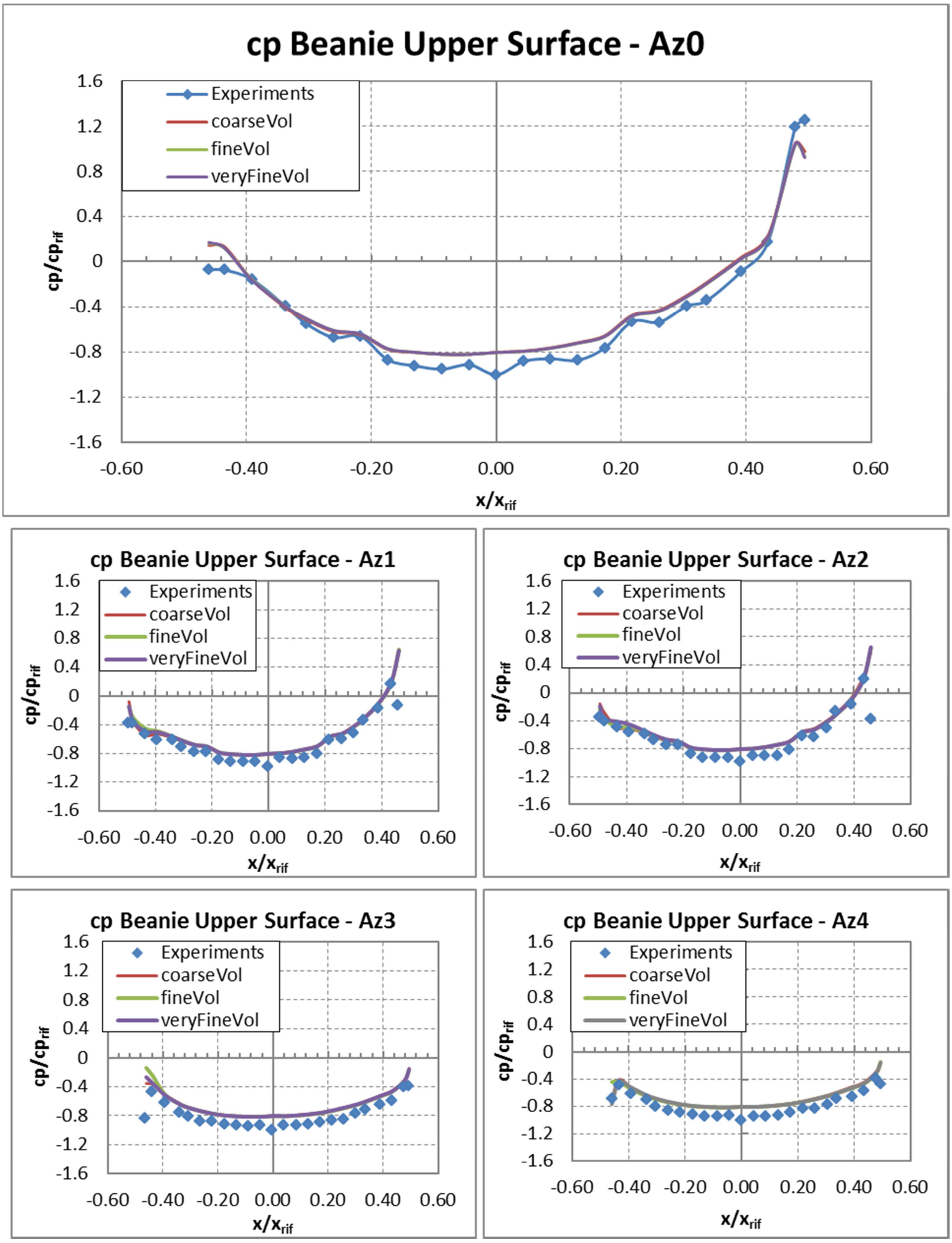

**Figure 2.12: STEP 2 – The non-dimensionalized static pressure coefficient over the beanie upper surface at different azimuthal angles.**

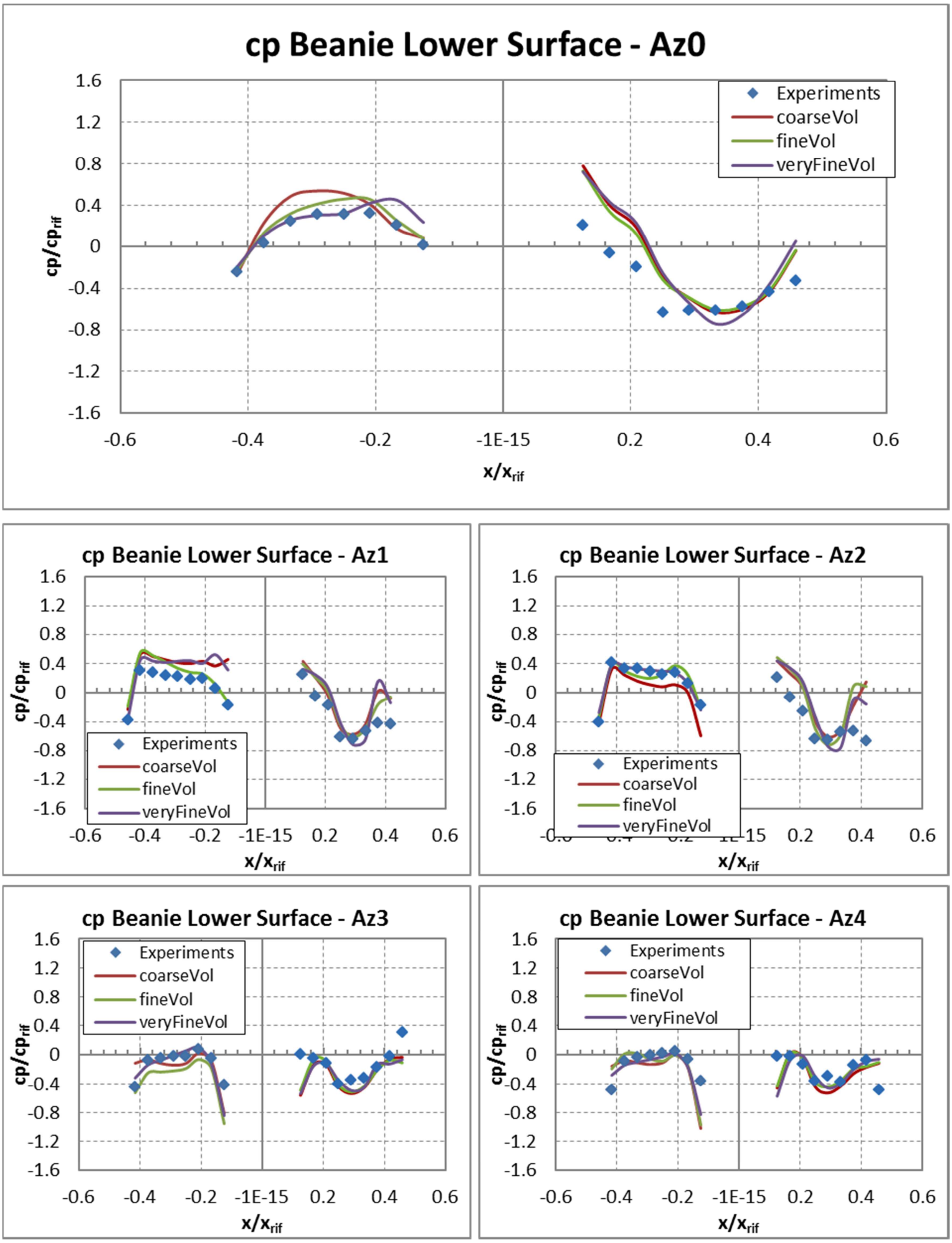

**Figure 2.13: STEP 2 – The non-dimensionalized static pressure coefficient over the beanie lower surface at different azimuthal angles.**

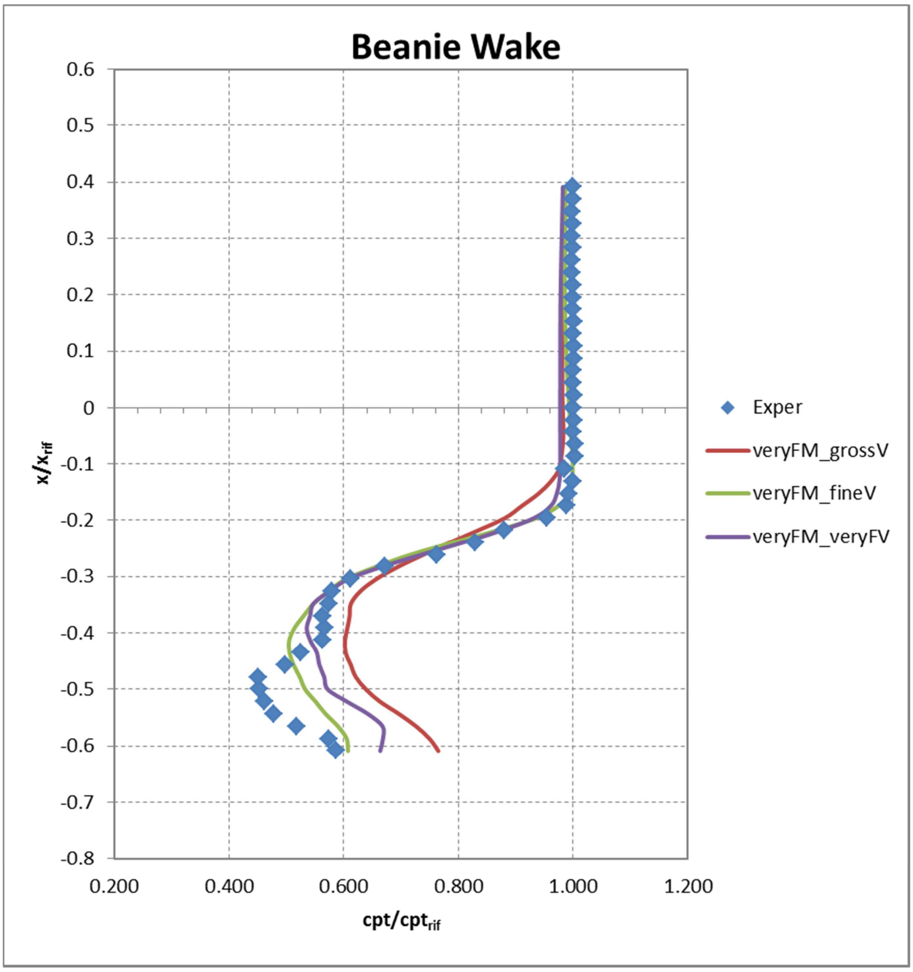

**Figure 2.14: STEP 2 – The non-dimensionalized total pressure coefficient distribution at the wake rake.**

In the **third step**, three cases characterized by increasing longitudinal length of the virtual wind tunnel were analysed. Once again, the static pressure distribution over the beanie upper surface followed the trend described before (Figure 2.15), while some changes were observed at the beanie lower surface. (Figure 2.16). As far as the total pressure coefficient at the beanie wake rake is concerned, there was an excellent agreement between CFD results and experimental data, as apparent from Figure 2.17. The discrepancies that could be seen in the 4x4x11.5m case were due to the fact that the mesh was a little bit coarser than the other volume meshes to keep the required computational time and resources to an acceptable limit.

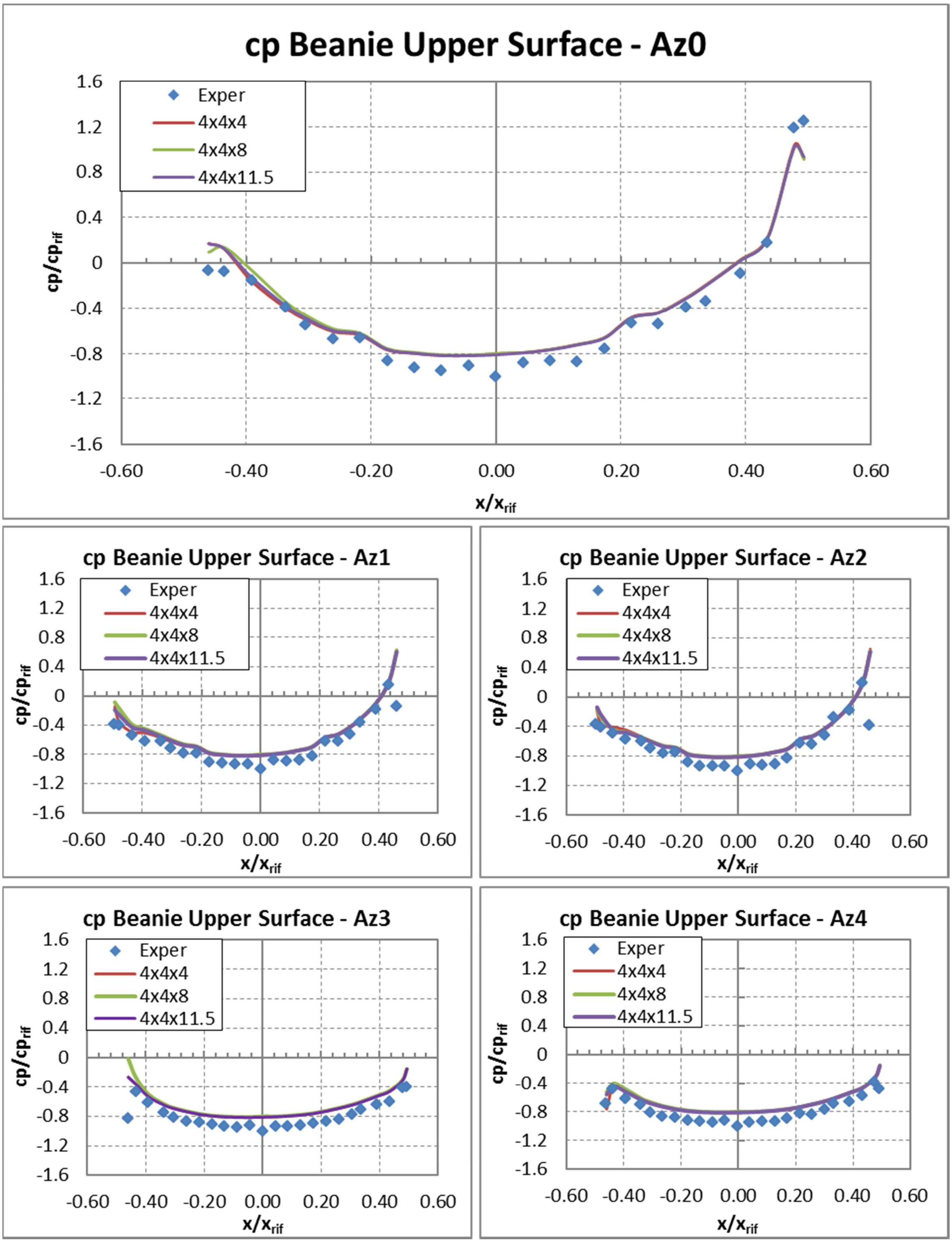

Figure 2.15: STEP 3 – The non-dimensionalized static pressure coefficient over the beanie upper surface at different azimuthal angles.

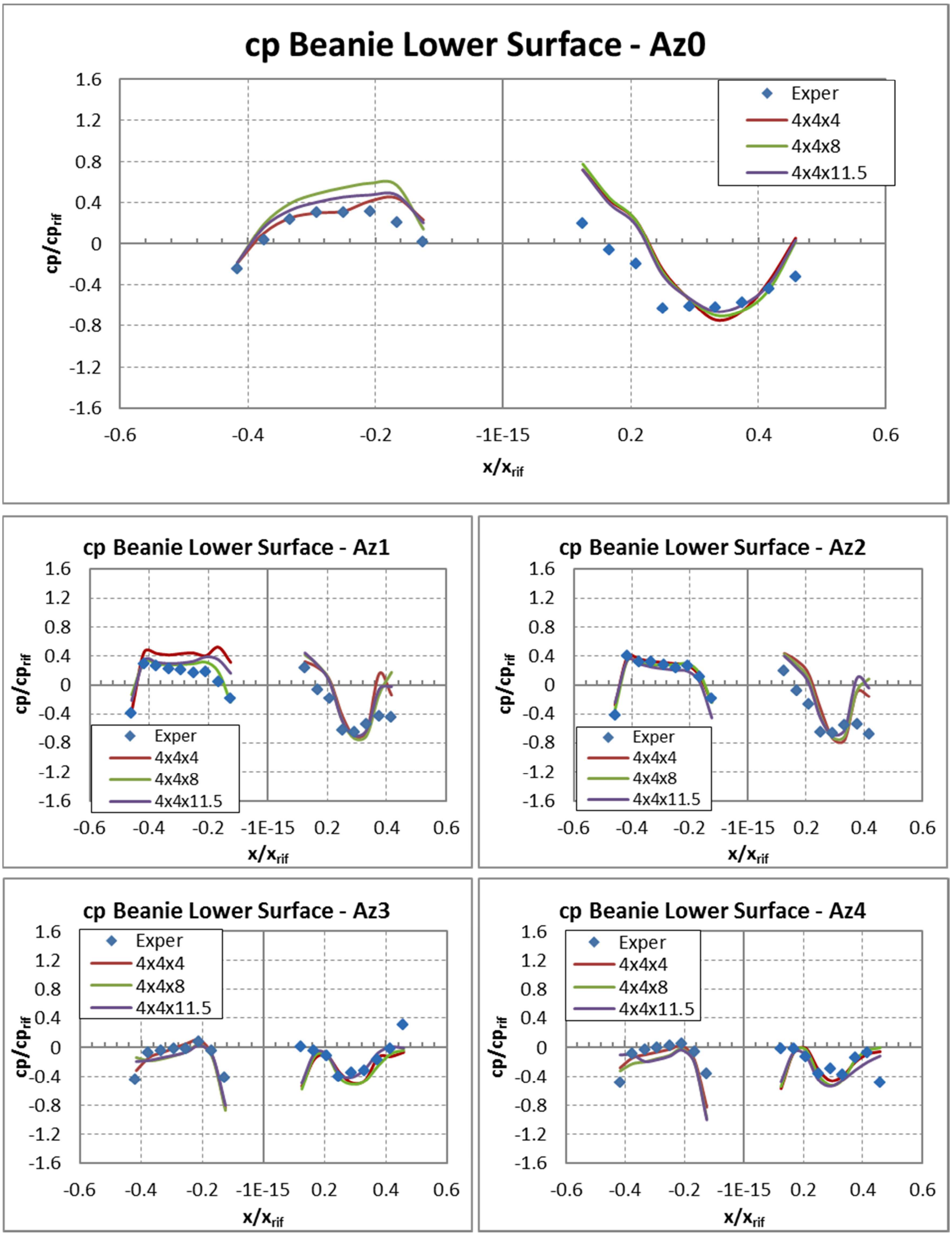

**Figure 2.16: STEP 3 – The non-dimensionalized static pressure coefficient over the beanie lower surface at different azimuthal angles.**

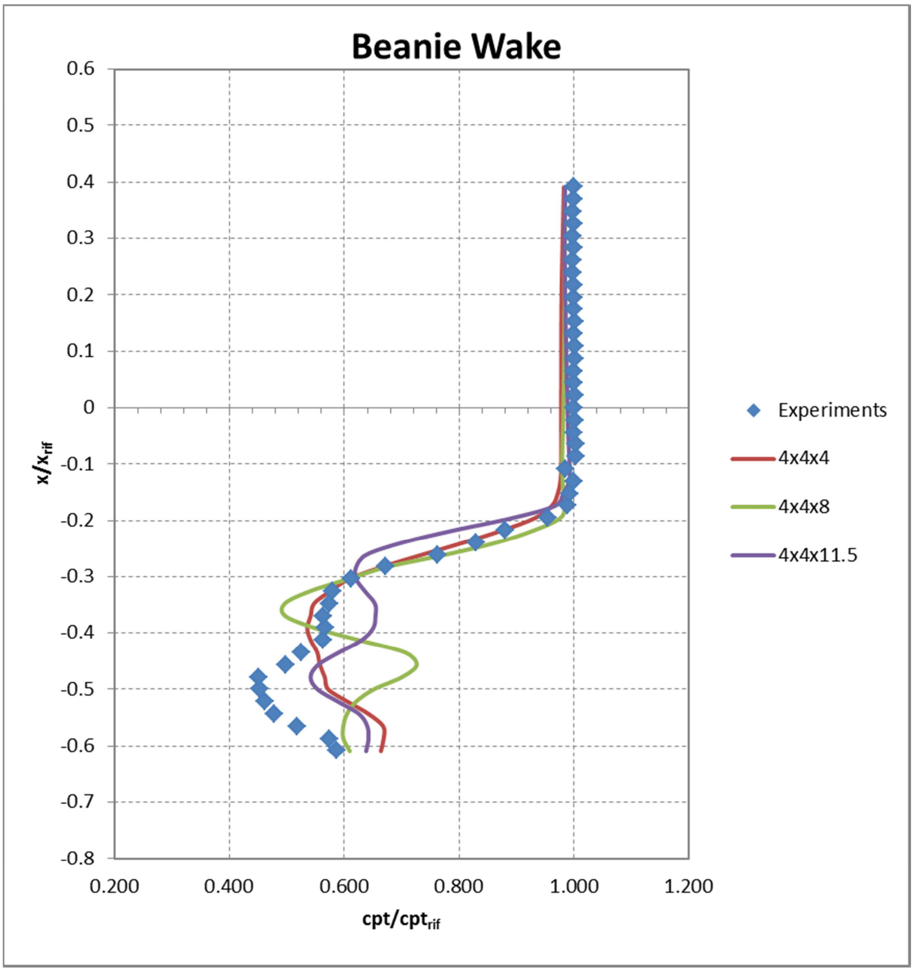

**Figure 2.17: STEP 3 – The non-dimensionalized total pressure coefficient distribution at the wake rake.**

The effects of using different discretization schemes on the CFD final results were analysed during the **fourth step**. Generally speaking, the solution accuracy improves with the increase of the discretization schemes to the detriment of the RSM residuals. Therefore, the CFD results obtained by means of the First Order, Second Order and Third Order MUSCL discretization schemes were compared to experimental results. The test case was created following the criteria drawn during the previous analyses.

The static pressure coefficient distribution over the beanie surfaces depicted in Figure 2.18 and Figure 2.19 showed that the first order scheme was not sufficient to obtain accurate results, especially at the fore part of the beanie, where the largest discrepancies were observed. However, both the second and the third order schemes seemed both to provide better results also as far as the total pressure coefficient the beanie wake was concerned (Figure 2.20).

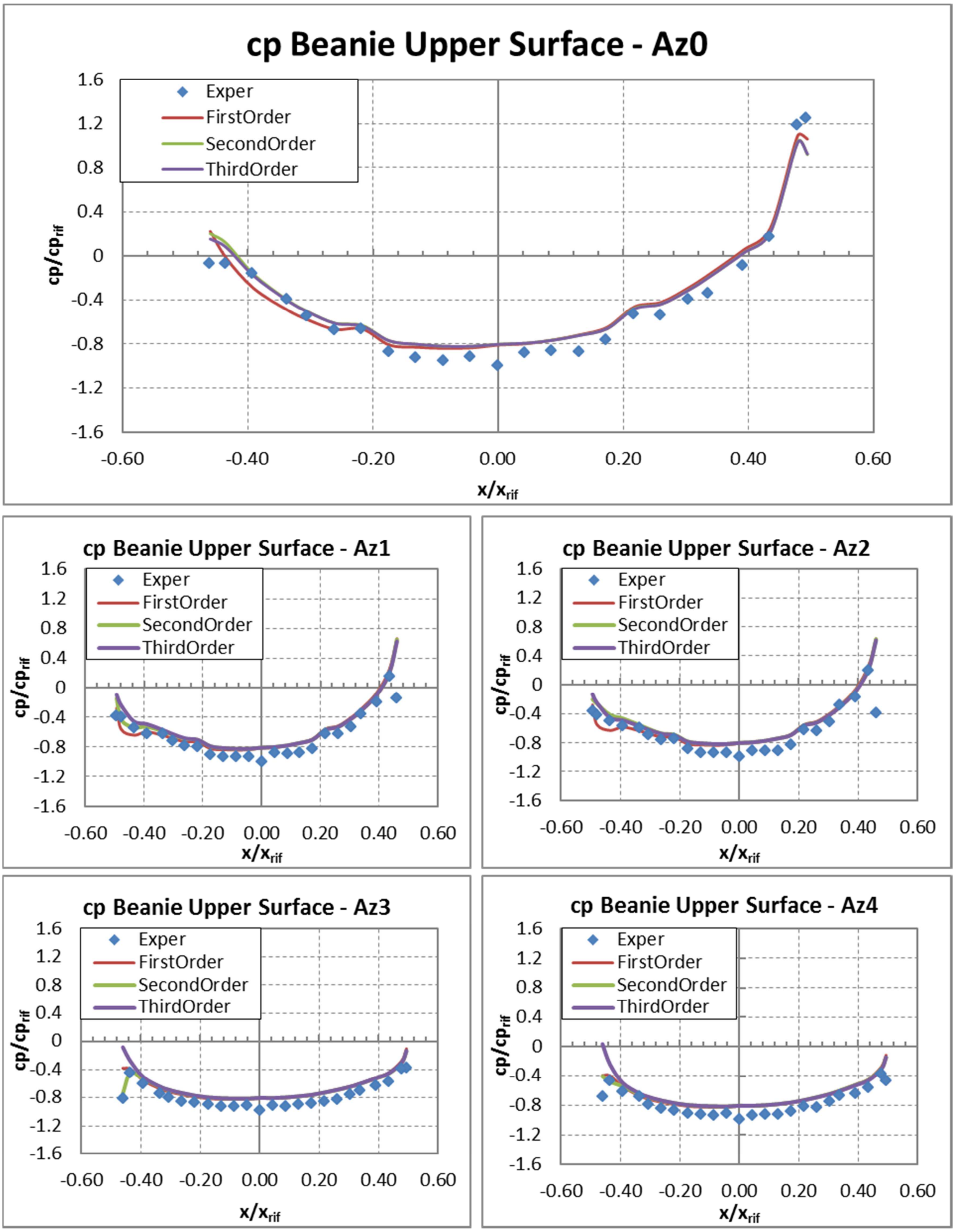

**Figure 2.18: STEP 4 – The non-dimensionalized static pressure coefficient over the beanie upper surface at different azimuthal angles.**

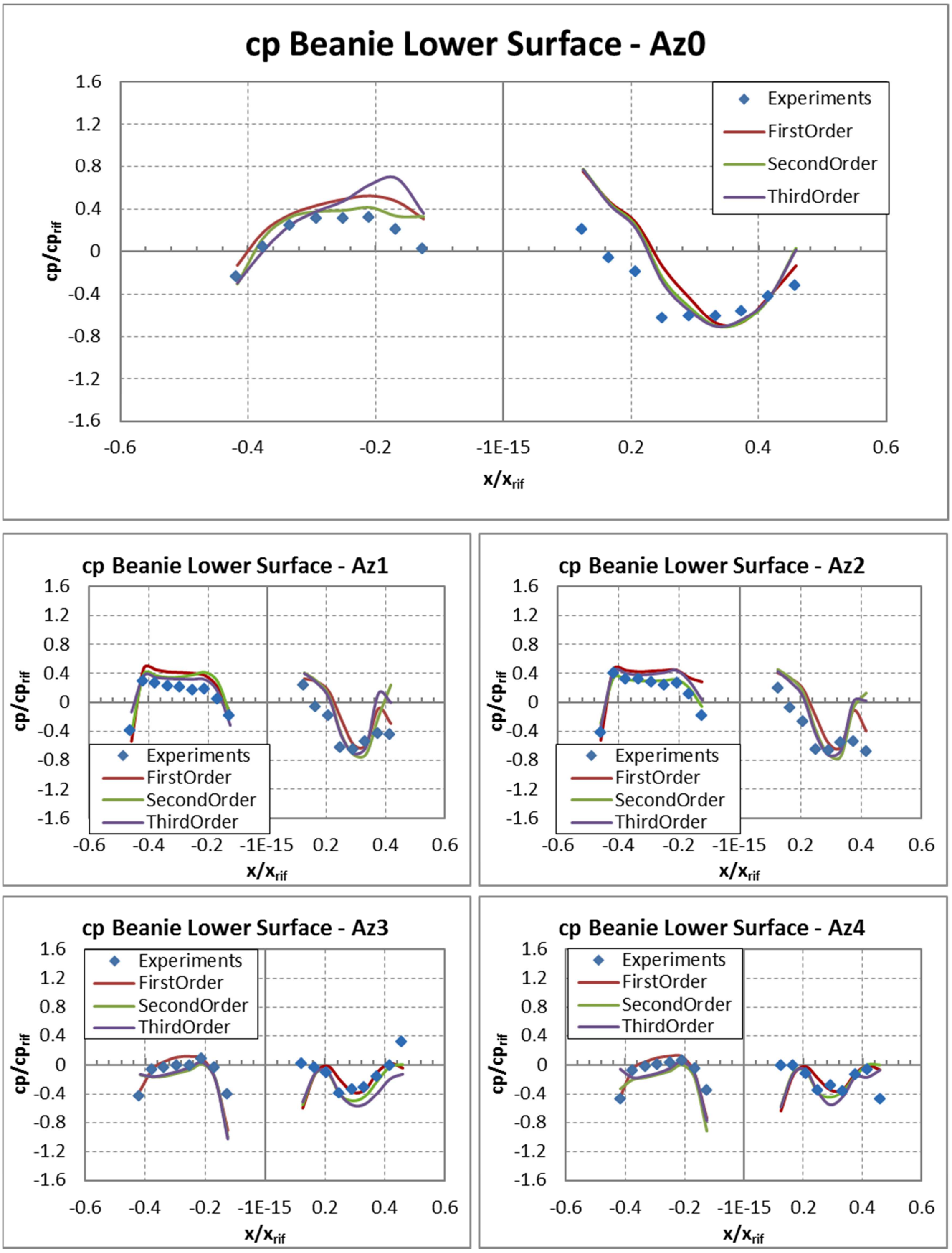

**Figure 2.19: STEP 4 – The non-dimensionalized static pressure coefficient over the beanie lower surface at different azimuthal angles.**

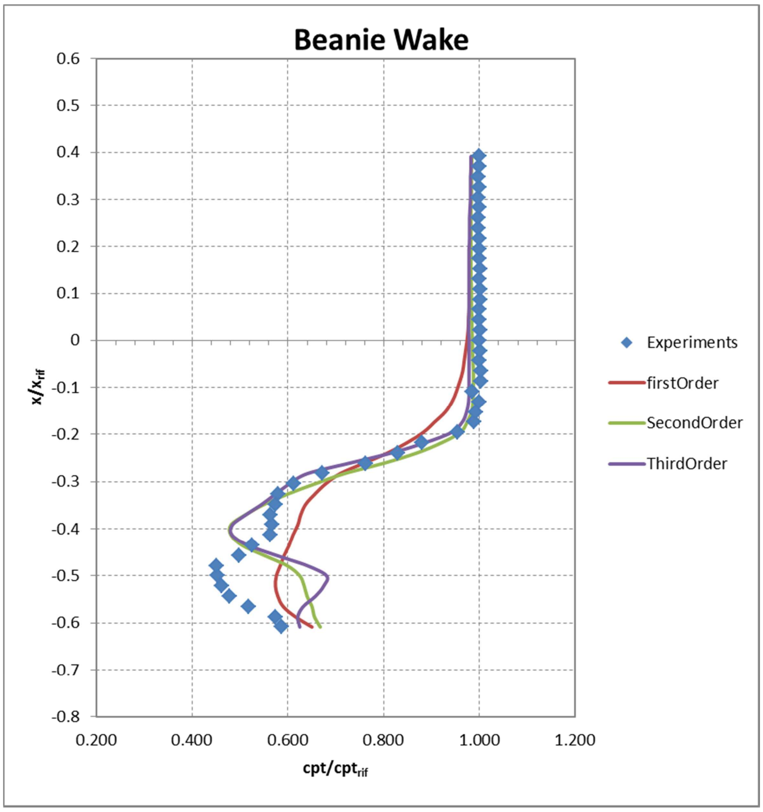

**Figure 2.20: STEP 4 – The non-dimensionalized total pressure coefficient distribution at the wake rake.**

Finally, the beanie was analysed at four different attack angles in the **fifth step**, and the results are reported in Figure 2.21. The CFD simulations well capture the distribution of the static pressure coefficient over the beanie upper surface, though some discrepancies were still observed at the beanie lower surface especially at highly negative attack angles (-10°) where the correlation became not satisfactory due to a large flow separation.

The total pressure coefficient distribution at the wake rake was always well captured, except in the case of negative attack angles (Figure 2.22). This trend was expected because the influence of the test rig on the rake became more important as incidence decreased. Therefore, the lack of agreement with the experimental data, especially in the lower portion of the rake, was mainly due to the simplifications of the CAD model relating to the experimental apparatus and the beanie retaining system.

Finally, the Figure 2.23 shows the comparison concerning the steady lift, drag and pitching moment coefficients, between the experimental data and CFD results. As apparent, there was a good correlation for $\alpha \geq -5°$, while moderate discrepancies could be observed at highly negative incidence angles, due to both the geometrical simplification and the large flow detachment under the beanie. However, the general trend was always captured.

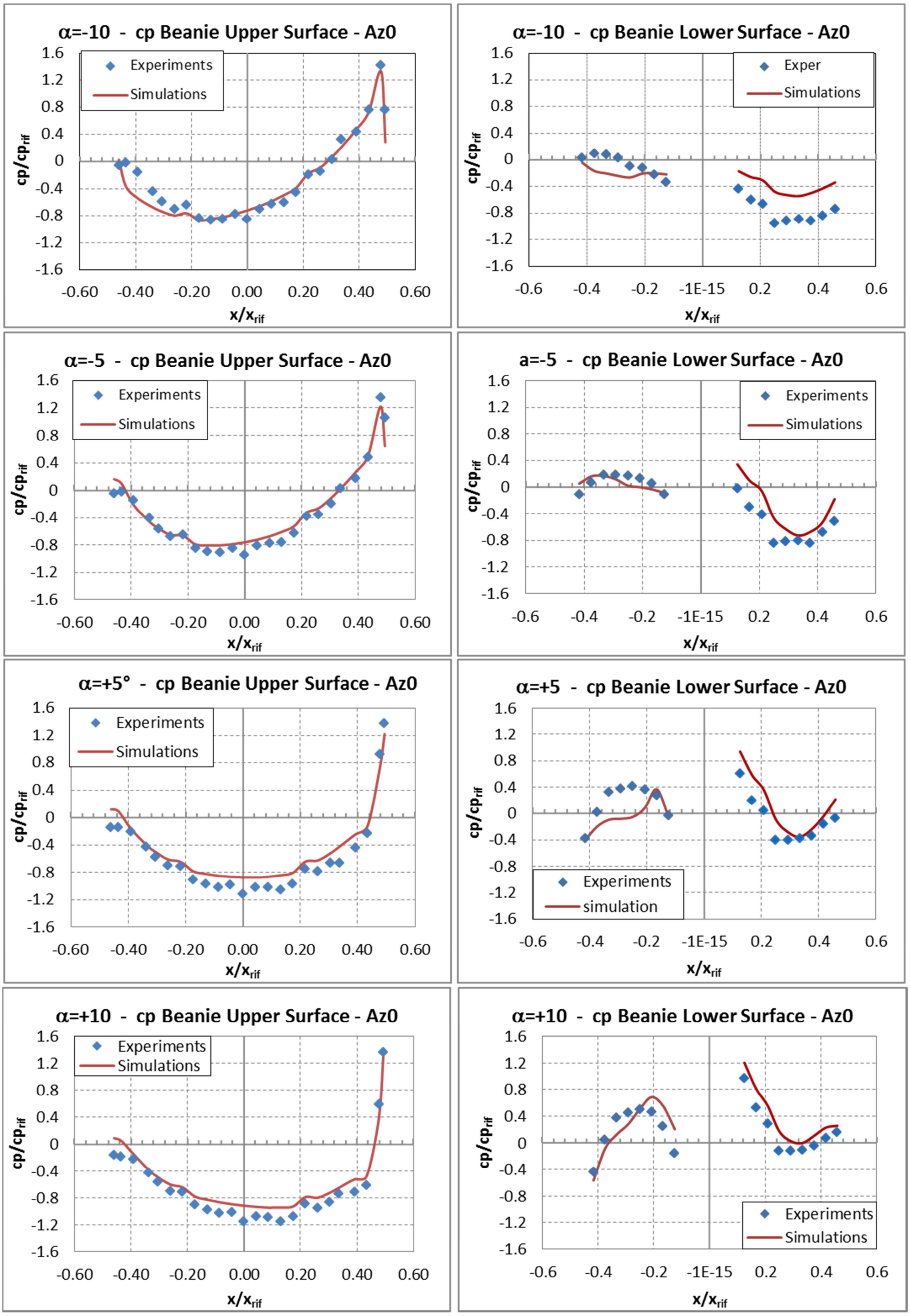

Figure 2.21: STEP 5 – The non-dimensionalized Cp distribution over the beanie (left column) and lower (right column) surfaces at different angles of attack.

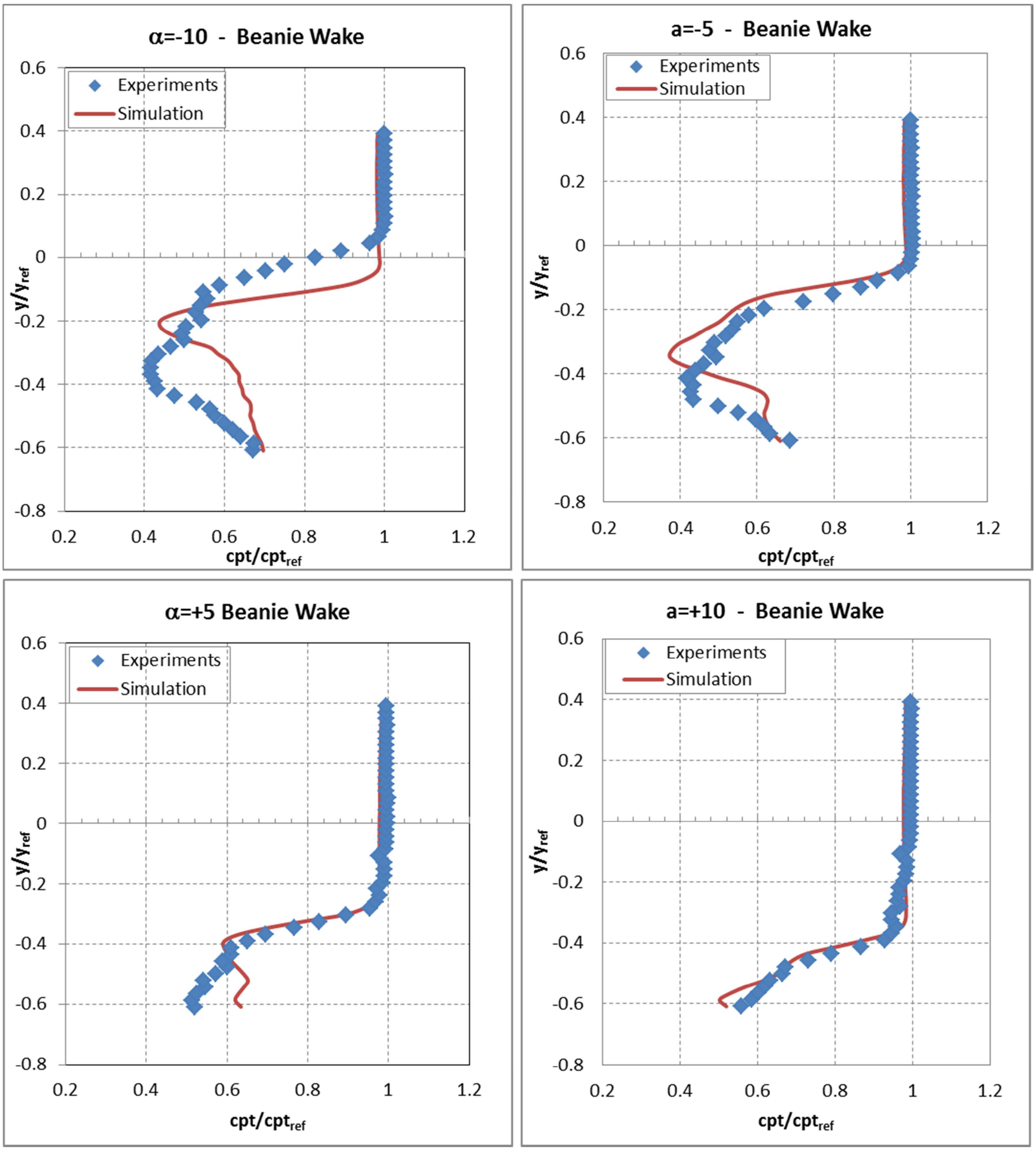

**Figure 2.22: STEP 5 – The non-dimensionalized total pressure coefficient at the wake rake at different angles of attack.**

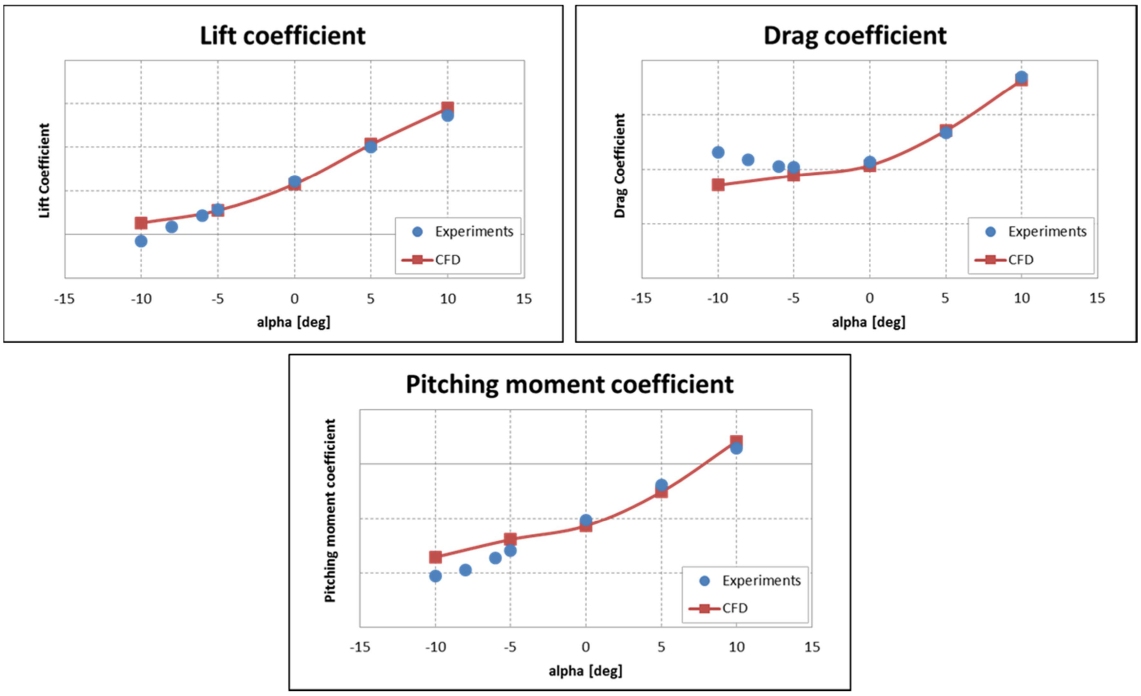

**Figure 2.23: STEP 5 – The beanie polars.**

## 2.3 *The AW109 beanie CFD validation*

A similar validation activity to the one described in the previous paragraph was carried out on the AW109 beanie. The experimental data were acquired in wind tunnel test campaign at the “Politecnico di Milano” in 2004. The test conditions were the same used in the AW139 analyses, though the experimental apparatus consisted only of static pressure taps placed over the beanie. Therefore, the global forces acting on it, as well as the total pressure distribution downstream of the beanie could not be measured. A series of tests at different angles of attack were carried out in order to completely cover the attitudes envelope required for the certification of the AW109 hub cap. At each test, the data of the static pressure distribution over the beanie upper and lower surface were acquired and collected in [15].

Due to the similarities between the AW109 and AW139 wind tunnel test campaign, no direct investigation on the grid sensitivity was performed in this case, but the indication drawn in the previous paragraph, that were proven to guarantee a satisfactory correlation to experimental data, were followed for the set-up of the AW109 beanie numerical model. However, some minor changes in the mesh refinement parameters were implemented, in order to reduce the required computational resources. In fact, in this case it was not mandatory to increase the number of elements downstream of the beanie to correctly capture the total pressure losses, since no experimental data on the wake were available for validation purposes.

The comparison between experimental acquisitions and numerical results were carried out in terms of static pressure coefficients over the beanie upper and lower surfaces. Moreover, the simulated lift, drag and moment polars will be presented, even if no direct comparison with experimental data was possible. In fact, as already mentioned, no extensimetric apparatus was installed in the wind tunnel model, so the global forces acting on the beanie at the various tested conditions could not be acquired.

### 2.3.1 The wind tunnel test campaign

The model used for these tests was the exact full scale reconstruction of the AW109 hub fairing, which was mounted on a pylon and installed in a wind tunnel with a transversal section 4mx4m large. A proper interface between the pylon and the beanie was created in order to allow straightforward modifications of the component's angle of attack during the tests. Unlike the test rig used in [13], no force transducer was installed in this case.

The acquisition of the static pressure coefficients was carried out using 86 pressure taps distributed over the upper and lower surfaces of one half of the beanie, the location of which is depicted in Figure 2.24. The origin of the local coordinate system used to define the pressure taps position was located at the intersection of the beanie rotational axis and its upper surface. Finally, unlike the AW139 case, due to the model symmetry it was not necessary to rotate the beanie around its axis to acquire the pressure distribution over its second half (i.e. the portion not equipped with pressure taps).

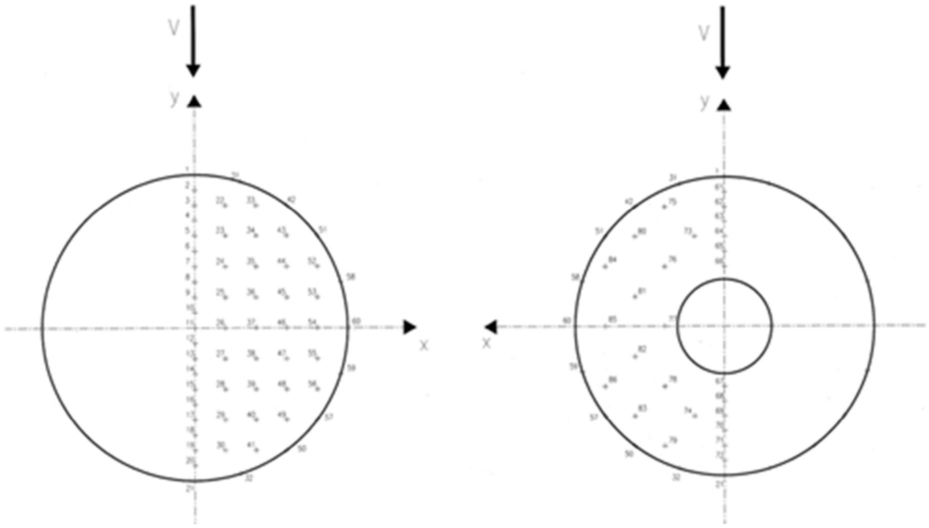

Figure 2.24: Location of the pressure taps over the beanie.

As already mentioned, the tests were carried out at the "Politecnico di Milano Wind Tunnel". The model was installed within the 4x4 $m^2$ closed tests section, using a particular supporting system described in §2.2.1

The beanie was connected by means of two flanges to the supporting system, which was the exact reproduction of the balance used in for the AW139 beanie validation analysis, though no real extensimetric balance was installed in this case. This element was then positioned on a rotating bracket in order to be able to test the beanie at different angles of attack (in the range of $-21° \leq \alpha \leq 24°$). All the cables were arranged in such a way to reduce their influence on test results as much as possible. Finally, the experimental runs were carried out at the conditions already presented in Table 2.1.

### 2.3.2 The numerical model

The beanie geometric model was created within CATIA V5® following the indications provided by *AgustaWestland*. The balance and main supporting system were the same described in §2.2.2. As already pointed out hereinbefore, for the sake of simplicity the actual balance and supporting system used in the wind tunnel campaign were slightly modified in the CAD model: specifically, some of the geometry details that could have become troublesome in the meshing phase were removed. Moreover, some details were simplified because of the lack of reference CAD models. The CAD model of the beanie is represented in Figure 2.25, while in Figure 2.26 a side view of the supporting system is depicted. Only the upper portion of the shaft was reproduced in the CAD model because the lower portion, connected to the floor, was assumed not to influence the tests. Consequently, the beanie was suspended within the wind tunnel, though at the same height of the real case.

The model was inserted into a 4mX4mX8m bounding box geometry representing the virtual wind tunnel: the bounding box dimensions were selected following the indications drawn in the AW139 beanie analysis. In fact, the 4mX4mX8m bounding box was proven to be the best trade-off solution between the wind tunnel length and the subsequent number of elements in grid, that still realistically represent the undisturbed flow conditions that are to be imposed over the inlet and outlet sections.

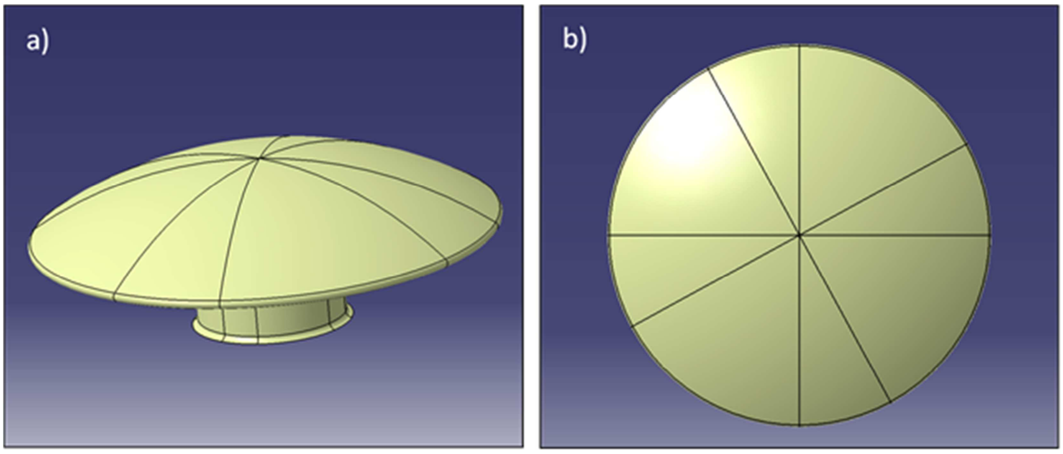

**Figure 2.25: The CAD model of the AW109 beanie.**

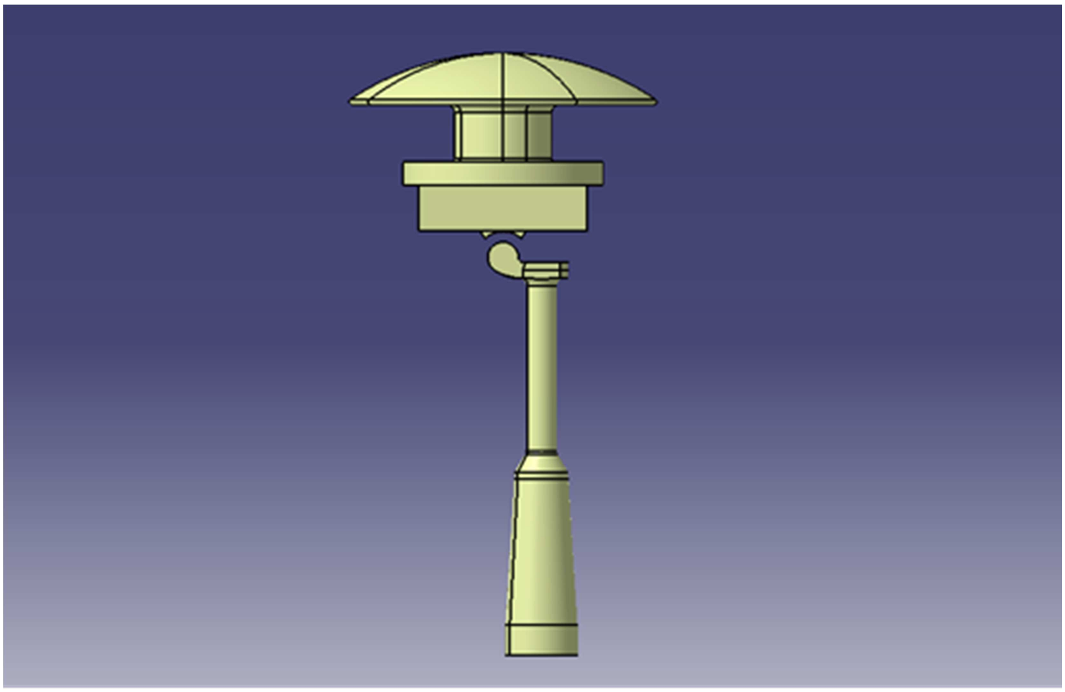

**Figure 2.26: Side view of the CAD model of the beanie supporting system.**

The superficial meshes over the AW109 beanie and its supporting system, as well as the mesh of the bounding box representing the wind tunnel, were generated using a dedicated tool within CATIA®. The selected parameters as quality indicators for the mesh were its aspect ratio and skewness. In particular, the latter has to be kept below a maximum value of 0.75 in order for the mesh quality not to adversely affect the calculations.

In this specific case, a whole of 21,000 triangle based, linear type elements were generated over the beanie and its supporting system. Both skewness and aspect ratio values of all the generated superficial grids are within the suggested ranges. Figure 2.27 shows some views of the superficial grids.

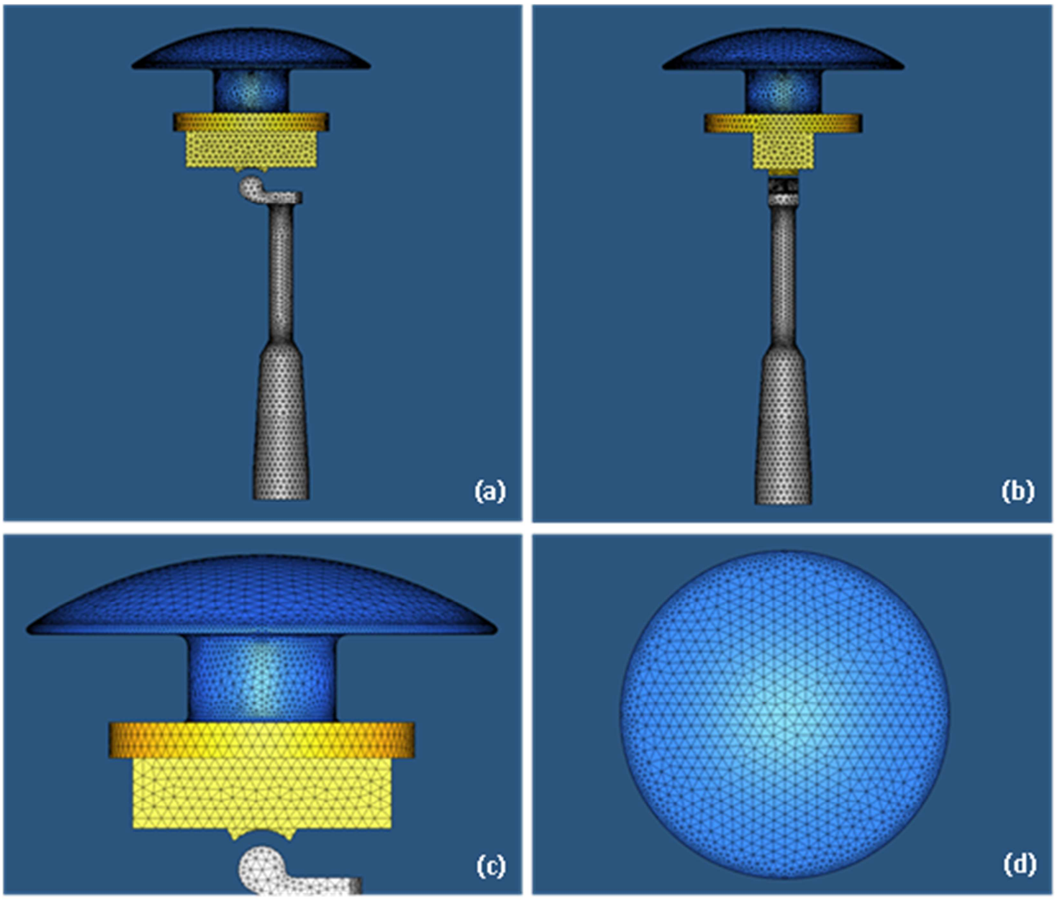

**Figure 2.27: The beanie and supporting system surface meshes: side view of the beanie (a), front view of the beanie (b), close-up of the beanie side view (c), top view of the beanie (d).**

As far as the volumetric mesh is concerned, it was generated using TGrid® V5 and following the indications drawn in the analysis of the AW139 beanie. It was unstructured with some structured elements over the beanie and its supporting system surface in order to better simulate the boundary layer. However, as the CFD calculations were carried out using conventional turbulence models, it was not necessary to create an extremely fine boundary layer mesh. The drivers in the boundary layer mesh parameters selection were both a low growth rate, which could lower the cell aspect ratio of the boundary layer, and a total boundary layer high enough to reach a total height which could correctly represent the physical boundary layer. The parameters used in the generation of the prismatic cells were substantially derived from the AW139 sensitivity analysis, though some minor changes were carried out in order to reduce the total number of elements and thus lower the required computational resources. Actually, the selected set-up was shown to guarantee that for all the examined test cases the non-dimensional mesh thickness at the beanie surface y+ fall between 30 and 290, which is consistent with the discretization levels (y+=30÷500) suggested for the wall functions implemented in the conventional turbulence models to work properly.

Finally, the fluid domain inside the virtual wind tunnel was filled in using tetrahedral elements. By looking at Figure 2.28, it is apparent that the mesh refinement was lower than that used in the analysis of the AW139 beanie. This choice was viable here because a volumetric grid refinement downstream the beanie was no longer required for simulation of the wake pressure losses, since the AW109 experimental model was not equipped with a wake rake and hence no validation of the simulated wake behaviour was possible. Therefore, a global decrease of the volumetric growing rate was allowed without excessively increasing the total number of elements. Specifically, 730,000 cells were created on the whole for each of the analysed angle of attack. Once the volumetric grid was generated, its quality indices were always optimized by means of some TGrid® tools in order for the mesh quality to be improved, so that potential difficulties in calculations' convergence due to the most distorted elements could be prevented.

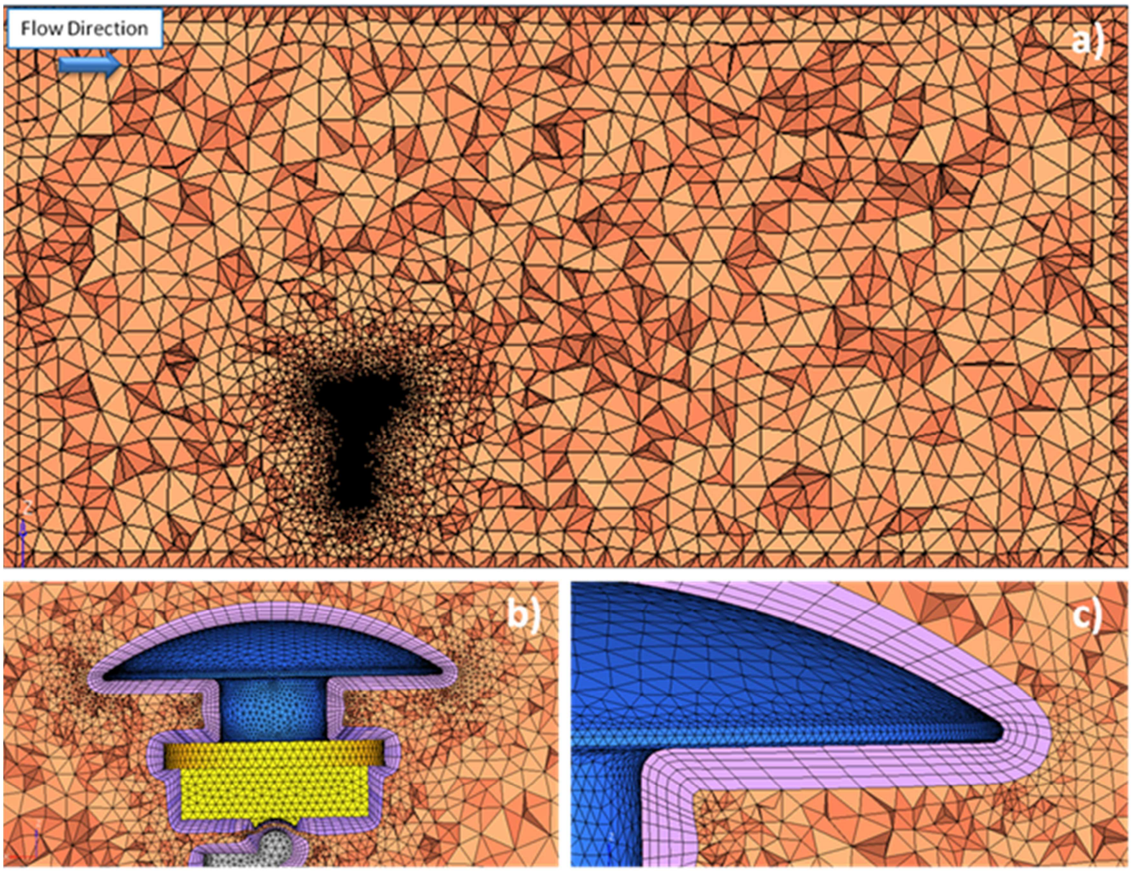

**Figure 2.28: The volumetric mesh around the beanie and the supporting system in the case of α=-1 deg; a) global longitudinal view; b) close up of the beanie; c) close up of the prismatic layers over the beanie.**

### 2.3.3 The CFD simulations

CFD simulations were carried out using ANSYS Fluent® v.12. A pressure-based solver type with absolute velocity formulation and steady approach was used for the calculations. The k-ω SST turbulence model was selected for simulation of viscous effects. The air was treated as an ideal gas having constant specific heats, which automatically enabled the energy equation resolution. Fluid viscosity was modelled using the pre-defined three-coefficients Sutherland law.

Similarly to the simulations carried out in the case of the AW139 beanie, the following boundary conditions were prescribed: a total pressure condition based on experimental data was imposed at the wind tunnel inlet, while a static pressure was assigned on the outlet section. Total pressure and total temperature were calculated based on the wind tunnel static pressure, static temperature and speed of the selected condition, which are reported in Table 2.3.

| **Operating Conditions** | |
|---|---|
| Static pressure | 101325 Pa |
| Static temperature | 293.16 K |
| Speed | 40 m/s |

**Table 2.3: Selected operating conditions for the CFD simulations of the AW109 beneie.**

As far as the turbulence specification method is concerned, a turbulence intensity of 5%, along with a hydraulic diameter equal to the beanie mean diameter were prescribed. All the beanie and supporting system surfaces were treated as hydraulically smooth and adiabatic, while a symmetry condition was used for the lateral surfaces of the wind tunnel box. The adopted boundary conditions for each test case are the same used in the AW139 analyses and are summarized in Table 2.2.

Moreover, A SIMPLE scheme was adopted as the solution algorithm. The discretization scheme was varied from the First Order Upwind to the Third Order MUSCL since a higher order is suggested for improving the solution accuracy, despite the increase of both the simulation time and the normalized RMS residuals. The under-relaxation factors were left unchanged to their default values.

The solution was initialized by assessing the fluid values of the inlet section over the fluid domain and by using an absolute reference frame, in order for the iterative process to start from a reasonable solution to speed up the convergence.

For each simulation, the convergence criterion was established when the RMS residuals were less than $6 \cdot 10^{-3}$. Furthermore, the difference between the mass flow rate between inlet and outlet was monitored in order to make sure it reached a stabilized value at the end of the simulations.

Finally, The variation of the angle of attack was performed by rotating the virtual wind tunnel and the supporting system of an angle equal and opposite to the required beanie incidence. Therefore, the beanie remained fixed with the absolute reference system, so that tap coordinates did not change at each trim. Then, the volumetric mesh was generated as discussed in the previous paragraph.

Specifically, nine different configurations at nine angles of attack were simulated and the results were compared to the experimental data. The numerical simulations' test plan is reported in Table 2.4. As mentioned above, it is worth noting that the AW109 main rotor mast is tilted by an angle equal to -6° with respect to the fuselage vertical axis.

| α fuselage (deg) | **α beanie (deg)** | Experimental Test reference number [15] |
|---|---|---|
| -15 | **-21** | 5 |
| -10 | **-16** | 7 |
| -5 | **-11** | 9 |
| 0 | **-6** | 11 |
| 5 | **-1** | 13 |
| 10 | **4** | 15 |
| 15 | **9** | 17 |
| 20 | **14** | 19 |
| 30 | **24** | 23 |

**Table 2.4: AW109 Beanie CFD simulation test program.**

### 2.3.4 Results of the CFD test campaign

First of all, the results of the CFD simulations are illustrated and compared to the experimental data in terms of the static pressure distribution over the beanie upper and lower surface at each of the simulated angles of attack. To this purpose, five longitudinal sections of the beanie were created, so that the normal distance of each plane to the successive one was kept constant and equal to 0.04 m along y negative direction. The five section planes are represented in Figure 2.29.

It is worth noting that the all data presented in the following were normalized with respect to specific reference values due to industrial proprietary reasons.

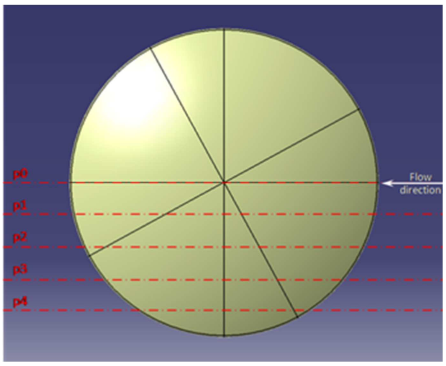

**Figure 2.29: The five beanie sections analyzed during the validation process. $\Delta y/yref=|0.40|$.**

The comparison between experimental data and CFD results in terms of static pressure coefficient distribution at different angles of attack is shown from Figure 2.30 to Figure 2.39. For the sake of simplicity, only five among the analysed configurations are reported in this work. As apparent, correlation with experiment is excellent over the beanie upper surface for all the analysed angles of attack. Some minor discrepancies are evidenced at the beanie edges for some specific values of incidence angle ($\alpha$=+9° and $\alpha$=+14°), due to some geometry simplifications carried out during the CAD model set up. A moderate lack of correlation on the upper surface was found at $\alpha$=+24°, as a consequence of the beanie stall. In fact, as evidenced also in the contour of total pressure for the above-mentioned condition, reported in Figure 2.42, this was the only one among the simulated angles of attack at which a large flow separation occurred over the upper surface of the beanie.

As far as the beanie lower surface is concerned, the general trend of pressure coefficient was captured: however, moderate discrepancies were observed with experimental data, in particular over the fore portion of sections p0, p1 and p2, where a large flow separation region was observed at highly negative angles of attack, which seemed far from being accurately captured in the simulations. This was also confirmed by the total pressure losses visualization (from Figure 2.40 to Figure 2.42), which highlighted how the influence of the test rig became more important as incidence decreases. Therefore, the lack of agreement with the experimental data was mainly connected to the simplifications of the CAD model relating to the experimental apparatus and the beanie retaining system. Correlation with wind tunnel data became better at positive incidence angles, even if some minor disagreements were still evidenced due to both experimental uncertainty and CAD model simplifications of the experimental apparatus.

These results were fully consistent with what was found in analysis of the AW139 beanie.

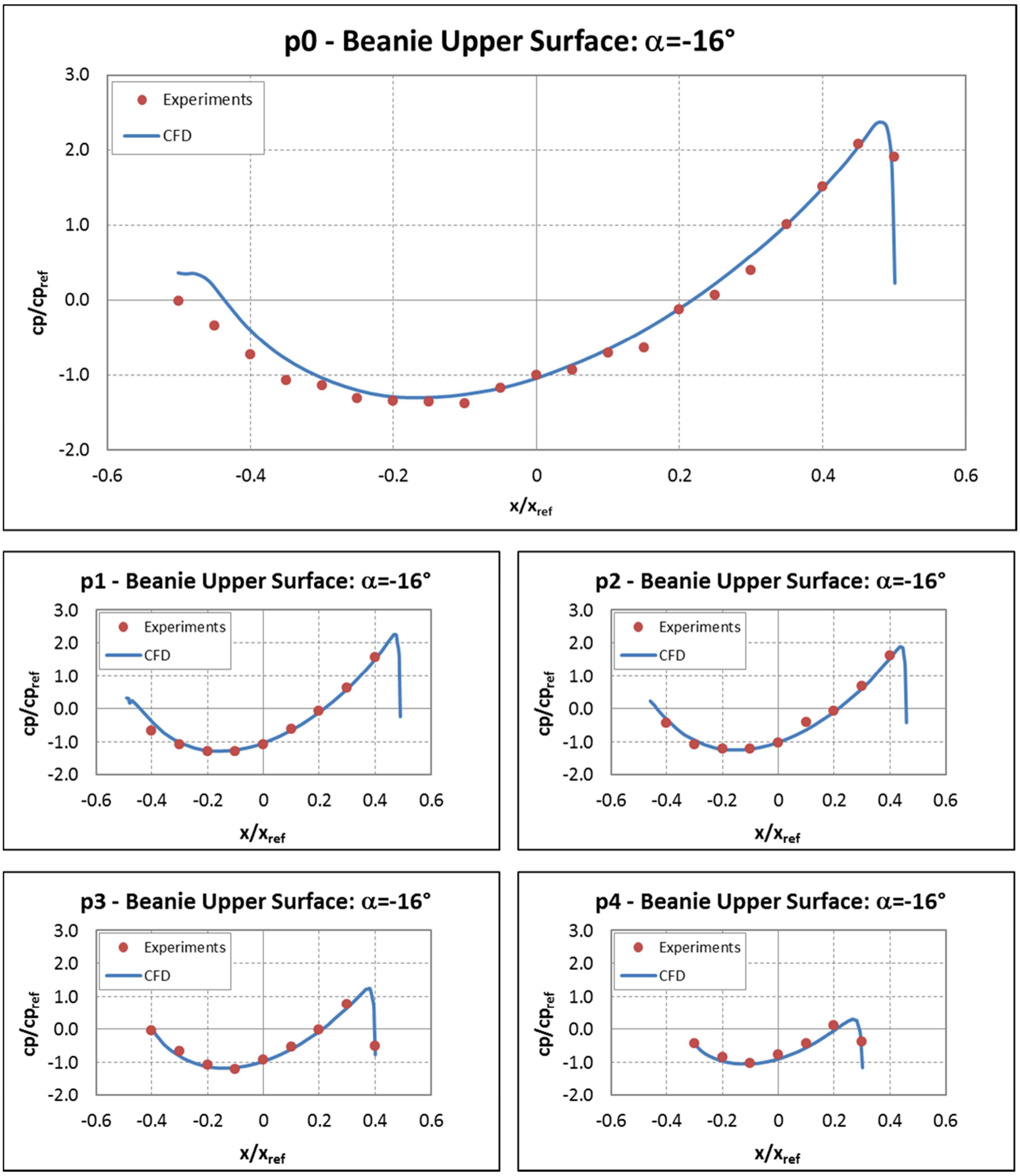

**Figure 2.30: Cp distribution over the beanie upper surface, angle of attack α=-16°.**

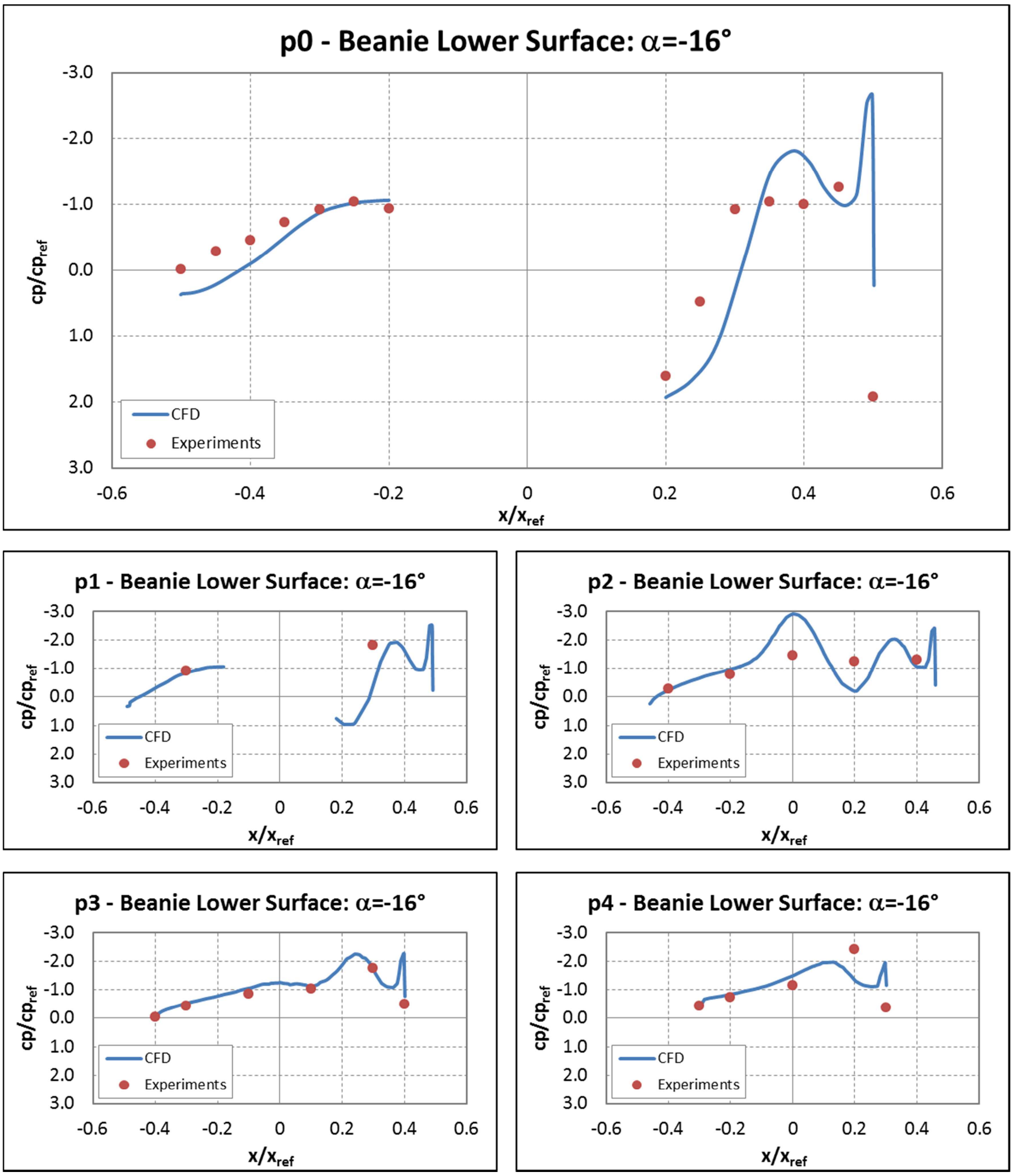

Figure 2.31: Cp distribution over the beanie lower surface, angle of attack α=-16°.

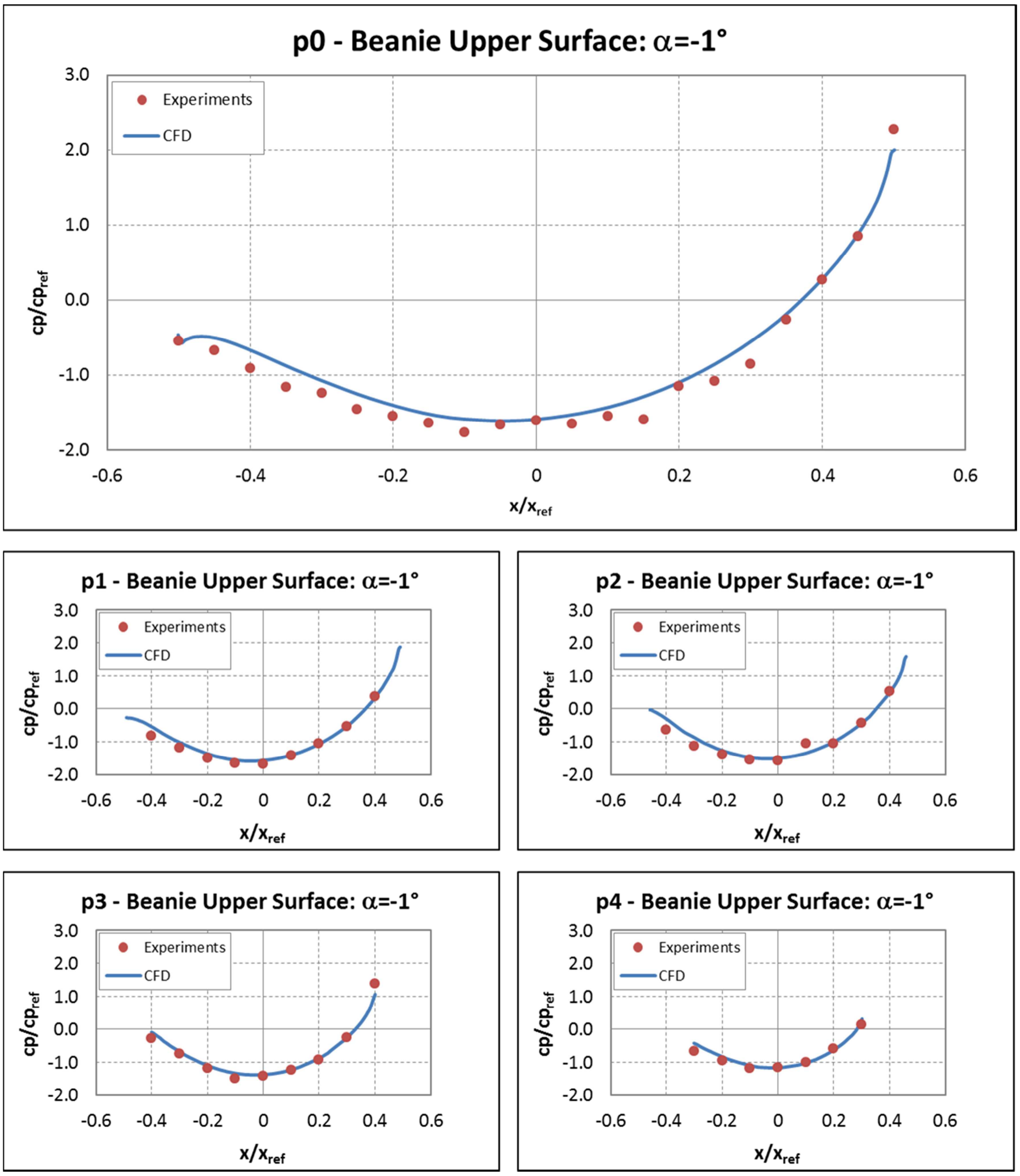

Figure 2.32: Cp distribution over the beanie upper surface, angle of attack α=-1°.

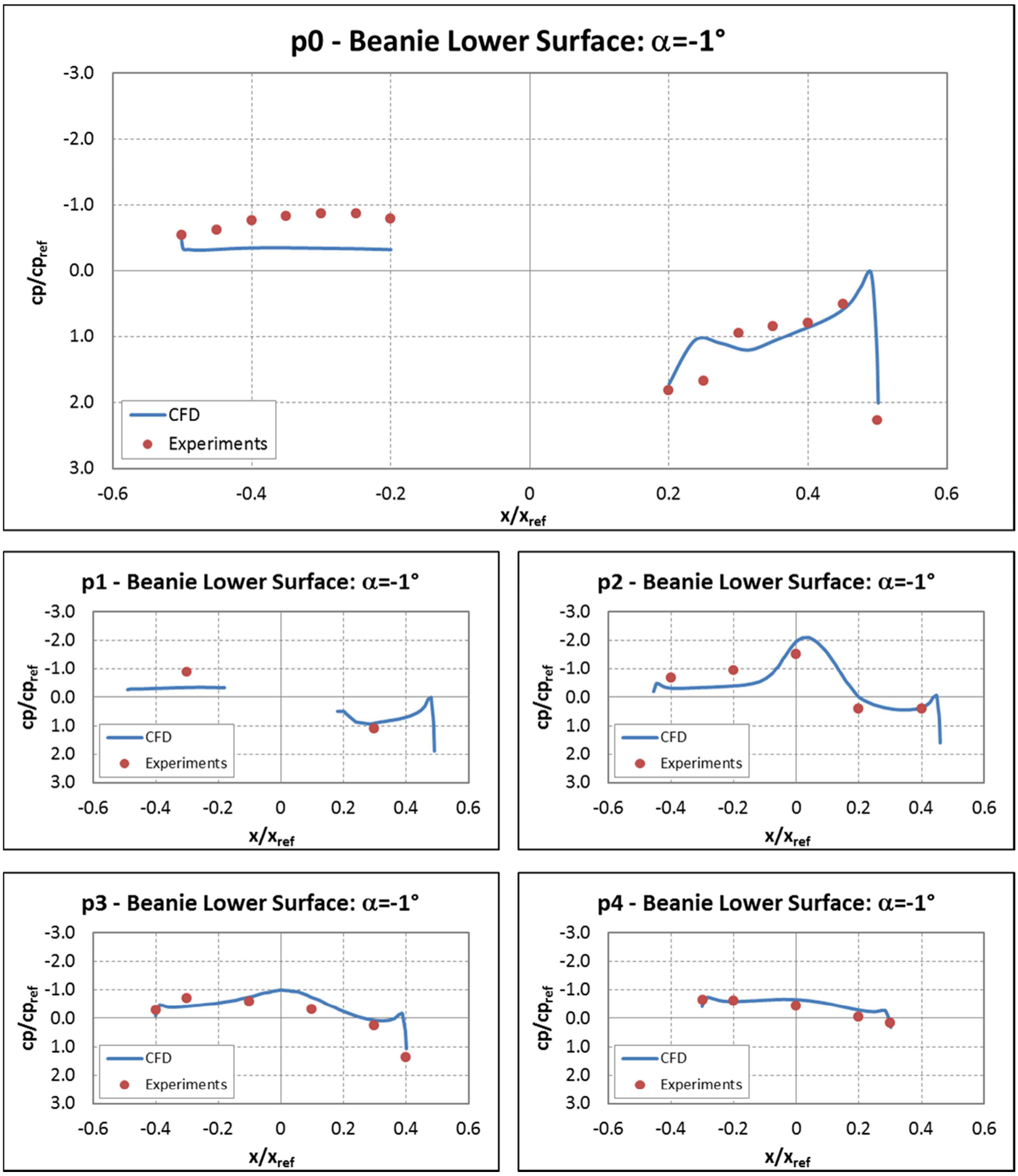

Figure 2.33: Cp distribution over the beanie lower surface, angle of attack α=-1°.

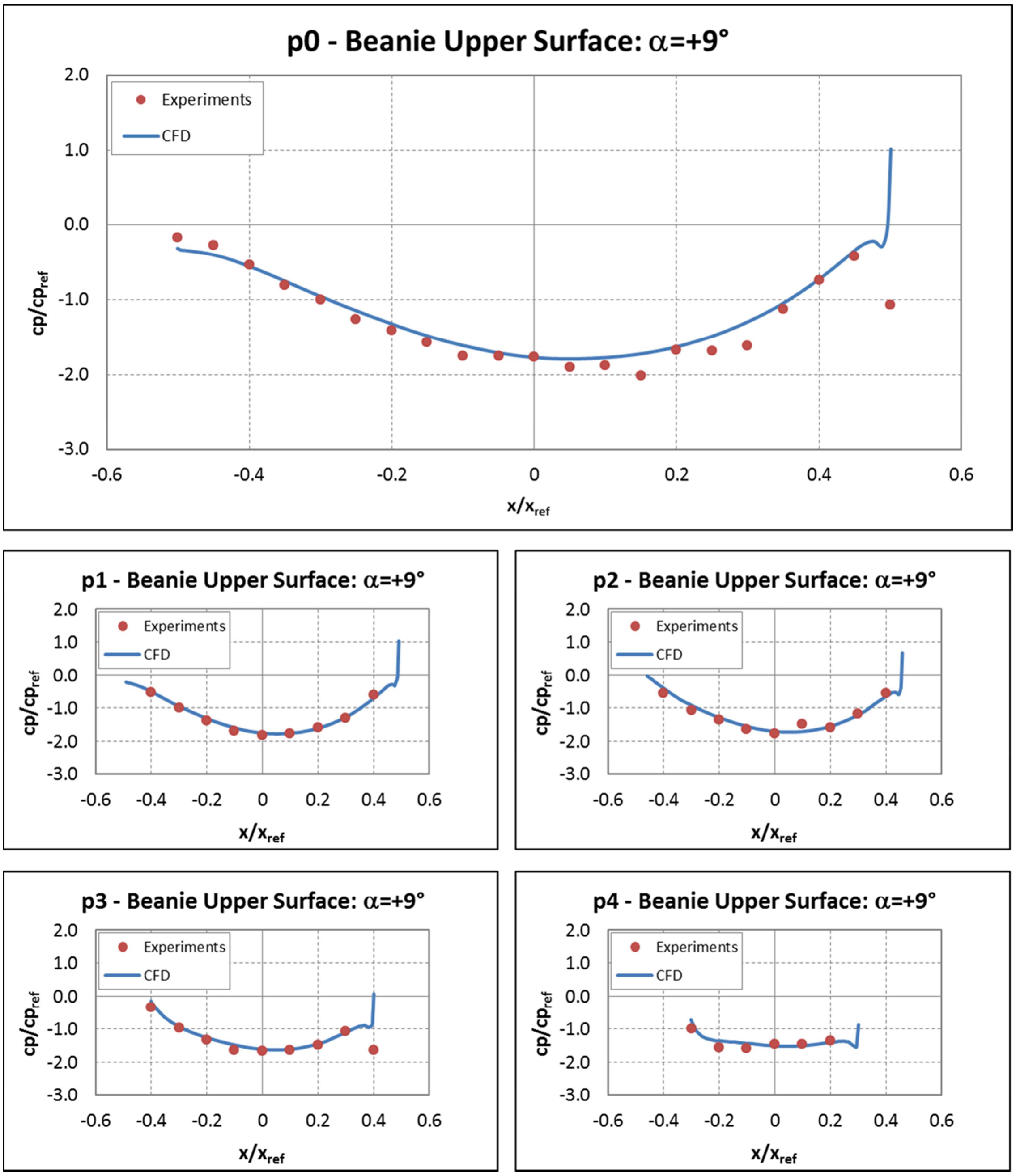

Figure 2.34: Cp distribution over the beanie upper surface, angle of attack α=+9°.

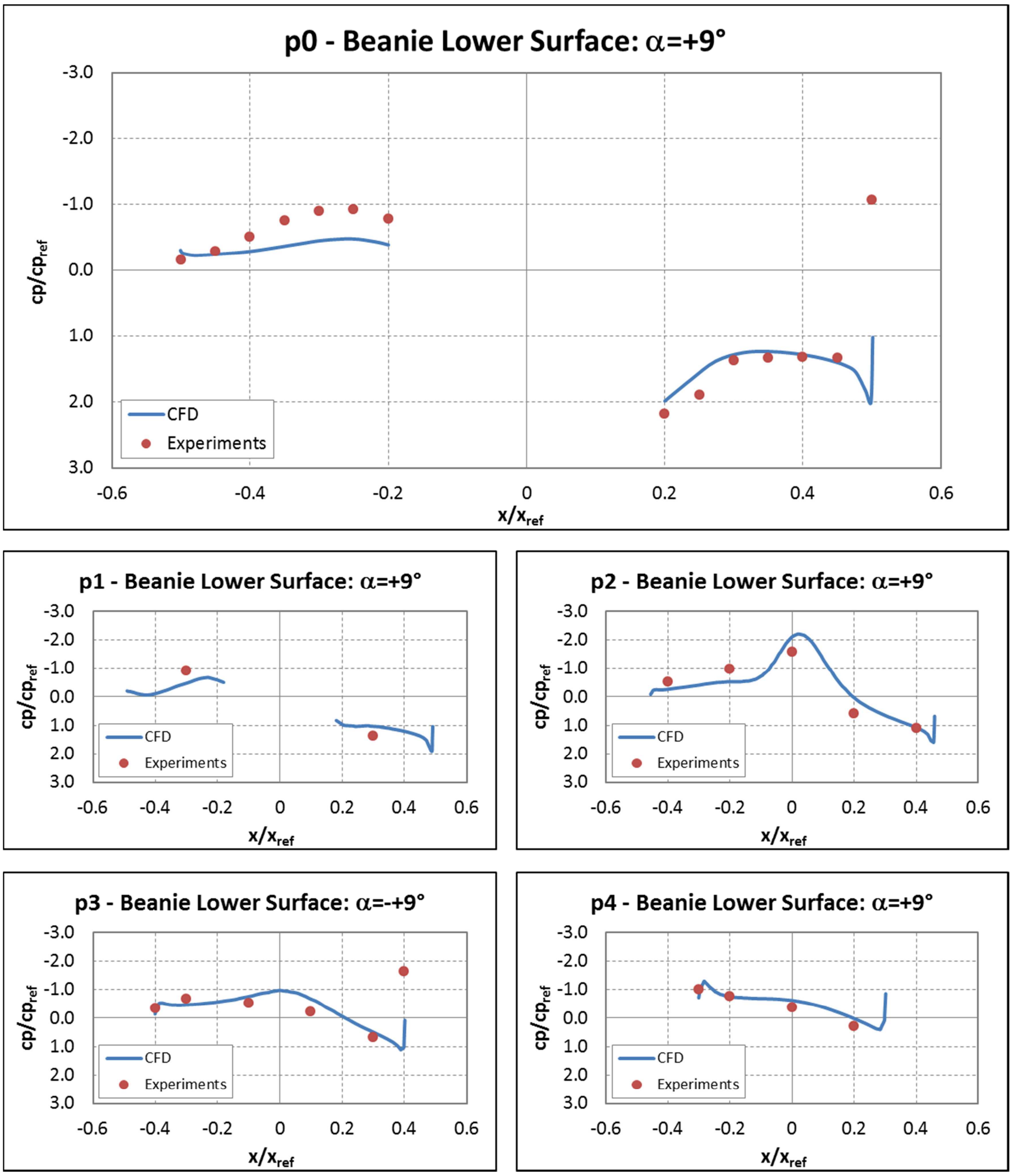

Figure 2.35: Cp distribution over the beanie lower surface, angle of attack α=+9°.

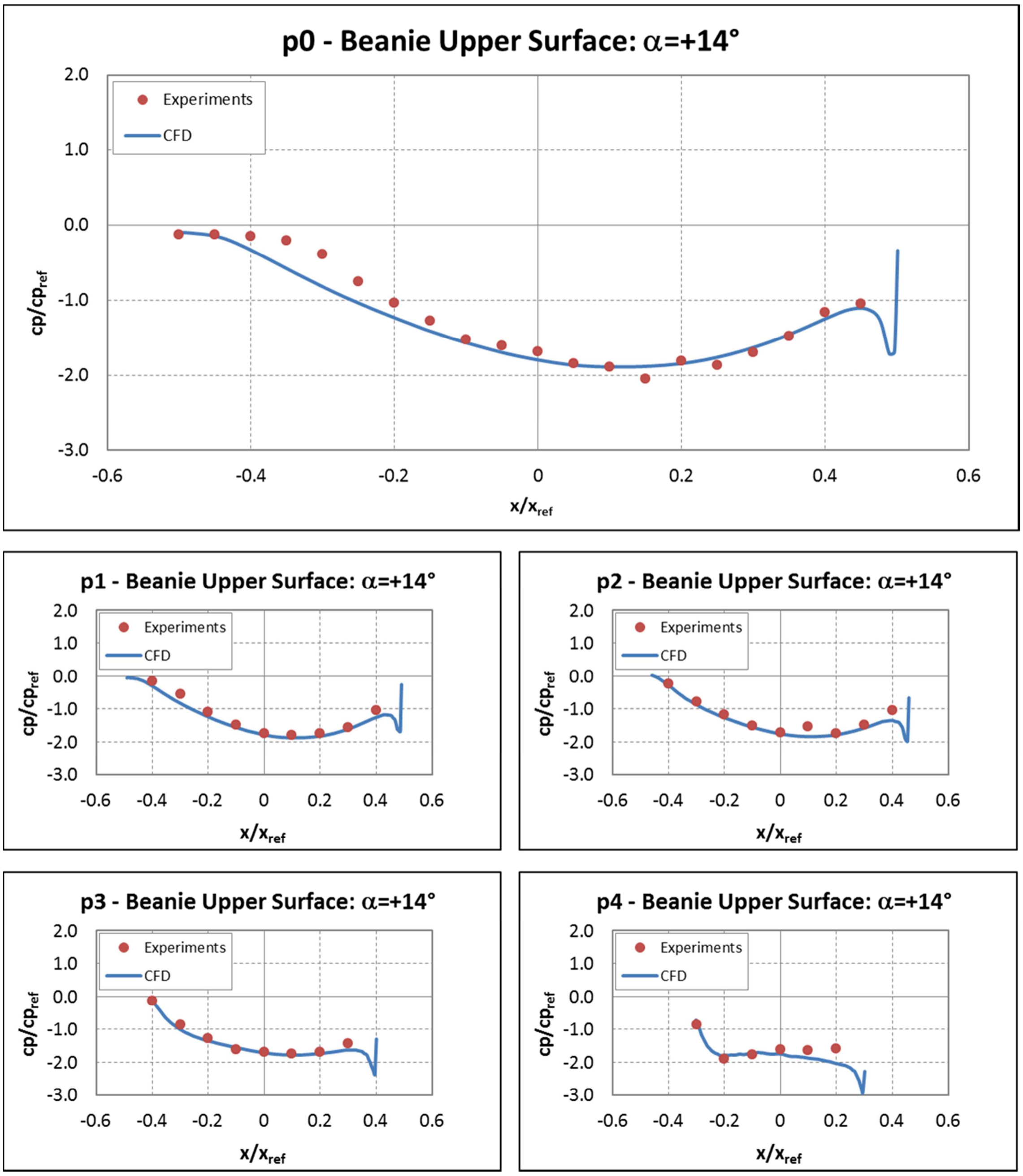

Figure 2.36: Cp distribution over the beanie upper surface, angle of attack α=+14.

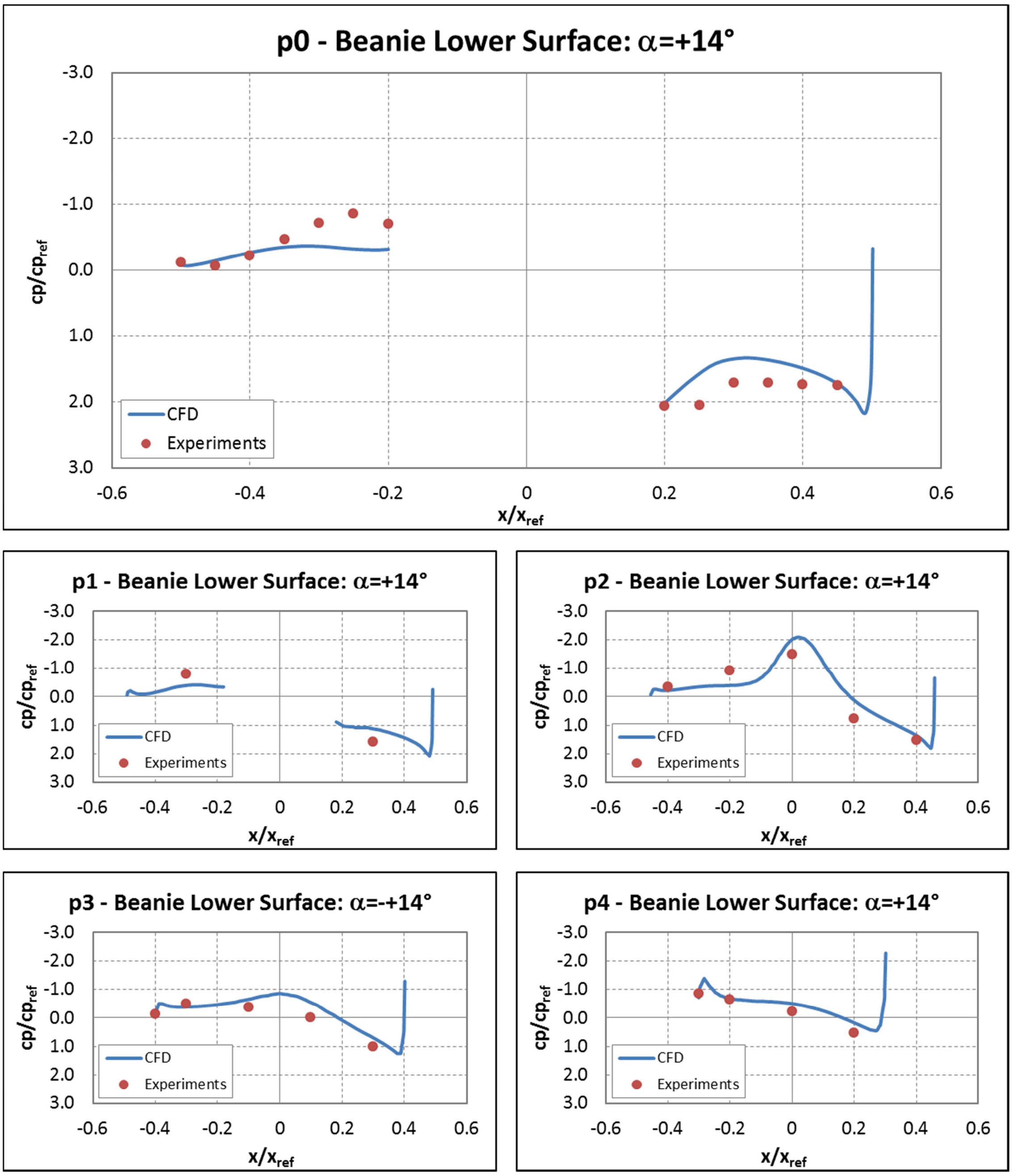

Figure 2.37: Cp distribution over the beanie lower surface, angle of attack α=+14

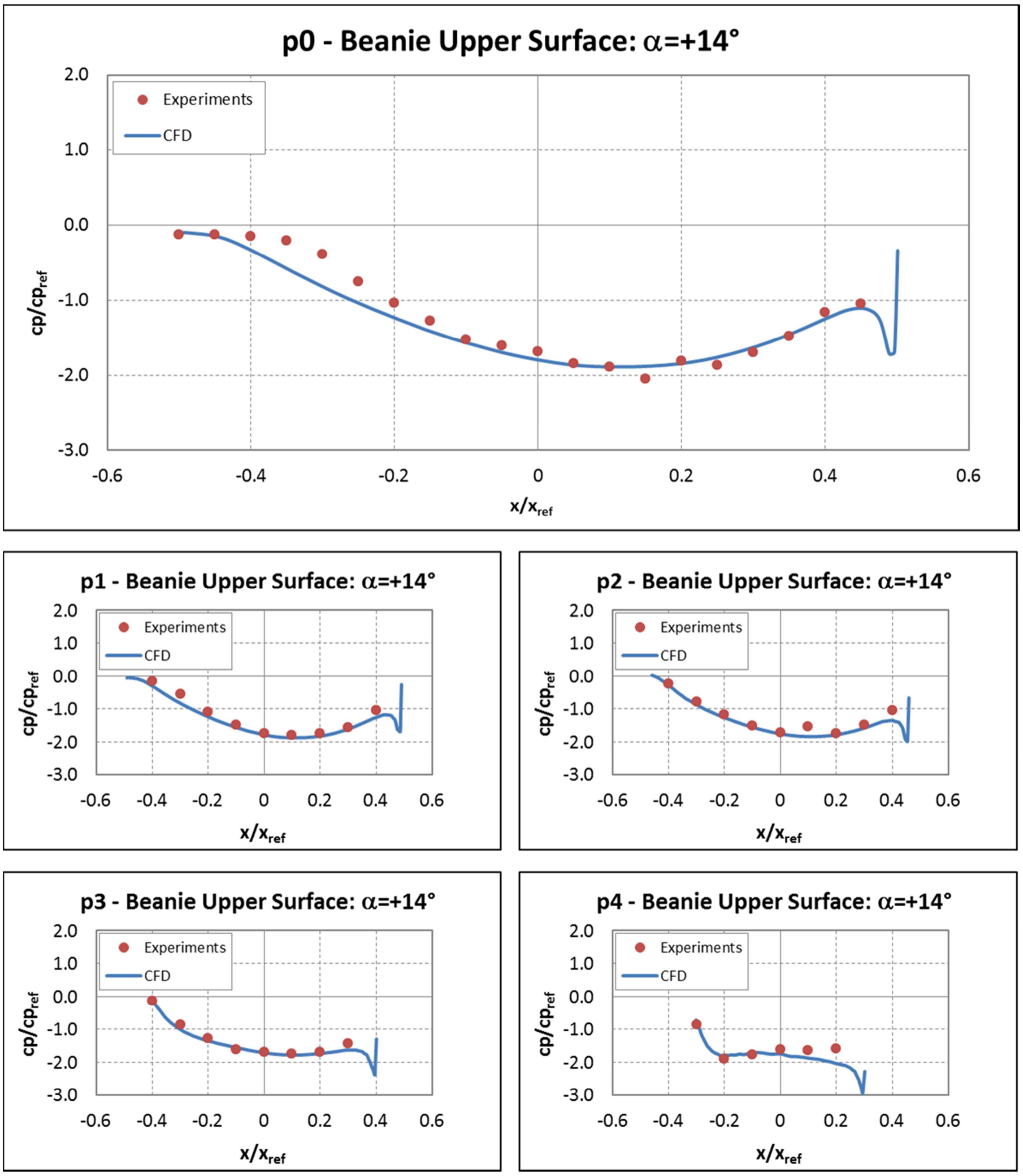

Figure 2.38: Cp distribution over the beanie upper surface, angle of attack α=+24°.

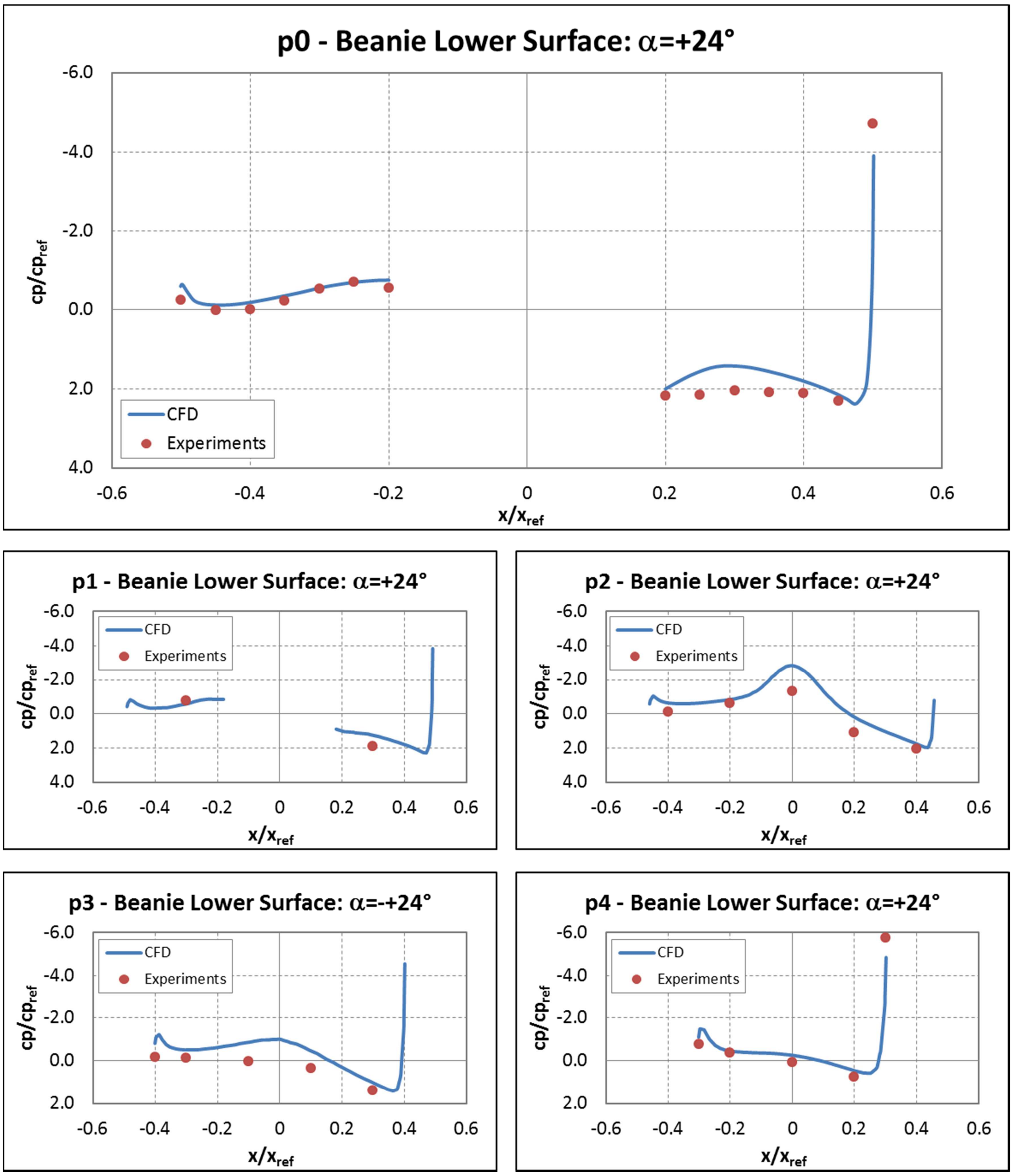

**Figure 2.39: Cp distribution over the beanie upper surface, angle of attack α=+24°.**

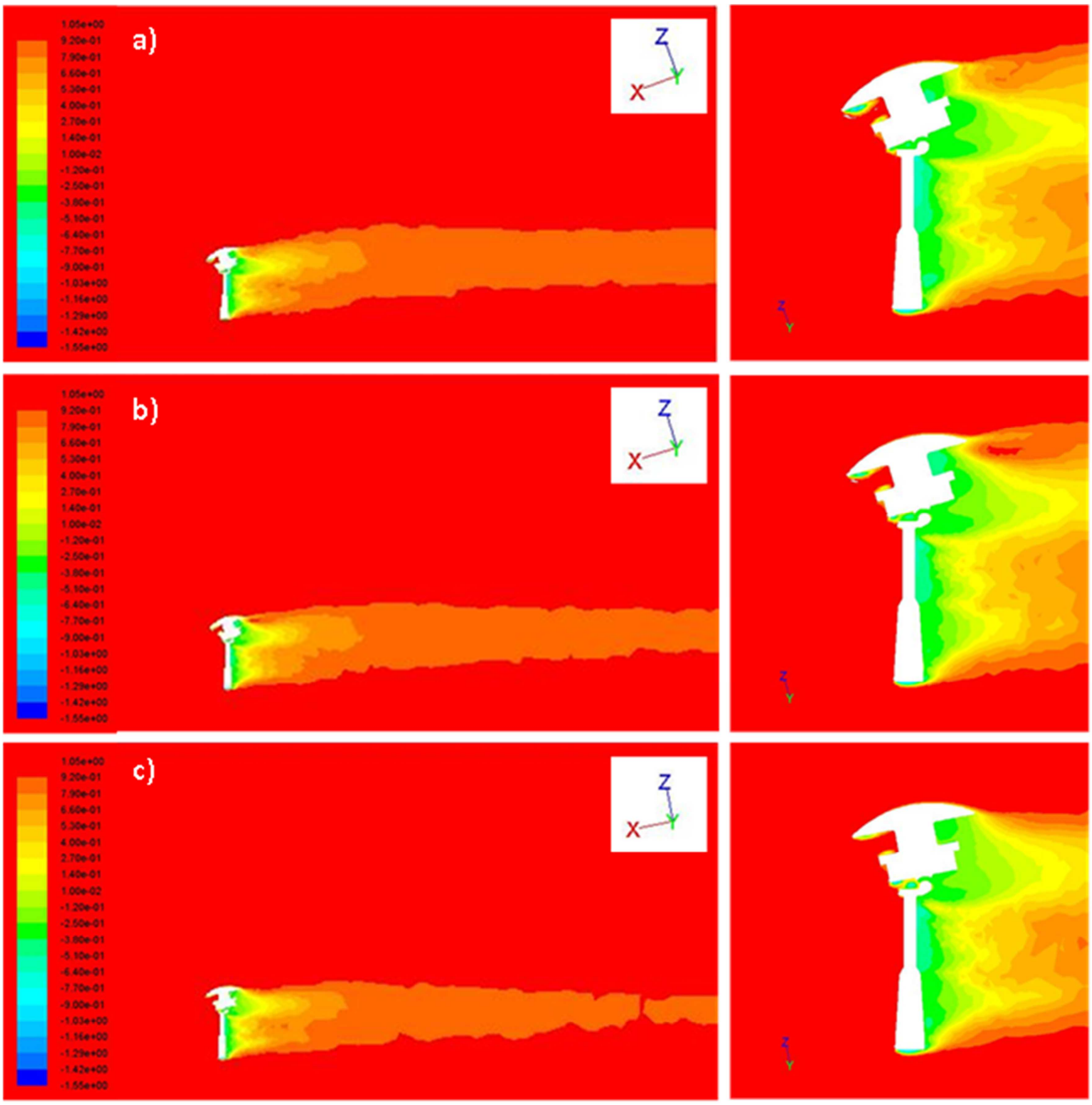

**Figure 2.40: Total pressure coefficient contour plots at the virtual wind tunnel mid-section at different angles of attack: (a) α=-21°, (b) α=-16°, (c) α=+11°.**

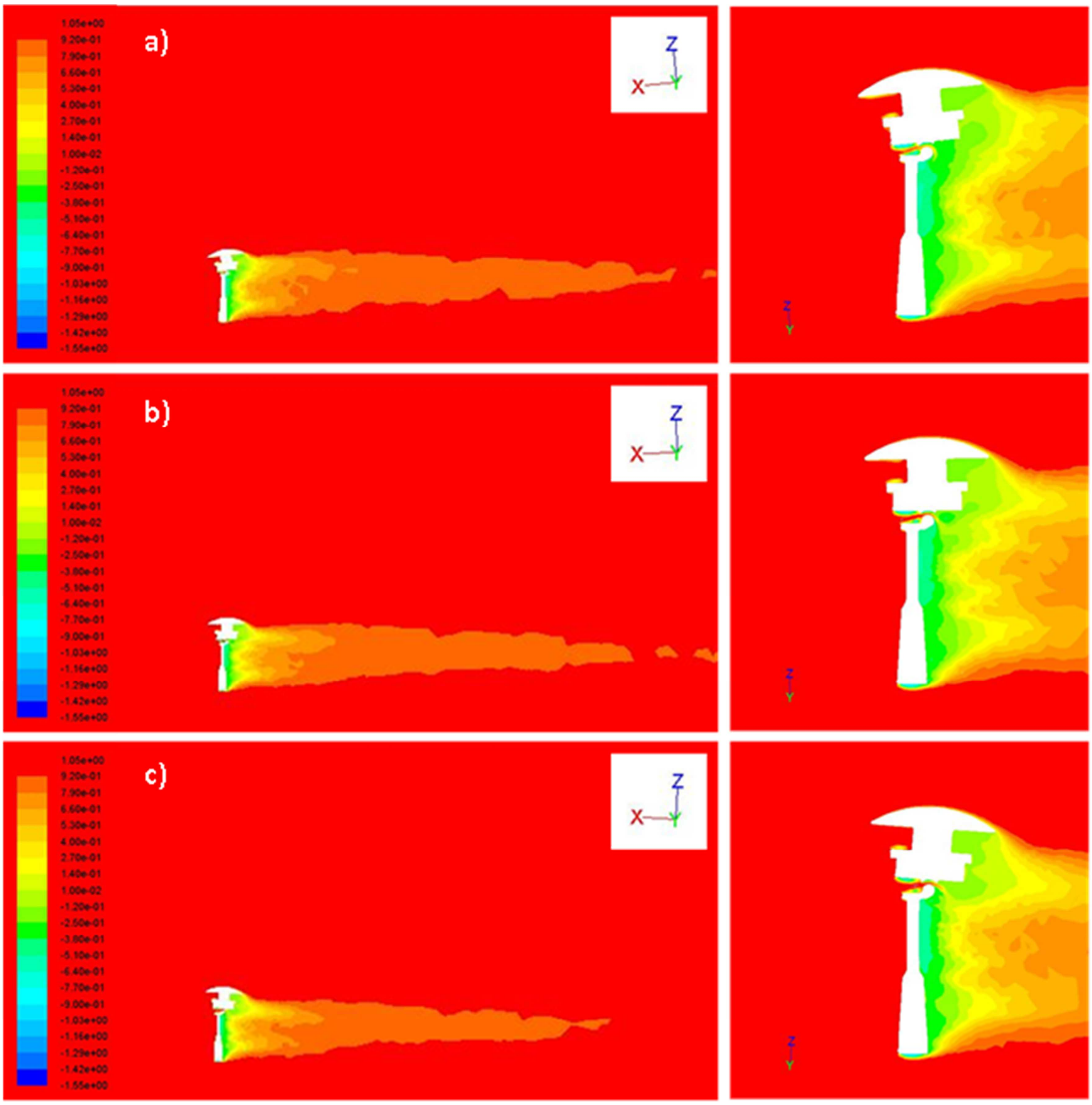

Figure 2.41: Total pressure coefficient contour plots at the virtual wind tunnel mid-section at different angles of attack: (a) α=-6°, (b) α=-1°, (c) α=+4°.

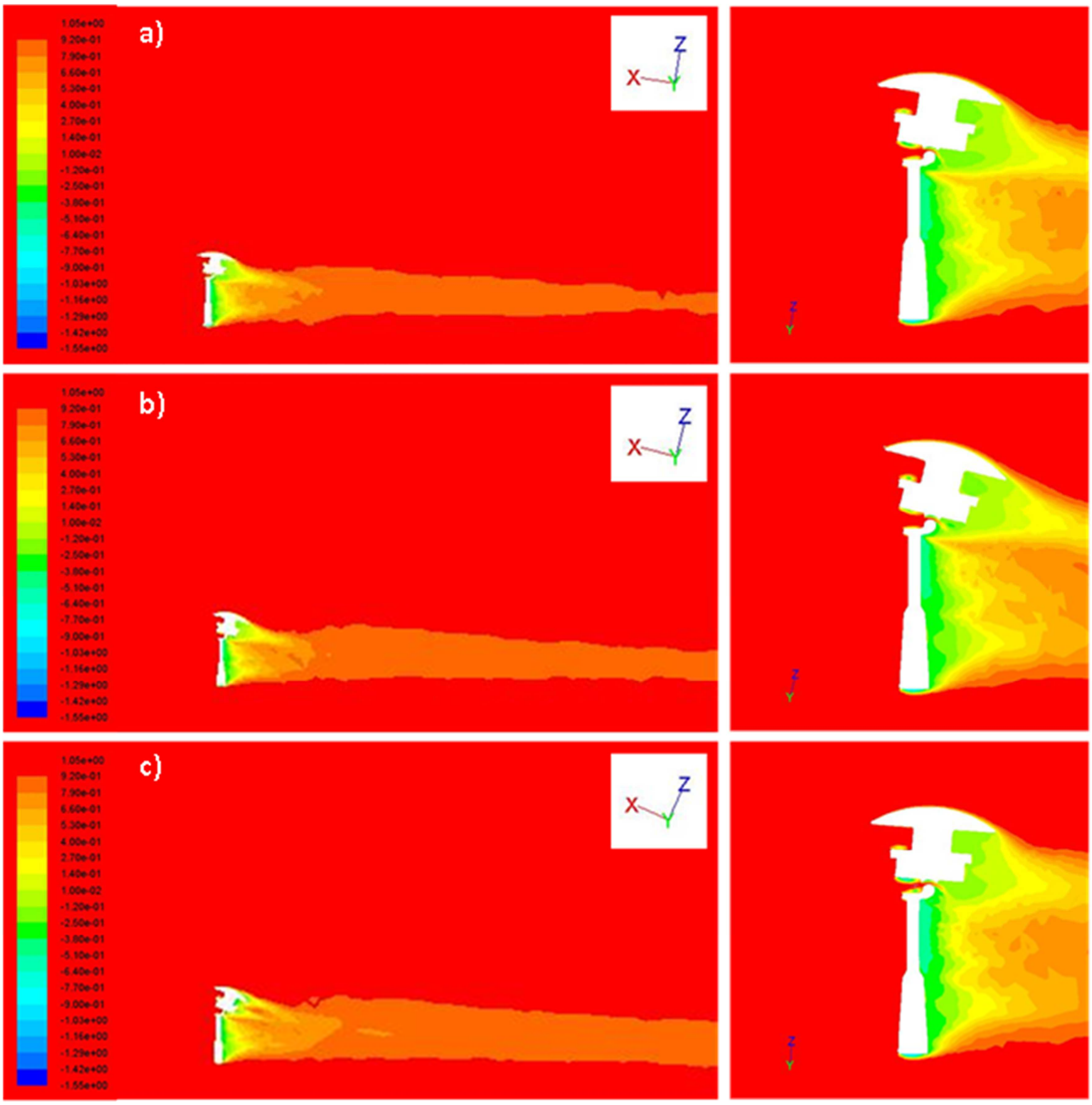

**Figure 2.42: Total pressure coefficient contour plots at the virtual wind tunnel mid-section at different angles of attack: (a) $\alpha$=+9°, (b) $\alpha$=+14°, (c) $\alpha$=+24°.**

Finally, the lift, drag and moment coefficients of the beanie at different incidences were extracted and the corresponding polars calculated, even though no direct comparison with experiment was possible due to the lack of data. In Figure 2.43 the numerical values are removed from the ordinate due to industrial proprietary reasons.

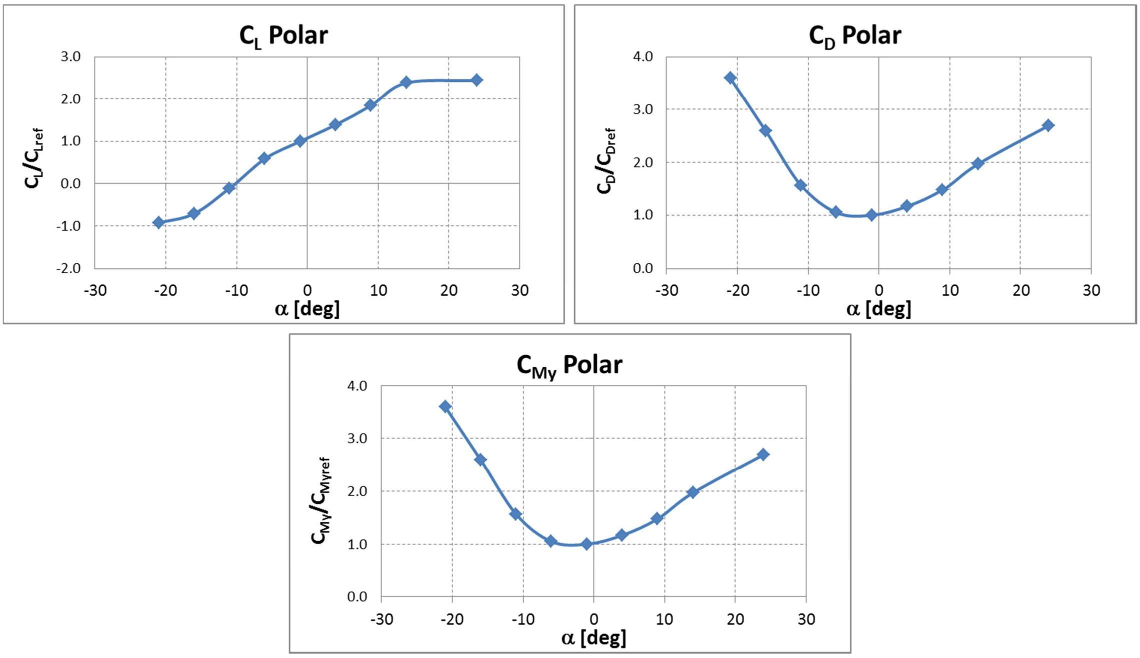

**Figure 2.43: Simulated lift, drag and pitching moment polars of the AW109 beanie.**

## *2.4 Aerodynamic characterization of the AW101 beanie model*

The analyses described in the previous paragraphs concerning the AW139 and AW109 beanie models were preparatory for the aerodynamic characterization of the AW101 helicopter beanie that is described in this section. Specifically, this study aimed at investigating the effects of the presence of the engine upper deck on the downward deflection induced by the AW101 beanie on the oncoming flow stream. In particular, the attention was focused on the characteristics of the wake at the tail fin location.

To this purpose, both the AW101 isolated beanie and the beanie in presence of the engine upper deck were simulated. Each case was analysed in both steady and rotating configurations (the latter using the Moving Reference Frame approach), in order to investigate the effects induced in the flow field by the rotational speed of the beanie.

Since no experimental data were available on the AW101 beanie, no direct validation of the generated numerical models was possible. However, an extensive analysis was already carried out in the case of the AW139 and AW109 beanie geometries, over which some experimental data were provided by *AgustaWestland* for validation purposes. The indications drawn in these studies on the assessment of a suitable numerical model for characterization of such components were followed for the AW101 beanie model set up as well, in order to guarantee an adequate accuracy of the CFD simulations.

### 2.4.1 Numerical model geometry

The CAD model used for the simulation campaign was made up of two elements, i.e. the beanie and a portion of the upper deck of the AW101 helicopter. The first component (Figure 2.44) was partially modified within CATIA® in order to smooth sharp edges that could have led to a low quality mesh. As already mentioned, some modifications needed to be applied to the engine upper deck as well, with the aim of avoiding the generation of fictitious wakes in the CFD simulations: to this purpose, the end section of the upper deck was extruded along the helicopter longitudinal axis up to the tail fin (Figure 2.45).

The fuselage was given a null angle of attack; therefore, as a consequence of the components' relative position, the beanie axis was tilted by -4° degrees (nose down). As the Moving Reference Frame (MRF) approach needed to be used in the fluid dynamic analyses, an additional reference frame which encompassed the beanie was defined. In this particular case, the MRF was selected to be a cylinder surrounding the beanie.

As far as the isolated beanie simulations are concerned, the CAD model of the beanie was the same one used for calculations including the engine upper deck. Even the dimensions of the rotational reference frame cylinder were left unchanged.

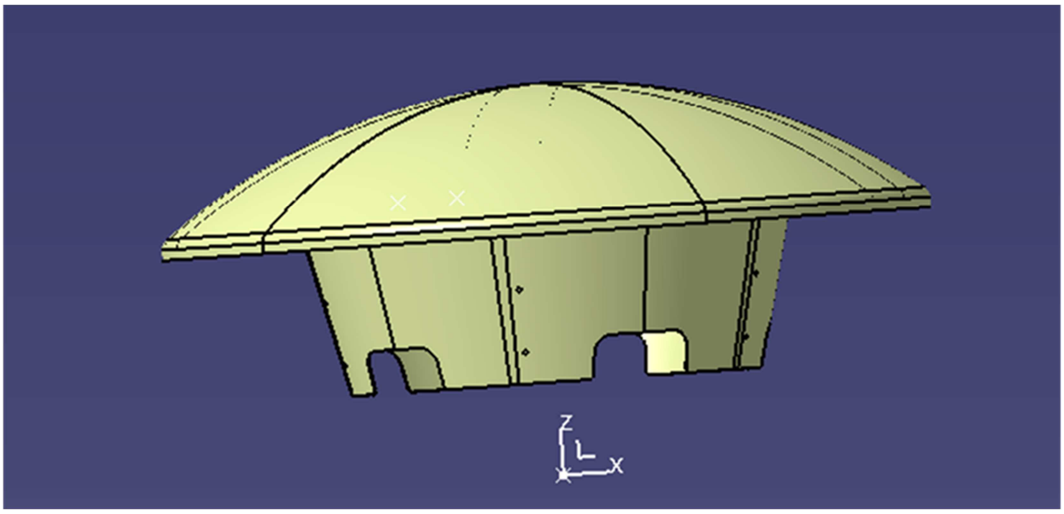

**Figure 2.44: The CAD model of the AW101 beanie.**

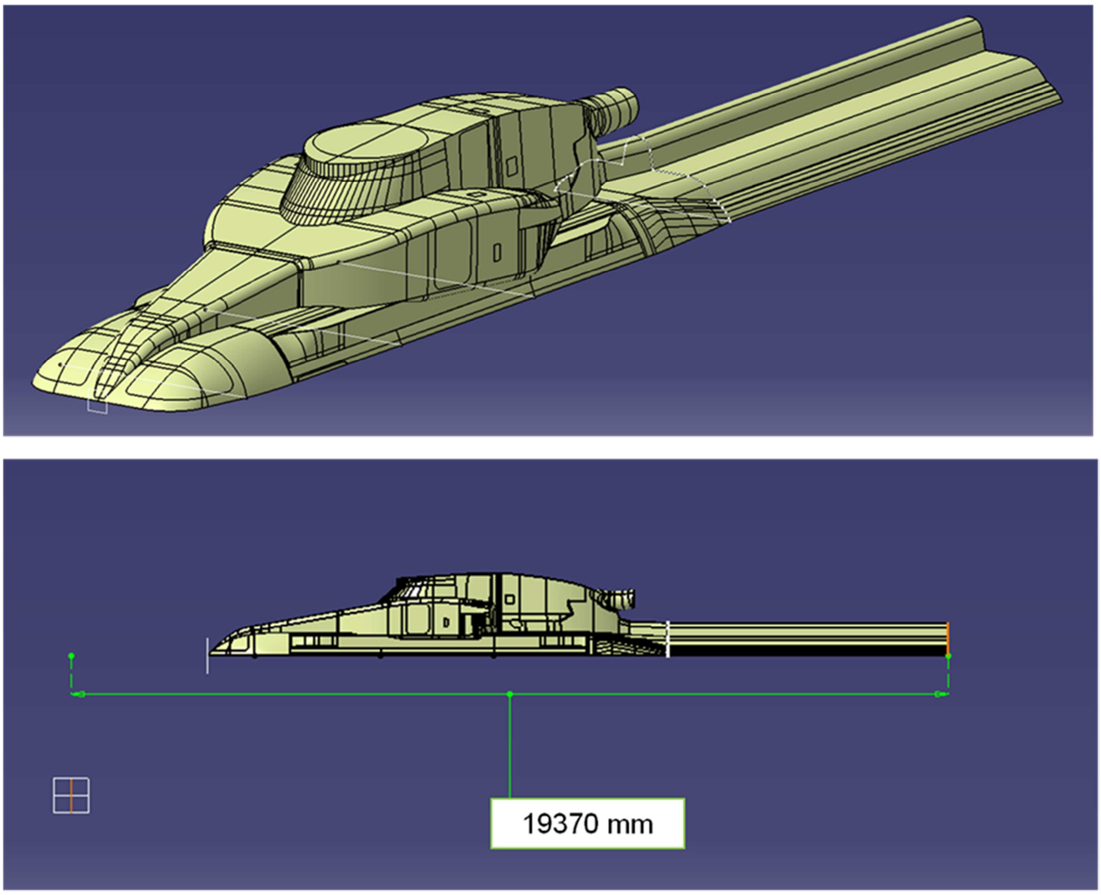

**Figure 2.45: CAD model of the AW101 upper deck.**

The superficial meshes over the AW101 beanie and engine upper deck, as well as the surface mesh over the bounding box, were generated using a specific tool within CATIA®. The selected parameters as quality indicators for the mesh were its aspect ratio and skewness. Figure 2.46 illustrates the triangle based, linear type elements superficial grids over the beanie and engine upper deck: a whole of 95,000 triangular elements were generated over the beanie, while 116,400 elements were created over the engine fairing.

The beanie and engine upper deck were then inserted into a virtual wind tunnel whose dimensions were 10m x 10m x 75m. Actually, a sensitivity analysis to the dimensions of the wind tunnel on the numerical simulations results was already performed in the CFD analyses concerning the AW139 beanie, where the transversal section was given the same dimensions of the actual wind tunnel were the experiments were carried out, in order to get a blockage factor similar to the experimental one. Moreover, as far as the length of the virtual wind tunnel was concerned, three different dimensions were tested in §2.2 with the aim of assessing the effects of the external volume dimensions on simulation results. To this purpose, a trade-off needs to be achieved between the wind tunnel length and the subsequent number of elements in the grid. In fact, the longer the wind tunnel, the more realistic the undisturbed flow conditions that are to be imposed over the inlet and outlet sections. As obvious, this implies an increasing number of elements, which needs to be kept to reasonable levels due to computational resource limits. Following the indications drawn in the AW139 validation analysis, the same proportions were maintained in the present work between the model to be analysed and the virtual wind tunnel.

As mentioned before, pitch incidence of the fuselage was given a null value, as requested: hence, as a consequence of the components' relative position, the beanie angle of attack was set to -4° (nose down), while the other attitude angles were kept at null values.

In Figure 2.47, a longitudinal view of the virtual wind tunnel used in the CFD simulations is depicted.

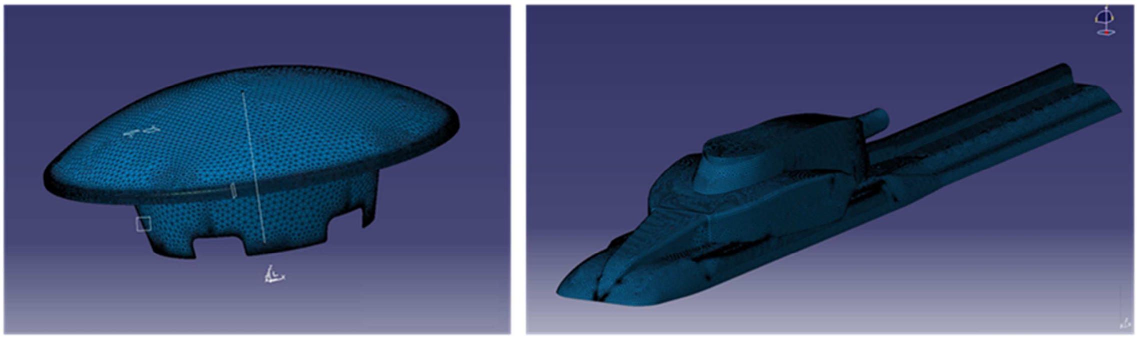

**Figure 2.46: Superficial mesh over the beanie (on the left) and the upper deck (on the right).**

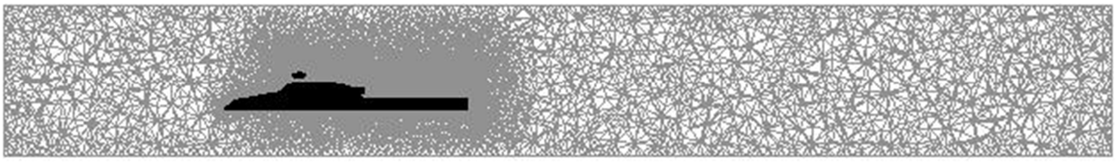

**Figure 2.47: Longitudinal view of the virtual wind tunnel surrounding the model.**

The volumetric mesh was generated using TGrid® V5. Similarly to the case already analysed in §2.2.2, it was unstructured, with some structured elements over the beanie and the upper deck surface in order to better simulate the boundary layer. However, as the CFD calculations were carried out using conventional turbulence models, it was not necessary to create an extremely fine boundary layer mesh. The drivers in the parameters selection were always both a low growth rate, which could lower the cell aspect ratio of the boundary layer, and a total number of layers high enough to reach a total height which could correctly represent the physical boundary layer. The boundary layer mesh parameters were chosen on the basis of the indications drawn in the AW139 beanie validation study, however some minor changes were necessary in order to reduce the total number of elements and keep required computational resources to a reasonable level. Actually, the selected set up was shown to guarantee that for the examined test case the non-dimensional mesh thickness at the beanie and upper deck surfaces y+ fell between 30 and 290, which is consistent with the discretization levels (y+=30÷500) suggested for the wall functions implemented in the conventional turbulence models to work properly.

Moreover, a volumetric grid refinement was necessary downstream the beanie up to the tail fin in order to avoid numerical dissipation and correctly capture both the wake trajectory and the total pressure losses. To this purpose, a box surrounding the beanie and extending through the global domain to the tail fin location was built, which is illustrated in Figure 2.48.

A total number of 4.1 million cells were created. Once the volumetric grid was generated, its quality indices were optimized by means of some TGrid® tools in order for the mesh quality to be improved, so that potential difficulties in calculations' convergence due to the most distorted elements could be prevented.

As far as the case of the isolated beanie is concerned, only the unstructured grid within the bounding box was recreated, while the meshes (both structured and unstructured) within the moving reference frame were left unchanged. The new mesh was generated following the criteria already presented hereinbefore. Furthermore, the same volumetric grid refinement was applied, so that the mesh differences with the case including the engine upper deck were minimized. This resulted in a total number of elements equal to 3.4 million cells.

In Figure 2.49 some views of the volumetric mesh around the beanie and upper deck are depicted, while Figure 2.50 represents the cylindrical moving reference frame.

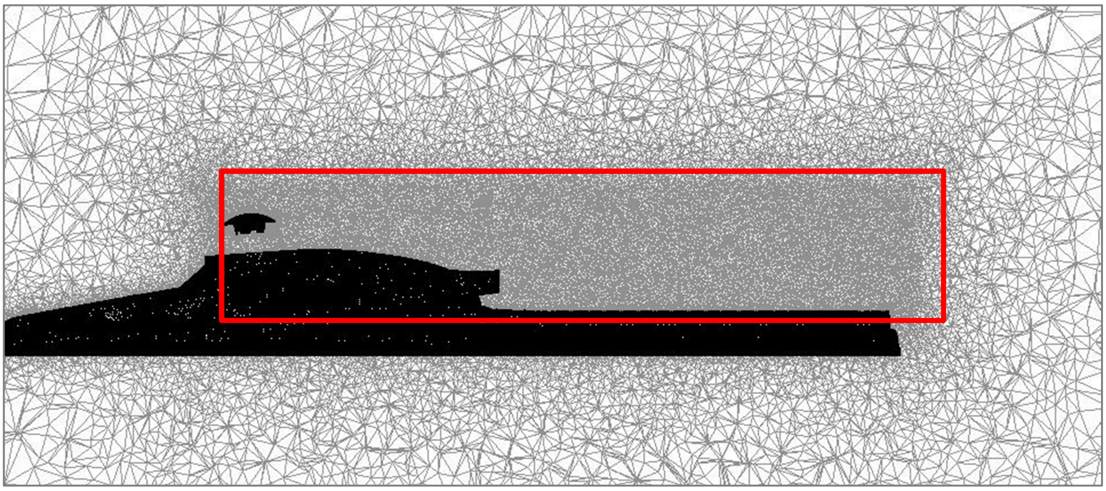

**Figure 2.48: Refinement box for wake capturing downstream the AW101 beanie.**

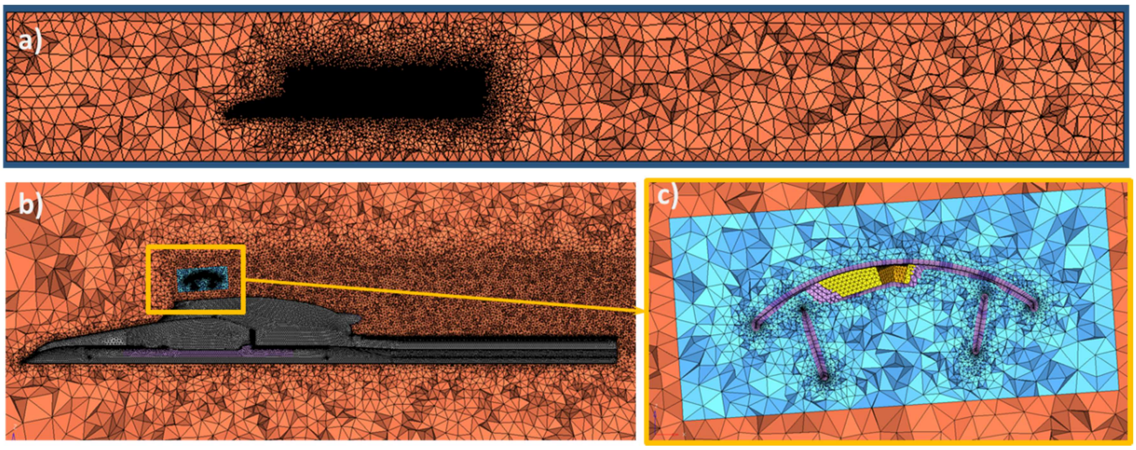

**Figure 2.49: The volumetric mesh around the beanie and upper deck: a) global longitudinal view; b)close-up near the helicopter surface; c) close-up of the rotating cylinder sorrounding the beane**

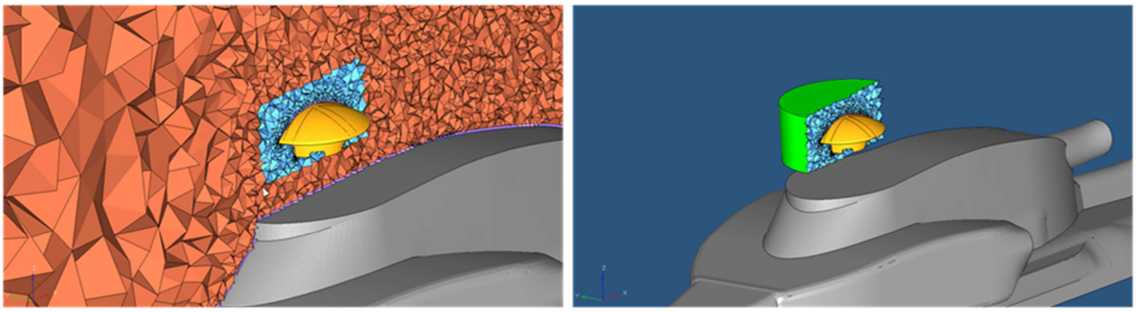

**Figure 2.50: The cylindrical Moving Reference Frame.**

## 2.4.2 CFD simulations

CFD simulations were carried out using ANSYS Fluent® V.12. The same approach described in §2.3.3 was used also for the analyses of this specific case. In particular, a steady, pressure-based solver type was chosen for the steady simulations; a k-ω SST turbulence model was selected for the simulation of the viscous effects; the air was treated as an ideal gas having constant specific heat, while fluid viscosity was modelled using the pre-defined three-coefficients Sutherland law.

As far as the boundary conditions are concerned, a total pressure condition was imposed at the wind tunnel inlet, while a static pressure condition was assigned at the outlet section. Moreover, a turbulence intensity of 5%, along with an hydraulic diameter equal to the beanie mean diameter were set to complete the specification of the chosen selected turbulence model. The beanie and the upper deck surfaces were treated as hydraulically smooth and adiabatic walls, while a symmetry condition was used for the lateral surfaces of the wind tunnel box.

The adopted boundary conditions for the steady simulations are summarized in Table 2.5

MRF analyses required some adjustments in the boundary conditions. In fact, the *fluid zone* contained in the rotational reference frame had to be changed from steady to moving reference frame entering the required parameters (i.e. rotational velocity and rotational axis which cannot be specified because they are proprietary information). Furthermore, the wall zone representing the beanie was changed from a stationary wall condition to a moving wall condition. As the wall rotates at the same speed of the rotating frame, the beanie relative angular speed was set to zero, while the parameters concerning the rotational axis (i.e. point and direction) were the same used for the setup of the fluid zone.

| | | | | |
|---|---|---|---|---|
| **Viscous Model** | k–ω SST | | | |
| **Fluid** | Air | Ideal Gas | | |
| | | Sutherland low for viscosity | | |
| **Boundary Conditions** | Pressure Inlet | Gauge Total Pressure= 1586.4632 Pa | | |
| | | Total Temperature= 261.03 K | | |
| | Pressure Outlet | Gauge pressure= 0 Pa | | |
| | | Backflow Total temperature= 259.13K | | |
| | Symmetry | All lateral surfaces | | |
| | Wall | No-slip wall | | |
| **Operating Conditions** | Pressure | 61262.2289 Pa | x | 62 (m) |
| | | | y | 4.9 (m) |
| | | | z | 9.5 (m) |
| | Gravity | Deactivated | | |

**Table 2.5: Boundary condition settings**

A SIMPLE scheme was adopted as the solution algorithm for the steady simulations. The discretization scheme was varied from the First Order Upwind to the Third Order MUSCL, since a higher order is suggested for improving the solution accuracy, despite the increase of both the simulation time and the normalized RMS residuals.

While the under-relaxation factors were left unchanged to their default values in the case of the beanie mounted over the upper deck, the analysis of the isolated beanie required an adjustment of the under-relaxation factors in order to improve the residuals convergence. In particular, the pressure under-relaxation was increased to 0.6, while the momentum was decreased to 0.4.

The solution was initialized by assigning the fluid values of the inlet section over the fluid domain and by using an absolute reference frame, in order for the iterative process to start from a reasonable solution and speed up the convergence.

For each simulation, the convergence criterion was established when the RMS residuals were less than $1 \cdot 10^{-4}$. Furthermore, the difference between the mass flow rate between inlet and outlet was monitored in order to make sure it reached a stabilized value at the end of the simulations.

As far as the MRF analyses are concerned, the residuals may be less stable as the rotational speed increases, as the rotation of the reference frame can lead to a complex forces in the flow. One of the controls that can be applied is to start with the final solution of the steady simulation that has already converged. Moreover, the rotational speed can be slowly increased in some steps until the operating speed is reached. All these expedients were used in the analysis of the AW101 beanie.

### 2.4.3 Results and discussion

The results of the CFD simulations for both the isolated beanie and the beanie in presence of the engine fairing, in both steady and rotating conditions are illustrated and compared in terms of:

- static pressure coefficients distribution over the beanie upper surface;
- total pressure coefficient losses registered at specific section rakes;
- path of specific streamlines impinging the beanie;
- global aerodynamic coefficients of the beanie.

The total pressure coefficients, the reference Cartesian coordinates, as well as the aerodynamic coefficients are normalized with respect to some reference data for industrial proprietary reasons.

For the analysis of the static pressure coefficient distribution over the beanie surfaces in the four analysed configurations, five longitudinal sections of the beanie were created, as depicted in Figure 2.51. The beanie lower surface was not taken into account due to its geometrical complexity.

The pressure coefficient distribution over the isolated beanie is depicted in Figure 2.52 for both the steady and rotating conditions, while the corresponding distributions in presence of the engine upper deck are illustrated in Figure 2.53. As expected, the non-rotating, isolated beanie was characterized by a symmetrical distribution of the Cp, with a minimum located approximately at the beanie midsection. The presence of the upper deck caused a remarkable drop in the mean pressure coefficient values, as apparent also from the pressure coefficient curves along the selected planar sections, which are represented in Figure 2.54 and Figure 2.55; however the general trend remained unchanged.

On the other hand, the Cp distribution changed significantly when the beanie was given a rotational speed. Specifically, the area of minimum Cp was no longer symmetrical with respect to the flow direction, but it was rather shifted along the positive y direction, as clearly depicted in Figure 2.54 and Figure 2.55. The upper deck did not seem to influence the general trend of the static pressure coefficient over the beanie upper surface, even in the rotating configuration: also in this case, the Cp curves in presence of the engine fairing were similar to those of the isolated beanie, though translated downward by 50% in average.

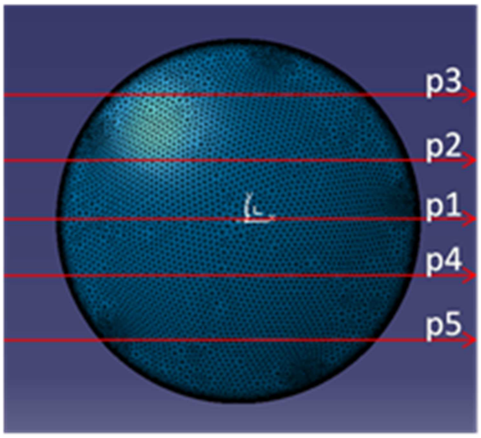

**Figure 2.51: The five longitudinal sections of the beanie used for the Cp analyses. Δy/yref=|0.15|.**

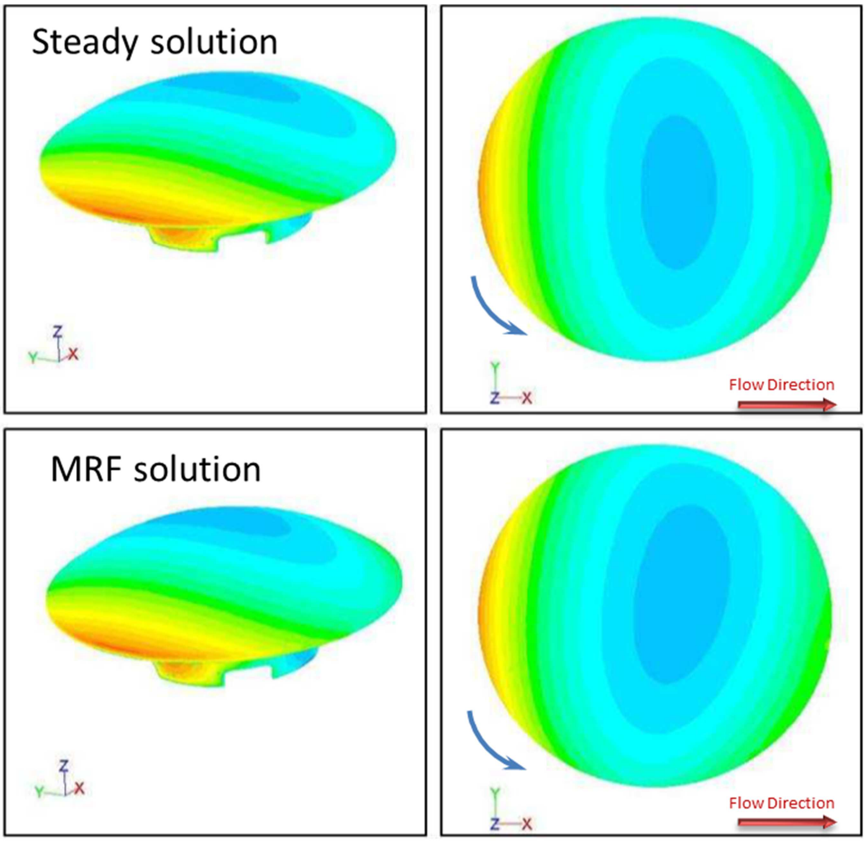

**Figure 2.52: Contour plots of static pressure coefficient over the isolated beanie in both steady and rotating conditions.**

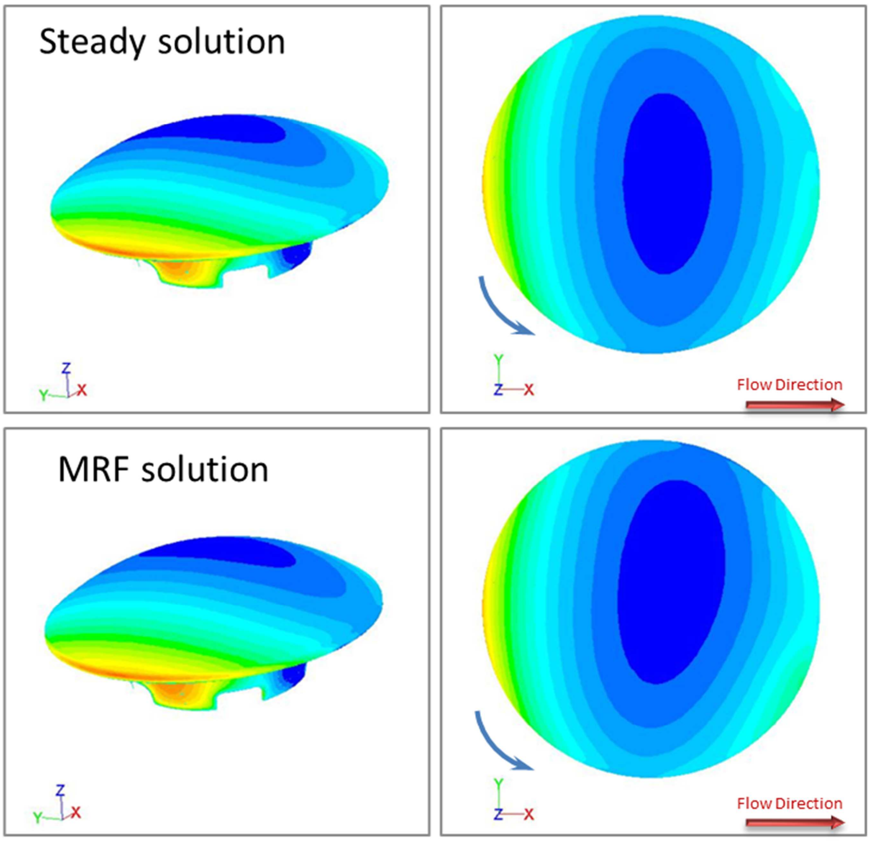

**Figure 2.53: Contour plots of static pressure coefficient over the beanie in presence of the upper deck in both steady (top) and rotating (bottom) conditions.**

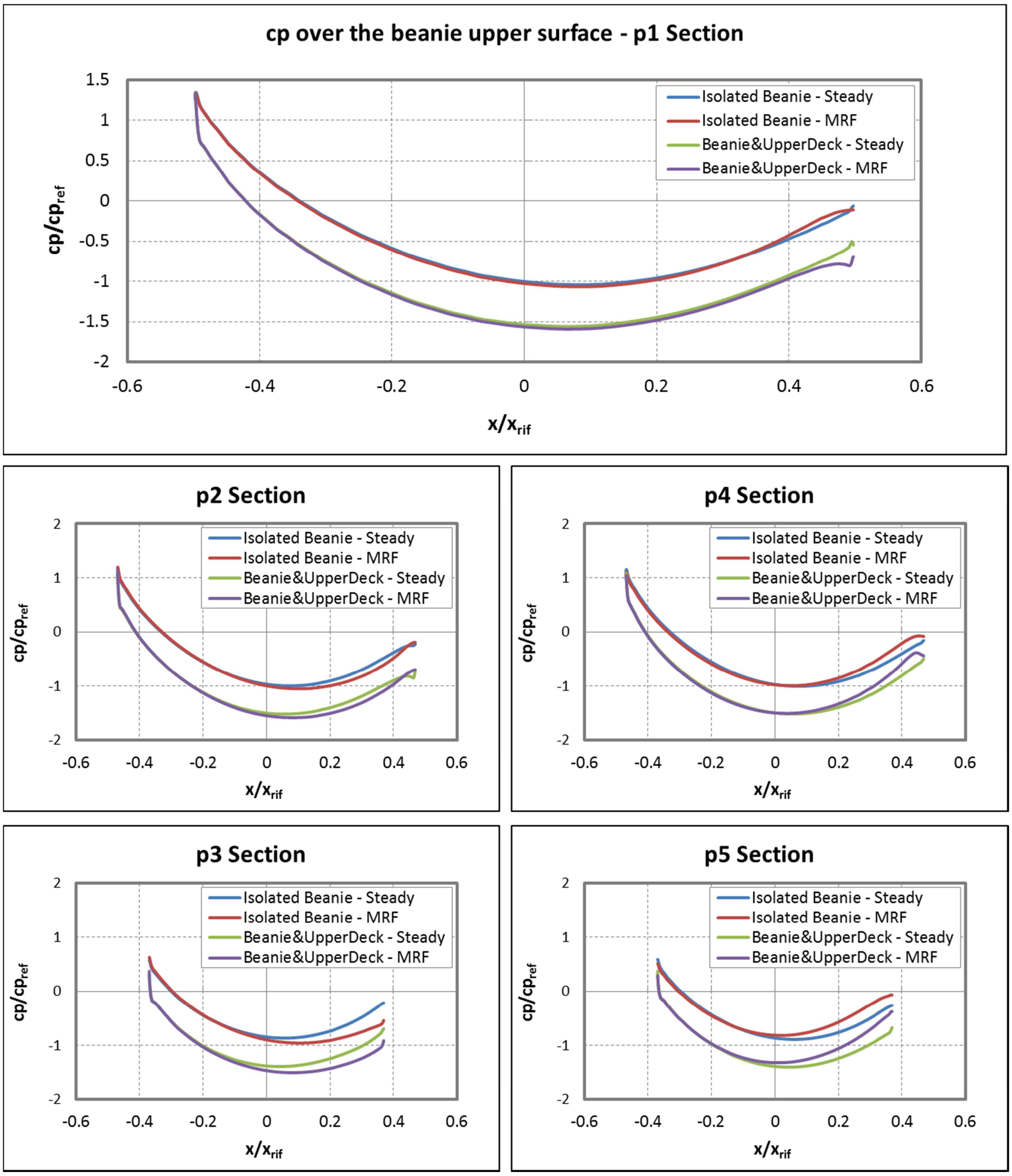
cp over the beanie upper surface - p1 Section

p2 Section

p4 Section

p3 Section

p5 Section

**Figure 2.54: Cp distribution over the beanie upper surface along five planar sections: comparison between isolated beanie and beanie in presence of the upper deck in both steady and rotating conditions.**

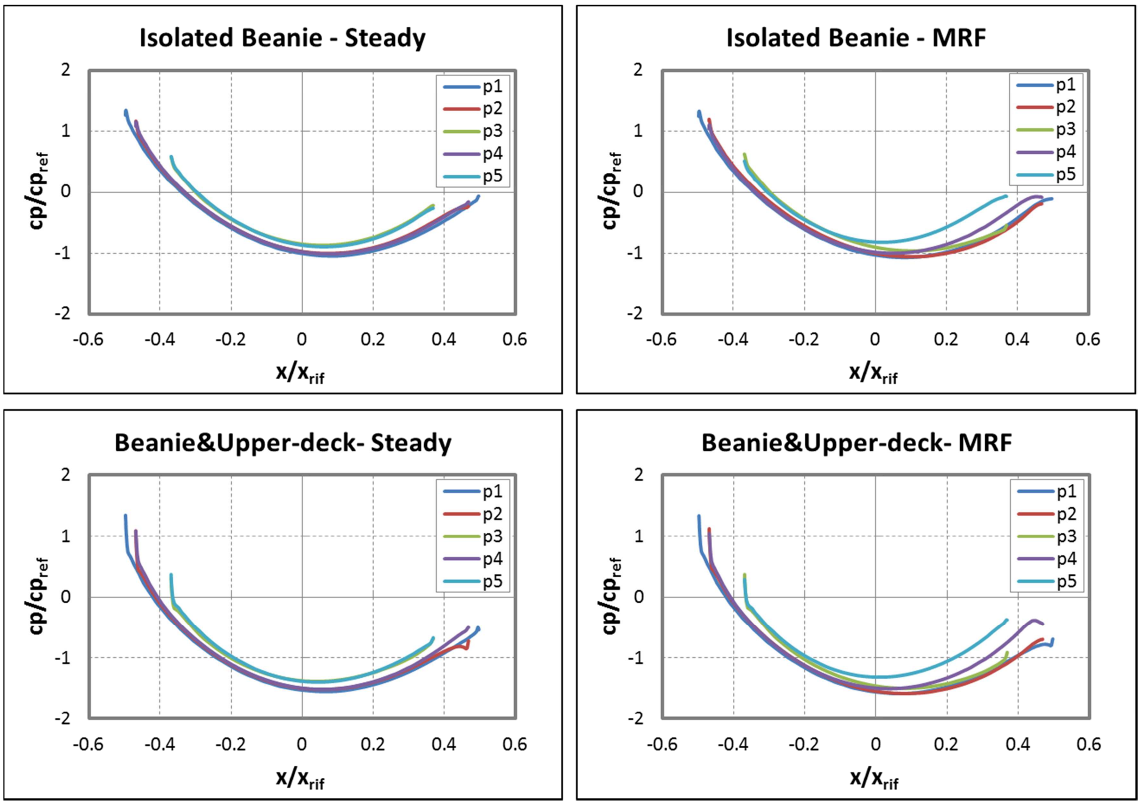

**Figure 2.55: Cp distribution over the beanie upper surface in the four analyzed configurations.**

In Figure 2.56, the contour plots of the non-dimensionalized total pressure over the helicopter longitudinal midsection are depicted for all the analysed configurations. It is apparent that the rotational speed of the beanie introduced significant modifications to the wake propagating downstream, both in the cases of isolated beanie and in presence of the engine fairing. Specifically, in the steady solution with upper deck included, the beanie wake impacted over the upper deck and then it seemed to be absorbed by the engine fairing wake. However, in the rotating simulations the beanie wake appeared more intense and it extended downstream the upper deck. More pronounced pressure losses were observed in this case and the beanie wake was less deflected downward than in the steady condition. This trend was confirmed also in the isolated beanie simulations, where with the beanie in steady conditions the wake downward deflection was more prominent.

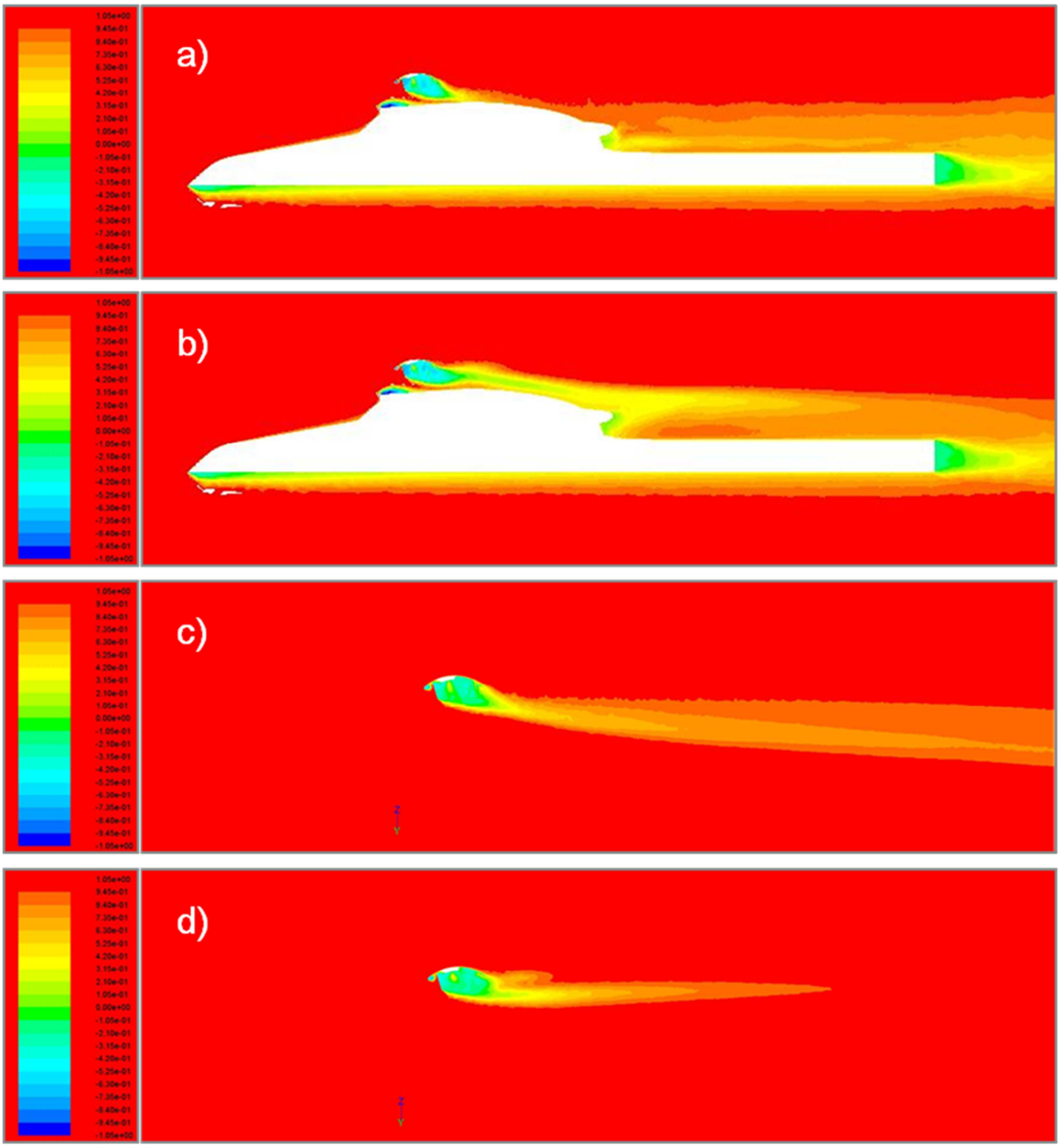

**Figure 2.56: Contour plots of the non-dimensionalized total pressure coefficient at the longitudinal midsection: a) Beanie&Upper-Deck non-rotating beanie; b) Beanie&Upper-Deck rotating beanie; c) Isolated non-rotating Beanie; d) Isolated rotating Beanie.**

A series of transversal sections, whose location is illustrated in Figure 2.57, were obtained over the helicopter model, where the contour plots of the non-dimensionalized total pressure were analysed. Results are reported in Figure 2.58 and Figure 2.59 for the beanie mounted over the upper deck and the isolated beanie respectively. As apparent, in the first case the steady beanie generated two nearly symmetrical vortices that were then absorbed by the upper deck wake. The partial asymmetry that can be observed at the top of Figure 2.58 was due to the peculiar upper deck geometry and in particular to the central engine exhaust. On the other hand, as far as the rotating beanie is concerned, a single intense vortex departed from the beanie and it extended downstream the upper deck, being deflected rightward with respect to the flow direction. In section 3 of Figure 2.58, the black solid line represents the trace of the tail fin: while the wake impinged the fin in the case of the steady beanie, it affected only the left part of the fin when the beanie was given its rotational speed. Also the higher intensity of the rotating beanie wake was confirmed in the plots of the total pressure coefficient over the transversal sections, in particular at the final section rakes.

As far as the isolated beanie is concerned, the simulations results confirmed the general trend already observed in presence of the upper deck. In particular, the beanie rotation caused the upper portion of the wake to be deviated rightward with respect to flow direction, as illustrated in Figure 2.59, while the flow remained nearly symmetrical with respect to the x-axis in the case of steady beanie. In general the rotating beanie generated a more intense wake than that coming from the non-rotating beanie.

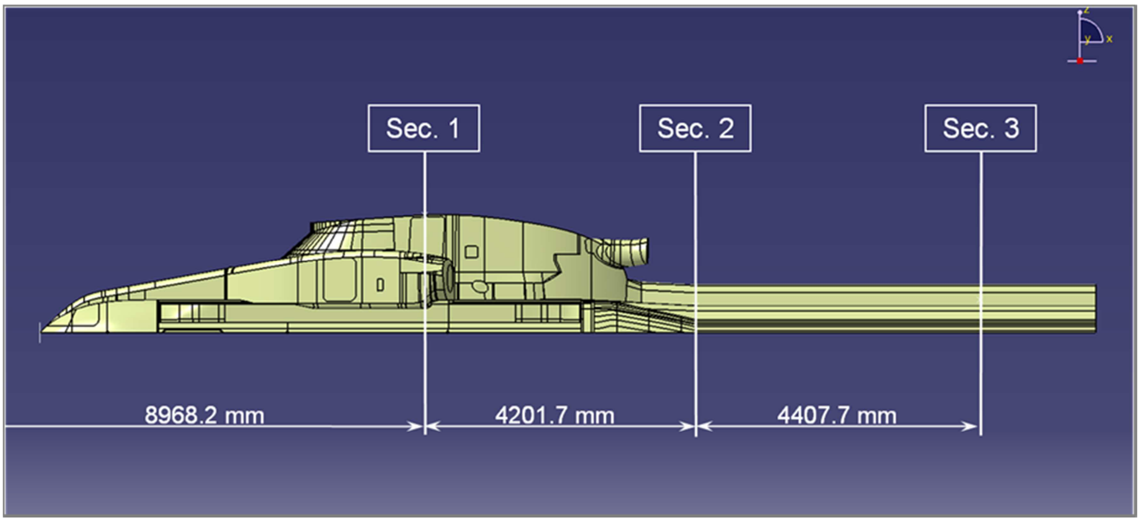

**Figure 2.57: Location of the sections used for the toal pressure analyses.**

In Figure 2.60 and Figure 2.61 the streamline path over the beanie is illustrated for the beanie in presence of the upper deck and the isolated beanie respectively, for both rotating and steady conditions. The rotational motion of the beanie appeared to affect the capability of the beanie to deflect the oncoming flow, since a less pronounced downward deflection of the streamlines in rotating conditions was evidenced in the longitudinal views, both with and without engine fairing included: in fact, the wake in rotating conditions was higher (with respect to the z axis) than the one generated by the fixed beanie. This aspect was corroborated also by the lift coefficient analysis, as will be discussed in the following. Moreover, from the top views the sideward deviation of the wake when the beanie was rotating is clearly apparent.

Finally, a series of wake rakes were placed over the transversal sections depicted in Figure 2.57 at various lateral positions, and the two dimensional curves of total pressure losses over these rakes were traced for each of the analysed configurations, in order to highlight the effects of the upper deck on the beanie wake. The wake total pressure losses over section 1, 2 and 3 are depicted in Figure 2.62, Figure 2.63 and Figure 2.64 respectively.

As apparent from Figure 2.62, the presence of the upper deck induced a more pronounced lateral diffusion of the wake in section 1, which was the most upstream of the analysed planes: in fact, at $y/y_{ref}$=-0.5 and $y/y_{ref}\geq1$ no pressure losses were evidenced for the isolated beanie, while the wake was clearly visible in presence of the engine fairing. At the intermediate lateral positions, the curves with and without inclusion of the upper deck were very similar in both steady and rotating conditions in terms of both wake intensity and vertical displacement.

On the other hand, in section 2, which is located immediately downstream the engine upper deck, the same wake lateral diffusion already observed in section 1 and induced by the engine fairing was noticed at $y/y_{ref}$=-0.5 and $y/y_{ref}\geq1$. However, in this case, a more pronounced influence of the upper deck on the wake behaviour was apparent also at the intermediate lateral positions. Specifically, in presence of the engine fairing the wake was more intense and exhibited a more pronounced downward deflection (Figure 2.63). This occurred in both steady and rotating conditions.

The same considerations hold true in general for transversal section 3, which is represented in Figure 2.64. However in this case the more prominent downward deflection of the wake induced by the engine fairing was more evident with the beanie in rotating conditions, while in steady state the difference was almost negligible. Finally, unlike the two preceding sections, also the wake of the isolated beanie was diffused in the lateral direction, since total pressure losses were evidenced also at $y/y_{ref}$=-0.5 and $y/y_{ref}\geq1$.

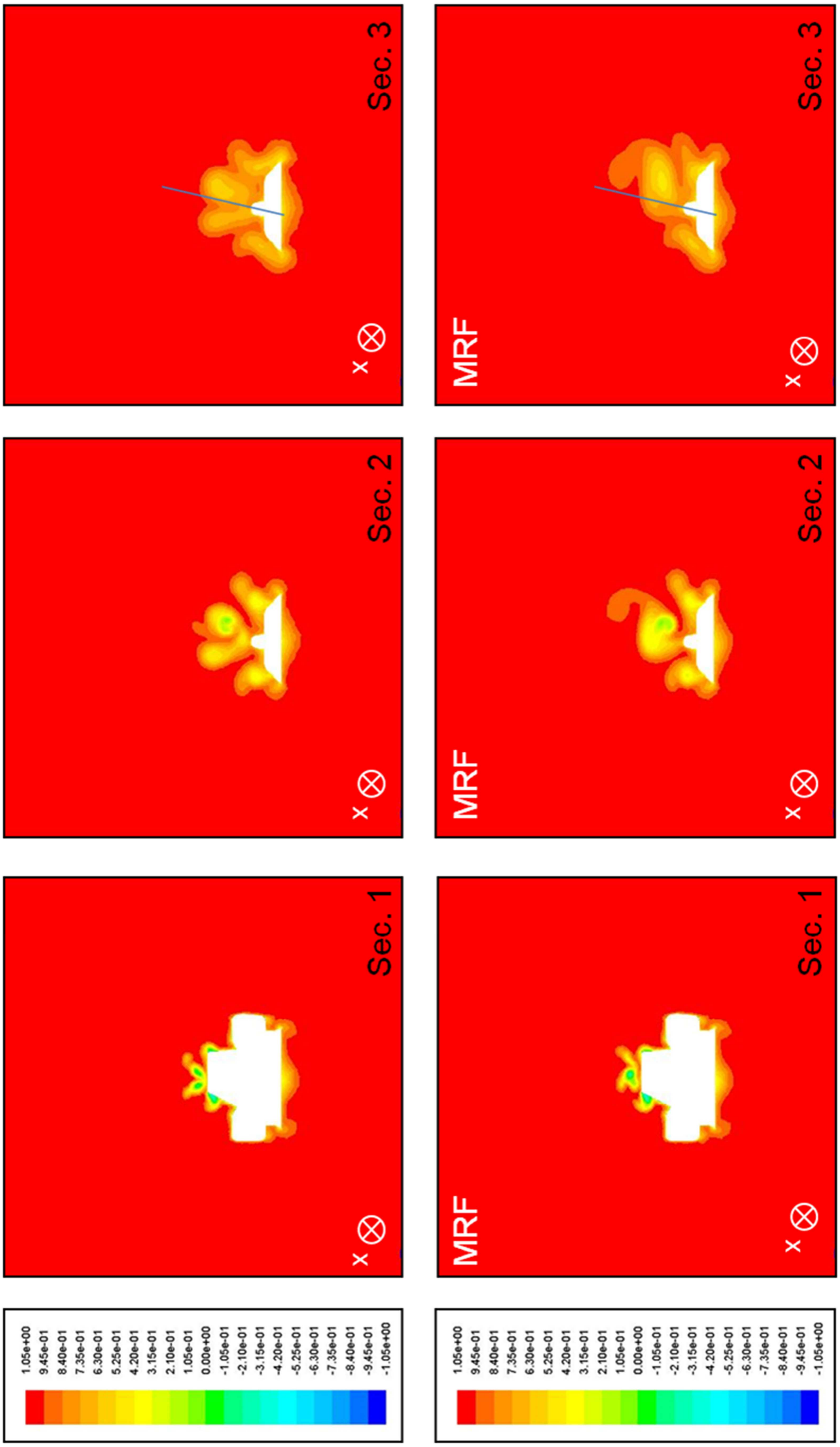

**Figure 2.58: Contour plots of the non-dimensionalized total pressure coefficient at three sections in the case of the beanie&UpperDeck.**

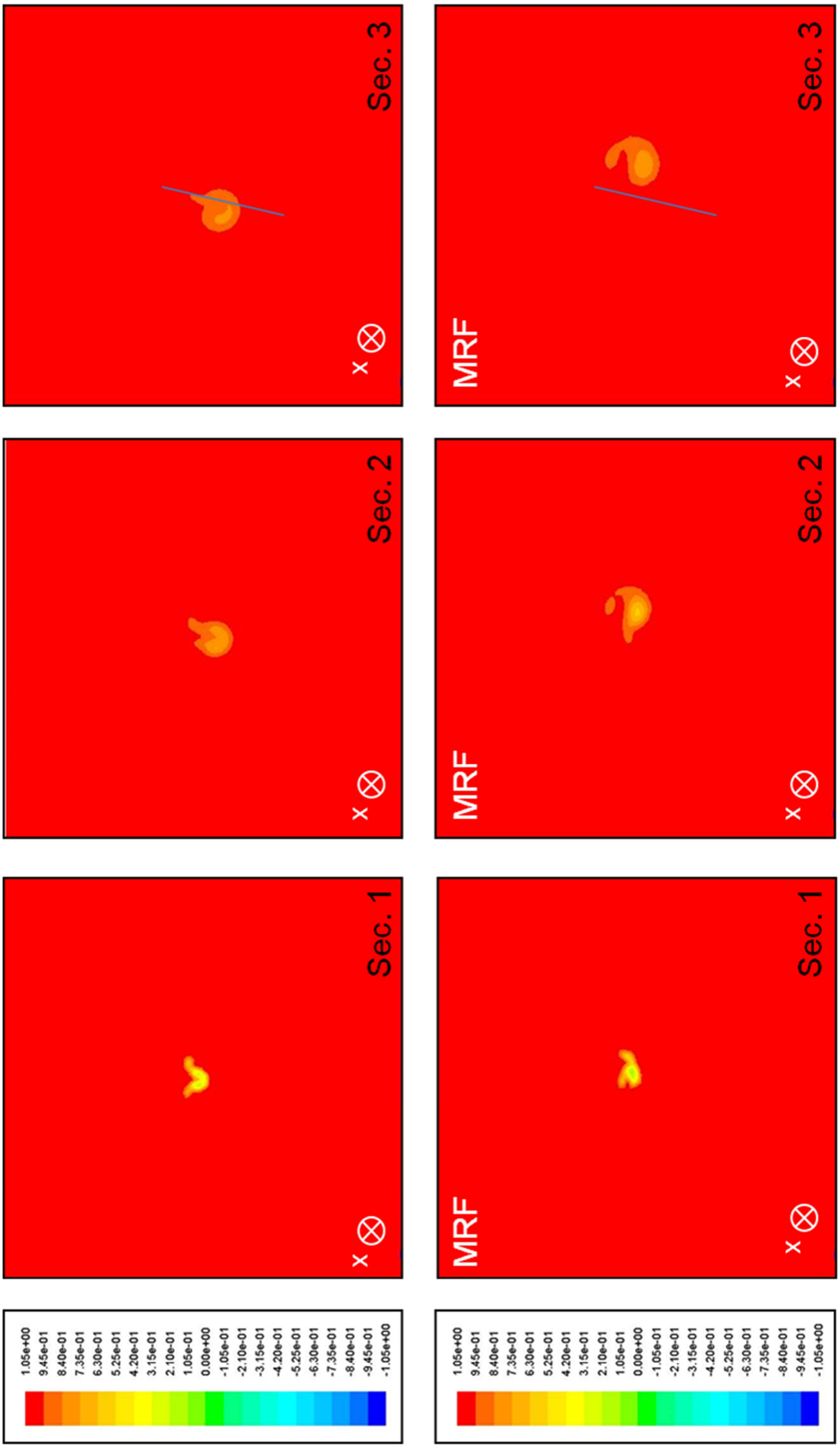

**Figure 2.59: Contour plots of the non-dimensionalized total pressure coefficient at three sections in the case of the isolated beanie.**

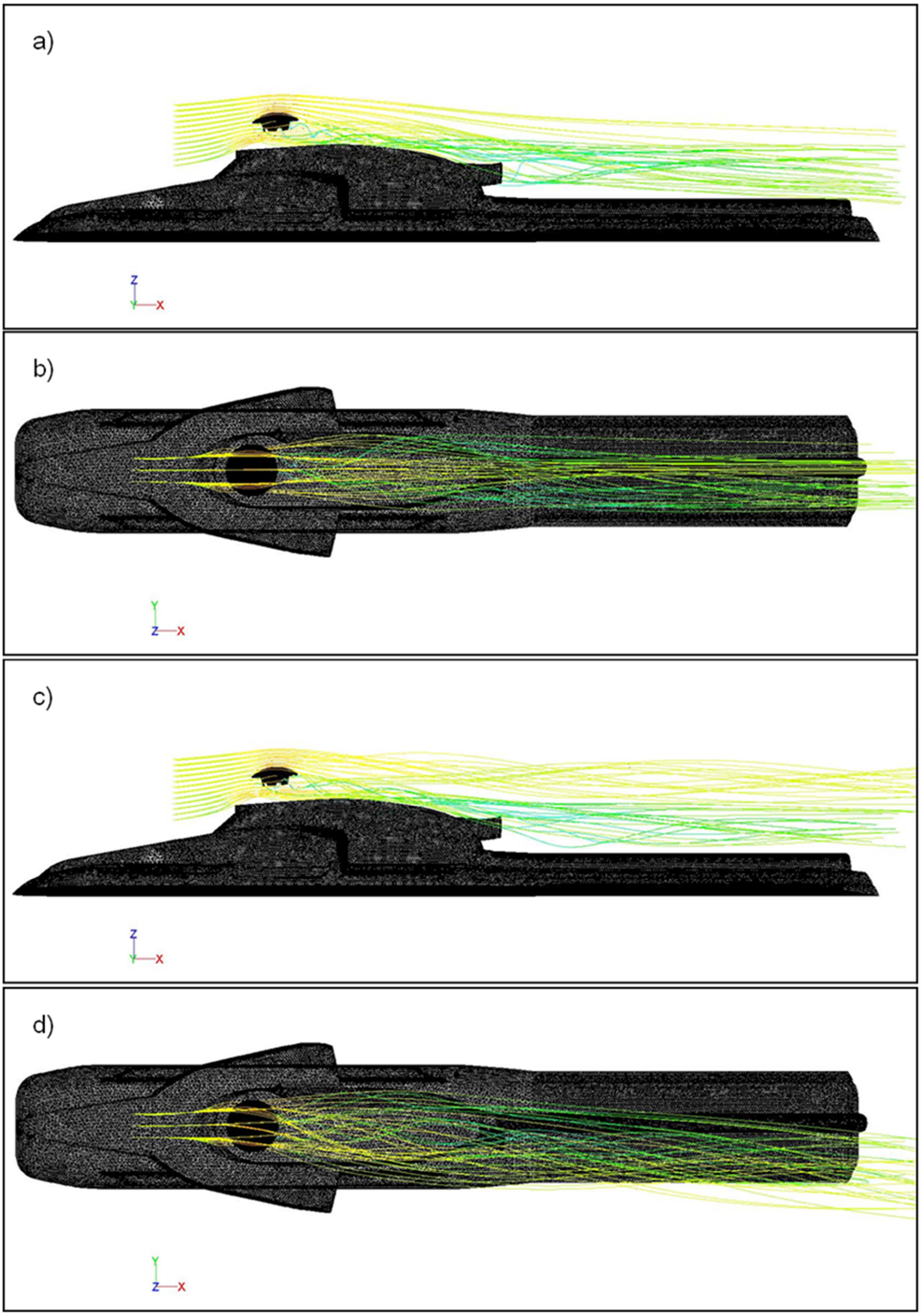

**Figure 2.60: Beanie&Upper-Deck: Streamlines in the case of the non-rotating beanie (a), (b) and of the rotating beanie (c),(d).**

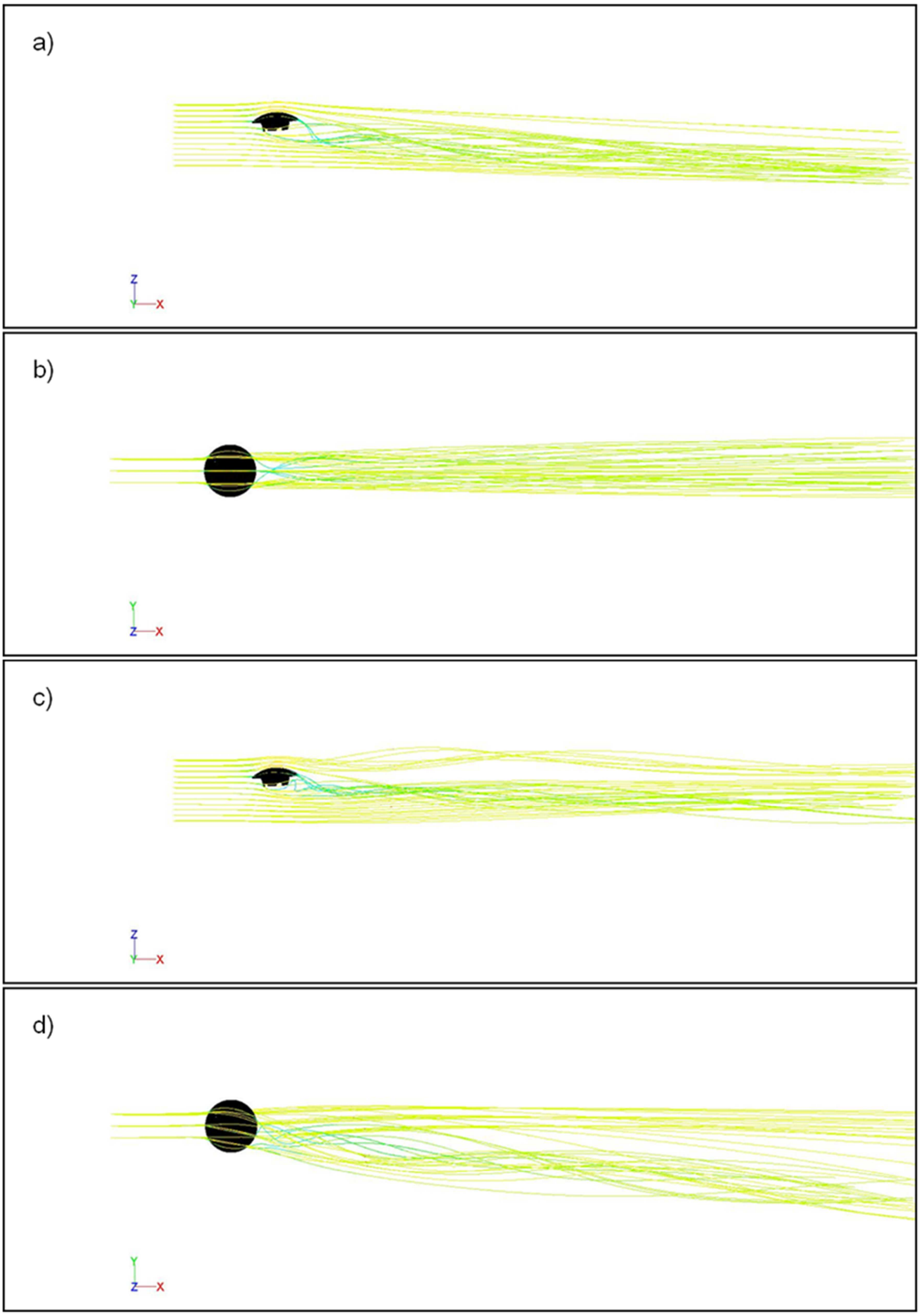

**Figure 2.61: Isolated Beanie: Streamlines in the case of the non-rotating beanie (a), (b) and of the rotating beanie (c), (d).**

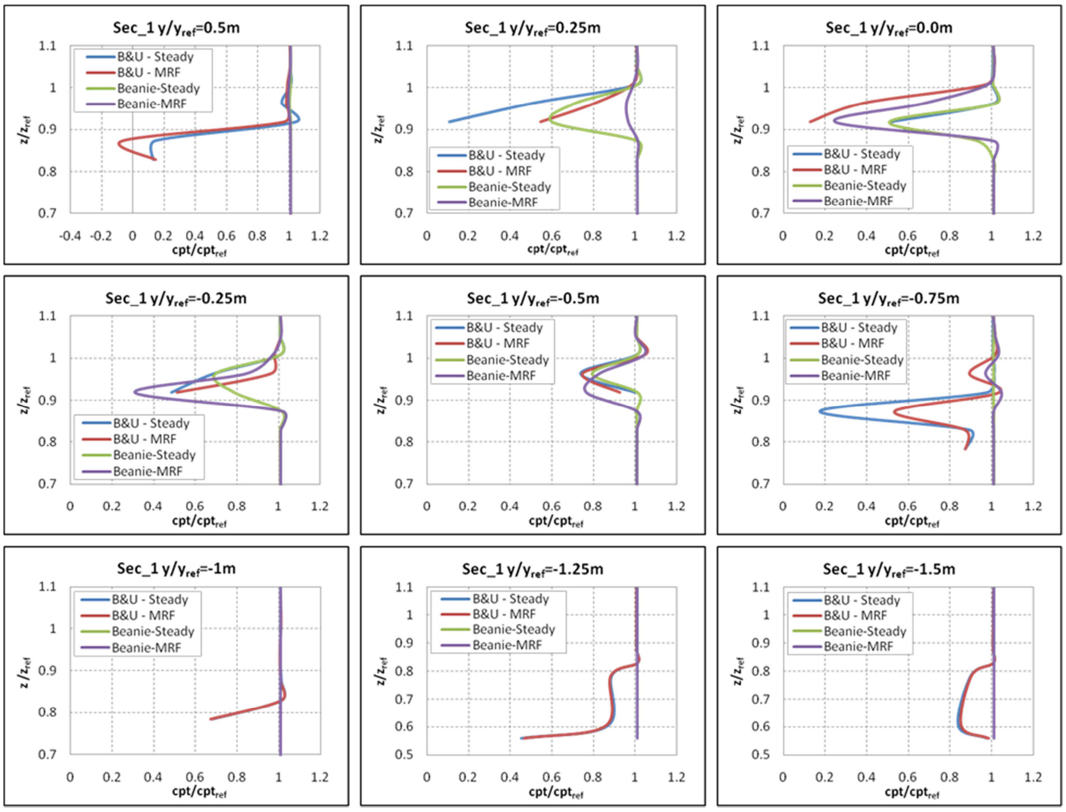

Figure 2.62: Two dimensional total pressure losses at different lateral positions over transversal section 1.

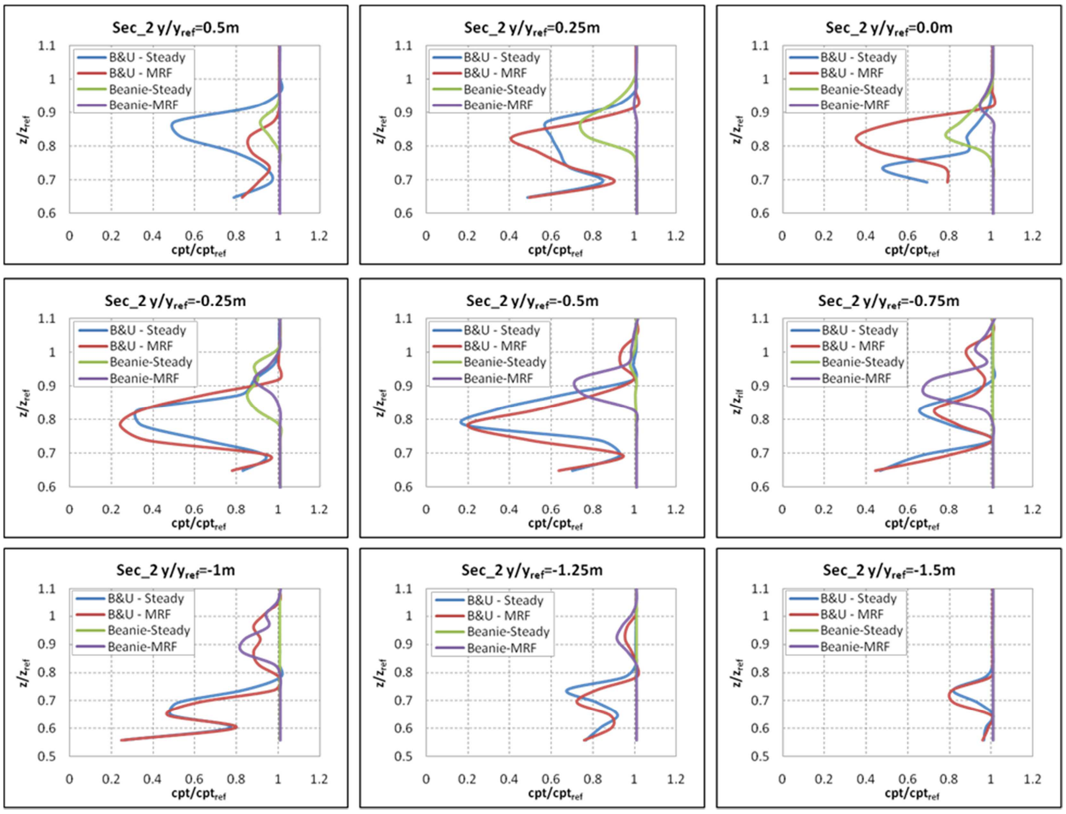

Figure 2.63: Two dimensional total pressure losses at different lateral positions over transversal section 2.

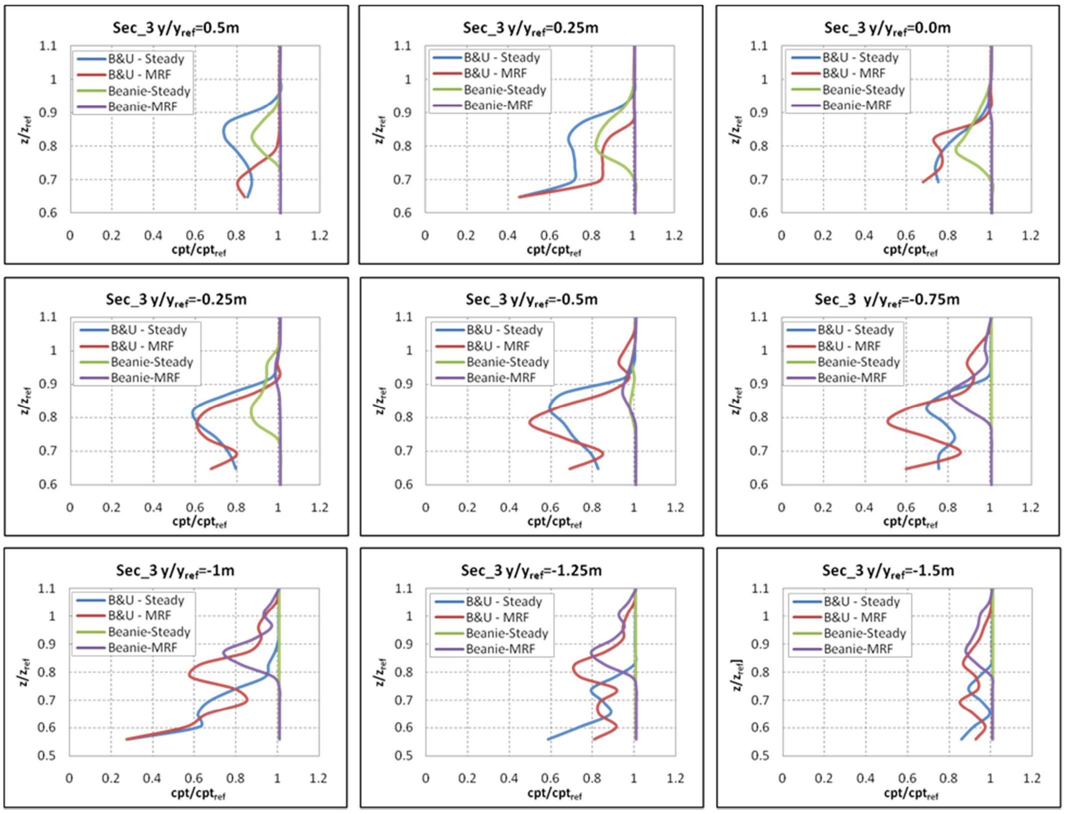

**Figure 2.64: Two dimensional total pressure losses at different lateral positions over transversal section 3.**

Finally, the lift, drag, and pitching moment acting on the beanie at the four analysed configurations were compared. However, these coefficients oscillated around a mean value and they did not reach a stable value during the simulations. These instabilities, together with the fact that residuals on continuity and turbulence parameters did not fall under $10^{-4}$, may suggest that the phenomenon could be intrinsically unsteady, due to both the large flow detachment under the beanie and the relevant wake downstream the beanie and upper deck. This behaviour was already evidenced in the analyses of the AW139 and AW109.

In Table 2.6, the forces and moments coefficients over the beanie are summarized for each of the analysed configurations: due to the above mentioned instabilities, the reported coefficients were obtained as mean values over the last 500 iterations.

As apparent, the beanie rotational speed (whether the upper deck is present or not) induced a reduction of the lift coefficient and thus a minor capability of the beanie to deflect the oncoming flow. On the other side, the rotation of the beanie caused the drag coefficient to increase, even though with a lower rate than the lift coefficient decrease.

Moreover, the effects of the presence of the upper deck were relevant in terms of the force coefficients. In fact, the oncoming flow was deflected by the engine fairing upstream the beanie, causing the angle of incidence to decrease from its nominal value (-4°), as apparent also from the streamlines path in Figure 2.60. In light of this, the beanie lift was increased by around 75%, with a simultaneous drag coefficient augmentation equal to 25%. To this purpose, both the non-rotating and the rotating configurations showed the same trend. Finally, the presence of the upper deck induced higher values of all the moment coefficients around the three axes, especially as far as the rotating beanie is concerned.

| | **Beanie& Upper-Deck** | | **Isolated Beanie** | |
|---|---|---|---|---|
| | **Steady** | **MRF** | **Steady** | **MRF** |
| **$cl/cl_{ref}$*** | 0.394 | 0.379 | 0.241 | 0.216 |
| **$cd/cd_{ref}$*** | 0.254 | 0.267 | 0.203 | 0.208 |
| **$cm_x/cm_{xref}$** | -0.0026 | -0.0122 | -0.0029 | -0.0025 |
| **$cm_y/cm_{yref}$** | 0.0613 | 0.0601 | 0.0092 | 0.0145 |
| **$cm_z/cm_{zref}$** | 0.0030 | 0.0046 | 0.0023 | -0.0016 |

**Table 2.6: Force and moment coefficients over the beanie coming from CFD simulations. (*average values of the last 500 iterations*)**

# 3. EVALUATION OF BEANIE AERODYNAMIC LOAD

## *3.1 Introduction*

The limit loads over a generic component are defined as the maximum loads acting on it throughout the whole design envelope: the component must be able to withstand the limit loads without incurring in permanent deformations. Therefore, the determination of these limit loads is necessary for the design and certification of helicopter beanies.

The overall limit loads include both aerodynamic and inertial loads, though this specific activity the attention was mainly focused on the analysis of the aerodynamic contribution only. Furthermore, as is the case for the standard aerodynamic loads, the aerodynamic limit loads can be provided either in the form of concentrated forces and moments or as distributed static pressure values, or both.

The beanie design envelope aerodynamic loads are not easy to be calculated, especially during the design phase. In fact, the helicopter flight envelope is usually given as a locus of points in the altitude-speed plane, where the flight conditions are referred to the fuselage reference system. The determination of the actual beanie angle of attack for each flight condition is not straightforward, so that the pertinent aerodynamic coefficients can be determined only using a rationale criterion that guarantees the required accuracy for certification purposes.

Basically, three different approaches may be used to identify the limit loads over the beanie:

- The simplest approach relies on a **semi-empirical method based on the strip theory**. Using this method, the aerodynamic limit loads are calculated based on the assumption that the most demanding conditions for the beanie airloads correspond to the stall of the component at some prescribed flight conditions in the design envelope. Specifically, the beanie is divided into small segments parallel to the upstream flow: then, a maximum lift and a maximum drag coefficient are assigned to each segment, whose values are derived from the literature. Finally, the total forces and moments are obtained by integrating the local contributions of each strip over the whole beanie surface. The main advantage of this method lies in the fact that it does not require the determination of the actual stall angle; however, the resultant aerodynamic loads might be extremely conservative, since they are based on two-dimensional coefficients extended to the whole beanie.

- The aerodynamic forces acting on the beanie can also be **evaluated experimentally in wind tunnel test campaigns**. To this purpose, two approaches are usually adopted:
    a) A full-scale non rotating beanie is aerodynamically characterized by measuring both forces and moments and surface static pressure distributions at different beanie incidence angles.
    b) A large scale rotating main rotor hub mounted on a dedicated test rig is aerodynamically characterized by measuring forces and moments acting on the hub itself (with and without the beanie included) at different test rig setting angles and advance ratio values with respect to the free stream.
- Finally, the aerodynamic limit loads acting on the beanie may be **evaluated directly via CFD simulations**.

The above-mentioned methodologies were applied to both the AW139 and AW101 beanies. In the following, both the strip-theory and the experimental-based approaches for determination of the beanie limit loads will be described in details, together with the adopted CFD methodology. Moreover, the obtained results will be discussed and compared to each other with the final aim of identifying a sound rational criterion for determination of the aerodynamic limit loads to be used for the design and certification of different beanies.

This activity was carried out with the support of *AgustaWestland*, and the results were summarized in technical report [16], which was submitted to the company for the final review and approval.

## 3.2 The simplified method

### 3.2.1 Method description

The semi-empirical simplified methodology used to determine the loads acting on the beanie is described in [17] and [18] respectively. As already mentioned, the approach is based on the strip theory: specifically, the beanie is divided into small segments parallel to the upstream flow and the aerodynamic forces acting on each strip are evaluated using some empirical correlations found in the literature ([19] and [20]). The total forces and moments are then obtained by summing up the contribution given by each strip.

The main assumption of this method is that the limit aerodynamic loads correspond to the beanie stall condition.

Being the experimental values of lift and drag coefficients at these peculiar conditions unknown, they were derived from [19] and [20], where the $c_l$ vs α and $c_d$ vs $\alpha$ curves for different Reynolds numbers are reported for bi-dimensional circular arc sections similar to the shape of a generic beanie longitudinal section.

For each section, the local contribution to the overall lift and drag is then calculated as follows:

$$L_i = \frac{1}{2}\rho V_{L_i}^2 A_i C_{L_i} \qquad \textbf{Eq. 1}$$

$$D_i = \frac{1}{2}\rho V_{L_i}^2 A_i C_{D_i} \qquad \textbf{Eq. 2}$$

where $C_{Li}$ and $C_{Di}$ are the 2D **$Cl_{max}$** and the associated $C_D$ coefficients of the strip respectively, $A_i$ is the strip area and $V_{Li}$ is the total velocity of each strip, i.e. the free stream velocity corrected for each section of the beanie in order to take into account the tangential velocity induced by the beanie rotation:

$$V_{Li} = V_\infty + V_{tip} cos\varphi_i \, , \qquad \textbf{Eq. 3}$$

being $V_{tip}$ the tangential velocity of the beanie tip and $\varphi_i$ an angle defining the azimuthal location of each strip of the beanie (Figure 3.1).

For the sake of consistency, the velocities must be taken and summed up as True Air Speed (TAS), being the rotational speed independent from the Pitot tube reading.

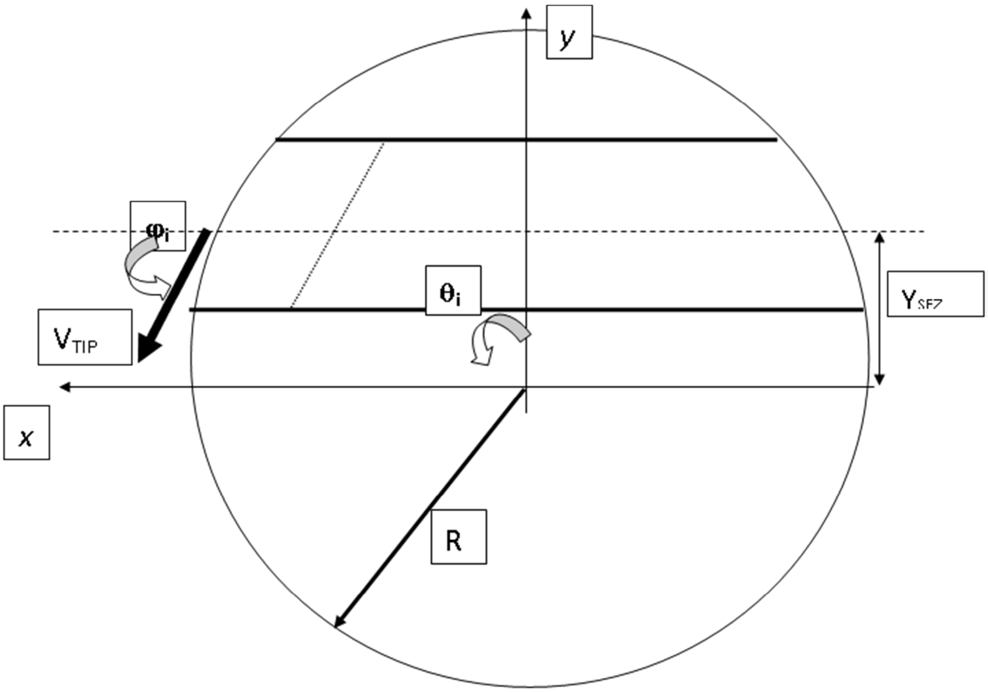

**Figure 3.1: Identification of the angle $\varphi_i$ defining the azimuthal location of each beanie strip ([18]).**

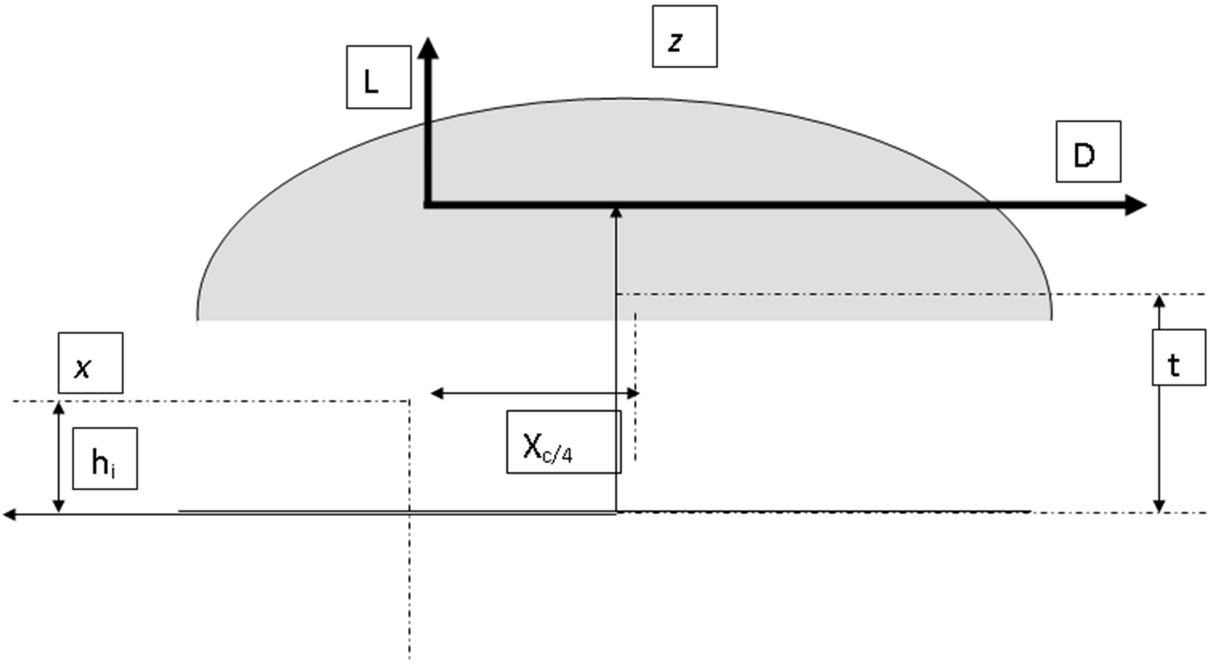

**Figure 3.2: Lift and Drag forces ([18]).**

Though also the moment values in the three directions (Mx, My, and Mz) were calculated in [17] and [18] with respect to the beanie centres, the equations used to compute them are not reported here, since the moment values are not of interest in the present analysis.

For the aerodynamic limit loads determination at design conditions, being the beanie angle of attack at stall conditions unknown, the total lift and drag are applied in the shaft axes reference system (Figure 3.2): hence, using the notation previously defined:

$$Z = L$$

$$H = D.$$

Obviously, this is a simplified approach featuring some margins of error. The work illustrated in the next sections is devoted to quantify the level of approximation of such an assumption and to remove all the related uncertainties.

The main advantage of this method is its straightforward implementation, while the main issue is the unavailability of the discretized loads over the beanie surface (i.e. local pressure distribution).

### 3.2.2 Application to the AW139 and AW101 beanies

The method described in the previous paragraph was used to determine the forces acting on both the AW139 and AW101 beanies at the flight conditions that were prescribed by *AgustaWestland*. In particular, these conditions were considered the most severe in the beanie flight envelope, i.e. maximum lift coefficient (stall conditions) at the helicopter design air speed (Vd) in presence of wind gust and at the rotor power-off rotational speed. Geometrical similitude between beanie sections and the shape indicated in [19] and [20], along with Reynolds number similitude, allow for the use of the maximum values of cl and cd , shown respectively in Fig.6, § 4-5 of [19] and in Fig.18, § 6-13 of [20].

The aerodynamic limit loads acting on the AW101 and AW139 beanies calculated using the simplified method described above are summarized in Table 3.1. The values are non-dimensionalized with respect to specific reference values due to industrial proprietary reasons.

| | $Z/Z_{ref}$ | $H/H_{ref}$ | $My/My_{ref}$ |
|---|---|---|---|
| **AW101** | 19.2 | 3.1 | 22.5 |
| **AW139** | 28.8 | 8.6 | 47.9 |

**Table 3.1: Aerodynamic limit loads calculated using the simplified method for the AW101 and AW139 beanies.**

## 3.3 Experimental based methods

### 3.3.1 Experimental method description

As mentioned in the in introduction of this chapter, the first experimental approach used to gather aerodynamic loads on the beanie is based on the full scale test of the non-rotating beanie. Specifically, the acquisition of several static pressure taps data over the beanie surface is the basis of the present methodology. The data are acquired at different beanie setting angles, which are coincident with the incidence angles ($\alpha=\theta$) in the case of isolated beanies. Then, the global aerodynamic loads are calculated from the integration of the pressure data over the beanie surface. The main advantage of this approach is the complete consistency of pressure distributions and total concentrated loads. Moreover, the rig can also be tested in parallel using a dedicated balance with the aim of comparing acquired global loads with those coming from to the pressure integration. On the other hand, a major drawback of this method is that it does not allow accounting for any interference effects from bodies located close to the beanie, like for instance the helicopter fuselage.

The second experimental approach concerns balance measurement of the aerodynamic loads on a large-scale test rig including cowlings, mast fairings and rotating main rotor hub. In this case, the beanie is characterized through comparison of the rig forces and moments with and without the beanie installed. The main advantage of this method consists in including into the beanie aerodynamic characterization the overall interference effects due to body and partial blades components. On the contrary, the main drawback is the unavailability of the beanie local pressure distributions.

### 3.3.2 Full scale non rotating AW139 isolated beanie

As already described in §2.2, a wind tunnel test campaign was carried out on the AW139 full scale, non-rotating beanie in order to assess the static pressure distribution over the beanie upper and lower surfaces for structural design purposes. The beanie was equipped with 81 static pressure taps distributed over a 72° sector on both the upper and lower surfaces of the component. During the tests, the beanie was rotated around its axis with the aim of acquiring the pressure data over different azimuth angles. Therefore, 401 pressure measures were acquired on the whole at each analysed angle of incidence. Furthermore, the experimental apparatus included an extensimetric balance which was used to measure the global forces acting on the beanie at the various test conditions

However, the acquired data during the above mentioned wind tunnel campaign could not be used directly for the beanie design and certification. To this purpose, Table 3.2 summarizes the flight conditions to be applied for the beanie airloads determination: these conditions cover the matrix point defined in [21], but were different form the wind tunnel test conditions (i.e.: ambient pressure and temperature, TAS=40m/s, and beanie in non-rotating mode). Therefore, the data acquired during that test campaign needed to be corrected in order to account for three major effects related to the design flight conditions, specifically the compressibility, the beanie rotation and the modified temperature.

| **VTAS at Temperature Condition 1 (TC1)** | **VTAS at Temperature Condition 2 (TC2)** | **VTAS at Temperature Condition 3 (TC3)** | $\alpha_{Fuselage}$ (positive nose up) [deg] | $\alpha_{Beanie}$ (positive nose up) [deg] | $\theta_{Beanie}$ (positive nose up) [deg] |
|---|---|---|---|---|---|
| a | - | - | -17<br>24 | -22<br>19 | -22<br>19 |
| b | - | - | -13<br>22 | -18<br>17 | -18<br>17 |
| c | - | - | -10<br>20 | -15<br>15 | -15<br>15 |
| d | - | - | -5<br>18 | -10<br>13 | -10<br>13 |
| e | - | - | 2<br>5 | -3<br>0 | -3<br>0 |

**Table 3.2: Flight conditions for the AW139 beanie airloads' determination ([22]).**

In particular, the values of the acquired static pressure coefficient reported in [13] were used to calculate the corrected differential static pressure ($\Delta P$), through the application of the following equation:

$$\Delta P = C_{PWT} * (0.5 * \rho_{\infty} * V_{TTAS}^{2}) * 1.05 \quad \textbf{Eq. 4}$$

where $\Delta P$ is the differential pressure, defined as the difference between the external and internal static pressure acting locally on the component, $C_{PWT}$ is the pressure coefficient as measured in the wind tunnel [13], $\rho_\infty$ is the free stream air density and $V_{TTAS}$ is the total true airspeed defined as:

$$V_{TTAS} = V_{\infty TAS} - \Omega * y \qquad \textbf{Eq. 5}$$

being $V_{\infty TAS}$ the free stream air speed, $\Omega$ the main rotor rotational speed and $y$ the local BL value.

For consistency, the velocities must be taken and summed up as True Air Speed (TAS), being the rotational speed independent from the Pitot tube reading.

The corrected pressure values were then integrated over the whole surface in order to calculate the aerodynamic forces acting on the beanie in the design flight conditions. To this purpose, a specific computer program was implemented to integrate the static pressure data over the beanie surfaces in order to determine the global aerodynamic forces. The program was first validated against the forces measured in the baseline conditions using the extensimetric balance installed in the wind tunnel, and then it was used to calculate the beanie limit airloads via integration of the corrected pressure data reported in [22]. Generally speaking, the net pressure force vector $\boldsymbol{F}$ acting on a surface may be computed as

$$\boldsymbol{F} = \oint p\boldsymbol{n}\, dA \qquad \textbf{Eq. 6}$$

where $p$ is the local pressure value, $\boldsymbol{n}$ is the local normal unit vector and $dA$ is the differential local surface area. For a discretized model the force can be calculated as follows:

$$\boldsymbol{F} = \sum_{i=1}^{m} p_i\, \boldsymbol{n}_i A_i \qquad \textbf{Eq. 7}$$

where $m$ indicates the number of faces in which the global surface is split, $A_i$ is the area of the $i^{th}$-face, $p_i$ is the pressure acting on $A_i$, and $\boldsymbol{n}_i$ is the unit vector normal to $A_i$.

Equation 7 was implemented in a computer program specifically created to calculate the aerodynamic forces acting on the beanie at different angles of incidence, using the values of the static pressure data acquired during the wind tunnel tests. The program requires an input file describing the characteristics of a meshed model of the beanie in HMASCII (HyperMesh® ASCII file) format and a second file containing the coordinates of the pressure taps and the pertinent differential static pressure values. Within the program, the mesh over the beanie is automatically subdivided into 401 sub-areas which encompass the triangular elements around a single pressure tap. For each element belonging to a single sub-area, the local contribution to the force $\boldsymbol{F_i}$ (and its components $F_{ix}$, $F_{iy}$ and $F_{iz}$) is calculated using Equation. 7 where $A_i$ is the area of the *i-th* element and $p_i$ is the static pressure measured by the tap related to the pertinent sub-area of that element.

First of all, the baseline data reported in [13] were used to test the accuracy of the program in determining the global aerodynamic forces acting on the beanie. Actually, thanks to the simultaneous acquisition of the local pressures and the overall loads, the lift and drag obtained by integrating the static pressures over the beanie surfaces could be compared with the global forces measured with the extensimetric balance.

The results of comparison are presented in Figure 3.3, where the values of both the lift and drag measured during the wind tunnel tests are reported together with the aerodynamic forces calculated by the program. The comparison on the lateral force was not possible due to the lack of experimental data. As apparent, there is an excellent correlation between overall experimental loads and the results derived by the integration of the local pressures. Only a slight discrepancy is observed in the drag which is probably due to two main factors:

- the program calculates the forces due to static pressure only, without taking into account the viscous contribution;
- in the wind tunnel tests, the pressure taps were positioned only over the beanie surfaces. Therefore, the program could not calculate the forces due to the beanie hub and supporting system.

Based on the results of validation, the program was then used to calculate the aerodynamic forces using the corrected differential static pressure data. The outcomes of the integration process in wind axis and shaft axis are reported in Table 3.3 and Table 3.4 respectively.

Moreover, with the purpose of further investigating the capabilities of the current approach, a further analysis was carried out at a selected flight condition aimed at highlighting the effects of the beanie rotation on the aerodynamic forces. In particular, the condition 2 and an equivalent airs speed (EAS) indicated by the letter “e” in Table 3.2 were selected. Specifically, the results of integration of the corrected pressures using Equation 4 and Equation 5 were compared to those obtained setting to zero the value of $\Omega$ in Equation 5 for the non-rotating beanie. The results of this analysis are illustrated in Figure 3.4 where the aerodynamic forces in the so-called wind axis system are reported.

Therefore, for a future comparison with the simplified method described in §3.2, the transformation in the Shaft axis system is necessary.

As apparent, while the effect of the beanie rotation on both lift and drag is negligible, a significant impact is shown as far as the side force is concerned. In particular, the side force of the steady beanie is nearly zero throughout the whole range of examined incidences, while it grows quadratically with the angle of attack when the beanie is given a rotational speed.

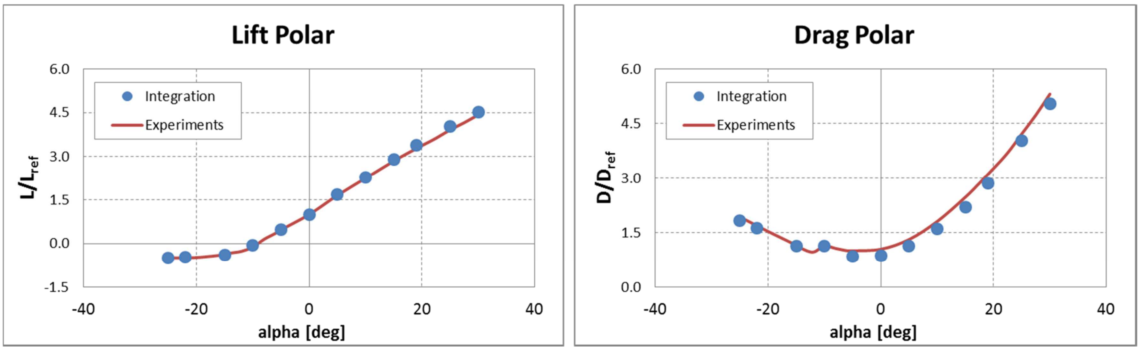

**Figure 3.3: Lift and drag polars of the AW139 beanie at wind tunnel conditions: comparison between the experimental values and the results of the integration process.**

| Aerodynamic forces in wind axis at the design envelope: corrected pressure integration | | | | | | | | | | |
|---|---|---|---|---|---|---|---|---|---|---|
| V (EAS) | **alpha Beanie** | **Condition 1** | | | **Condition 2** | | | **Condition 3** | | |
| | [deg] | $L/L_{rif}$ | $D/D_{rif}$ | $S/S_{rif}$ | $L/L_{rif}$ | $D/D_{rif}$ | $S/S_{rif}$ | $L/L_{rif}$ | $D/D_{rif}$ | $S/S_{rif}$ |
| a | **-22** | -1.4 | 4.9 | -2.2 | -1.4 | 4.9 | -2.5 | -1.4 | 4.9 | -2.1 |
| | **19** | 10.3 | 8.7 | -12.7 | 10.4 | 8.7 | -14.0 | 10.3 | 8.7 | -12.0 |
| b | **-18** | -1.6 | 5.2 | -2.1 | -1.6 | 5.2 | -2.4 | -1.6 | 5.2 | -2.0 |
| | **17** | 12.6 | 10.1 | -12.9 | 12.6 | 10.2 | -14.3 | 12.6 | 10.1 | -12.2 |
| c | **-15** | -2.0 | 5.6 | -2.1 | -2.0 | 5.6 | -2.4 | -2.0 | 5.6 | -2.0 |
| | **15** | 14.4 | 11.0 | -12.6 | 14.4 | 11.0 | -14.0 | 14.4 | 11.0 | -12.0 |
| d | **-10** | -0.5 | 6.2 | -2.4 | -0.5 | 6.2 | -2.7 | -0.5 | 6.2 | -2.3 |
| | **13** | 16.3 | 11.8 | -12.3 | 16.4 | 11.8 | -13.6 | 16.3 | 11.8 | -11.6 |
| e | **-3** | 5.0 | 6.0 | -4.4 | 5.0 | 6.0 | -4.9 | 5.0 | 6.0 | -4.2 |
| | **0** | 7.3 | 6.3 | -5.4 | 7.3 | 6.4 | -5.9 | 7.3 | 6.3 | -5.1 |

**Table 3.3: Aerodynamic forces in wind axis over the AW139 beanie at design flight conditions obtained by integration of the corrected pressures over the beanie surfaces.**

| **Aerodynamic forces in shaft axis at the design envelope: corrected pressure integration** | | | | | | | | | | |
|---|---|---|---|---|---|---|---|---|---|---|
| V (EAS) | **alpha Beanie** | **Condition 1** | | | **Condition 2** | | | **Condition 3** | | |
| | [deg] | $Z/Z_{rif}$ | $H/H_{rif}$ | $Y/Y_{rif}$ | $Z/Z_{rif}$ | $H/H_{rif}$ | $Y/Y_{rif}$ | $Z/Z_{rif}$ | $H/H_{rif}$ | $Y/Y_{rif}$ |
| a | **-22** | -2.1 | 3.3 | -2.2 | -2.1 | 3.3 | -2.5 | -2.1 | 3.3 | -2.1 |
| | **19** | 11.0 | 0.2 | -12.7 | 11.0 | 0.2 | -14.0 | 10.9 | 0.2 | -12.0 |
| b | **-18** | -2.2 | 3.8 | -2.1 | -2.2 | 3.8 | -2.4 | -2.2 | 3.8 | -2.0 |
| | **17** | 13.3 | 1.0 | -12.9 | 13.3 | 1.0 | -14.3 | 13.3 | 1.0 | -12.2 |
| c | **-15** | -2.5 | 4.2 | -2.1 | -2.5 | 4.2 | -2.4 | -2.5 | 4.2 | -2.0 |
| | **15** | 15.1 | 1.7 | -12.6 | 15.1 | 1.7 | -14.0 | 15.1 | 1.7 | -12.0 |
| d | **-10** | -0.9 | 5.9 | -2.4 | -1.0 | 5.9 | -2.7 | -0.9 | 5.9 | -2.3 |
| | **13** | 17.0 | 2.8 | -12.3 | 17.1 | 2.8 | -13.6 | 17.0 | 2.8 | -11.6 |
| e | **-3** | 4.9 | 6.6 | -4.4 | 4.9 | 6.6 | -4.9 | 4.9 | 6.6 | -4.2 |
| | **0** | 7.3 | 6.3 | -5.4 | 7.3 | 6.4 | -5.9 | 7.3 | 6.3 | -5.1 |

**Table 3.4: Aerodynamic forces in shaft axis over the AW139 beanie at design flight conditions obtained by integration of the corrected pressures over the beanie surfaces.**

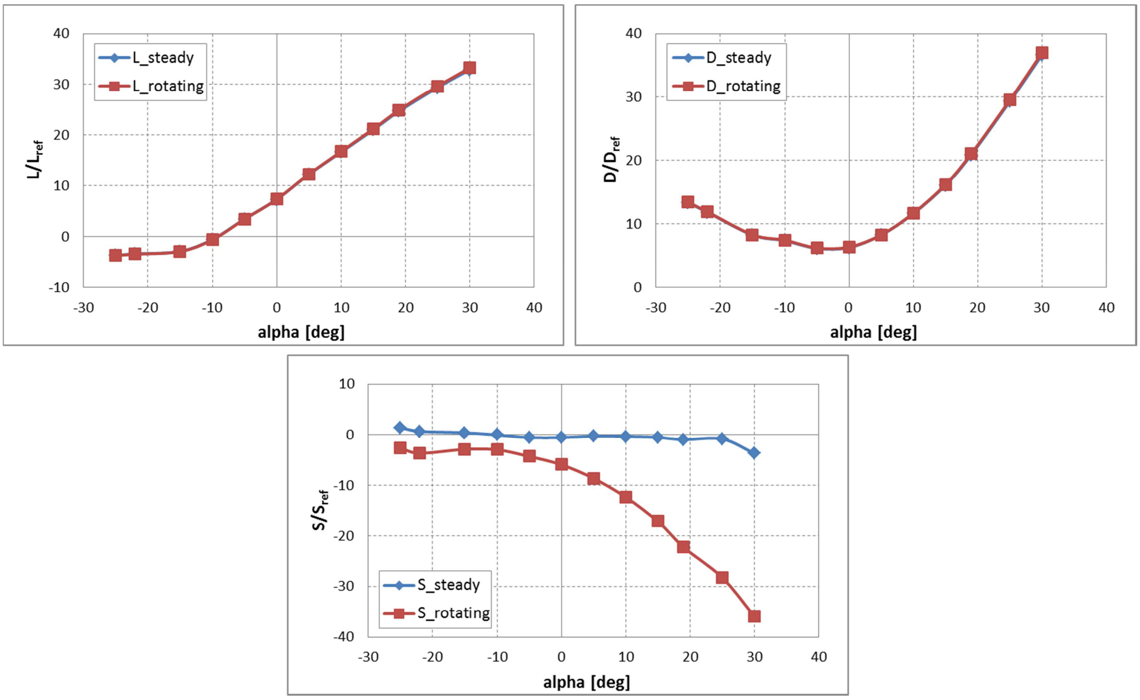

**Figure 3.4: Effects of beanie rotation on the global aerodynamic loads of AW139 beanie: lift (top left), drag (top right) and side force (bottom) at TC2 and EAS= "e".**

### 3.3.3 Large scale AW139 beanie on a rotating test rig

A further experimental activity was carried out in September 2007 on a 1/3.5 scaled model of the AW139 main rotor hub at the "Politecnico di Milano" wind tunnel, with the aim of acquiring the loads acting on the hub in presence of the whole helicopter fuselage, with and without the simulation of rotor rotation [23].

The tested model was made up of the fuselage and the main rotor hub, constituted in turn by the main rotor hub ring, the tension links, the dampers, the pitch link layer, the compasses, the blade root and the main rotor fairing (see Figure 3.5). As far as the blade collective motion was concerned, only settings between -10° and +16° were allowed. The rotor was powered by a 1.5kW motor which made it possible to achieve a rotational speed up to 1000 RPM. The loads acting on the main rotor hub were measured using a six components strain-gauge balance installed between the model frame and the hub assembly.

**Figure 3.5: AW139 large-scale beanie on the rotating test rig.**

The model was tested both in hover and in forward flight conditions. In particular:

- Hover: two blade pitch settings (i.e. 5.1° and 7.3°) and three different rotational velocities (i.e. 700, 900 and 1000 RPM) were considered. The tests were carried out with and without the main rotor hub fairing (beanie).
- Forward Flight: two blade pitch settings (i.e. 5.1° and 7.3°) and a rotational velocity of 900 RPM were considered; the wind tunnel velocity was limited to 42 m/s due to safety reasons. Finally, the configurations with motor off and the rotor blocked in position "x" and "+" were examined.

Specifically, the aerodynamic loads acting on the fuselage in typical flight conditions with and without the presence of the beanie at three different pitch angles were analysed and properly corrected in order to allow for direct comparison with the results of the previous analyses.

Table 3.5 summarizes the results of the wind tunnel tests carried out to evaluate the effects of the presence of the beanie on the rotor hub in forward flight conditions at three different fuselage pitch angles. Specifically, the values of horizontal, vertical and lateral forces on the main rotor hub measured in the rotor plane reference system with and without the presence of the beanie are given for each condition. Moreover, the absorbed rotor power (Q) with and without the beanie installed was measured as well.

From the analysis of data reported in Table 3.5, some considerations may be drawn on the effect of the presence of the beanie on the main rotor hub airloads. In particular,

- the beanie is responsible for an increased drag of the main rotor hub, especially with decreasing fuselage incidence;
- the presence of the beanie increases the hub lift, though with a lower ratio than it does for the drag;
- finally, the beanie acts in the direction of decreasing the absorbed rotor power, regardless of the fuselage attitude.

The data reported in Table 3.5 were used to derive the loads acting on the beanie simply by subtracting the forces acquired without the beanie ($F_{no\_beanie}$) form the forces acquired with the beanie installed ($F_{+\_beanie}$):

$$\Delta_0 = F_{+\_beanie} - F_{no\_beanie} \qquad \textbf{Eq. 8}$$

where $\Delta_0$ is the generic force acting on the beanie at the wind tunnel test conditions.

| Forward Flight: Beanie Effects | | | | |
|---|---|---|---|---|
| | Alpha fuselage | | | |
| | -5 | 0 | 5 | |
| $H/H_{ref}$ | 0.94 | 0.93 | 0.88 | no beanie |
| | 1.03 | 0.98 | 0.89 | + beanie |
| Δ% | 9.8 | 6 | 0.8 | |
| $S/S_{ref}$ | 0.21 | 0.05 | -0.14 | no beanie |
| | 0.26 | 0.08 | -0.17 | + beanie |
| Δ% | 24.4 | 55 | 24.8 | |
| $Z/Z_{ref}$ | 0.96 | 1.22 | 1.49 | no beanie |
| | 1.03 | 1.28 | 1.55 | + beanie |
| Δ% | 7.3 | 4.7 | 4.1 | |
| $Q/Q_{ref}$ | 1.71 | 1.78 | 1.75 | no beanie |
| | 1.67 | 1.71 | 1.73 | + beanie |
| Δ% | -2.6 | -4 | -1.6 | |

**Table 3.5: Aerodynamic loads on the AW139 1/3.5 scaled model main rotor hub and rotor power in forward flight conditions with and without the presence of the beanie. The data are referred to the rotor plane reference system.**

However, the resultant forces needed to be corrected in order to be directly compared to the results of §3.3.2. In fact, the wind tunnel test conditions (in particular the air speed and the air temperature) were different from the flight conditions used for the beanie certification. To this purpose, the loads were properly corrected as follows:

$$\Delta = \Delta_0 \cdot C^2 \cdot \frac{q}{q_0} \qquad \textbf{Eq. 9}$$

where $\Delta$ is the generic force at the desired flight conditions, $\Delta_0$ derives from Eq.8, *C* is the scale factor equal to 3.5 in this specific case, *q* is the dynamic pressure at the design flight conditions and $q_0$ is the dynamic pressure at the wind tunnel test conditions.

As described in §3.3.2 and referring to Table 3.2, the EAS named “d” and “e”, together with the “temperature conditions 2” were used to calculate the updated dynamic pressure *q* in Eq.9 to be used for correcting the forces acting on the beanie in wind tunnel conditions derived from Eq. 8.The results of these operations are listed in Table 3.4, where the beanie Z-force and H-force in both the rotor plane and the helicopter reference systems at both wind tunnel test and design flight conditions are reported. Surprisingly enough, it comes out that the beanie H-force decreases with increasing angle of attitude θ: this behaviour is probably due to both the rotor stubs and fuselage interference effects.

| **Horizontal Force Ratio** | | | | | | |
|---|---|---|---|---|---|---|
| | | rotor plane reference system (H force) | | | helicopter reference system | |
| Alpha fuselage α [deg] | **Attitude beanie θ [deg]** | Wind Tunnel | EAS=”d” TC2 | EAS=”e” TC2 | EAS=”d” TC2 | EAS=”e” TC2 |
| -5 | **-10** | 0.91 | 5.82 | 6.99 | 4.89 | 5.88 |
| 0 | **-5** | 0.54 | 3.49 | 4.19 | 2.73 | 3.28 |
| 5 | **0** | 0.07 | 0.44 | 0.53 | -0.36 | -0.43 |

| **Vertical Force Ratio** | | | | | | |
|---|---|---|---|---|---|---|
| | | rotor plane reference system (Z force) | | | helicopter reference system | |
| Alpha fuselage α [deg] | **Attitude beanie θ [deg]** | Wind Tunnel | EAS=”d” TC2 | EAS=”e” TC2 | EAS=”d” TC2 | EAS=”e” TC2 |
| -5 | **-10** | 0.68 | 4.38 | 5.26 | 4.58 | 5.50 |
| 0 | **-5** | 0.56 | 3.59 | 4.31 | 3.70 | 4.45 |
| 5 | **0** | 0.60 | 3.82 | 4.59 | 3.82 | 4.59 |

**Table 3.6: Aerodynamic forces acting on the AW139 beanie at both wind tunnel test conditions and design flight conditions, normalized with respect to sepcific reference value.**

## *3.4 Comparison of the simplified and experimental-based approaches*

The simplified methodology described in §3.2 is based on a semi-empirical approach aimed at calculating the aerodynamic forces acting on the beanie at the stall conditions using the strip theory. Since the actual values of the lift and drag coefficients of the beanie at stall are unknown, they were derived from two-dimensional coefficients over circular arc sections reported in the literature and applied to each beanie segment. The overall lift and drag calculated using this semi-empirical approach are independent from the incidence angle. Moreover, this method does not allow for the assessment of the side force, due to the lack of empirical correlations on the side force coefficient.

On the other hand, the experimental-based methods described in §3.3 rely on the data acquired in a series of wind tunnel test campaigns. This data needs to be corrected, since the original values are referred to test conditions which could not be directly used for design purposes.

### 3.4.1 AW139 beanie aerodynamic forces in wind axes

Figure 3.6 illustrates the comparison of results from integration of the corrected pressures and the simplified method applied to the AW139 beanie: specifically, the forces acting on the beanie in the wind axes reference system are reported at the flight condition used for application of the simplified method. The forces coming from the wind tunnel acquisitions over the 1/3.5 scaled model of the AW139 main rotor hub are not reported in the same diagrams since they are referred to the shaft axes reference system.

As apparent, the lift coming from the simplified method is close to the values found from integration of the corrected pressures at the highest polar angles.

On the other hand, the drag calculated using the simplified method is close to the lower portion of the drag polar coming from pressures' integration: actually, the drag value at the highest angles of attack is much larger than that found through the simplified method.

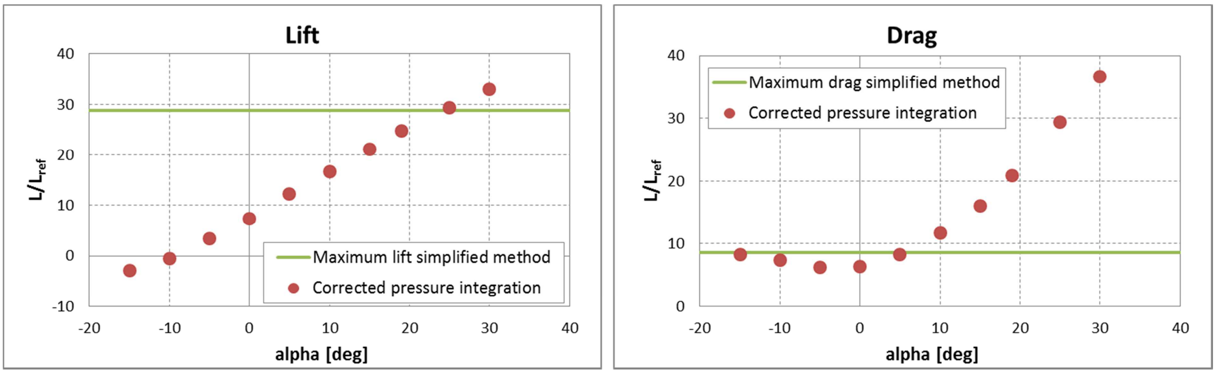

**Figure 3.6: Lift and drag forces values of the AW139 beanie: comparison of results from pressures' integration and simplified method.**

### 3.4.2 AW139 beanie aerodynamic forces in shaft axes.

The comparison of results from integration of the corrected pressures and the wind tunnel acquisitions on the 1/3.5 scaled model of the AW139 main rotor hub is illustrated in Figure 3.7, where the forces acting on the beanie in the shaft axes reference system are reported for the same flight condition used for application of the simplified method. The forces coming from the simplified method are not reported in the same diagrams since the corresponding beanie angle of attack remains undefined, so that the transformation into shaft axes cannot be carried out.

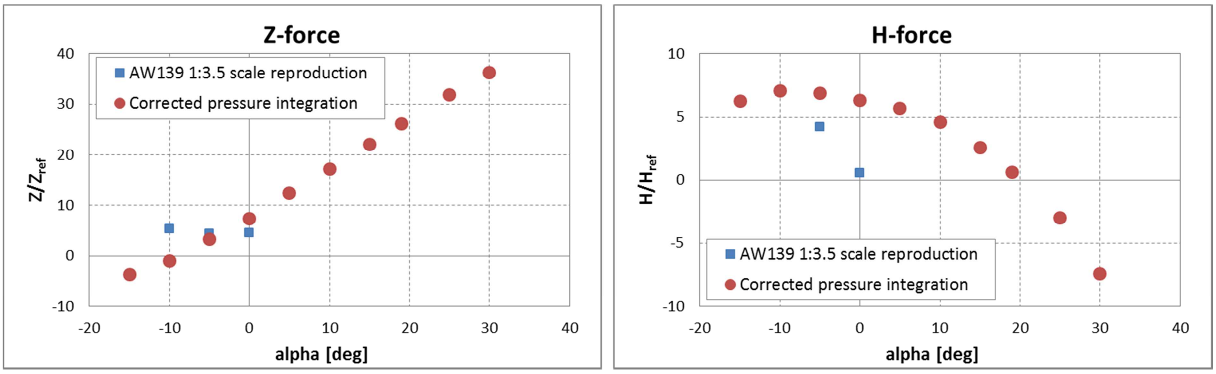

**Figure 3.7: Normal and H forces values of the AW139 beanie: comparison of results from pressures' integration and wind tunnel acquisitions**

As apparent, the normal force measured over the 1/3.5 scaled beanie model is quite in good agreement with the results of corrected pressure integration at the analysed flight condition, except for $\alpha=-10$ degrees, where the measured normal force on the hub model is larger than that at higher incidence angles, maybe due to interference effects with the hub and the fuselage. Moreover, the horizontal force values on the scaled model exhibit a decreasing trend at increasing angles of attack, as mentioned before. The H-force on the isolated beanie coming from the integration of corrected pressures has the same general trend; however, correlation with acquired wind tunnel data is quite poor, maybe due to the interference effects of other components not being included. In particular, while at $\alpha$ =-10 degrees the influence of the fuselage upper deck on the horizontal force seems negligible, this does not hold true for increasing values of the incidence angles. In fact, for $\alpha$ =-5 degrees and $\alpha$ =*0* degrees the measured horizontal force on the 1/3.5 scaled model is much lower than that coming from the integration of corrected pressures.

### 3.4.3 Aerodynamic limit loads: first assessment on the available methodologies

The outcomes of the methodologies described in the previous sections are then used to determine the aerodynamic limit loads acting on the beanie at the design conditions prescribed by *AgustaWestland.* To this purpose, the results of corrected pressures integration in shaft axes reference system are reported in Figure 3.8.

Moreover, as already mentioned in §3.2.1, the stall loads coming out from the simplified method at design conditions are applied in the shaft axes reference system for determination of the limit loads, being the beanie angle of attack at stall conditions unknown. The results of application of the simplified method are reported in Figure 3.8 as well. However, it is worth noting that the airloads obtained using the simplified methodology are not fully consistent with those coming from the integration of pressures, since no information concerning the side force is available from the strip theory. Moreover, the stall loads from the strip theory were calculated only at EAS=”e”.

From the analysis of the airloads’ envelope, the following conclusions can be drawn:

- first of all, the effect of temperature on the airloads for a given flight speed are almost negligible;
- as far as the Z force is concerned, the envelope of the fuselage design conditions applied to the isolated beanie is within the limit calculated using the simplified method;
- the vector sum of the Horizontal and Side forces for the isolated beanie at all the considered design conditions is within the limit defined by the H force calculated using the simplified method.

Moreover, in Figure 3.9 the limit loads calculated using the simplified method are compared with both the pressure integration and the wind tunnel acquisitions at the design conditions corresponding to a equivalent air speed named “e” at sea level and an air temperature condition number 2 (TC2). As apparent, also the wind tunnel acquisitions on the scaled hub model are within the limits defined by the simplified method.

Some general conclusions may then be drawn on the current methodologies adopted in *AgustaWestland* to determine the beanie aerodynamic limit loads:

a) the application of the stall forces calculated using the simplified method based on the strip theory and their imputation to the shaft axes reference system, though being a simplification, is a conservative approach, since it envelopes all the concentrated loads in the design conditions evaluated using the current methods;

b) the experimental methodologies do not allow for the assessment of the Reynolds number variation effects when the full scale beanie is to be considered rather than a scaled model for wind tunnel tests; hence, this first assessment still features some margins of uncertainty and needs to be further investigated using CFD;

c) the presence of the upper deck causes the horizontal force to decrease at a given incidence with respect to the isolated beanie; on the other hand, concerning the normal force, the fuselage interference effects seem to act in the direction of flattening the lift curve (at least for the analysed incidences ranging from $\alpha$=*-10* deg to $\alpha$=*0* deg) with respect to the isolated beanie.

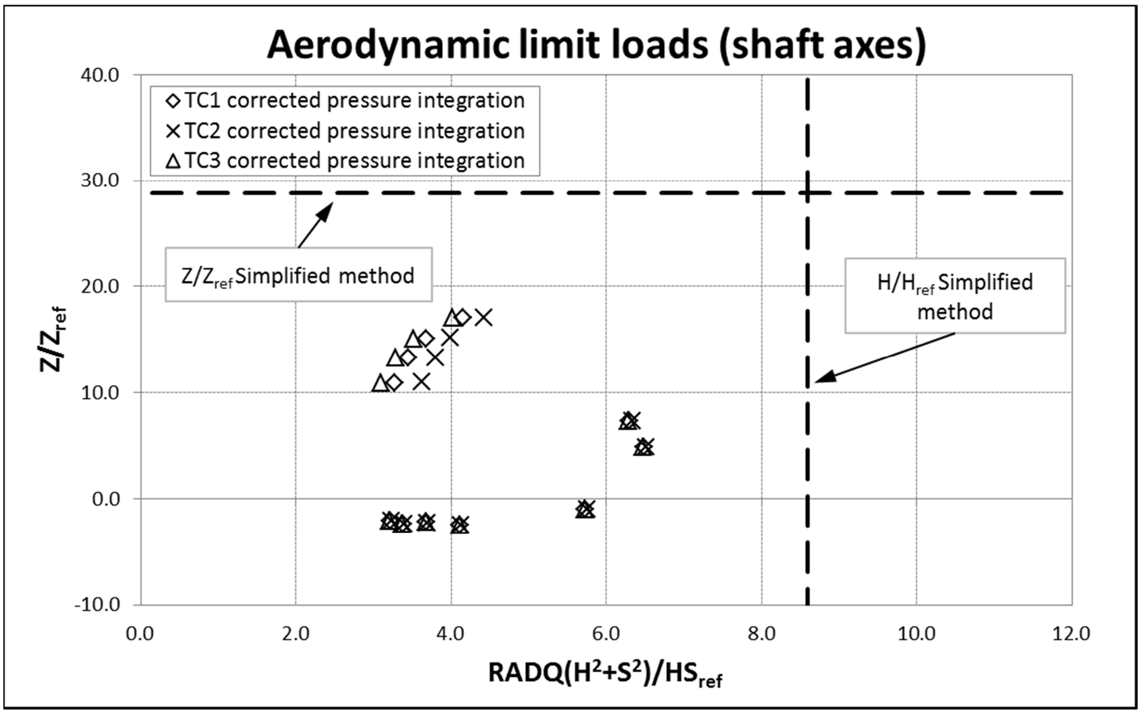

**Figure 3.8: Aerodynamic limit loads of the AW139 beanie in the shaft-axes reference system.**

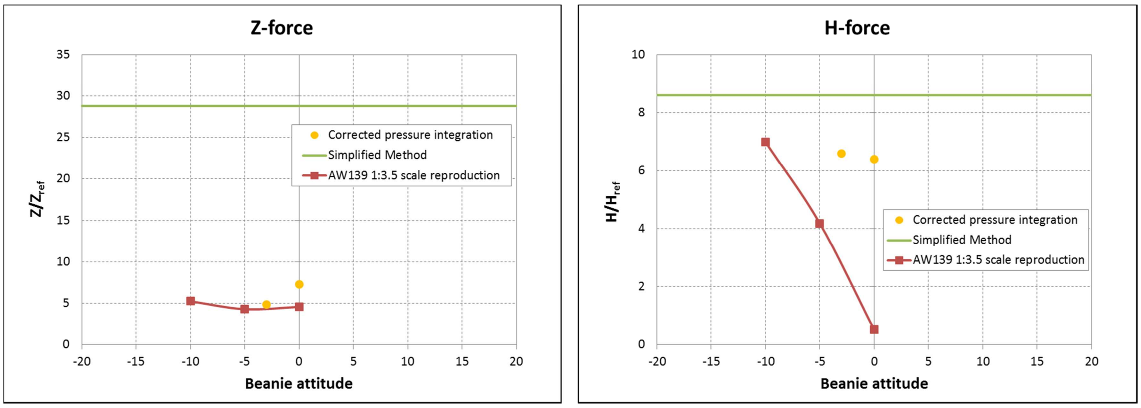

**Figure 3.9: Aerodynamic design limit loads of the AW139 beanie: comparison of the simplified method, the pressures' integration and the wind tunnel acquisitions**

## *3.5 CFD methodologies*

### 3.5.1 Introduction

An extensive simulation campaign was carried out with the aim of supporting the experimental data analysis of the previous paragraphs and identifying a new self-consistent method for the Aerodynamic Limit Loads evaluation. The obtained numerical results were compared with those coming from both the simplified semi-empirical method and the experimental acquisitions.

To this purpose, the numerical models of both the AW139 and AW101 beanies were analysed. The AW139 beanie model was set up following the indications drawn in Chapter 2, where this specific model was tested and validated against experimental data at different operating conditions and configurations. However, some minor modifications regarding the virtual wind tunnel dimensions and the parameters concerning the volumetric mesh generation were necessary to create a numerical model that fulfilled the constraints imposed by the new boundary conditions and turbulence models selected for the CFD simulations. The numerical test campaign aimed at identifying the stall angles of attack and the pertinent forces acting on the beanie at the most severe conditions among the ones prescribed by the certification rules. Then, the CFD methodology developed to numerically calculate the beanie aerodynamic forces at stall conditions was validated through direct comparison with the simplified methods described above.

The conclusions drawn for the AW139 main rotor hub fairing could be extended to other beanie models, whose numerical models cannot be validated against experimental data, due to the lack of dedicated wind tunnel test campaigns, as is the case for the AW101.

To this purpose, a CFD test campaign was carried out on the AW101 beanie as well. The numerical model of the AW101 beanie was generated following the indications drawn for the AW139 beanie validation, though some modifications were implemented. First of all, the isolated AW101 beanie was analysed in steady configuration at the same flight conditions used for the application of the semi-empirical method based on the strip theory ([17]), in order to compare directly the CFD stall loads with the lift and drag calculated using the simplified method. Then, the simulations were repeated in presence of the helicopter upper deck. In fact, in §2.4 it was proven that the engine fairing noticeably affects the beanie aerodynamic behaviour; therefore, it is reasonable to assume that the design of the beanie should take into account the mutual influence between these two components. The CFD analyses were carried out at the four prescribed conditions of the design envelope which were used for the beanie certification. The aerodynamic loads were determined for all the prescribed conditions, since it was not possible to identify *a priori* the most demanding one. It is worth noting that the analysis of the influence of the upper deck on the beanie was preceded by a further investigation aimed at verifying whether modelling the only engine fairing (without the rest of the fuselage) was sufficient to derive the impact of installation on the beanie aerodynamic behaviour, especially at high angles of attack. In fact, at highly positive incidences, the isolated engine fairing could produce a fictitious wake that might affect the beanie performance. To exclude that possibility, two models were generated: the first one was made up of the beanie and the isolated upper deck, while the second one included the whole AW101 fuselage. The two models were then simulated at two different angles of incidence and the results were compared in terms of lift, drag and pitching moment.

## 3.5.2 Application to the AW139 beanie

### 3.5.2.1. The AW139 CFD numerical model

A series of CFD analyses were performed over the AW139 beanie with the aim of determining the limit loads directly by simulation. The basic indications drawn in §2.2 were retained in the present analysis to set up a suitable CFD numerical model of the beanie, though some modification were required. For instance, some minor changes were implemented regarding the virtual wind tunnel dimensions, in order to guarantee that the undisturbed flow conditions to be imposed over the inlet and outlet sections were realistic, especially at high incidences. In particular, the virtual wind tunnel length and height were respectively increased up to 12 m and 5 m. Moreover, the cylinder surrounding the beanie, which represents the moving reference frame, was created, though the MRF approach was not used in the these specific fluid dynamic analyses.

The superficial meshes were created using triangular, linear type elements, while the volumetric grid was unstructured with some structured elements over the beanie surface to better simulate the boundary layer. It is worth noting that, in order to meet the requirements prescribed by the conventional turbulence model used in the CFD simulations, the parameters governing the boundary layer mesh generation were slightly modified with respect to the indications drawn in §2.2. In particular, the new selected set up was changed to guarantee that for all the analysed configurations the non-dimensional mesh thickness at the beanie surface y+ fell within a range that was consistent with the discretization levels (y+=30÷500) suggested for the wall functions implemented in the conventional turbulence models to work properly.

Unlike the grid used in §2.2 for the computations of total pressure losses in the wake, the mesh was not refined downstream the beanie in the present analyses, because the refinement was proven to have negligible effects on both the static pressure distribution and the aerodynamic forces values at stall. The volume grid generated around the beanie is illustrated in Figure 3.10.

A total number of 2.9M of elements were created for each analysed configuration. The mesh quality indices were optimized by means of some TGrid® tools to prevent potential difficulties in calculation’s convergence.

The variation of the beanie angle of attack was obtained by rotating only the virtual wind tunnel of an angle equal and opposite to the desired one and keeping the beanie fixed. The beanie and the MRF volume remained fixed to the absolute reference system, and the volume meshes related to these components were not modified. However, the unstructured grid within the virtual wind tunnel was created from scratch for each angle of attack, following the criteria described above.

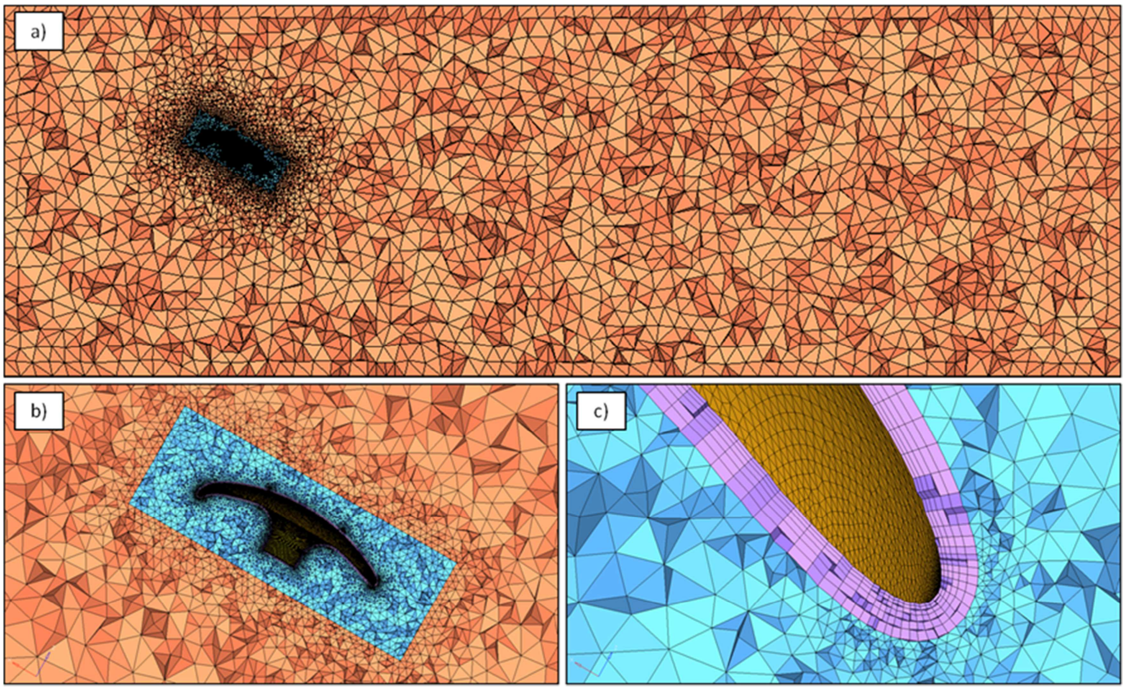

**Figure 3.10: The volumetric mesh around the beanie (α=30°): a) global longitudinal view; b) close-up of the rotating cylinder surrounding the beanie; c) close-up of the prismatic layers over the beanie.**

#### 3.5.2.2. The AW139 CFD test campaign

CFD simulations were carried out using ANSYS Fluent® v.12. A pressure-based solver type with absolute velocity formulation and steady approach was used for the simulations. The $\kappa-\omega$ SST turbulence model was selected for simulation of viscous effects. The air was treated as an ideal gas having constant specific heats, which automatically enabled the energy equation resolution. Fluid viscosity was modelled using the pre-defined three-coefficients Sutherland law.

A total pressure condition at the wind tunnel inlet and a static pressure condition at the outlet section were the prescribed boundary conditions. Static pressure, static temperature, and speed values, necessary for the calculation of the respective stagnation quantities, were derived from the indications drawn in §3.3.2. Actually, the analyses carried out in §3.3.2 made it possible to identify the most severe conditions from the beanie airloads point of view among all the design conditions prescribed by *AgustaWestland*. Specifically, these two conditions are both at TC2 and are characterized by an equivalent air speed (EAS) equal to “d” and “e”.

The beanie surface was treated as a hydraulically smooth and adiabatic wall, while a symmetry condition was used for the lateral surfaces of the wind tunnel box. Finally, as far as the turbulence specification method is concerned, a turbulence intensity of 5%, along with a hydraulic diameter equal to the beanie mean diameter were prescribed.

The solution was initialized by assessing the fluid values of the inlet section over the beanie and using an absolute reference frame, in order for the iterative process to start from a reasonable solution to speed up the convergence.

A SIMPLE scheme was adopted as the solution algorithm. The discretization scheme was varied from the First Order Upwind to the Third Order MUSCL, since a higher order is suggested to improve the solution accuracy, despite the increase of both the simulation time and the normalized RMS residuals. The under-relaxation factors were changed from the default values to in order to improve the residual convergence. In particular, the pressure was increased to 0.7, while the momentum was decreased to 0.3.

For each simulation, the convergence criterion was established when the RMS residuals were less than $1\bullet10^{-4}$. Furthermore, the trend of aerodynamic forces, along with the difference between the mass flow rate between inlet and outlet, were monitored in order to make sure they reached a stabilized value at the end of the simulations.

Two kinds of analyses were carried out on the AW139 beanie: the first one aimed at finding the beanie stall angle and the pertinent airloads, while the second one was focused on the CFD simulation of the beanie at the angles of attack reported in Table 3.2 (for the two design conditions named “d” and “e” at TC2), in order to compare the CFD results to the experimental data reported in §3.3.2.

The CFD simulation test program is summarized in Table 3.7.

| **Simulation test program at Sea Level** | | | | | |
|---|---|---|---|---|---|
| EAS =”d” | | | EAS =”e" | | |
| **CFD test number** | $\alpha_{Fuselage}$ [deg] | $\alpha_{Beanie}$ [deg] | **CFD test number** | $\alpha_{Fuselage}$ [deg] | $\alpha_{Beanie}$ [deg] |
| **1** | -5 | -10 | **7** | 2 | -3 |
| **2** | 18 | 13 | **8** | 5 | 0 |
| **3** | 35 | 30 | **9** | 35 | 30 |
| **4** | 41 | 36 | **10** | 41 | 36 |
| **5** | 43 | 38 | **11** | 43 | 38 |
| **6** | 45 | 40 | **12** | 45 | 40 |

**Table 3.7: AW139 beanie CFD simulations test program.**

#### 3.5.2.3. Results of the AW139 beanie test campaign

The simulated steady forces and moments coefficients of the AW139 beanie at TC2 and EAS=”d” and EAS=”e” for each of the analysed angles of attack are illustrated in graphical form in Figure 3.11 and Figure 3.12 respectively.

First of all, it was noticed that for all the analysed angles of attack the aerodynamic coefficients of the beanie oscillated around a mean value without reaching a stable behaviour. This kind of instabilities were already observed in §2.2 and §2.3: in addition to the fact that the residuals on continuity and turbulence parameters did not fall under $10^{-4}$, they might suggest that the flow field around the beanie could be intrinsically unsteady, due to both large flow detachment and the relevant wake downstream the beanie (especially at the stall conditions).

Moreover, it was observed that the difference in the air speed between the two analysed conditions does not have a significant influence on the aerodynamic coefficients. In fact, an increase of around 10% in EAS corresponds to a modest reduction (approximately 2%) of the lift, drag and side forces, while the pitching moment coefficient is increased by 2%.

As apparent, the stall of the AW139 isolated, steady beanie occurred at an angle of attack of approximately 38 degrees at both the examined design conditions: the stall angle may be clearly identified, since an increase in the angle of attack of 2 degrees with respect to the stall value is followed by an abrupt drop in lift, drag, and side force and pitching moment coefficients.

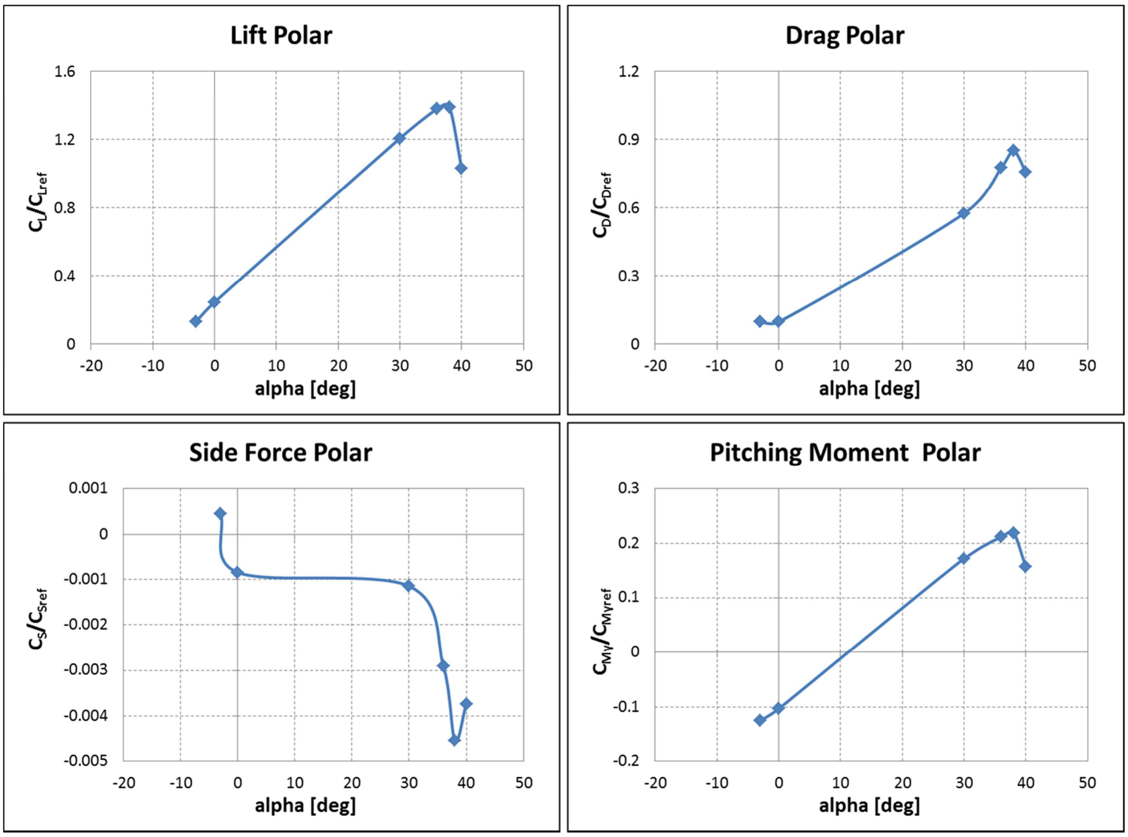

**Figure 3.11: Simulated aerodynamic coefficient polars of the AW139 beanie at EAS="d" and TC2.**

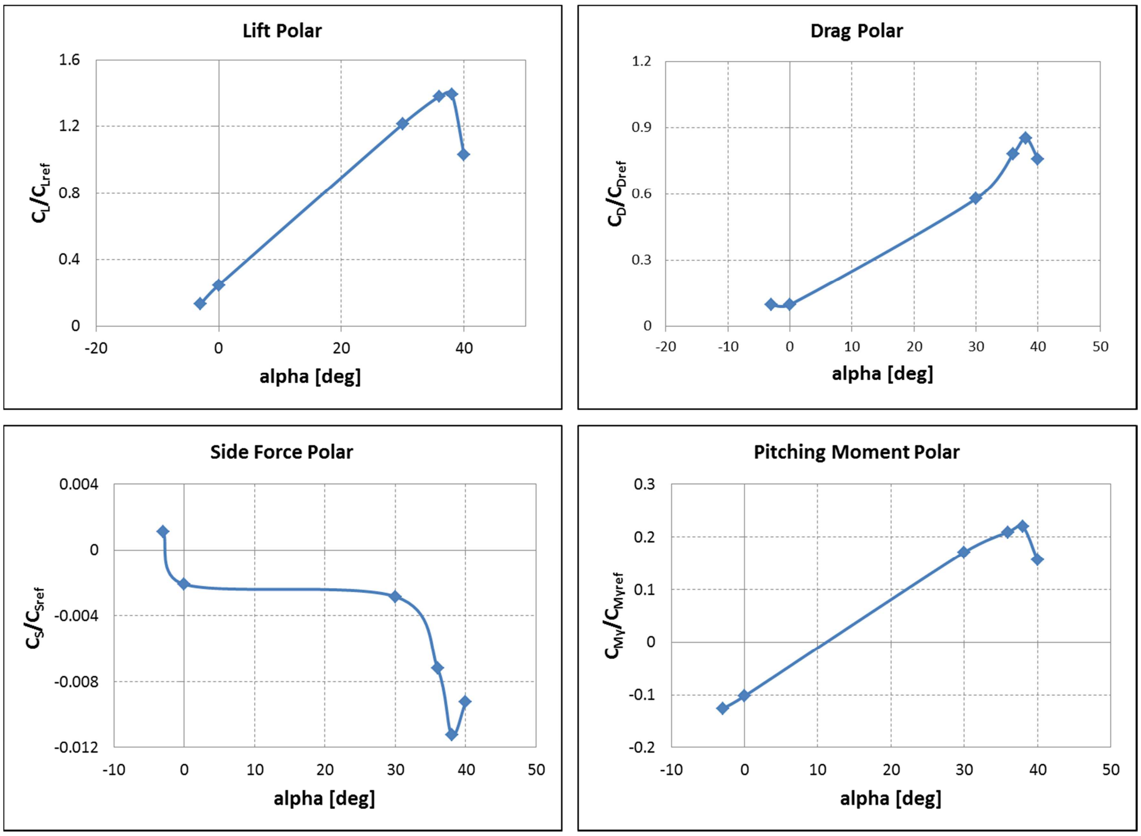

**Figure 3.12: Simulated aerodynamic coefficient polars of the AW139 beanie at EAS="e" and TC2.**

#### 3.5.2.4. Reynolds effects

The numerical results presented in the previous sections may be directly compared to those reported in §2.2 in order to highlight the Reynolds number variation effects on the aerodynamic coefficients of the AW139 beanie.

The effects of Reynolds number variations on the beanie lift and drag are depicted in Figure 3.13, where the lift and drag coefficients coming from the CFD simulations at the test conditions listed in Table 3.8 are reported. From Figure 3.13, it can be deduced that the variation of Reynolds number due to the different operating conditions does not have any appreciable effect on the drag, so that the wind tunnel data may be used directly for the limit loads. On the other hand, the slope of the linear portion of the lift curve seems to increase with increasing Reynolds number, thus suggesting that some corrections need to be implemented when extrapolating the wind tunnel acquisitions to the design operating conditions.

| **Simulation Conditions** | **EAS** **[kts]** | **T** **[K]** | **Re** |
|---|---|---|---|
| wind tunnel | 77.09 | 293.15 | 2.360E06 |
| design conditions#1 | “d” | TC2 | 7.653E06 |
| design conditions#2 | “e” | TC2 | 8.390E06 |

**Table 3.8: Reynolds number values (based on the full scale beanie diameter) on the operaing conditions analysed via CFD.**

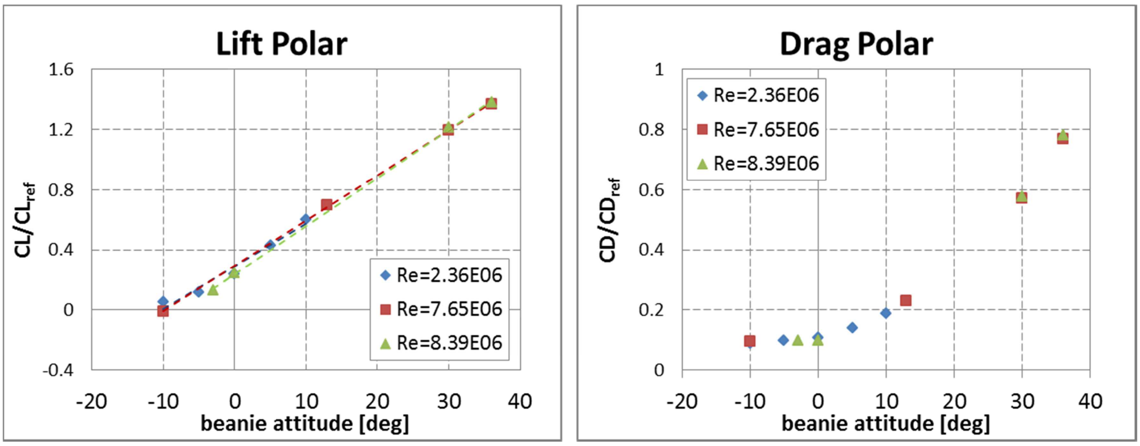

**Figure 3.13: Lift and drag polars of the AW139 full scale isolated non-rotating beanie at varying Reynolds number.**

#### 3.5.2.5. Comparison of CFD results with simplified and experimental-based methods in wind axes

As already discussed above, the methods currently used at *AgustaWestland* for the determination of the beanie limit loads for design and certification purposes are based either on semi-empirical approaches or on wind tunnel experiments. In §3.4 the outcomes of these two methods applied to the AW139 beanie were compared and some discrepancies in the results were evidenced. In particular, the semi-empirical approach was shown to be inadequate to predict the beanie drag.

The CFD simulations on the AW139 beanie described in the previous chapters were carried out at the most severe conditions from the aerodynamic loads point of view, according to the results provided by the simplified methods. The CFD simulation campaign aimed not only at determining the stall angle of attack and the pertinent forces acting on the beanie at those conditions, but also at comparing the CFD results to the available experimental data for validation purposes.

In Figure 3.14 and Figure 3.15, the results given by both the simplified method and the integration of corrected pressures are illustrated and compared with the CFD simulations for the two conditions EAS=”d” (at TC2) and EAS=“e” (at TC2) in wind axes reference system. However, it is worth noting that the maximum lift and drag values coming from the simplified method were calculated only at the latter design condition. The forces coming from the wind tunnel acquisitions over the 1/3.5 scaled model of the AW139 main rotor hub are not reported in the same diagrams since they are referred to the shaft axes reference system.

The following conclusions may be drawn:

- as far as the beanie lift is concerned, there is quite a good agreement between the results obtained from the corrected pressures’ integration and the CFD at both the tested conditions, at least for low angles of attack. Furthermore, the lift load at stall predicted with the simplified method is in excellent agreement with the stall load given by the CFD simulations at EAS=”d” (at TC2). On the other hand, at EAS=“e” (at TC2) the simplified method underestimates the stall load by around 20% with respect to the numerical results;
- regarding the beanie drag, an excellent correlation between the CFD and the corrected pressures’ integration results was found at both the analysed conditions. On the other hand, the simplified method largely underestimates the drag at the stall condition given by CFD.

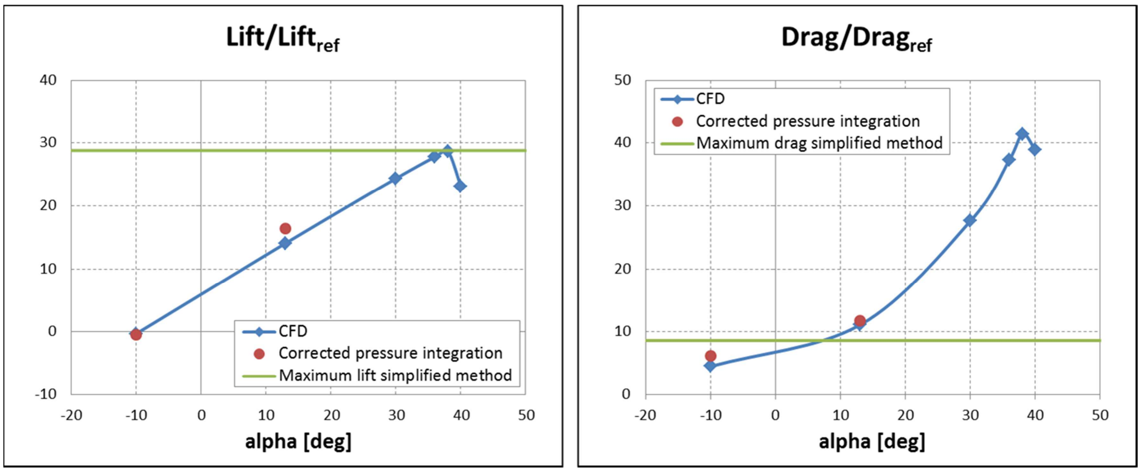

**Figure 3.14: AW139 beanie lift and drag polars at EAS=”d”(at TC2): comparison of CFD results with simplified and experimental-based methods.**

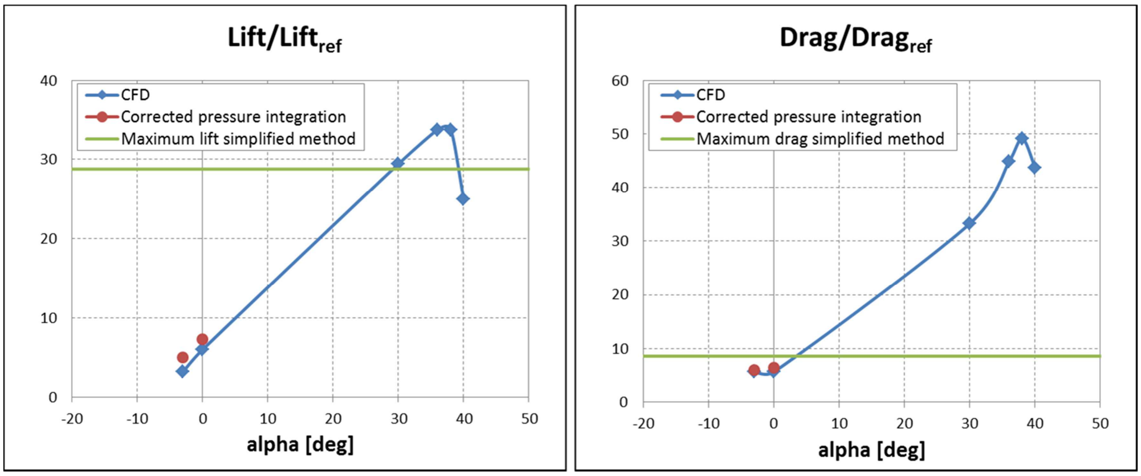

**Figure 3.15: AW139 beanie lift and drag polars at EAS=”e” (at TC2): comparison of CFD results with simplified and experimental-based methods.**

### 3.5.2.6. Comparison of CFD results with simplified and experimental-based methods in shaft axes

In Figure 3.16 and Figure 3.17 the results given by both the integration of corrected pressures and the wind tunnel acquisitions over the 1/3.5 model scaled AW139 main rotor hub are illustrated and compared with the CFD simulations for the two conditions EAS=”d” (at TC2) and EAS=“e” (at TC2) respectively in the shaft axes reference system. The forces coming from the simplified method are not reported in the same diagrams since the corresponding beanie angle of attack remains undefined, so that the transformation into shaft axes cannot be carried out.

The following conclusions may be drawn:

- as far as the beanie Z-force is concerned, there is a good agreement between the results obtained from the corrected pressures' integration and the CFD at both the tested conditions, at least for low angles of attack. Furthermore, the normal force at stall conditions predicted via CFD is much higher than the Z-force at design conditions coming from both CFD and the integration of corrected pressures. Finally, the data derived from the wind tunnel tests of the AW139 scaled model is in good agreement with the CFD results at both the examined conditions only at $\alpha$=-5 deg and $\alpha$= =0 deg, while correlation is worse at $\alpha$= =-10 deg; however, as already stated in §3.4, the measured lift on the AW139 1/3.5 scaled model shows quite a strange behaviour, with increasing lift at negative angles of attack, maybe due to interference effects with the hub and the fuselage;
- regarding the beanie horizontal force, an excellent correlation between the CFD and the corrected pressures' integration results was found at both the analysed conditions. Furthermore, the decreasing trend of the H-force with increasing incidence is captured by the CFD simulations as well. Moreover, correlation of acquired wind tunnel data on the AW139 1/3.5 scaled model with both CFD and corrected pressure's integration is quite poor, maybe due to the interference effects of other components not being included, as already stated in §3.4.2. In particular, while at $\alpha$=-10 degrees the influence of the fuselage upper deck on the horizontal force seems negligible, this does not hold true for increasing values of the incidence angles. In fact, for $\alpha$=-5 degrees and $\alpha$=0 degrees the measured horizontal force on the 1/3.5 scaled model is much lower than that coming from the integration of corrected pressures.

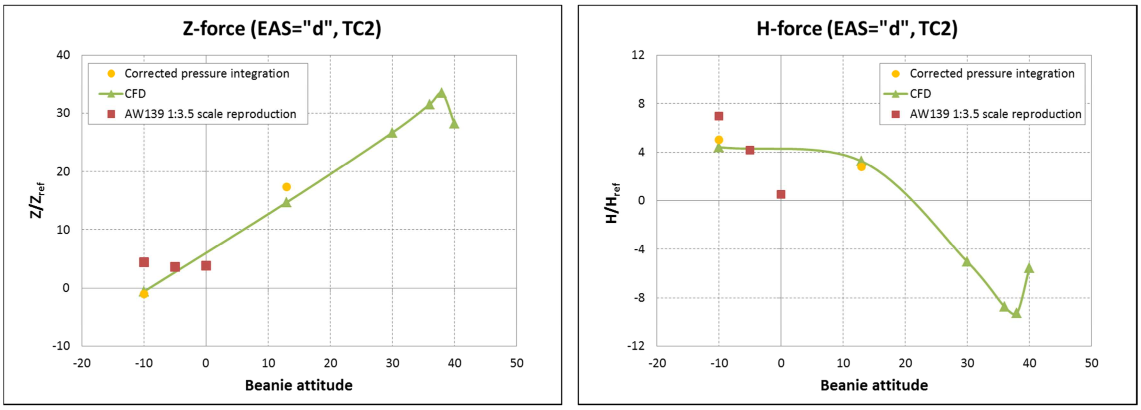

**Figure 3.16: AW139 beanie Z and H-forces polars at EAS="d"(at TC2): comparison of CFD results with integration of corrected pressures and wind tunnel acquisitions on the 1/3.5 model.**

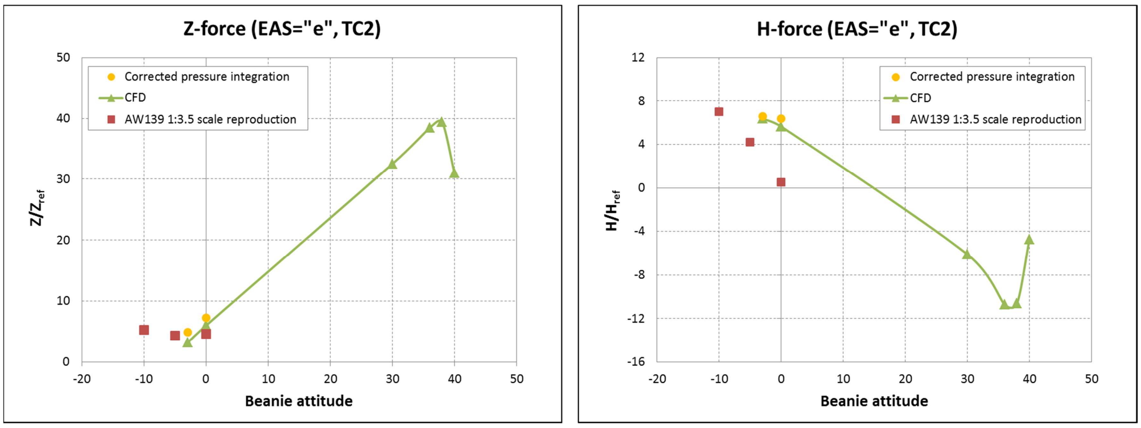

**Figure 3.17: AW139 beanie Z and H-forces polars at EAS=”e”(at TC2): comparison of CFD results with integration of corrected pressures and wind tunnel acquisitions on the 1/3.5 model.**

### 3.5.2.7. Aerodynamic limit loads: first assessment based on the AW139 outcomes

The outcomes of the CFD simulations on the beanie described in the previous sections are used to determine the aerodynamic limit loads at design conditions and compare them with the state-of-the-art methodologies currently in use at *AgustaWestland.*

To this purpose, a comprehensive comparison of the simplified method (calculated at EAS=“e” at TC2), the integration of corrected pressures at the design conditions listed in Table 3.2 and the CFD results in wind axes reference system is depicted in Figure 3.18. Once again, it is worth noting that the results of the simplified method are not fully consistent with the selected representation, since the simplified method does not provide any information on the side force to be combined with the drag.

In spite of the above mentioned approximations, the plot in Figure 3.18 shows that both the lift values calculated with the integration of corrected pressures and the CFD predicted values at the prescribed design conditions are well within the limits of the maximum lift calculated using the simplified method. On the other hand, the vector sum of the drag and side force coming from CFD simulations and integration of corrected pressures is larger than the maximum drag estimated using the simplified method for some values of the design angles of attack.

Finally, a comprehensive comparison of the integration of corrected pressures at the design conditions listed in Table 3.2, the CFD results, and the wind tunnel data over the 1/3.5 AW139 beanie scaled model in shaft axes reference system is depicted in Figure 3.19. Moreover, as already mentioned in §3.2.1, the stall loads coming out from the simplified method at design conditions are applied in the shaft axes reference system for determination of the limit loads, being the beanie angle of attack at stall conditions unknown, and they are reported in Figure 3.19 as well. However, as already stated in §3.4.3, it is worth noting that the airloads obtained using the simplified methodology are not fully consistent with those coming from the integration of pressures, since no information concerning the side force is available from the strip theory. Moreover, the stall loads from the strip theory were calculated only at EAS="e" at TC2.

From the observation of Figure 3.19 a series of considerations may be drawn: first of all, as far as the Z force is concerned, the envelope of the fuselage design conditions applied to the isolated beanie is well within the limit defined by the maximum lift calculated using the simplified method: this holds true for both the integration of corrected pressures and the CFD simulations. Moreover, the vector sum of the Horizontal and Side forces for the isolated beanie coming from both CFD and integration of corrected pressures at all the considered design conditions is within the limit defined by the maximum drag calculated using the simplified method. In addition, also the wind tunnel acquisitions on the 1/3.5 scaled model of the AW139 main rotor hub are much lower than the limits calculated using the simplified method as far as both the normal force and the vector sum of horizontal and side forces are concerned.

From the comparison of the various available methods for determination of the aerodynamic limit loads in shaft axes reference system, the following conclusions can be drawn:

- the application of the stall forces calculated using the simplified method based on the strip theory and their imputation to the shaft axes reference system, though being a simplification, is a conservative approach, since it envelopes all the concentrated loads in the design conditions evaluated using the current methods;
- moreover, also the CFD loads at stall are highly conservative if compared to the concentrated loads in the design conditions calculated from experimental acquisitions;
- once again, it has to be underlined that the CFD methodology is the only one that allows taking into account the Reynolds number variation effects when the full scale beanie is to be considered rather than a scaled model for wind tunnel tests;
- finally, the interference effects of the upper deck do not have remarkable effects as far as the aerodynamic limit loads are concerned, since the concentrated loads on the beanie at design conditions in presence of the

fuselage still are much lower than the limits defined by the simplified method at stall over the isolated beanie.

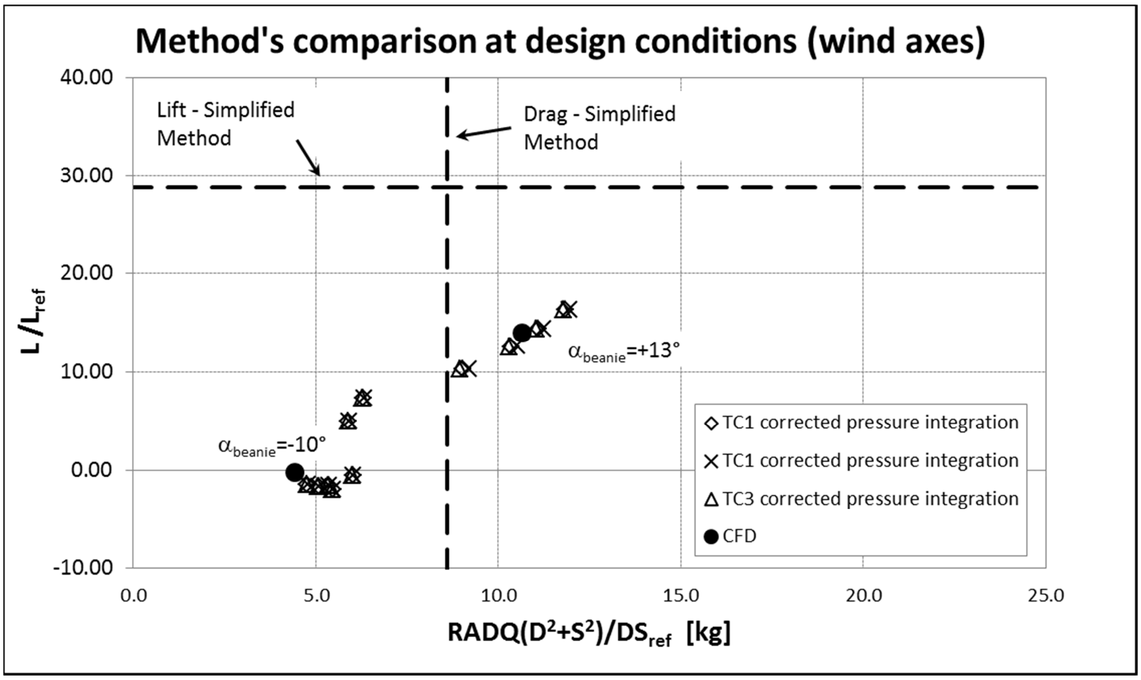

**Figure 3.18: AW139 beanie limit airloads in wind axes: methods' comparison at design conditions.**

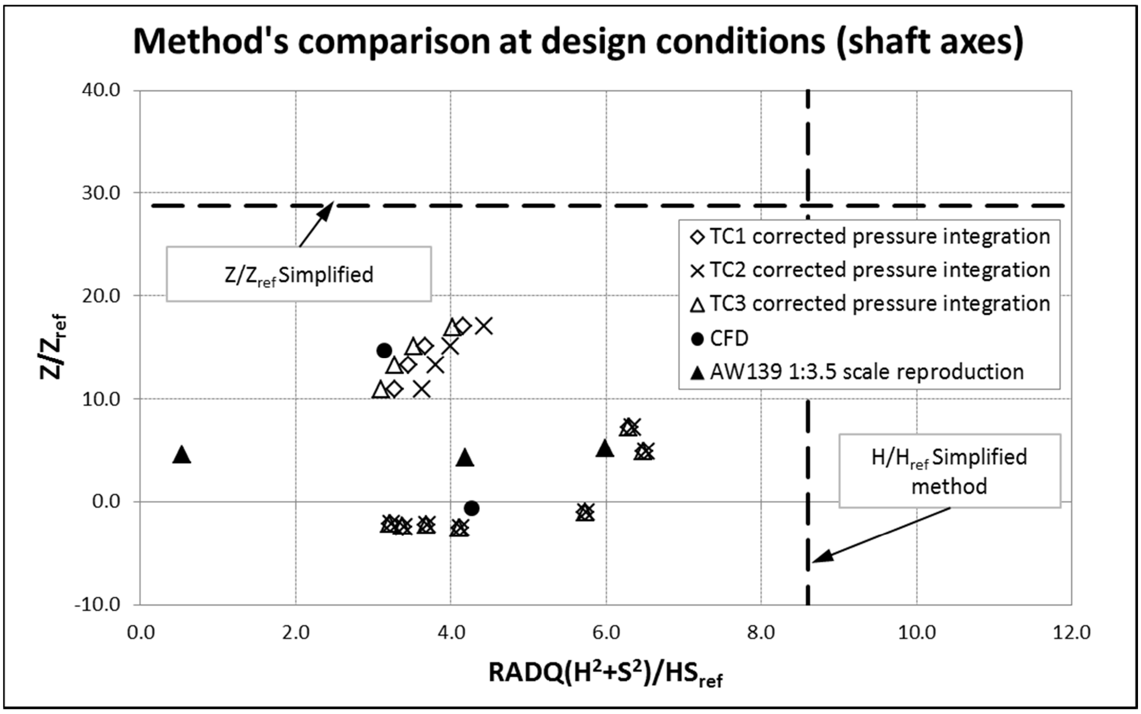

**Figure 3.19: AW139 beanie limit airloads in shaft axes: methods' comparison at design conditions.**

### 3.5.3 Application to the AW101 beanie

Based on the conclusions drawn on the AW139 beanie, a CFD test campaign was carried out on the AW101 beanie with the aim of determining the aerodynamic stall loads: as already mentioned, in this case the numerical results could not be validated against experimental data, due to the lack of dedicated wind tunnel test campaigns on the AW101 beanie. Hence, numerical results can be compared only with the simplified method that, as already explained, applies to stall condition only.

Moreover, unlike the AW139, the flight conditions to be applied for the beanie airloads determination were available only in terms of free stream speed, temperature and altitude, while the pertinent helicopter attitudes were not specified. Due to this, the CFD simulations were devoted to identify the beanie stall loads at the operating conditions corresponding to the design envelope.

The simulations carried out in Chapter 2 over different beanie geometries, along with the indications gathered in §3.4, were used in this paragraph to set up a suitable numerical model for the full scale AW101 beanie CFD test campaign.

The same tools used for the simulations of the AW139 beanie were applied for the numerical analyses of the AW101 beanie; specifically, CATIA V5® was used to create the beanie geometry, make it mesh ready, generate the surface mesh and create the virtual wind tunnel surrounding the beanie; TGrid V5® was selected to generate the volumetric mesh on the fluid domain around the beanie; finally, ANSYS Fluent® was chosen as the fluid dynamic solver.

#### 3.5.3.1. Numerical model geometry

Unlike the AW139 beanie, which was simulated only in isolated conditions, the effects of installation over the helicopter on the aerodynamic behaviour of the AW101 beanie were investigated here. In particular, the non-rotating AW101 beanie was simulated both in isolated conditions and in presence of some fuselage portions. For this reason, three different components were involved in the AW101 beanie simulation campaign:

- the AW101 beanie (Figure 2.44), whose CAD model was directly derived from §2.4 without applying any modifications to the geometry. Specifically, even in this case the MRF cylinder surrounding the beanie was created following the indications drawn in [12];
- a section of the helicopter upper deck (Figure 2.45); this component was extruded along the helicopter longitudinal axis up to the tail fin with the aim of avoiding the generation of fictitious wakes in the CFD simulations;

- the AW101 fuselage (Figure 3.20): the complete model of the AW101 fuselage was included in the present work in order to better understand the effects of the fuselage on the beanie aerodynamic behaviour.

The virtual wind tunnel dimensions were larger than those of the model used in §2.4 in order to allow the simulation of higher angles of attack. The new box including the isolated beanie or the beanie with the upper deck measured 75m x 15m x 45m, while it was 110m x 90m x 90m large in the case of the complete AW101 fuselage.

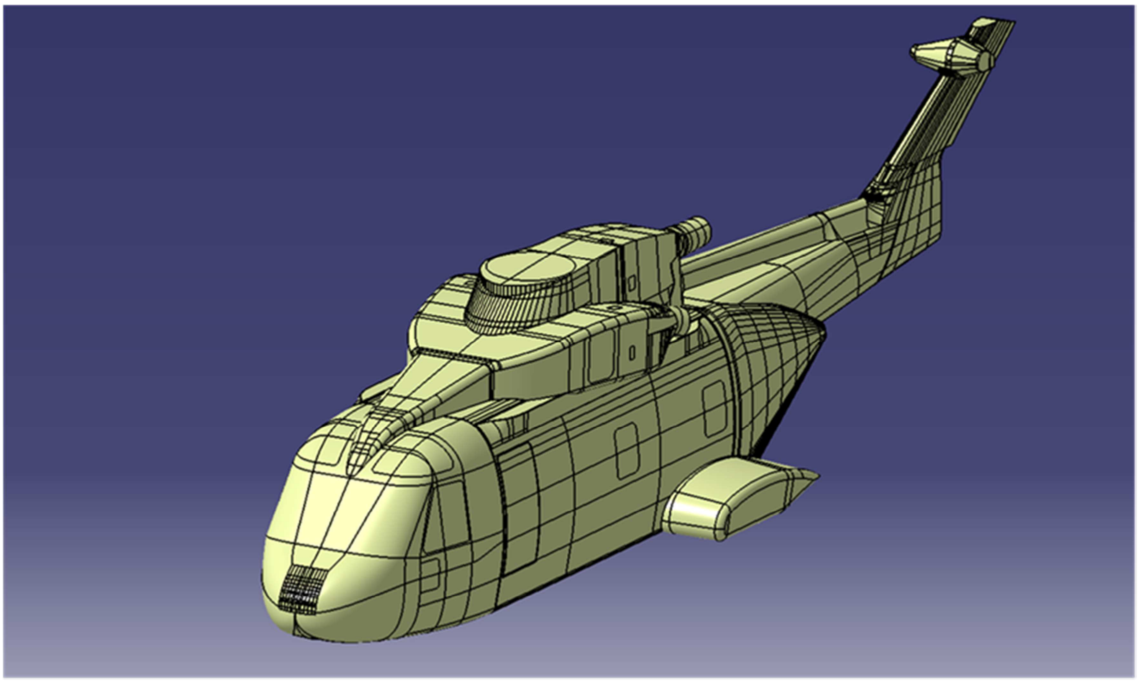

**Figure 3.20: CAD model of the AW101 fuselage**

As far as the superficial meshes are concerned, they were created by means of a CATIA® specific tools. The beanie and the upper deck meshes were directly derived from the analyses carried out in §2.4, while the superficial meshes of the AW101 fuselage and of the 110m x 90m x 90m virtual wind tunnel were directly provided by *AgustaWestland.*

Al the triangular, linear type element grids were generated so that the skewness and the aspect ratio are all within the suggested ranges, in order not to adversely affect the CFD calculation. Finally, the superficial meshes over the beanie, the upper deck, and the AW101 fuselage are illustrated in Figure 3.21

The volumetric mesh was created using TGrid V5®. All the generated meshes were unstructured with some structured elements over the beanie, the upper deck and the AW101 fuselage in order to better simulate the boundary layer. The peculiar operating conditions to be simulated required the implementation of a different set up for the generation of the volumetric mesh with respect to that reported in §2.4. However, this new particular set up guaranteed to get a low cell aspect ratio and a total number of layers high enough to correctly represent the physical boundary layer. Moreover, also the requirements needed for the wall function implemented in the conventional turbulence models used in the CFD simulations to work properly were satisfied.

A volumetric grid refinement was implemented downstream the beanie up to the tail fin in order to avoid numerical dissipation. To this purpose, a box surrounding the beanie and extending through the global domain to the tail fin location was built following the indications presented in §2.4. Some changes in the set up were required in order to keep the overall number of grid elements to a reasonable level. In particular, the maximum cell volume, the growth rate, and the outside range were increased, while the box geometrical characteristics (shown in Figure 2.48) were left unchanged. It is worth noting that the same volumetric grid refinement was applied to all the meshes generated in the present work, so as to minimize the grid differences among the three analysed cases (i.e.: isolated beanie, beanie over the upper deck and beanie over the whole fuselage).

The beanie aerodynamic behaviour was analysed at different angles of attack in order to determine the stall angle and the pertinent aerodynamic loads. To this purpose, the virtual wind tunnel was rotated by an angle equal and opposite to the desired one, while both the beanie and the MRF volume (along with the volumetric mesh within it) remained fixed with the absolute reference system. Therefore, only the unstructured grids within the virtual wind tunnel were generated from scratch for each angle of attack using the aforementioned set up.

A total number of 3,9M and 4,8M elements were created in the case of the isolated beanie and the beanie with the upper deck respectively. Once the volumetric grids were generated, their quality indices were optimized by means of some TGrid® tools to improve the mesh quality and to prevent potential difficulties in calculations' convergence due to the most distorted elements. Actually, the variation of the angle of attack resulted in different grids characterized by slightly skewness and aspect ratio values.

In Figure 3.22, some views of the volumetric mesh around the beanie and the upper deck are depicted at an angle of attack of +20 degrees, while in Figure 3.23 a detail of the prismatic layers over the beanie and the upper deck is illustrated.

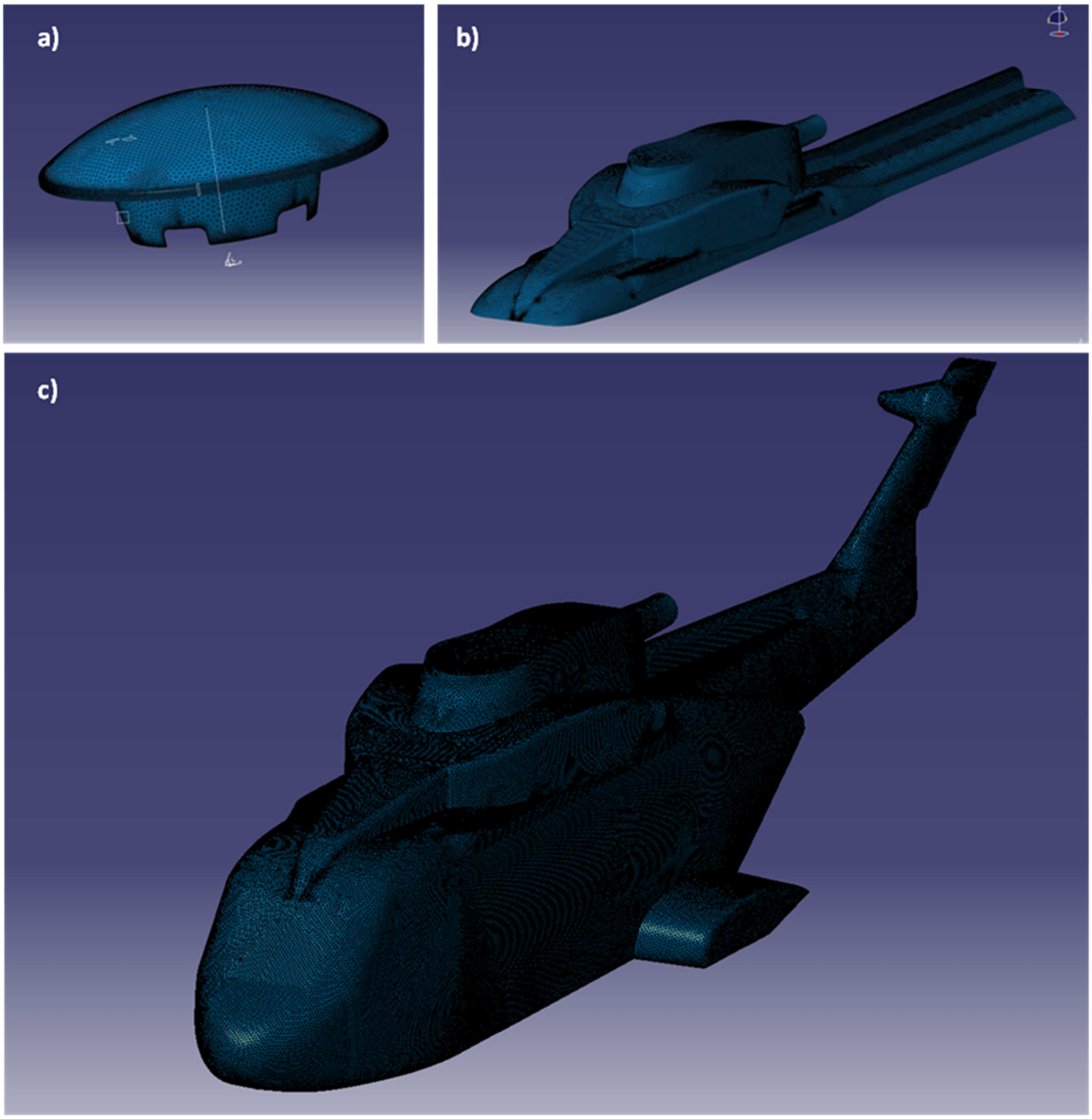

Figure 3.21: Superficial meshes over the beanie (a), over the upper deck(b), and over the AW101 fuselage (c).

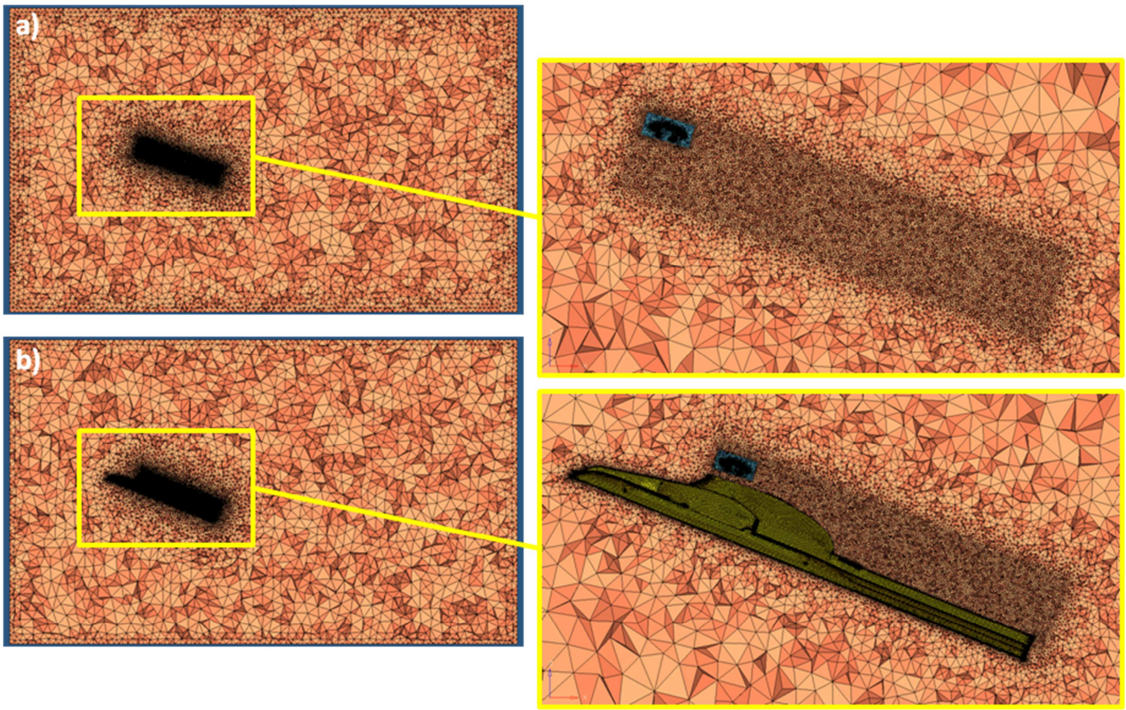

**Figure 3.22: Volumetric mesh around the isolated beanie (a) and the beanie over the upper deck (b).**

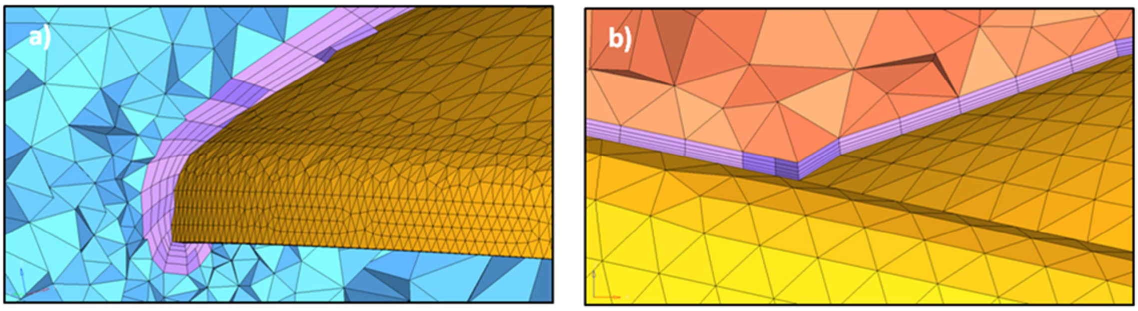

**Figure 3.23: Close-up of the prismatic layers over a) the beanie; b) the upper deck.**

As already mentioned, the potential effects that the presence of the upper deck might have on the beanie aerodynamic behaviour were analysed here. However, the wake generated by the section of the engine fairing at high angles of incidence could negatively affect the CFD results, being the cut geometry not consistent with the complete helicopter model. To this purpose, two additional test cases were simulated: the first one involved only the beanie and the upper deck section, while the second one included the whole AW101 fuselage. In the latter case, a new and larger bounding box had to be created in order for the whole fuselage to be correctly simulated, especially at high angles of attack.

The superficial meshes of the beanie, the MRF surface and the upper deck were the same described before. The structured meshes, along with the tetrahedral elements within the MRF volume, were generated following the criteria discussed above, while the unstructured grid within the new virtual wind tunnel was created using an advance front refinement method within TGrid®. The same volume grid refinement illustrated above was applied to reduce the numerical dissipation and to minimize the differences among the different models analysed in the present work. Figure 3.24 illustrates the volume mesh created for the test case at a null angle of incidence, while some details of the prismatic layers over the beanie, the upper deck and the AW101 fuselage are shown in Figure 3.25. A total number of 3.7M and 4.9M elements were created in the case of the beanie installed on the upper deck and on the whole fuselage respectively.

The simulations with the beanie mounted over the upper deck and the whole fuselage were carried out at two different angels of incidence. To achieve the desired beanie incidences, the virtual wind tunnel was rotated around the y-axis by an angle equal and opposite to the required one, while the beanie, the upper deck and the AW101 fuselage remained fixed at their original position. The unstructured grid for each value of the angle of attack was generated from scratch.

The selected set-up applied to these two new models was shown to guarantee that for all the analysed configurations the non-dimensional mesh thickness at the beanie, upper deck and AW101 fuselage was always consistent with the discretization levels suggested for the wall function implemented in the conventional turbulence models to work properly.

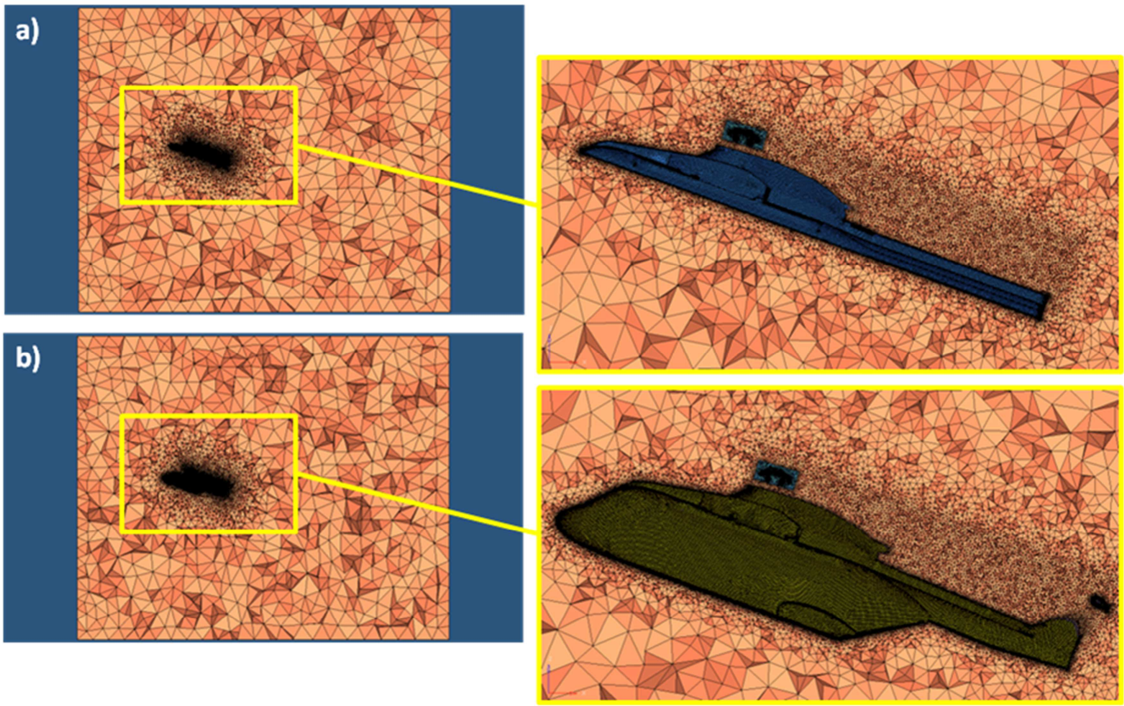

**Figure 3.24: Volumetric mesh around the beanie and the upper deck (a) and around the beanie and the AW101 fuselage (b) at $\alpha$=+20°.**

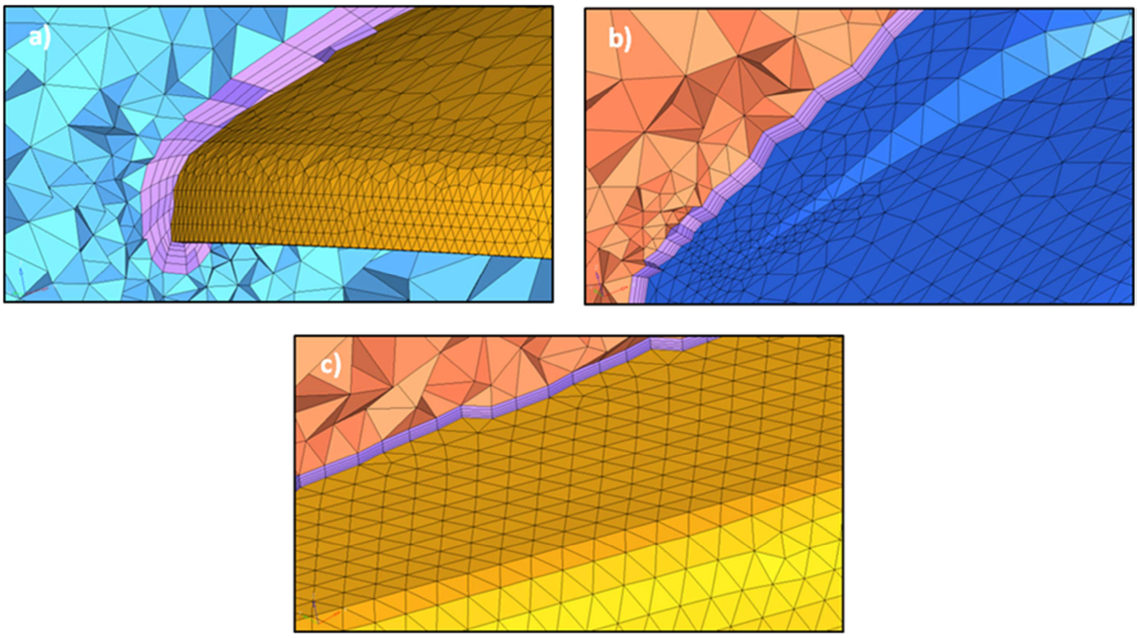

**Figure 3.25: Close up of the beanie (a), the upper deck (b) and the AW101 fuselage (c) boundary layers.**

#### 3.5.3.2. CFD test program

As already mentioned, three different analyses were carried out on the AW101 beanie.

First, the isolated beanie was simulated with the aim of comparing the CFD aerodynamic loads at stall conditions with the maximum lift and drag calculated using the simplified method (§3.2). To this purpose, the beanie was tested at the conditions summarized in Table 3.9, which were the same reported in [17] for application of the simplified method.

Then, the beanie aerodynamic behaviour was fully characterized at design conditions taking into account the installation effects as well. The AW101 beanie design conditions are listed in Table 3.10, while the pertinent temperature-pressure altitude envelope is represented in Figure 3.26. Moreover, as already discussed in §3.5.3, only the free stream speed, temperature and altitude at design conditions are known for the AW101 beanie, while the pertinent angles of attack are not specified. Due to this, the determination of the aerodynamic limit loads acting on the beanie was not possible and CFD simulations were rather dedicated to identify the beanie stall angles and related stall loads at the operating conditions corresponding to the design envelope.

The beanie installed over a section of the AW101 upper deck was simulated and the beanie stall angles and pertinent airloads were determined at the four design conditions summarized in Table 3.10. As already mentioned, the peculiar geometry of the upper deck could have generated a fictitious wake that might have influenced the beanie aerodynamic behaviour, especially as far as highly positive angles of incidence were concerned.

In order to exclude that possibility, a third analysis was carried out, aimed at comparing the results of a CFD model including only the upper deck with those of a model including the whole AW101 fuselage. These two models were tested at only one of the design conditions for verification purposes: the selected condition for comparison is reported in Table 3.11 (it corresponds to condition BC-3 in Table 3.10).

| **Pressure** [Pa] | **OAT** [°C] | **VD** [kts] | **Vgust** [ft/s] | **KEAS** [kts] | **EAS** [m/s] |
|---|---|---|---|---|---|
| 101325 | +15 | 185 | 30 | 202.5 | 104.25 |

**Table 3.9: Selected operating conditions for the CFD simulations for the AW101 isolated beanie.**

| **Operating Condition** | **Hp** [ft] | **OAT** [°C] | **VD** [kts] | **Vgust** [ft/s] | **KTAS** [kts] | **KEAS** [kts] | **TAS** [m/s] |
|---|---|---|---|---|---|---|---|
| **BC-1** | 0 | -40 | 185 | 30 | 182.388 | 202.76 | 93.821 |
| **BC-2** | 0 | 50 | 185 | 30 | 214.723 | 202.76 | 110.454 |
| **BC-3** | 15000 | -40 | 185 | 30 | 242.789 | 202.76 | 124.891 |
| **BC-4** | 15000 | ISA+35 | 185 | 30 | 272.368 | 202.76 | 140.106 |

**Table 3.10: The selected operating conditions for the CFD simulations of the AW101 beanie with the upper deck.**

| **Operating Condition** | **Hp** [ft] | **OAT** [°C] | **VD** [kts] | **Vgust** [ft/s] | **KTAS** [kts] | **TAS** [m/s] |
|---|---|---|---|---|---|---|
| **BC-3** | 15000 | -40 | 185 | 30 | 242.789 | 124.891 |

**Table 3.11: The selected operating conditions for the CFD simulation of the beanie with the AW101 fuselage.**

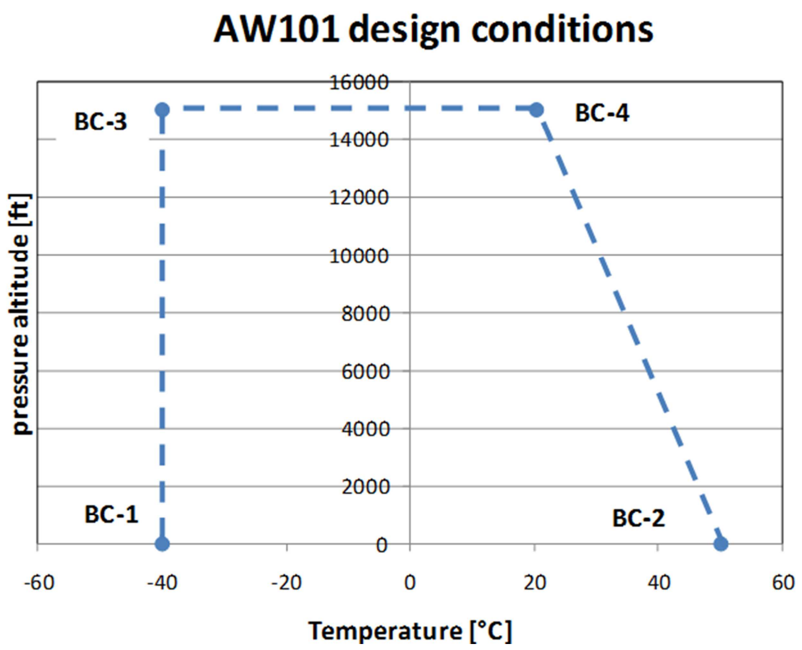

**Figure 3.26: Design envelope of the AW101 beanie on the plane Temperature-pressure altitude.**

All the CFD simulations were carried out using ANSYS Fluent® v.12. In particular, a pressure-based solver type with absolute velocity formulation and steady approach was used for the simulations. The κ–ω SST turbulence model was selected for simulation of viscous effects. The air was treated as an ideal gas having constant specific heats, which automatically enabled the energy equation resolution. Fluid viscosity was modelled using the pre-defined three-coefficients Sutherland law.

A total pressure condition at the wind tunnel inlet and a static pressure condition at the outlet section were the prescribed boundary conditions. Static pressure, static temperature, and speed values, necessary for the calculation of the respective stagnation quantities, were derived from the operating conditions summarized in Table 3.9, Table 3.10, and Table 3.11 respectively.

The beanie, the upper deck, and the AW101 fuselage surfaces were treated as hydraulically smooth and adiabatic walls, while a symmetry condition was used for the lateral surfaces of the wind tunnel boxes. Finally, as far as the turbulence specification method was concerned, a turbulence intensity of 5%, along with a hydraulic diameter equal to the beanie mean diameter were prescribed.

Similarly to the AW139 beanie simulations, for all the analysed configurations the solution was initialized by assessing the fluid values of the inlet section and using an absolute reference frame, in order for the iterative process to start from a reasonable solution to speed up the convergence.

A SIMPLE scheme was adopted as the solution algorithm. The discretization scheme was varied from the First Order Upwind to the Third Order MUSCL since a higher order is suggested to improve the solution accuracy, despite the increase of both the simulation time and the normalized RMS residuals. The under-relaxation factors were changed to in order to improve the residual convergence. In particular, the pressure was increased to 0.7, while the momentum was decreased to 0.3.

For each simulation, the convergence criterion was established when the RMS residuals were less than $1•10^{-4}$. Furthermore, the trend of aerodynamic forces, along with the difference between the mass flow rate between inlet and outlet, were monitored in order to make sure they reached a stabilized value at the end of the simulations.

As already mentioned, the CFD analyses carried out on the AW101 beanie were aimed at finding the beanie stall angle and the pertinent airloads at the operating conditions corresponding to the design envelope. Moreover, as discussed before, three different geometric models were simulated:

- The isolated beanie: the beanie, isolated and suspended within the 75m x15m x45m large virtual wind tunnel, was simulated at different angles of attack to determine the beanie stall conditions and the pertinent airloads at the conditions described in Table 3.9, which were the same used for application of the simplified method. Then, the CFD results were compared to the values calculated using the simplified method illustrated in §7.1. The numerical simulation test plan is summarized in Table 3.12 (it is worth noting that the AW101 main rotor mast is tilted by an angle equal to -4 degrees with respect to the fuselage vertical axis).
- The beanie with the AW101 upper deck section: the aim of this test campaign (carried out using the 75m x15m x45m large bounding box) was the calculation of the beanie stall at the four specific design conditions listed in Table 3.10 in presence of the interference effects due to the upper deck. The CFD test program is reported in Table 3.13.
- The beanie with the AW101 fuselage: this CFD model was analysed at two angles of attack, using the operating condition listed in Table 3.11. The results of simulations were compared with the values obtained by simulating the beanie mounted over the only upper deck section. These analyses were carried out using the 110m x90m x90m large virtual wind tunnel. The pertinent test program is summarized in Table 3.14.

| CFD test Number | | 1 | 2 | 3 | 4 | 5 | 6 |
|---|---|---|---|---|---|---|---|
| alpha fuselage | [deg] | 20 | 28 | 30 | 32 | 34 | 40 |
| alpha beanie | [deg] | 16 | 24 | 26 | 28 | 30 | 36 |

Table 3.12: Isolated beanie CFD simulation test program.

| BC-1 | | | BC-2 | | |
|---|---|---|---|---|---|
| CFD test number | alpha fuselage [deg] | alpha beanie [deg] | CFD test number | alpha fuselage [deg] | alpha beanie [deg] |
| **7** | 20 | 16 | **11** | 20 | 16 |
| **8** | 22 | 18 | **12** | 22 | 18 |
| **9** | 24 | 20 | **13** | 24 | 20 |
| **10** | 26 | 22 | **14** | 26 | 22 |
| | - | - | | - | - |
| | - | - | **15** | 30 | 26 |
| | - | - | | - | - |
| | - | - | | - | - |

| BC-3 | | | BC-4 | | |
|---|---|---|---|---|---|
| CFD test number | alpha fuselage [deg] | alpha beanie [deg] | CFD test number | alpha fuselage [deg] | alpha beanie [deg] |
| **16** | 20 | 16 | **24** | 20 | 16 |
| **17** | 22 | 18 | | - | - |
| **18** | 24 | 20 | **25** | 24 | 20 |
| **19** | 26 | 22 | **26** | 26 | 22 |
| **20** | 28 | 24 | **27** | 28 | 24 |
| **21** | 30 | 26 | **28** | 30 | 26 |
| **22** | 34 | 30 | | - | - |
| **23** | 40 | 36 | **29** | 40 | 36 |

Table 3.13: Simulation test program for the beanie installed on the upper deck.

| | CFD test number | alpha fuselage [deg] | alpha beanie [deg] |
|---|---|---|---|
| beanie + Upper deck | **30** | 0 | -4 |
| | **31** | 20 | 16 |
| beanie + AW101 fuselage | **32** | 0 | -4 |
| | **33** | 20 | 16 |

Table 3.14: Numerical simulation test plan for comparing the aerodynamic loads acting on the beanie in presence of the upper deck section and in presence of the whole AW101 fuselage.

### 3.5.3.3. Results of the CFD test campaign: isolated AW101 beanie

The simulated steady forces in wind axes of the AW101 isolated beanie at the conditions reported in Table 3.9 for each of the analysed angles of attack are summarized in Table 3.15. The values are non-dimensionalized with respect to specific lift, drag and side force reference values for industrial properties reasons. The beanie lift and drag polars are illustrated in a graphical form in Figure 3.27.

As apparent, the stall of the AW101 isolated steady beanie occurred at an angle of attack of approximately 26 degrees. The drop in the lift after stall is more pronounced than that observed for the AW139 isolated beanie. Moreover, the drag has a monotone increasing behaviour with increasing angle of attack, at least for the examined incidence range.

Moreover, the aerodynamic coefficients of the beanie oscillated around a mean value without reaching a stable behaviour. These instabilities are similar to those already observed in §2.4 and, similarly to the AW139 beanie case, they might suggest, in addition to the fact that the residuals on continuity and turbulence parameters did not fall under $10^{-4}$, that the flow field around the beanie could be intrinsically unsteady, due to both flow detachment and the wake downstream the beanie (especially at the stall conditions).

| **Isolated Beanie** | | | | |
|---|---|---|---|---|
| **alpha fuselage [deg]** | **alpha beanie** [deg] | **Lift** **$L/L_{ref}$** | **Drag** **$D/D_{ref}$** | **Side Force** **$S/S_{ref}$** |
| **20** | 16 | **18.8** | **18.8** | **3.1** |
| **28** | 24 | **25.9** | **29.3** | **3.9** |
| **30** | 26 | **27.6** | **32.9** | **4.1** |
| **32** | 28 | **27.3** | **35.5** | **5.7** |
| **34** | 30 | **24.1** | **35.3** | **23.2** |
| **40** | 36 | **18.9** | **40.3** | **1.9** |

**Table 3.15: The CFD lift, drag and side force over the isolated AW101 beanie at the design conditions prescribed in Table 3.9.**

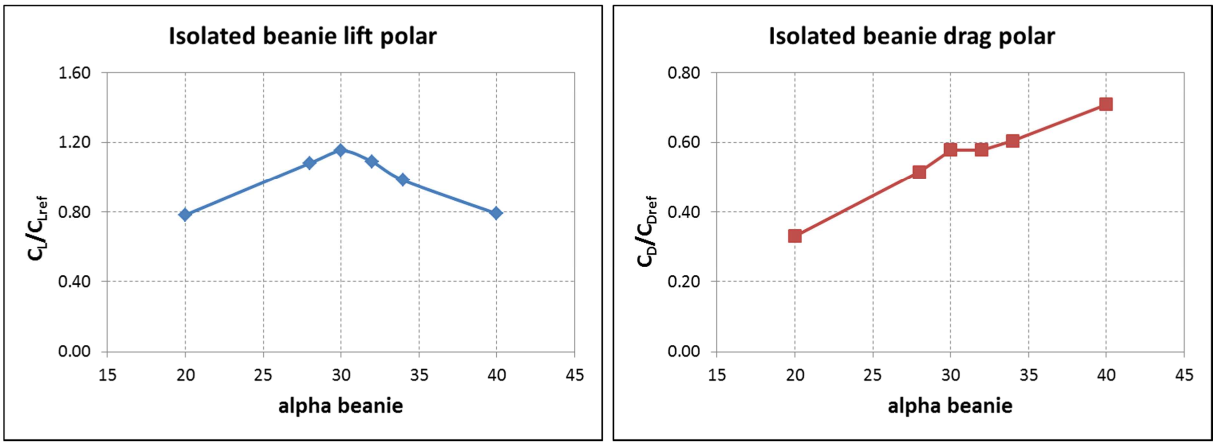

**Figure 3.27: Simulated aerodynamic coefficient polars of the isolated, steady AW101 beanie at the design conditions prescribed in Table 3.9.**

### 3.5.3.4. Results of the CFD test campaign: AW101 beanie at design condition in presence of fuselage.

As mentioned above, a preliminary analysis was carried out aimed at comparing CFD results of the beanie in steady conditions with the upper deck section with those obtained using the whole AW101 helicopter fuselage.

To this purpose, the BC-3 design condition was selected and the two geometrical configurations (i.e. beanie mounted over the upper deck and beanie mounted on the whole fuselage) were simulated at two different conditions, as reported in Table 3.11: the first one at angle of incidence equal to -4 deg (corresponding to a null fuselage angle of attack) and the second one at an angle of incidence of 20 degrees. The two cases were compared in terms of lift, drag and pitching moment. The results of this test campaign are summarized in Table 3.16. As apparent, forces and moments over the beanie in the two configurations are very similar at both the examined angles of attack. Specifically, the beanie lift tends to slightly increase at the analysed incidences when the overall fuselage is included in the simulations, while the differences in drag are negligible. Finally, regarding the pitching moment, it is slightly higher when the whole fuselage is considered at $\alpha$=-4 deg, while the inclusion of the fuselage seems to have no effect at $\alpha$ =16 deg.

Therefore, for the analysis of the installation effects on the aerodynamic performance of the beanie, it was decided to retain the model with the only upper deck rather than the whole fuselage, which required higher computational time and resources to be studied. In fact, the analysis carried out in the present paragraph proves that the wake generated by the upper deck does not affect the beanie aerodynamics at both null and high positive angles of incidence, since the effects of neglecting the rest of the fuselage on the overall beanie airloads are negligible.

| | **alpha fuselage [deg]** | **alpha beanie [deg]** | **$L/L_{ref}$ [kg]** | **$D/D_{ref}$ [kg]** | **$My/My_{ref}$ [kg]** |
|---|---|---|---|---|---|
| Upper Deck | **0** | -4 | 9.6 | 14.1 | 5.6 |
| AW101 Fuselage | **0** | -4 | 10.0 | 14.1 | 6.3 |
| **Δ%** | | | **3.9** | **0.3** | **12** |
| | | | | | |
| Upper Deck | **20** | 16 | 13.6 | 21.0 | 15.9 |
| AW101 Fuselage | **20** | 16 | 13.8 | 21.0 | 16.0 |
| **Δ%** | | | **1.1** | **0.2** | **0.4** |

**Table 3.16: Aerodynamic forces in wind axes acting on the beanie at BC3 in presence of the upper deck and of the whole AW101 fuselage**

#### 3.5.3.5. Results of the CFD test campaign: AW101 beanie at design condition in presence of the fuselage.

The CFD model of the AW101 beanie mounted on the upper deck was tested at the four operating design conditions listed in Table 3.10 in order to determine the stall angle of incidence and the pertinent airloads for each condition. All the data are non-dimensionalized with respect to specific reference values for industrial proprietary reasons. Also in this case, during the CFD simulations the aerodynamic coefficients of the beanie oscillated around a mean value without reaching a stabilized behaviour. As already discussed in §2.4 and similarly to what observed for the AW139 beanie, the oscillations suggest that the flow-field around the beanie could be intrinsically unstable, even in presence of the upper deck.

Table 3.17 reports the lift, drag and side force over the AW101 beanie for each of the analysed conditions. The related lift and drag polars are illustrated in Figure 3.28 and Figure 3.29 respectively. It may be observed that the beanie stall angle varies with the operating condition. In fact, in the cases named “BC-1” and “BC-2” the beanie stalls at approximately 18 degrees; as far as the “BC-3” condition is concerned, the stall angle is 20 degrees; finally, in the case named “BC-4” the beanie stalls at 21 degrees. On the other hand, only slight variations in the stall lift values are evidenced at varying flight conditions, with maximum differences around 4%. Moreover, the beanie drag at stall conditions seems quite insensitive to the peculiar operating condition used: actually, the curves in Figure 3.29 are nearly superimposed. Being the four analysed operating conditions characterized by the same EAS (equal to 202.7 kts), it may be argued that the lift and drag values depend mainly on the operating dynamic pressure rather than on the peculiar temperature and pressure values of the operating conditions.

**Boundary Conditions - 1 (BC-1)**

| $\alpha$ Fuselage [deg] | $\alpha$ beanie [deg] | Lift $L/L_{ref}$ | Drag $D/D_{ref}$ | Side Force $S/S_{ref}$ |
|---|---|---|---|---|
| 20 | 16 | 13.5 | 20.7 | -1.6 |
| 22 | 18 | 13.6 | 21.9 | -1.8 |
| 24 | 20 | 13.6 | 23.1 | -1.0 |
| 26 | 22 | 13.5 | 24.2 | -1.7 |

**Boundary Conditions - 2 (BC-2)**

| $\alpha$ Fuselage [deg] | $\alpha$ beanie [deg] | Lift $L/L_{ref}$ | Drag $D/D_{ref}$ | Side Force $S/S_{ref}$ |
|---|---|---|---|---|
| 20 | 16 | 13.5 | 20.9 | -1.1 |
| 22 | 18 | 13.5 | 21.9 | -1.5 |
| 24 | 20 | 13.5 | 23.0 | -1.7 |
| 26 | 22 | 13.4 | 23.9 | -2.6 |
| 30 | 26 | 12.7 | 25.9 | -2.5 |

**Boundary Conditions - 3 (BC-3)**

| $\alpha$ Fuselage [deg] | $\alpha$ beanie [deg] | Lift $L/L_{ref}$ | Drag $D/D_{ref}$ | Side Force $S/S_{ref}$ |
|---|---|---|---|---|
| 20 | 16 | 13.7 | 20.8 | -1.5 |
| 22 | 18 | 13.9 | 21.8 | -2.1 |
| 24 | 20 | 14.0 | 23.1 | -2.0 |
| 26 | 22 | 13.9 | 24.3 | -2.3 |
| 28 | 24 | 13.4 | 25.3 | -2.4 |
| 30 | 26 | 12.9 | 26.2 | -2.7 |
| 34 | 30 | 10.6 | 27.1 | -0.9 |
| 40 | 36 | 3.8 | 25.3 | -0.5 |

**Boundary Conditions - 4 (BC-4)**

| $\alpha$ Fuselage [deg] | $\alpha$ beanie [deg] | Lift $L/L_{ref}$ | Drag $D/D_{ref}$ | Side Force $S/S_{ref}$ |
|---|---|---|---|---|
| 20 | 16 | 13.5 | 20.7 | -2.4 |
| 24 | 20 | 14.0 | 23.1 | -2.3 |
| 26 | 22 | 13.9 | 24.3 | -2.3 |
| 28 | 24 | 13.5 | 25.3 | -2.6 |
| 30 | 26 | 12.8 | 26.1 | -2.7 |
| 40 | 36 | 3.8 | 24.9 | -0.7 |

**Table 3.17: Aerodynamic forces in wind axes acting on the AW101 beanie in presence of the upper deck at the design conditions listed in Table 3.10.**

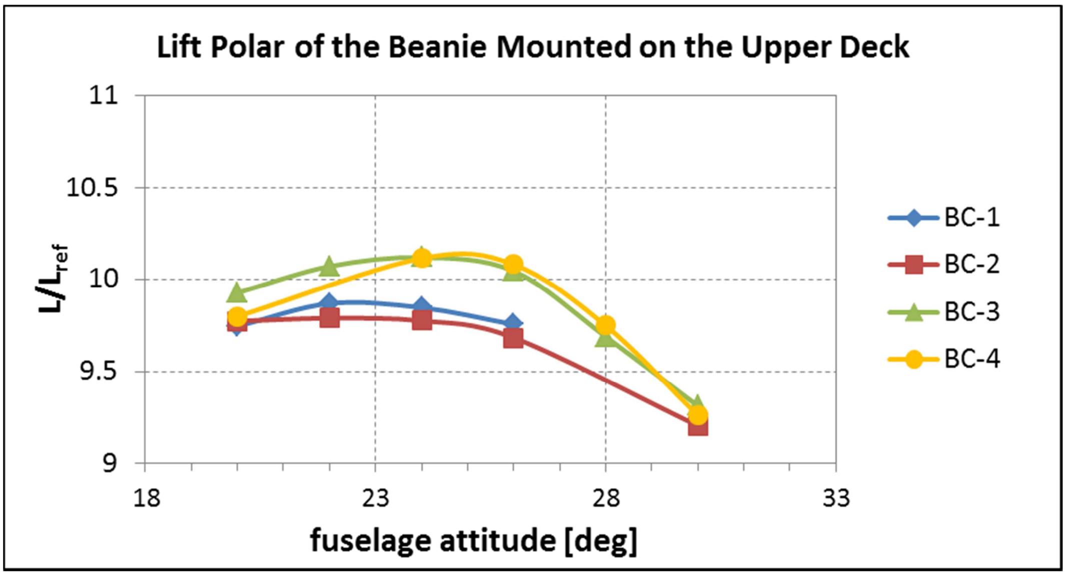

Figure 3.28: Near stall lift polars of the AW101 beanie in presence of the upper deck

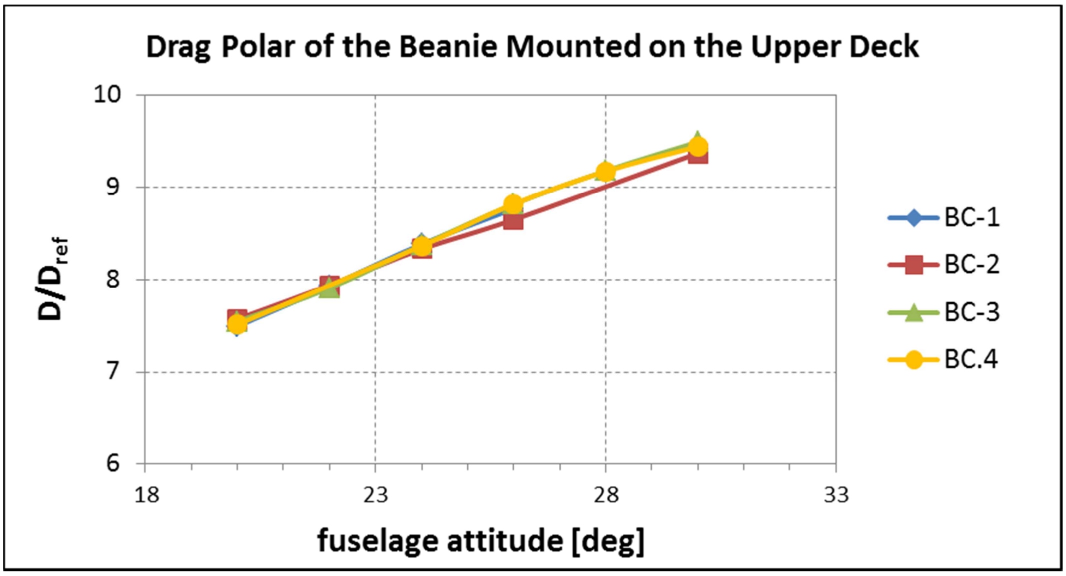

Figure 3.29: Near stall drag polars of the AW101 beanie in presence of the upper deck

Some indications may be drawn regarding the interference effects due to the presence of the upper deck at near-stall conditions: actually, even though the CFD simulations on the isolated beanie were performed at ISA Sea Level conditions, the pertinent EAS was the same as the design conditions listed in Table 3.10, so that a direct comparison of the two configurations may be carried out. Figure 3.30 illustrates the comparison of lift and drag coefficients of the isolated beanie and the beanie in presence of the upper deck. It may be observed that the upper deck has a great impact on the lift loads. Specifically, the stall angle of the beanie is lowered with respect to the isolated configuration (though in a slightly different operating condition), while the pertinent lift value is nearly halved.

The effect of the presence of the engine upper deck on the AW101 aerodynamic performance was already investigated in §2.4, where both the isolated beanie and the beanie over the engine fairing were simulated via CFD at typical operative flight conditions (far from stall) in both rotating and non-rotating configurations. The results of the above mentioned simulations were summarized in [24]: it was observed that the effects of the presence of the upper deck are relevant, since the oncoming flow is deflected by the engine fairing upstream the beanie, causing the angle of incidence to increase from its nominal value. In light of this, the beanie lift is increased by around 75% with respect to the isolated beanie in typical cruise conditions.

The analyses carried out in this chapter demonstrate that this does not hold true for the stall conditions: in fact, while the stall angle is decreased due to the engine fairing interference (which is consistent with the flow deviation over the beanie already observed in §2.4 and [24]), the upper deck acts in the direction of decreasing the lift over the beanie at stall.

Concerning the drag load at stall, it is reduced by around 30% with respect with the isolated beanie, while in 2.4 and [24] it was observed that the flow deflection induced by the engine fairing causes a drag coefficient augmentation equal to 25% with respect to the isolated beanie in typical operative flight conditions, both in non-rotating and rotating configurations.

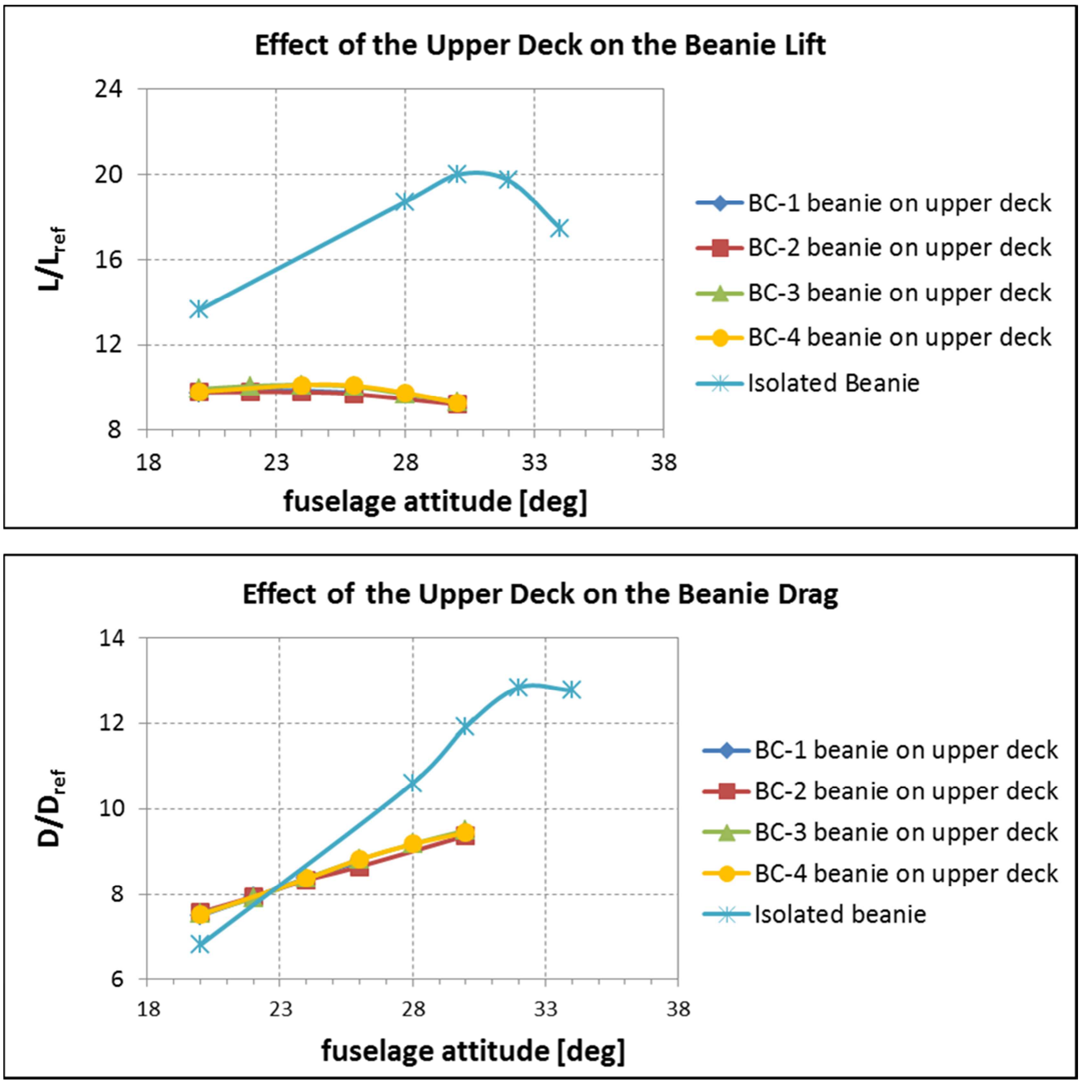

**Figure 3.30: Effects of the fuselage upper deck on the beanie lift and drag at the conditions listed in in Table 45**

Finally, the interference effects of the fuselage upper deck may be visualized also in the shaft axes reference system: to this purpose, Figure 3.31 illustrates the horizontal and vertical forces acting on the beanie in both the cases of isolated beanie and beanie mounted over the upper deck.

As apparent, the isolated beanie airloads at stall in shaft axis are very conservative when compared to those of the isolated beanie as far as the vertical Z-force is concerned; on the other hand, the presence of the upper deck increases the H-force with respect to the isolated beanie. These same effects can be assumed to occur at all the helicopter attitudes.

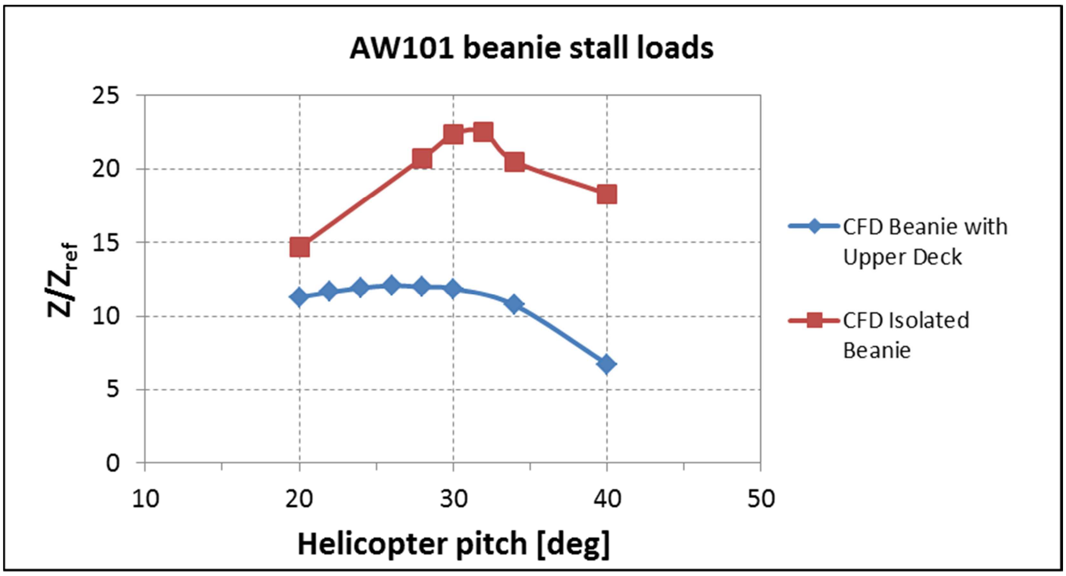

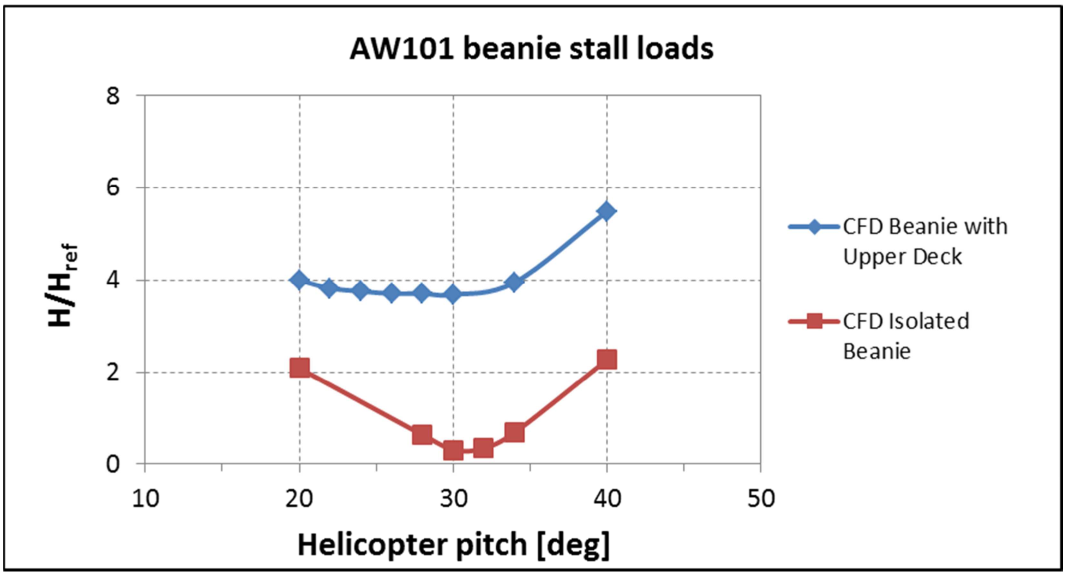

**Figure 3.31: Effects of the fuselage upper deck interference on the beanie Z force (top) and H force (bottom)**

#### 3.5.3.6. Comparison of CFD results with simplified method in wind axes

As already stated above, the methods currently used at *AgustaWestland* for the determination of the beanie limit loads for design and certification purposes are based either on semi-empirical approaches or on wind tunnel experiments. In the case of the AW101 beanie, no wind tunnel data are available. Due to this, the CFD results may be compared only with the outcomes of the simplified method.

Specifically, the CFD simulations on the AW101 isolated beanie described in §3.5.3.3 were carried out at the same conditions used for determination of stall loads using the strip theory, so that a direct comparison of the two methods can be performed. Similarly to the AW139 case, the CFD simulation campaign aimed not only at determining the stall angle of attack and the pertinent forces acting on the beanie at those conditions, but also at comparing the CFD results to the simplified method.

In Figure 3.32 the results given by the simplified method are illustrated and compared with the CFD simulations in wind axes reference system. A series of conclusions very similar to those already observed for the AW139 beanie may be drawn; in particular:

- as far as the beanie lift is concerned, the lift load at stall predicted with the simplified method is in excellent agreement with the stall load given by the CFD simulations at the tested condition: in particular, the maximum lift value coming from the strip theory underestimates the numerical one by around 6%;
- regarding the beanie drag, the simplified method largely underestimates the drag at the stall condition given by CFD.

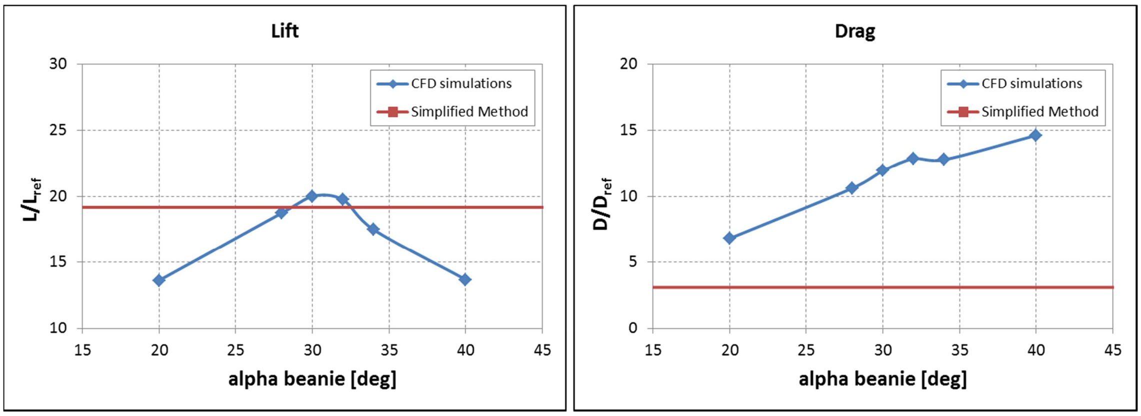

**Figure 3.32: AW101 isolated beanie lift and drag polars: comparison of CFD results with simplified method.**

### 3.5.3.7. Limit loads: CFD results and simplified method comparison (isolated beanie)

As described in §3.5.3, the AW101 beanie aerodynamic limit loads have been so far provided by means of the simplified method as presented in §3.2. As already mentioned in the case of the AW139, the stall loads coming from the simplified method apply strictly to the wind axes reference system; however, for determination of the limit loads, they are instead attributed to the shaft axes reference system. In Figure 3.32, the comparison between the CFD stall loads (transformed into shaft axes) and the simplified method limit loads is illustrated.

As apparent, the simplified method underpredicts the Z force by around 15%, while it is conservative as far as the H force determination is concerned. These conclusions are only applicable to the isolated beanie.

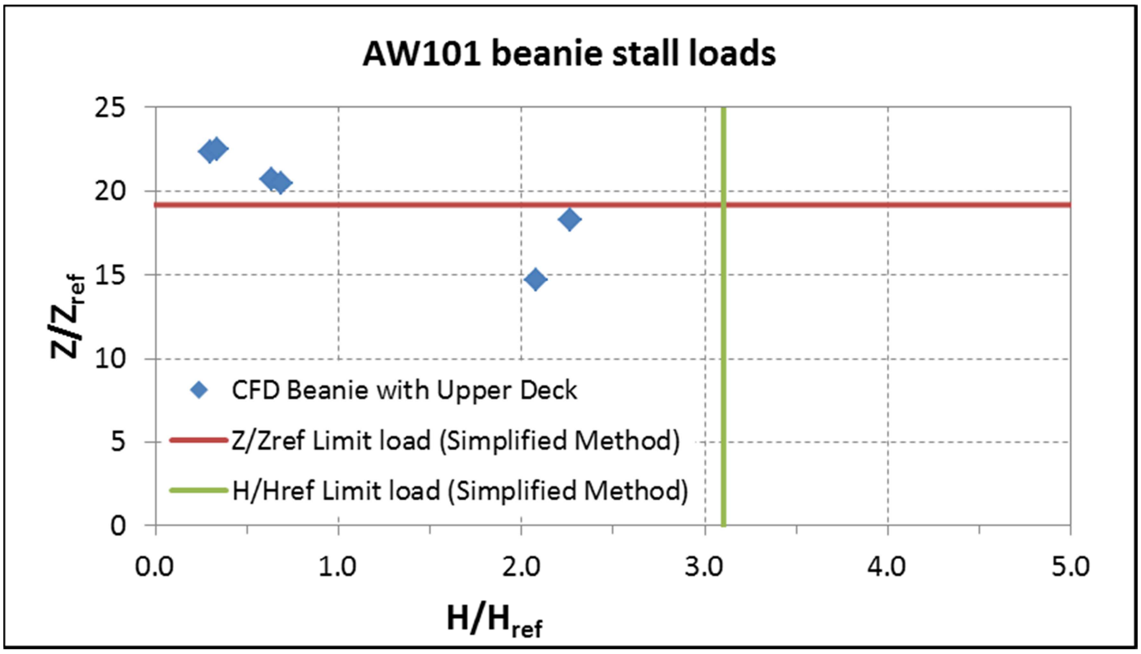

**Figure 3.33: AW101 Isolated beanie limit load comparison (CFD vs. simplified method)**

## 3.6 *General conclusions*

In this chapter, three different methodologies for the determination of the aerodynamic limit loads to be used for design and certification of helicopter beanies were analysed and compared.

The simplest approach consists in using a semi-empirical method based on the strip theory. Specifically, the beanie is divided into small segments parallel to the upstream flow: then, typical values of two-dimensional lift and drag coefficients at stall are derived from literature and applied to each beanie segment. Finally, the total forces and moments are obtained by integrating the local contributions of each strip over the whole beanie surface. The main advantage of this method lies in the fact that it does not require the determination of the actual stall angle; however, the resultant aerodynamic loads might be extremely conservative, since they are based on two-dimensional coefficients extended to the whole beanie. Moreover, the side force acting on the beanie cannot be assessed using this approach. The simplified method was applied to both the AW139 and the AW101 beanies at prescribed design conditions

The second approach consists in the experimental evaluation of aerodynamic forces acting on the beanie. To this purpose, two kinds of methodologies:

- the first experimental approach is based on the full scale test of the non-rotating beanie. Specifically, several static pressure taps located over the beanie surface are used to acquire the static pressure field over the beanie at different beanie setting angles. Then, the global aerodynamic loads are calculated from the integration of the pressure data over the beanie surface. The main advantage of this approach is the complete consistency of pressure distributions and total concentrated loads. Moreover, the rig can also be tested in parallel using a dedicated balance with the aim of comparing acquired global loads with those coming from to the pressure integration. On the other hand, a major drawback of this method is that it does not allow accounting for any interference effects from bodies located close to the beanie, like for instance the helicopter fuselage. To this purpose, the AW139 full scale, non-rotating beanie was analysed in a series of wind tunnel test campaigns. However, the acquired data needed to be corrected in order to account for the mismatch of the actual wind tunnel operating conditions with those prescribed by certification. Specifically, three major effects on the acquired static pressure values were considered, i.e. the beanie rotation, the temperature and the air speed. In the current work, a routine was specifically implemented aimed at integrating the corrected pressure data over the beanie surfaces, giving back the aerodynamic forces acting on the component. For these conditions, a further analysis was carried out to point out the effect of the beanie rotation on the aerodynamic forces. It came out that the beanie rotation causes a significant increase in the side force, which grows quadratically with the angle of incidence, while the lift and the drag are not significantly affected by the beanie rotation.
- The second experimental method concerns balance measurement of the aerodynamic loads on a large-scale test rig including cowlings, mast fairings and rotating main rotor hub. In this case, the beanie is characterized through comparison of the rig forces and moments with and without the beanie installed. The main advantage of this method consists in including into the beanie aerodynamic characterization the overall interference effects due to body and partial blades components. On the contrary, the main drawback is the unavailability of the beanie local pressure distributions. As far as the AW139 beanie is concerned, an experimental analysis was carried out on a 1:3.5 scaled model of the AW139 fuselage and main rotor hub. In particular,

the aerodynamic loads acting on the fuselage in typical flight conditions with and without the presence of the beanie at three different pitch angles were analysed and properly corrected in order to allow direct comparison with other experimental data.

Finally, the aerodynamic limit loads acting on the beanie may be evaluated directly via CFD simulations. In the present work, an extensive simulation campaign was carried with the aim of supporting the experimental data analysis and identifying a new self-consistent method for the Aerodynamic Limit Loads evaluation. The obtained numerical results were compared with those coming from both the simplified semi-empirical method and the experimental acquisitions. To this purpose, the numerical models of both the AW139 and AW101 beanies were analysed. Two kinds of analyses were carried out on the AW139 beanie: the first one aimed at finding the beanie stall angle and the pertinent airloads, while the second one was focused on the CFD simulation of the beanie at design conditions for determination of the aerodynamic limit loads. On the other hand, in the case of AW101 beanie the numerical results could not be validated against experimental data, due to the lack of dedicated wind tunnel test campaigns on the AW101 beanie. Moreover, unlike the AW139, the flight conditions to be applied for the beanie airloads determination were available only in terms of free stream speed, temperature and altitude, while the pertinent beanie angles of attack were not specified. Due to this, the determination of the aerodynamic limit loads acting on the AW101 beanie were devoted to identify the beanie stall loads at the operating conditions corresponding to the design envelope. Unlike the AW139 beanie, which was simulated only in isolated conditions, the effects of installation over the helicopter on the aerodynamic behaviour of the AW101 beanie were investigated. In particular, the non-rotating AW101 beanie was simulated both in isolated conditions and in presence of the fuselage upper deck.

A series of conclusions were drawn from the outcomes of the methodologies listed above:

- when considering the forces in wind axes reference system, both the lift values calculated with the integration of corrected pressures and the CFD predicted values at the design conditions are well within the limits of the maximum lift calculated using the simplified method. On the contrary, the vector sum of the drag and side force coming from CFD simulations and integration of corrected pressures is larger than the maximum drag estimated using the simplified method for some values of the design angles of attack.
- On the other hand, the application of the stall forces calculated using the simplified method based on the strip theory and their imputation to the shaft

axes reference system, though being a simplification, is a conservative approach, since it envelopes all the concentrated loads in the design conditions evaluated using experimental methods and CFD predictions.

- A very good match was found between the CFD results on the isolated beanie and the wind tunnel data obtained through the corrected pressures' integration, in terms of both lift and drag: in light of this, CFD simulations are judged to be a reliable method for determination of beanie airloads, and they can replace the wind tunnel tests, which are much more expensive.
- Moreover, it has to be underlined that the CFD methodology is the only one that allows taking into account the Reynolds number variation effects when the full scale beanie is to be considered rather than a scaled model for wind tunnel tests.
- The value of the beanie lift obtained using the simplified method was in good agreement with the lift at stall calculated by CFD. On the other hand, the simplified method significantly underestimates the drag with respect to the CFD results at stall.
- Moreover, also the CFD loads at stall are highly conservative if compared to the concentrated loads in the design conditions calculated from experimental acquisitions.
- The interference effects of the upper deck on the beanie aerodynamic behaviour were investigated via CFD in the case of the AW101. Specifically, the study carried out on the beanie mounted over the upper deck at four different design conditions made it possible to identify the effects of installation on the airloads acting on the beanie at near-stall conditions. A great impact of the upper deck on the lift loads was evidenced. Specifically, the stall angle of the beanie is lowered with respect to the isolated configuration, while the pertinent lift value is nearly halved. Concerning the drag load at stall, it is reduced by around 30% with respect to the isolated beanie.
- At stall conditions, the aerodynamic forces acting on the isolated beanie completely envelop the matrix of the maximum airloads obtained by simulating the beanie with the upper deck at the design conditions. Hence, the determination of the design loads can be carried out on the isolated beanie, since airloads at stall are highly conservative with respect to those of the beanie installed on the engine fairing. This allows using a much simpler numerical model for identification of the limit airloads, requiring less computational resources to be run.

- Moreover, the results of a series of simulations carried out in §2.4 on the AW101 beanie mounted over the engine upper deck at typical operative flight conditions (far from stall) in both rotating and non-rotating configurations allow to conclude that the effect of rotation on both the beanie lift and drag are negligible, at least for the examined flight conditions. This enables to neglect the beanie rotation in the CFD simulations for the identification of the limit loads, thus allowing a further simplification of the numerical model to be implemented.

On the basis of these analyses and conclusions, a series of rationale guidelines for determination of the aerodynamic limit loads acting on the beanie were proposed to *AgustaWestland*:

1. At the very early stage of the project, when the design flight envelope is not yet completely defined, the simplified method described in §3.2.1 guarantees the necessary conservative margin for a sound order of magnitude of the expected loads. Lift and Drag of the simplified method shall be applied as shaft axes forces.
2. Once the design flight envelope has been defined, the isolated beanie Z-force airload in shaft axes can be supplied either by:
   - I. full scale non rotating wind tunnel tests of the beanie at the equivalent helicopter attitudes. Reynolds effects are negligible, and so the wind tunnel data can be applied to the full scale Reynolds numbers as well:
   - II. CFD simulation of the beanie at the equivalent helicopter attitudes in non-rotating condition.

Both methods I and II will guarantee the same loads, for both concentrated and locally distributed data (static pressures). These loads have been judged conservative only for the Z-force determination.

On the other hand, for determination of H-force in shaft axes, both options I and II underestimate loads, due to the upper deck interferences: in this case, the value coming from the simplified method should be retained or, alternatively, the horizontal force coming either from option I or II must be increased by 50%, whichever is the highest. The static pressures distribution may be evaluated with options I or II as well.

# 4. THE AW101 AERODYNAMIC OPTIMIZATION OF MAIN ROTOR HUB BEANIE

## 4.1 Introduction

This chapter deals with the aerodynamic optimization of the isolated steady AW101 helicopter main rotor hub cap, aimed at minimizing the drag while maximizing the wake deflection downstream of the beanie. This particular aerodynamic component was already investigated at different flow conditions in Chapter 2 and Chapter 3. The previous analyses were used in the present activity as a starting point to set up a suitable numerical model for the optimization process of the beanie.

The original hub cap was characterized by a complex structure which had a negative impact on its overall performance, especially in terms of drag. Moreover, some geometrical aspects (e.g. sharp edges) precluded the possibility of manufacturing the component using composite materials (Kevlar and carbon fibre). Finally, due to its complex shape, the model could not be easily parameterized for optimization: this in turn could have caused the optimization algorithm to be severely limited in its capabilities to improve the beanie aerodynamic design and obtain the desired drag reduction.

In order to overcome these problems, some new beanie geometries were generated first starting from the original model. This phase was specifically devoted at modifying the surfaces that could be a major source of aerodynamic drag: these were mainly located in the component's lower portion. With the newly generated geometries, a parametric study was carried out: in particular, the performance of the new beanies was examined via CFD and the results were compared to those obtained over the initial AW101 model. This analysis, made it possible to identify a new beanie model, featuring improved aerodynamic performance, that could be profitably used as a starting point for the optimization.

The beanie optimization was carried out using a procedure based on the multi-objective evolutionary algorithm GeDEA ([24], [25], [26], and [27]) developed by the University of Padova. As reported in [24], the optimization process is subdivided into a series of different steps, which have to be completed sequentially in order to achieve the desired result.

First, the new beanie geometry which was chosen in the preliminary study as the baseline for optimisation was simulated again via CFD in order to analyse its behaviour at the specific operating conditions selected for optimization. In particular, the baseline analysis was necessary in order to identify the proper CFD model set up that could guarantee a stable convergence pattern, and the best trade-off between solution accuracy and required computational resources. To this purpose, the indications drawn in Chapter 2 were very useful, since they helped in determining a CFD model robust enough to be successfully used in the automated optimization. Finally, the baseline study was also fundamental in order to develop the most suitable procedure for the extraction of the selected objective function values.

Then, the beanie model was parameterized and the variables describing the main beanie geometrical characteristics were defined. Moreover, an accurate analysis of the design domain was carried out: in fact, the hub cap overall dimensions are constrained by the blade hinge fairings, whose motions reduce the allowed mesh deformation that could be investigated during the optimization. Therefore, some features of the optimization loop were modified in order to include these specific geometrical constraints.

Finally, the beanie shape optimization was carried out and the results discussed in terms of achieved margins of improvement with respect to the baseline.

The outcomes of the this optimization procedure were summarized in [29], and the document was submitted to *AgustaWestland* for the final approval.

## 4.2 Preliminary analyses of the beanie geometry

As mentioned before, the aerodynamic behaviour of the AW101 main rotor hub cap was already studied in detail, even though at different operating conditions than those used in the present analysis.

The AW101 beanie is made up of a spherical cap and a truncated-cone support, which is coupled with the main rotor hub. These two elements are connected by a star-shaped structure illustrated in Figure 4.1. The model is usually manufactured using metal sheets, and it is characterized by many cavities, sharp edges, and very small internal thickness. As mentioned before, this complex structure featured unsatisfactory drag characteristics, and in addition it made the original beanie geometry difficult to be parameterized. For these reasons, some new beanie geometries were generated starting from the original model and they were analysed via CFD. Obtained results were then compared to the original geometry. Since the new beanie is going to be realized in composite materials, some geometrical constraints on both internal thickness and minimum radius of curvature had to be satisfied.

The aim of this preliminary analysis was to find out a new beanie configuration suitable to be used as a starting point for the optimization: to this purpose, it had to be easily parameterized and potentially featuring a reduced drag with respect to the original one.

### 4.2.1 The new AW101 beanie geometries

Three different beanie geometries were modelled using CATIA® v.5. Specifically, only the lower surface of the original beanie was modified in this phase, while the upper surface was kept unchanged. The main geometrical characteristics of these newly generated models are reported in Figure 4.2, Figure 4.3, and Figure 4.4 respectively. In particular:

- MODEL_2: the original AW101 beanie upper surface was left unchanged. The lower surface was created by extracting a section of the original model and connecting it to the upper surface using a 12 mm fillet radius. The new beanie lower surface was then obtained by rotating that section around the z axis. Moreover, the beanie support was chosen to be cylindrical (similar to the AW139 beanie) with a base diameter equal to 479 mm. The support and the lower surface were connected together using a 50 mm fillet radius.
- MODEL_4: it was based on MODEL_2 but the beanie upper and lower surfaces were connected using a 5.6 mm fillet radius. Moreover, the support geometry was shaped as the original one, which is a truncated cone with a 27deg opening angle and a base diameter of 479 mm.
- MODEL_5: the upper surface and the support are similar to the original AW101 beanie, but the lower surface is completely flat (similar to the AW109 beanie model).

The superficial area values of the three new beanie models are reported in Table 4.1, where they are compared with the original AW101 geometry: these values can be used to calculate the weight of the different configurations.

| | **AW101 (original)** | **MODEL_2** | **MODEL_4** | **MODEL_5** |
|---|---|---|---|---|
| Upper_surf | 1 | 1 | 0.971 | 1 |
| Lower_surf | 1 | 0.91 | 0.63 | 0.69 |
| Support | 1 | 0.24 | 0.30 | 0.24 |
| **TOTAL** | 1 | 0.64 | 0.59 | 0.59 |

**Table 4.1: The area values of the newly generated beanie surfaces with respect to the original AW101 benaie.**

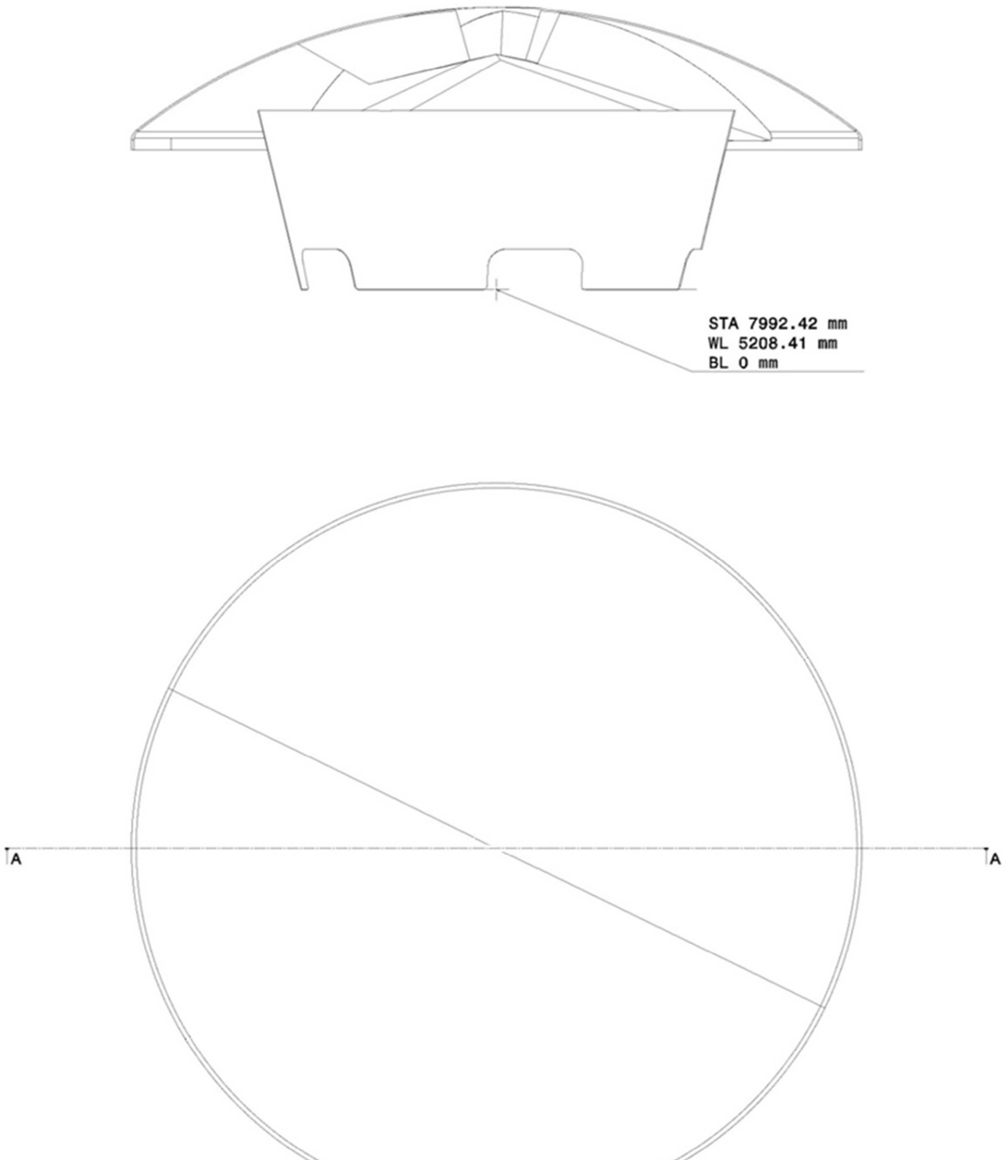

Figure 4.1: Main geometrical characteristics of the AW101 original beanie.

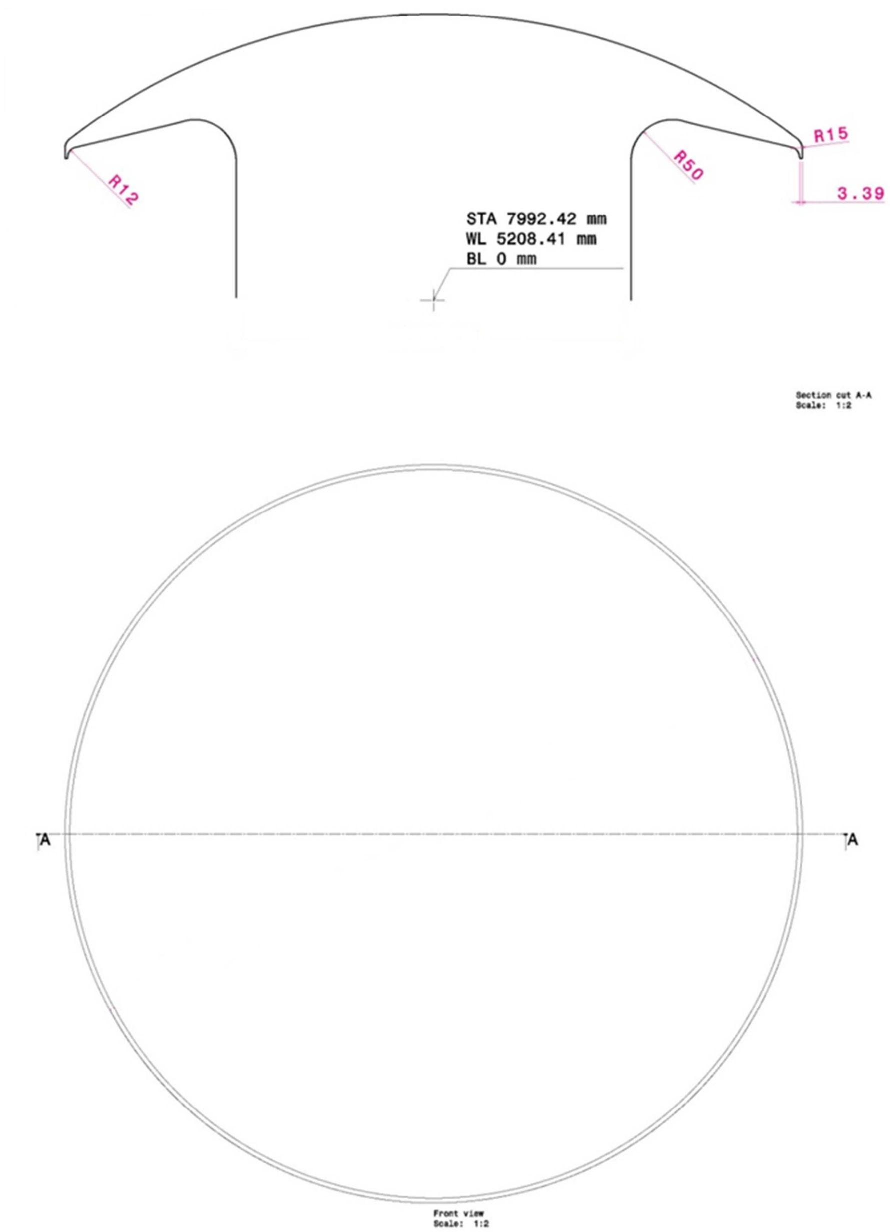

**Figure 4.2: Main geometrical characteristics of the MODEL_2 beanie.**

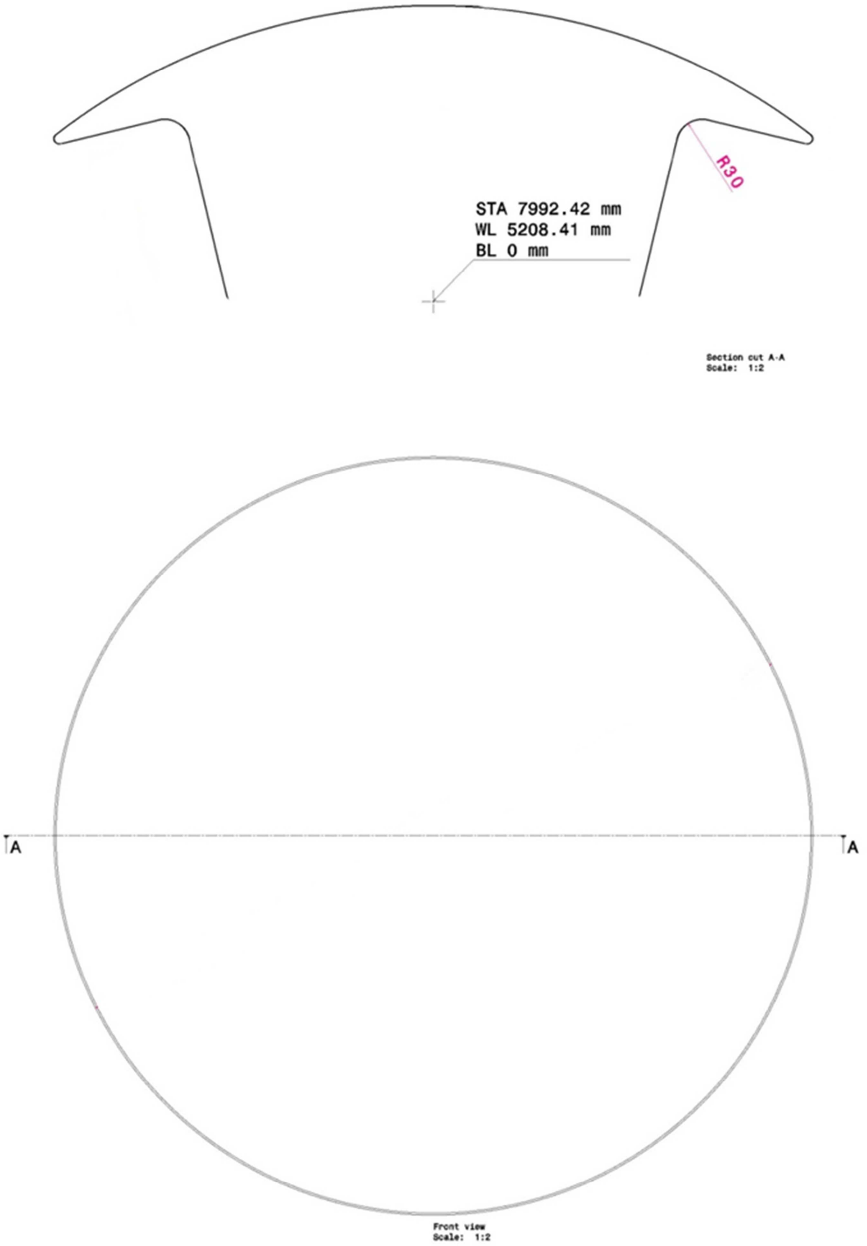

Figure 4.3: Main geometrical characteristics of the MODEL_4 beanie.

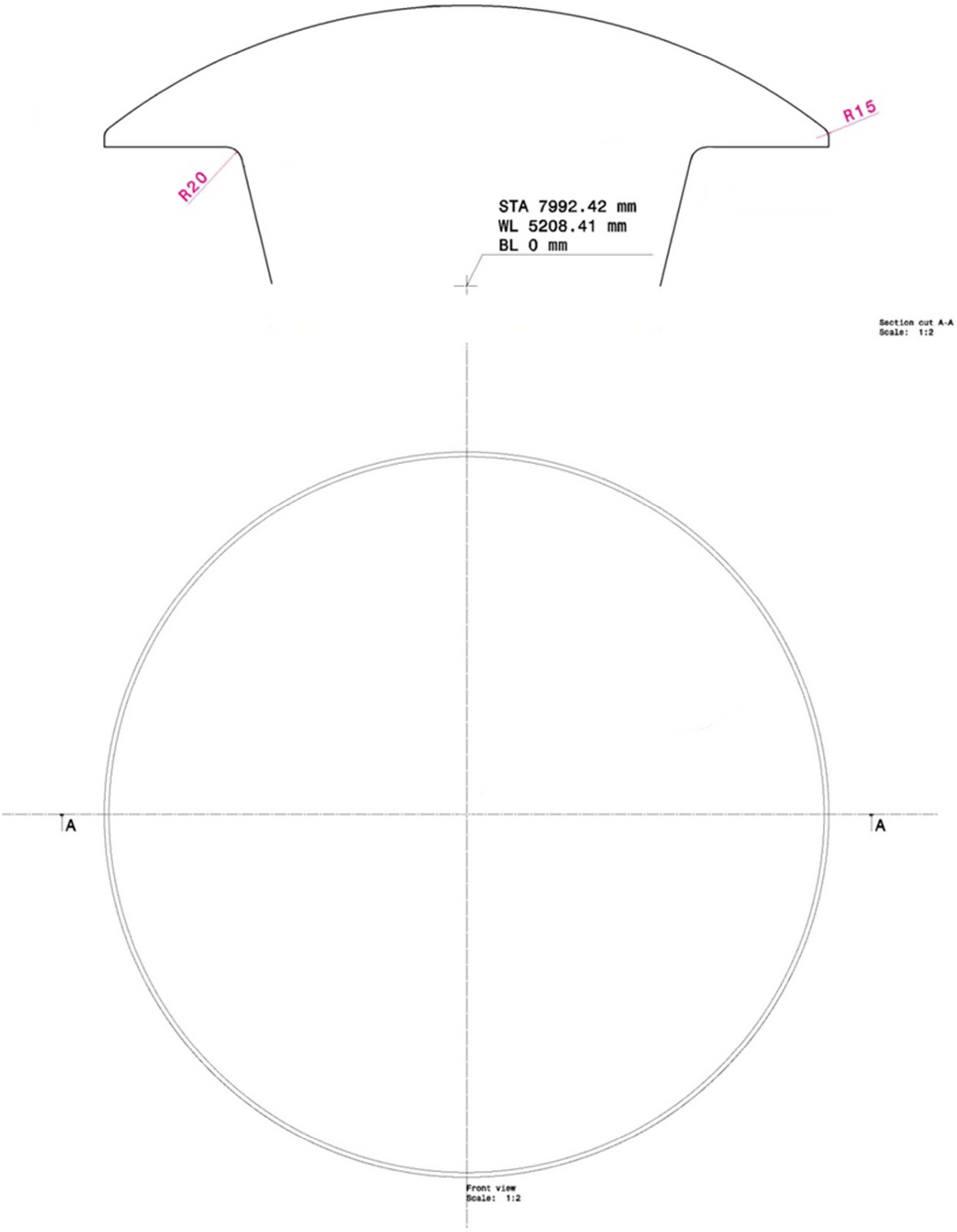

**Figure 4.4: Main geometrical characteristics of the MODEL_5 beanie.**

### 4.2.2 The numerical model

The numerical models for the newly generated beanies were set up following the criteria illustrated in §2.4. The beanie geometries and the virtual wind tunnel box were created and modified using CATIA V5®. This program was also used to generate the surface mesh by means of an internal dedicated tool. The values of maximum skewness and aspect ratio were always kept within the recommended ranges for a reliable CFD solution

The surface meshes were exported in a neutral format and loaded within ANSYS Tgrid® for the volume mesh generation.

It is worth noting that the pitch attitude of the fuselage was given a null angle, according to the chosen operating condition, hence the resulting beanie angle of attack was -4 degrees, as a consequence of the components' relative position.

The boundary layer region was modelled using prismatic cells, while the virtual wind tunnel was filled in with tetrahedral elements. The settings applied for the volume mesh generation are based on the results presented in §2.4, since they were shown to guarantee that for the examined test cases the non-dimensional mesh thickness at the beanie surfaces *y+* fell between 30 and 300, which is consistent with the discretization levels suggested for the wall functions implemented in the conventional turbulence models to work properly.

In addition, a volumetric grid refinement was necessary downstream of the beanie up to the tail fin in order to avoid numerical dissipation and correctly capture both the wake trajectory and the total pressure losses. To this purpose, a box surrounding the beanie and extending throughout the whole domain up to the tail fin location was built for mesh refinement following the criteria reported in §2.4.

Finally, the superficial meshes of the original AW101 beanie and of the three new configurations are illustrated in Figure 4.5, while in Figure 4.6 some details of the volumetric mesh around the beanie MODEL_4 are provided.

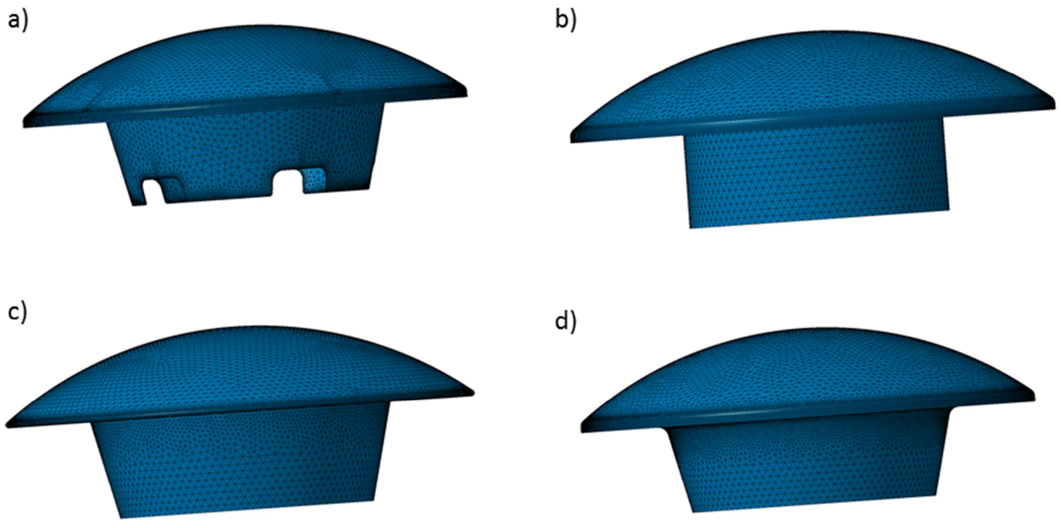

**Figure 4.5: Superficial meshes of a) the AW101 beanie, b) MODEL_2, c) MODEL_4, and d) MODEL_5.**

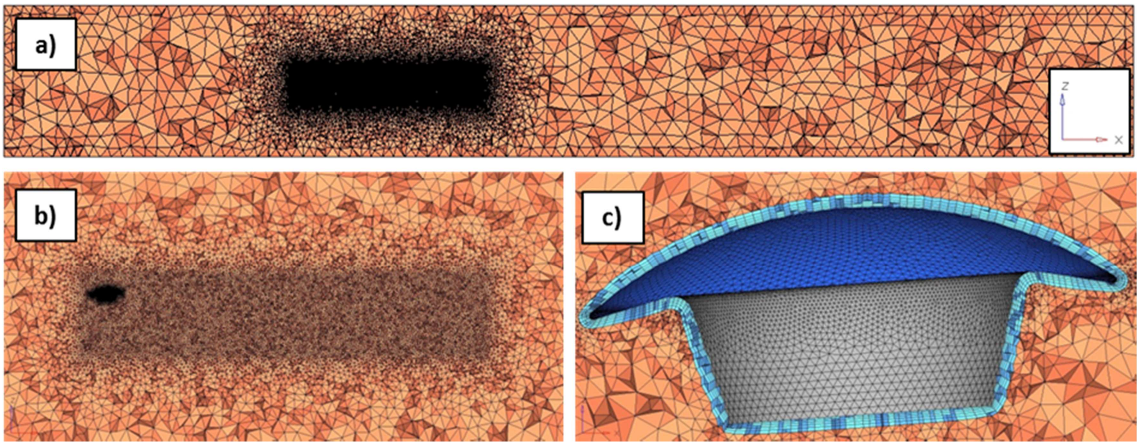

**Figure 4.6: An example of the volume mesh generated in the case of MODEL_4: a) global longitudinal view, b) close-up of the mesh refinement; c) a close-up of the beanie prismatic layers.**

### 4.2.3 The CFD simulations

CFD analyses were carried out using ANSYS Fluent® v.13. Specifically, a pressure-based with absolute velocity formulation and steady approach was adopted for the simulations. Furthermore, the k-ω SST model was selected for the turbulence treatment. The air was treated as an ideal gas, having constant specific heats, which automatically enables the energy equation resolution. Fluid viscosity was modelled using the pre-defined three-coefficients Sutherland low.

According to §2.4, the SIMPLE solution algorithm was selected for the steady simulations. A second order discretization scheme was selected for the pressure, while a Third Order MUSCL discretization scheme was chosen for the other variables, since a higher order is suggested for improving the solution accuracy, despite the increase of both the computational time and the normalized RSM residuals.

Furthermore, the Green-Gauss node based discretization scheme was adopted, since it is known to be more suitable, than the more common Green-Gauss cell based or Least-squares cell based schemes [28] for problems involving unstructured tetrahedral meshes.

The under-relaxation factors were partially modified to improve the residual convergence. In particular, the pressure relaxation factor was increased to 0.6, while the momentum was decreased to 0.4.

The boundary conditions for this preliminary study were selected according to the operating conditions described in §2.4. Specifically, a total pressure condition was applied on the wind tunnel inlet, while a static pressure was assigned over the outlet section. Total pressure and total temperature were calculated based on the static pressure, static temperature and speed of the selected operating conditions, which are reported inTable 4.2. The beanie surfaces were treated as hydraulically smooth and adiabatic walls, while a symmetry condition was used for the lateral surfaces of the wind tunnel box. Finally, as far as he turbulence specification method is concerned, a turbulence intensity of 5% along with a hydraulic diameter equal to the beanie mean diameter were prescribed, which are consistent with the values used in §2.4.

The solution was initialized by imposing the fluid values of the inlet section over the whole fluid domain with an absolute reference frame, in order for the iterative process to start from a reasonable solution and speed up the convergence.

For each simulation, the convergence criterion was established when the normalized RSM residuals were less than $1*10^{-4}$. Furthermore, the global aerodynamic coefficients were monitored, in order to make sure they reached a stabilized value at the end of the each simulation.

| | | | | |
|---|---|---|---|---|
| **Viscous Model** | k–ω SST | | | |
| **Fluid** | Air | Ideal Gas | | |
| | | Sutherland low for viscosity | | |
| **Boundary Conditions** | Pressure Inlet | Gauge Total Pressure= 1,586 Pa | | |
| | | Total Temperature= 261.03 K | | |
| | Pressure Outlet | Gauge pressure= 0 Pa | | |
| | | Backflow Total temperature= 259.13K | | |
| | Symmetry | All lateral surfaces | | |
| | Wall | No-slip wall | | |
| **Operating Conditions** | Pressure | 61,262 Pa | x | 62 (m) |
| | | | y | 4.9 (m) |
| | | | z | 9.5 (m) |
| | Gravity | Deactivated | | |

**Table 4.2: CFD boundary conditions settings for the preliminary analyses.**

### 4.2.4 Results

The original beanie and the three new geometries were analysed and compared in terms of (1) static pressure coefficient over the surfaces, (2) total pressure distribution at the beanie wake, and (3) global aerodynamic coefficients.

Figure 4.7 illustrates the contour plots of the static pressure coefficient over the beanies upper and lower surfaces. As apparent, all the geometries showed a similar Cp distribution over the upper surfaces (i.e. symmetrical with respect to the flow direction), though a more wide and intense suction region could be observed over both the original AW101 and the MODEL_2 beanies. As far as the lower surface is concerned, the Cp contour plots show quite different characteristics over the various geometries. In particular, it may be observed that the AW101 features the most complex distribution of the Cp caused by its peculiar geometrical characteristics. Moreover, MODEL_2 exhibits a bigger and more intense region of low static pressure than the other two cases in the fore portion. Finally, the region of high Cp near the stagnation point is less pronounced for the MODEL_2 than for MODEL_4 and MODEL_5.

In order to investigate the characteristics of the wake downward of the beanies, a series of wake rakes were placed over a transversal section located at 8.61m from the beanie centre along the longitudinal direction. That specific position was chosen since it represents the location of the AW101 helicopter tail fin. The two dimensional curves of total pressure losses over these rakes were traced for each beanie and the results are shown in Figure 4.8. The normalization of the total pressure coefficients was carried out for industrial proprietary reasons. When compared to the new models, the AW101 beanie is characterized by a stronger wake and by a more pronounced capability to deflect the wake downwards, as apparent also from Table 4.3, especially in the region of $y \geq 0$. Finally, it is also apparent that the three new models feature very similar total pressure loss distribution at wake rake location.

As far as the global aerodynamic forces are concerned, all the new beanie models showed an increase in lift and a remarkable decrease in drag (up to 30%), when compared to the respective values of the original AW101 beanie, as apparent from Table 4.4. Furthermore, a negative pitching moment is observed for both MODEL_2 and MODEL_5, while MODEL_4 features a positive, larger value of My than the original AW101. Finally, the absolute values of both the rolling and the yawing moments acting on the new beanie models are significantly smaller than the original geometry.

The observed variations in the global aerodynamic forces of the new geometries derived from the different distributions of static pressure over the beanie surfaces. For instance, the great reduction of the pitching moment in the case of MODEL_2 is probably related to the presence of both a stronger zone of low Cp and a narrower area of high Cp in the fore portion of the lower beanie surface than the other models. In turn, the reasons for the peculiar distribution of static pressure coefficient over MODEL_2 may be identified partly in the geometrical characteristics of the beanie edge, and partly in the different shape of the beanie support: in fact, this was cylindrical rather than conical, like in the MODEL_5 and MODEL_4.

Once the preliminary analysis was carried out, a series of trials were performed in order to identify a proper parameterization strategy. Since both MODEL_2 and MODEL_5 geometries could be obtained from MODEL_4 using the finally selected parameterization technique, MODEL_4 was chosen as the starting point for addressing the beanie optimization. Moreover, MODEL_4 featured a significant drag reduction and lower aerodynamic moments than the original AW101 (apart from the pitching moment), so it was considered a good baseline to be further improved through the optimization. Therefore, from this point on the beanie MODEL_4 will be simply referred to as "baseline".

| **AW101** | **MODEL_2** | | **MODEL_4** | | **MODEL_5** | |
|---|---|---|---|---|---|---|
| $z/z_{ref}$ | $z/z_{ref}$ | *Δ%* | $z/z_{ref}$ | *Δ%* | $z/z_{ref}$ | *Δ%* |
| 1 | 1.030 | *3.0* | 1.083 | *8.3* | 1.064 | *6.4* |

**Table 4.3: The z coordinate corresponding to the minimum of total pressure coefficient at the wake rake, measured at y=0.00m.**

| | **MODEL_2** | | **MODEL_4** | | **MODEL_5** | |
|---|---|---|---|---|---|---|
| | | *Δ%* | | *Δ%* | | *Δ%* |
| $L/L_{ref}$ | **1.25** | *24.6* | **1.01** | *0.8* | **1.03** | *3.4* |
| $D/D_{ref}$ | **0.79** | *-21.2* | **0.71** | *-28.7* | **0.70** | *-30.3* |
| $M_y/M_{yref}$ | **-5.06** | *-606.2* | **2.16** | *115.9* | **-0.67** | *-167.4* |
| $M_x/M_{xref}$ | **-0.37** | *-136.7* | **-0.05** | *-105.2* | **0.03** | *-97.2* |
| $M_z/M_{zref}$ | **0.08** | *-91.5* | **0.03** | *-97.2* | **-0.01** | *-101.4* |

**Table 4.4: Global aerodynamic forces acting on the different types of analysed beanies (average values over the last 500 iterations).**

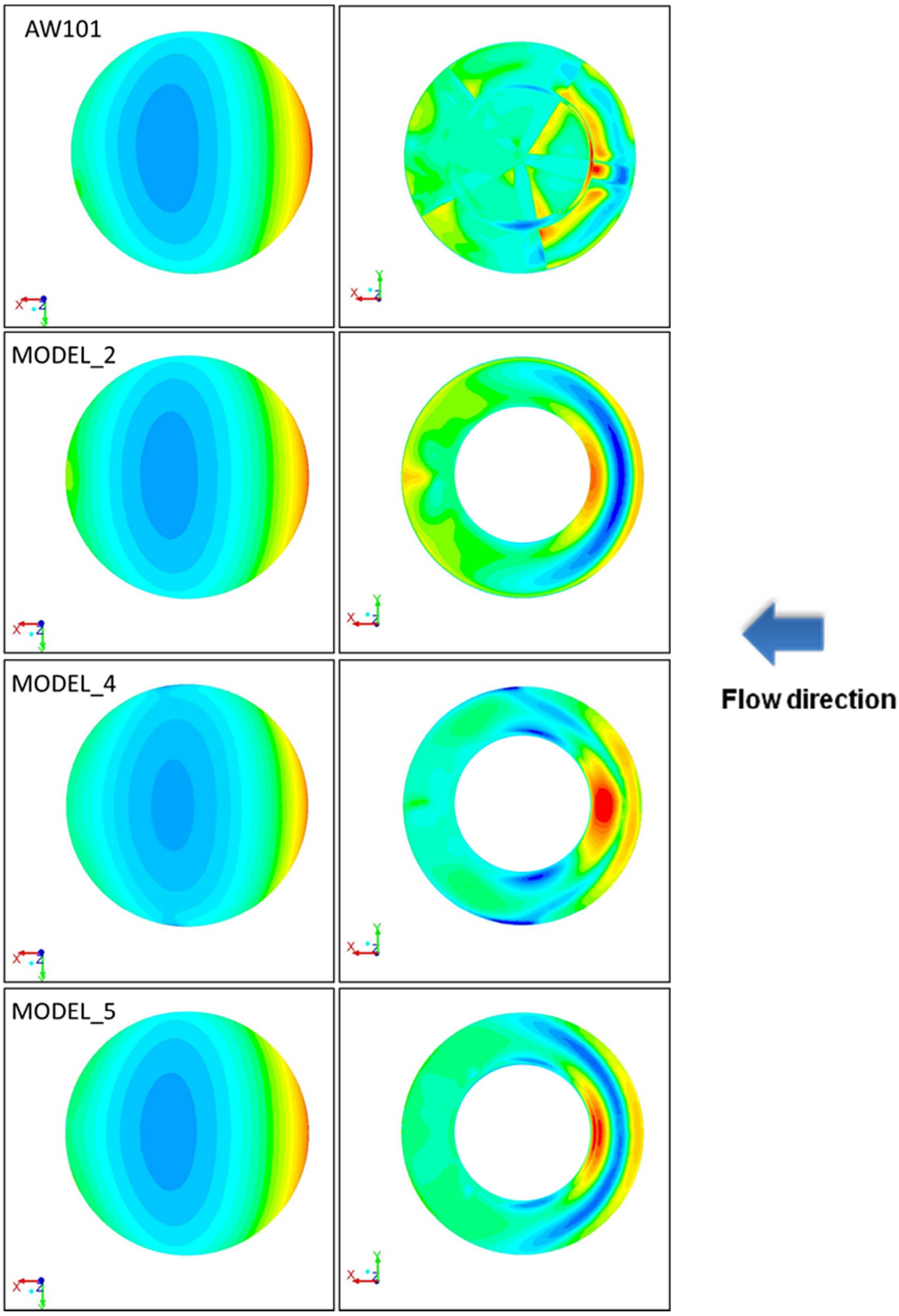

**Figure 4.7: Static pressure coefficient distribution over the beanies upper surfaces (on the left) and over the lower surfaces (on the right).**

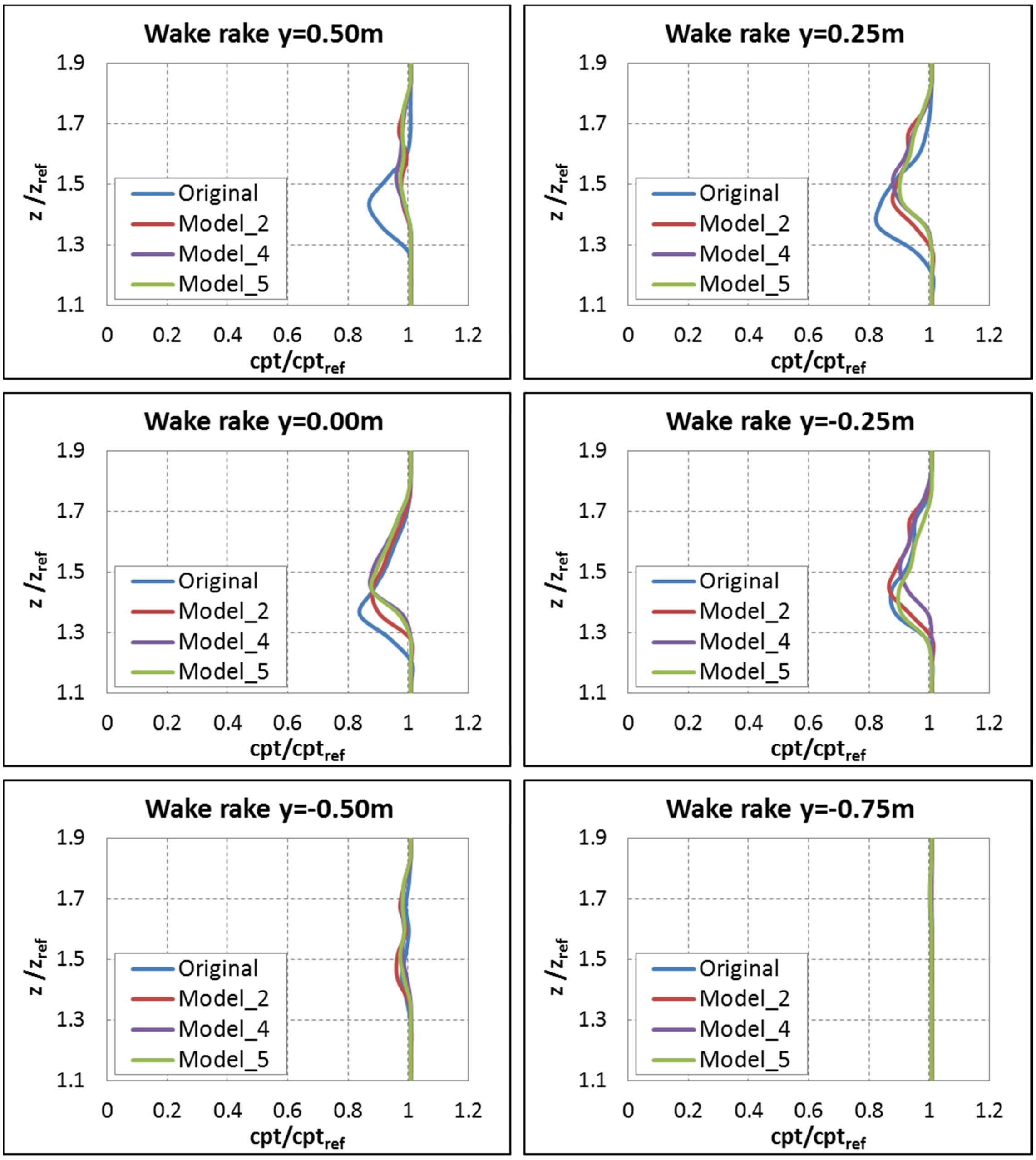

**Figure 4.8: Two dimensional total pressure losses at different lateral positions over transversal section located near the helicopter tail fin.**

## *4.3 Baseline beanie performance at optimization operating conditions.*

### 4.3.1 The beanie numerical model

The optimization was carried out on the steady, isolated beanie, mainly in order to simplify the numerical model to be used for optimization, hence allowing to reduce the computational time and resources required. This choice is supported by the conclusions drawn in [24] as well: in fact, CFD simulations showed no remarkable differences in the drag coefficient (which is one of the optimization objectives) between the steady and rotating beanies. Regarding the wake deflection (which is the second optimization objective), a less pronounced downward deflection of the streamlines in rotating conditions was evidenced than in steady simulations (Chapter 4): however, it is envisaged that maximizing the wake deflection of the isolated beanie would lead to positive effects on the rotating beanie as well.

As far as the presence of the upper deck is concerned, it acts in the direction of increasing the beanie drag of around 20% with respect to the isolated configuration. However, also in this case it is envisaged that minimizing the drag of the isolated beanie would decrease the drag of the installed one accordingly. Finally, no remarkable effects on the wake behaviour were evidenced due to the presence of the engine fairing, at least at the helicopter tail location.

Moreover, the beanie optimization was carried out at the operating conditions prescribed by *AgustaWestland*, which were different from the conditions used in the preliminary analysis of the new beanie models described in §4.2.

As already mentioned, the MODEL_4 described in Chapter 4 was chosen as the baseline geometry to be used in the optimization process. Since the selected operating conditions for optimization were different from those of the preliminary analyses, a new analysis of this model was required in order (1) to generate a mesh that could be easily parameterized and (2) to evaluate the baseline model aerodynamic performance.

The geometrical model of the baseline beanie and the virtual wind tunnel were the same described in §4.2.2. As far as the surface grid was concerned, no changes were made in the set-up of the specific meshing tool within CATIA® neither for the beanie nor for the virtual bounding box. Therefore, the reader is referred to §4.2.2 for further details on the types of element used, the elements mean size, the mesh dimensions and quality indices.

The overall procedure to create the volumetric mesh did not change, though some adjustments were required, since the helicopter fuselage was given a negative angle of incidence equal to -4.38 degrees. For this reason, the virtual wind tunnel was rotated around the y axis by an angle equal and opposite to the prescribed one. As a result of this operation, the measurement of the downward deflection of the beanie wake during the optimization process was much easier, since the wake rake positioned near the helicopter tail fin did not change its relative position with respect to the helicopter reference system.

The boundary layer region was modelled using prismatic cell, while the virtual wind tunnel was filled in with tetrahedral elements. Once created, the mesh was optimized by means of some ANSYS Tgrid® tools in order to improve the overall grid skewness and aspect ratio. The final volumetric mesh around the baseline beanie for optimisation is represented in Figure 4.9.

It is worth noting that, even though the operating condition were modified, the selected set up for the prismatic layers was still shown to guarantee that for the examined test case the non-dimensional mesh thickness at the beanie surfaces y+ fell between 30 and 370, which is consistent with the discretization levels suggested for the wall functions implemented in the conventional turbulence models to work properly.

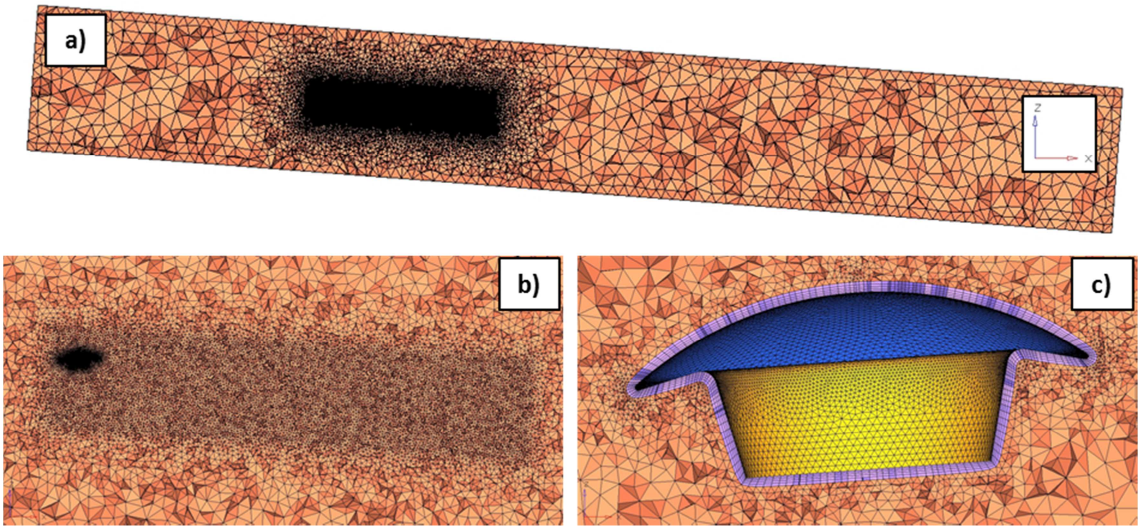

**Figure 4.9: Volumetric mesh over the baseline model: a) global longitudinal view, b) a close-up of the volume mesh grid refinement, and c) a close-up of the beanie prismatic layers.**

### 4.3.2 Fluid-dynamic model set up

Similarly to the preliminary analyses carried out in §152, the fluid dynamic computations were performed using ANSYS Fluent® v.13. Specifically, a pressure-based type with absolute velocity formulation and steady approach were adopted for the simulations. Furthermore, the $\kappa$–$\omega$ SST model was selected for the turbulence treatment. The energy equation resolution was automatically enabled, since the air was considered an ideal gas, having constant specific heats. Fluid viscosity was modelled using the pre-defined three-coefficients Sutherland low.

Unlike the simulations carried out in Chapter 2, a COUPLED scheme was adopted in this case, which solves the pressure and the momentum equations simultaneously, since this specific scheme was proven to decrease the number of the required iterations and the time needed to reach a good convergence (which is an essential feature for optimization), at the expense of a moderate increase of the required computational resources. The Courant number was decreased from 200 (i.e. the default value) to 20, as well as the explicit relaxation factors which were reduced from 0.75 to 0.5, in order to get a steep and stable solution convergence. The under-relaxation factors were left unchanged.

A second Order discretization scheme was selected for pressure, while a Third Order MUSCL discretization scheme was chosen for the other variables, since a higher order is suggested for improving the solution accuracy, despite the increase of both the computational time and the normalized RSM residuals.

Once again, the Green-Gauss node based discretization scheme was adopted.

The boundary conditions were set following the indications drawn in Chapter 2. In this case, the total pressure and total temperature were calculated based on the new operating condition prescribed by *AgustaWestland*. Table 4.5 shows the final CFD boundary conditions settings that were used during the optimization process.

For the baseline simulation, the solution was initialized by applying the fluid values of the inlet section over the whole fluid domain using an absolute reference frame. However, when simulating the deformed beanie geometries during the optimization run, an interpolation approach was preferred since it allowed a significant reduction in the required computational time. In fact, the morphed geometries were likely to feature a fluid dynamic variables distribution not so different from the baseline one. Therefore, starting from the converged solution of the baseline simulation, an interpolation file containing the data of pressure, temperature, velocity, k and $\omega$, was created.

For each simulation, the convergence criterion was established when the normalized RSM residuals were less than $1{*}10^{-4}$. Furthermore, the global aerodynamic coefficients were monitored, in order to make sure they reached a stabilized value at the end of the each simulation.

| | | | | |
|---|---|---|---|---|
| **Viscous Model** | k–ω SST | | | |
| **Fluid** | Air | Ideal Gas | | |
| | | Sutherland low for viscosity | | |
| **Boundary Conditions** | Pressure Inlet | Gauge Total Pressure= 2,219.02 Pa | | |
| | | Total Temperature= 286.09 K | | |
| | Pressure Outlet | Gauge pressure= 0 Pa | | |
| | | Backflow Total temperature= 284.19K | | |
| | Symmetry | All lateral surfaces | | |
| | Wall | No-slip wall | | |
| **Operating Conditions** | Pressure | 94,210 Pa | x | 62 (m) |
| | | | y | 4.9 (m) |
| | | | z | 9.5 (m) |
| | Gravity | Deactivated | | |

**Table 4.5: CFD boundary conditions settings used in the baseline simulation and in the whole optimization process.**

### 4.3.3 Results of the baseline simulation

The contour plots of the static pressure coefficient over the baseline beanie surfaces are depicted in Figure 4.10. The pressure field is symmetrical with respect to the flow direction and a large area of low Cp could be observed over the beanie upper surface and on the fore portion of the lower surface.

The characteristics of the wake downstream of the beanie were analysed by measuring the total pressure losses at a specific section located at a distance equal to 8.6 m downstream of the beanie (Figure 4.11). Specifically, a series of wake rakes were located at various lateral positions. The analysis highlighted that the wake is centred in y=0 and that the maximum losses are located at $z/z_{ref}$=1.07.

Finally, the baseline global aerodynamic coefficients and the wake deflection are reported in Table 4.6, where they are compared with the original AW101 beanie. As apparent, due to the modified operating conditions (especially the beanie angle of attack), the baseline drag in the optimization conditions is significantly larger than in the preliminary analyses for both the baseline and the AW101 original. Moreover, the baseline features a slightly larger lift than the original beanie and a lower drag (-16%). However, the wake is less deflected with the baseline beanie than the original one (+0.3m). Finally, a smaller absolute value of the pitching moment is observed for the baseline model.

| Baseline | | | | |
|---|---|---|---|---|
| $L/L_{ref}$ | 1.055 | | $My/M_{yref}$ | 0.685 |
| $D/D_{ref}$ | 0.838 | | $Mx/M_{xref}$ | -0.284 |
| $z/z_{ref}$ | 1.072 | | $Mz/M_{zref}$ | 0.129 |

**Table 4.6: Global aerodynamic forces and moments acting on the baseline model in the optimization operating conditions with respect to the original AW101 reference values.**

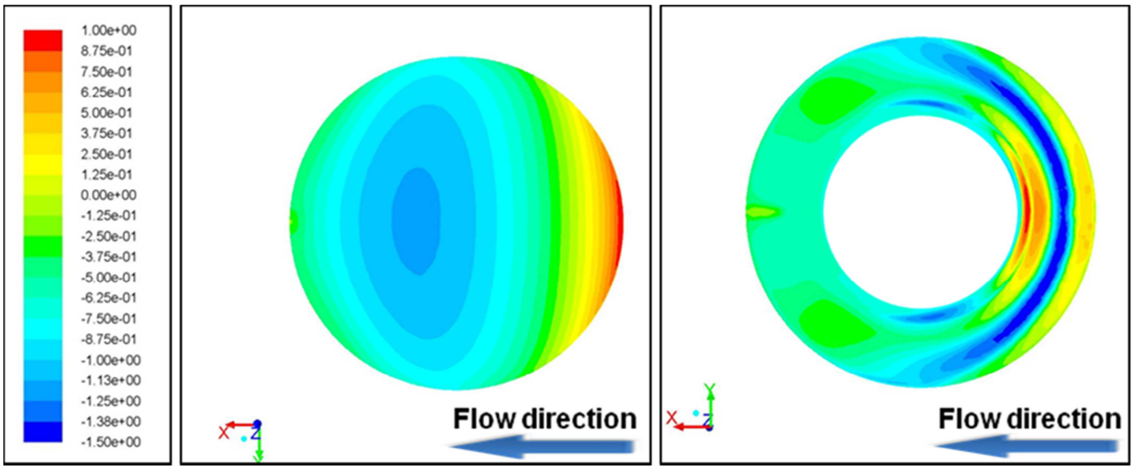

**Figure 4.10: Contour plots of the static pressure coefficient over the baseline model upper surface (on the left) and lower surface (on the right).**

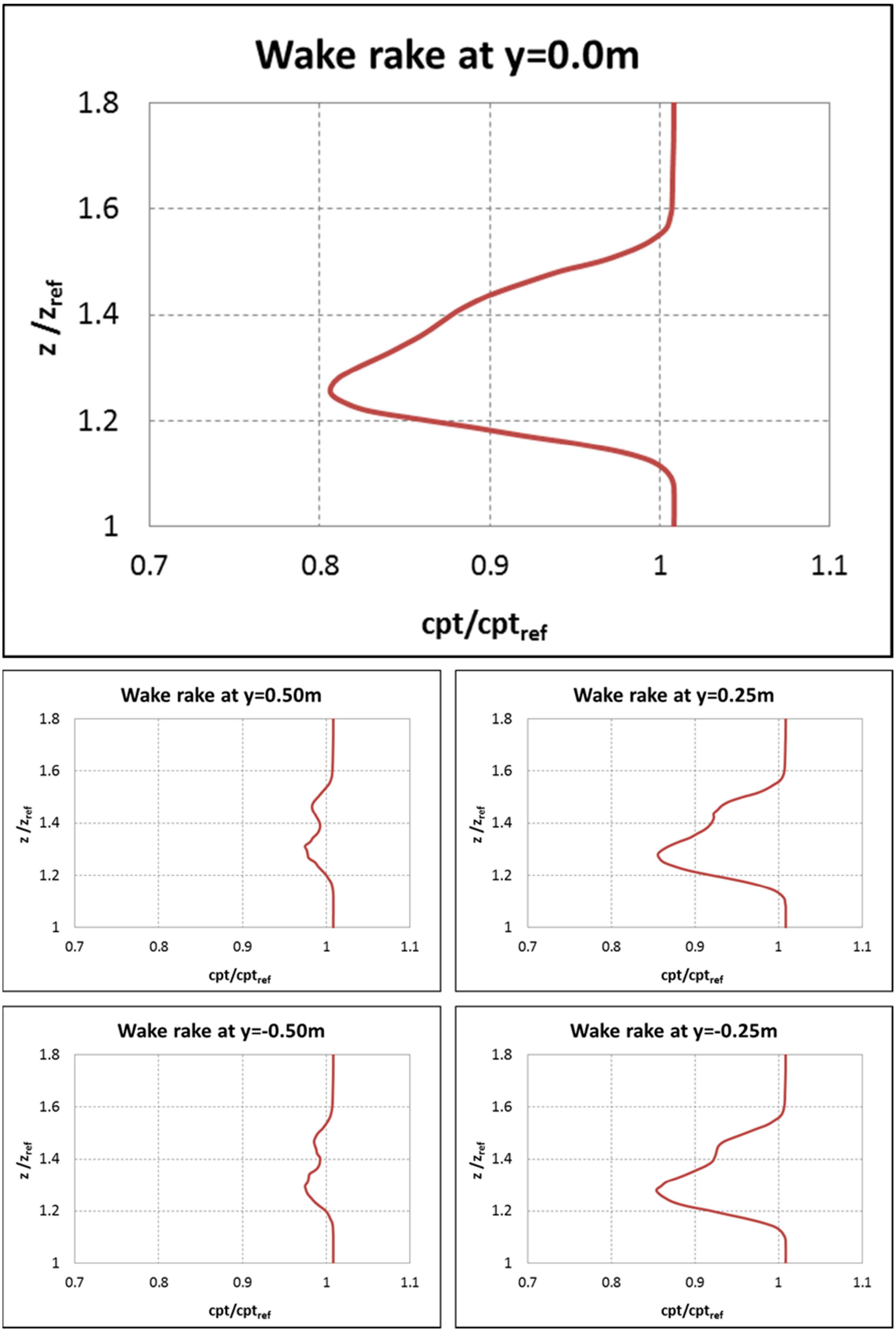

**Figure 4.11: Two dimensional total pressure losses at different lateral positions over the transversal section located approximately near the helicopter tail fin.**

## 4.4 Brief review of the optimization process

In this chapter, the whole sequence of the operations necessary to carry out an optimization study is briefly reviewed. The reader is referred to [25], [26] and [27] for further details on the adopted optimization methodology.

The optimization procedure consists of four main steps: (1) the baseline model analysis; (2) the model parameterization; (3) the optimization; (4) the results post-processing. The whole sequence of action carried out to address a multi-objective optimization problem is illustrated in Figure 13.

The first step is represented by the baseline model analysis which consists in a series of procedures for generation of the CFD model and performance analysis of the starting geometry. The surface mesh is usually generated using CATIA® v5, while the volume mesh is created using ANSYS Tgrid®. Then, the CFD case is set up using the commercial fluid dynamic solver ANSYS Fluent® v.13, which is the standard commercial software for the CFD simulation adopted by *AgustaWestland*.

Once the baseline analysis is completed, the mesh is parameterized using HyperMesh® by means of a powerful tool called HyperMorph®. In particular, a series of parameters describing the model geometry are identified and converted into design variables that can be automatically varied within a prescribed range.

Once these two initial and fundamental steps are completed the optimization process could finally be addressed. Specifically, the optimization is driven by a genetic evolutionary algorithm developed by University of Padova and called GeDEA [26].

The post-processing of the optimization results refers to the lower part of the flow chart in Figure 4.12. The output of the automatic optimization loop is the so-called Pareto frontier, which is the list of the best individuals solving the multi-objective problem. Actually, the designer is free to choose one or more individuals of interest from the Pareto front. Each individual is characterized by a specific set of design variable values which can be imported within HyperMorph® to obtain the deformed mesh, starting from the baseline one. Finally, some reverse engineering techniques can be used to generate the CAD surfaces starting from the morphed grid. This final step is usually accomplished using CATIA® v.5.

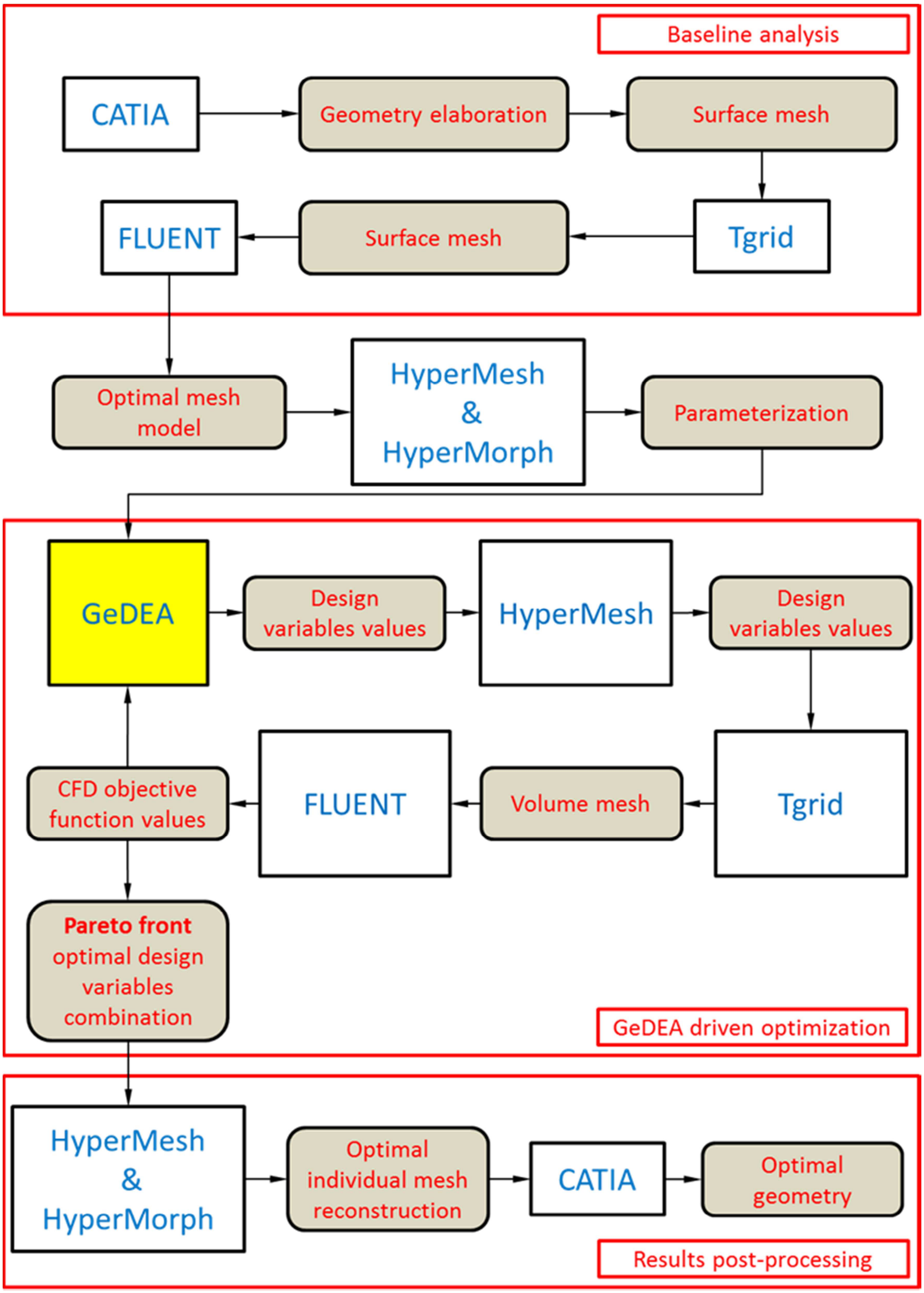

**Figure 4.12: Flow chart of the complete optimization procedure.**

## *4.5 The model parameterization.*

An important step in the optimization of a given geometry is represented by the model parameterization. This operation aims at identifying a proper set of design variables, able to govern those specific portions of the geometry featuring the major effects on the optimization objectives.

For the scope of the present work, the commercial software Altair HyperMesh® was adopted as the parameterization tool, due mainly to the versatile capabilities of its morphing tool called HyperMorph®.

In this specific case, a series of geometrical constraints were applied on the modified geometries, essentially related to the kinematics of the blade stubs during one rotor revolution. Therefore, the optimization procedure was partially modified in order to account for the above-mentioned constraints. This ensured that the final optimized solutions are suitable to be installed on the AW101 helicopter.

### 4.5.1 Definition of the design variables

The MODEL_4 described in §4.2 was chosen as the baseline model to parameterize, as already stated in the previous chapter. Seven design variables were identified for the geometrical control of the beanie surfaces. They were generated using two techniques, namely:

- The domain/handle morphing technique: this approach consists in the subdivision of the original mesh in a user-controlled number of sub-regions (domains) which are connected to one or more control points (handles). The displacement of the mesh nodes belonging to a given domain is calculated according to the movement applied to a handle associated to that specific domain.
- The map-to-geometry morphing technique: the model has to be subdivided into sub-regions (domains), then the elements belonging to a specific domain are mapped to a given line, node list, plane or surface.

When applied, the nodes displacements can be saved as perturbation vectors (shapes) and then reapplied to the baseline model with any given scaling factor. Therefore, the morphed geometries result from the linear combination of the user-defined shapes multiplied by their own scaling factor:

$$\boldsymbol{v} = \sum_{i=1}^{7} \alpha_i \cdot sh_i \qquad \textbf{Eq. 10}$$

where, v is the global displacement vector, $sh_i$ is the $i^{th}$ basic shape, and $\alpha_i$ is the $i^{th}$ shape scaling factor, which is actually the modified parameter during the optimization process for generation of each individual.

The selected design variables for the beanie optimization are illustrated from Figure 4.13 to Figure 4.19 and described in the following:

- ***sh1***: this shape is directly connected to the beanie diameter (Figure 4.13). The deformation range assigned to this variable is equal to [-60mm;+50mm];
- ***sh2***: the map-to-geometry approach was applied to the baseline mesh in order to obtain a shape that governs the characteristics of the beanie edge (Figure 4.14). Specifically, when sh2 is applied to the mesh, a geometry similar to the original AW101 beanie is obtained;
- ***sh3***: this shape governs the characteristics of the beanie upper surface geometry (Figure 4.15). In particular, it affects the dome convexity;
- ***sh4***: this is the second variable that affects the beanie upper surface geometry. Specifically, it modifies the shape of the central part of the upper surface by changing its slope (Figure 4.16);
- ***sh5***: this variable changes the characteristics of the beanie lower surface by flattening it on a plane parallel to the beanie base (Figure 4.17). This shape was obtained by means of the map-to-geometry approach;
- ***sh6***: this shape governs the beanie height (Figure 4.18). It was obtained by moving the upper and lower surfaces along the z direction, resulting in a stretch or in a compression of the beanie support;
- ***sh7***: this variable controls the cone opening angle of the beanie support by changing the diameter of the truncated-cone larger base (Figure 4.19). Specifically, a cylindrical support is obtained when sh7 assumes the values corresponding to its upper bound.

It is worth noting that in Figures from 13 to 19 the shape functions' scaling factors were given the maximum values in their allowed variability ranges, so the pictures illustrate the maximum effect of each variable on the beanie baseline geometry.

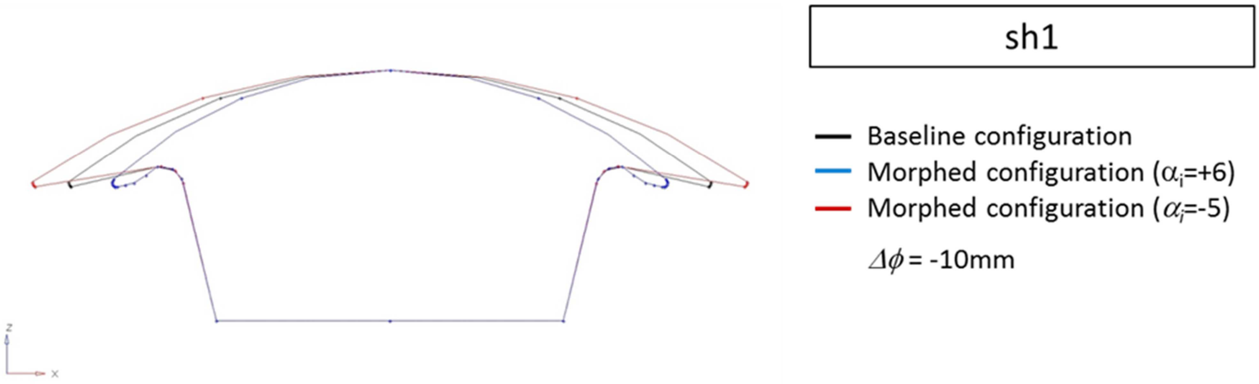

**Figure 4.13: Outline of the parametric shape *sh1* applied to the beanie with a scaling factor $-5 \leq \alpha_1 \leq 6$.**

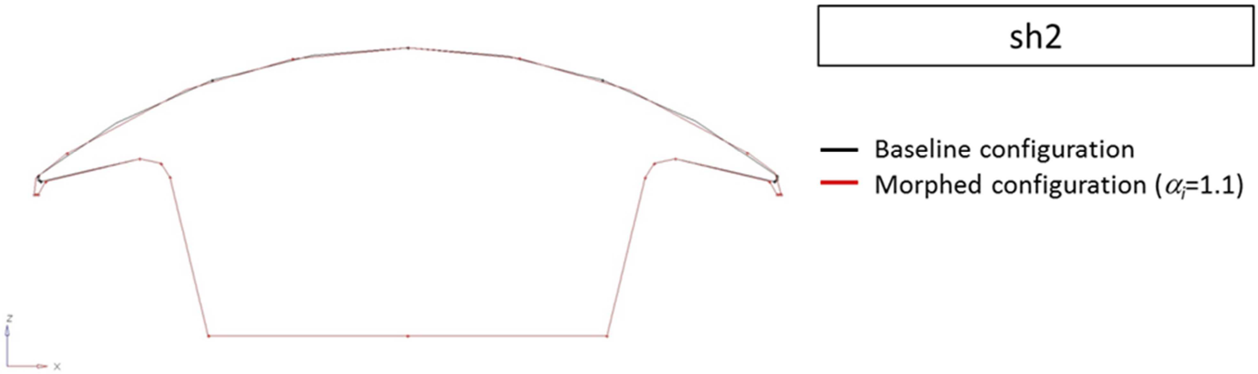

**Figure 4.14: Outline of the parametric shape *sh2* applied to the beanie with a scaling factor $\alpha_2$=+1.1.**

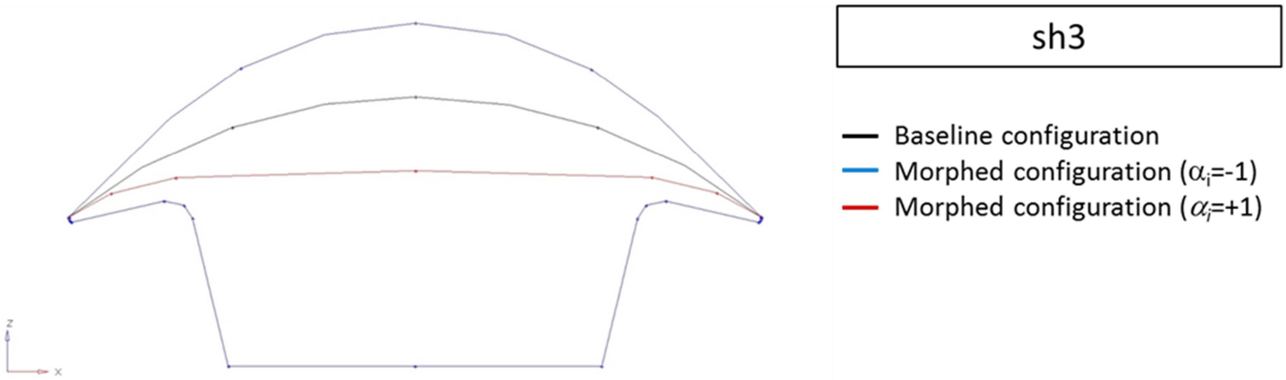

**Figure 4.15: Outline of the parametric shape *sh3* applied to the beanie with a scaling factor $\alpha_3$=+1.**

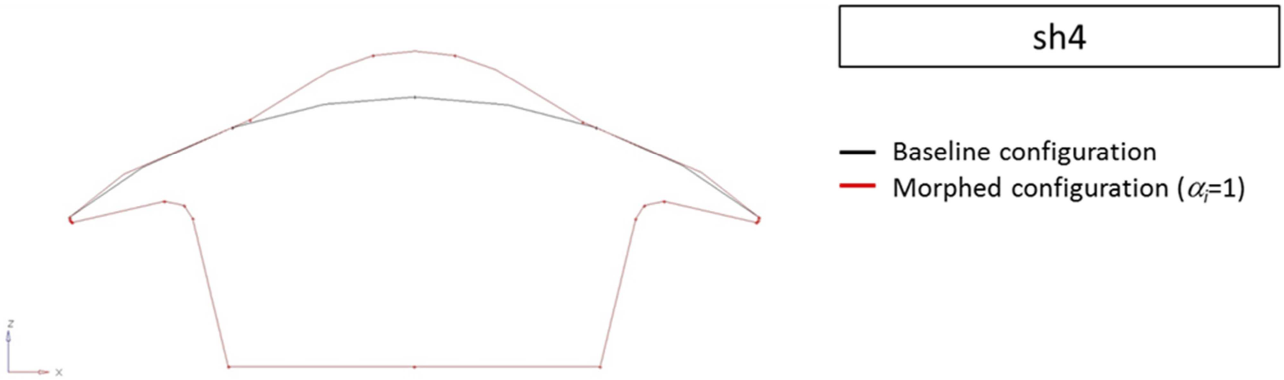

**Figure 4.16: Outline of the parametric shape *sh4* applied to the beanie with a scaling factor *$\alpha_4$=+1.***

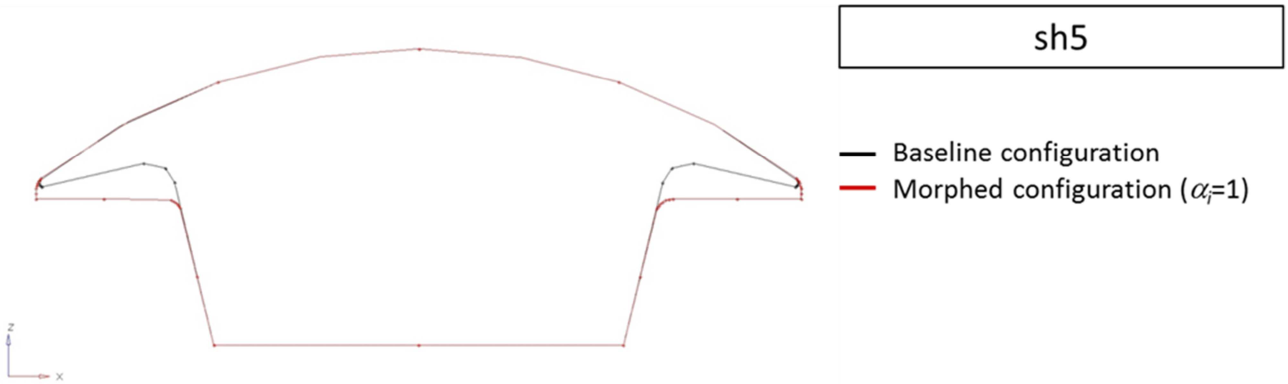

**Figure 4.17: Outline of the parametric shape *sh5* applied to the beanie with a scaling factor *$\alpha_5$=+1.***

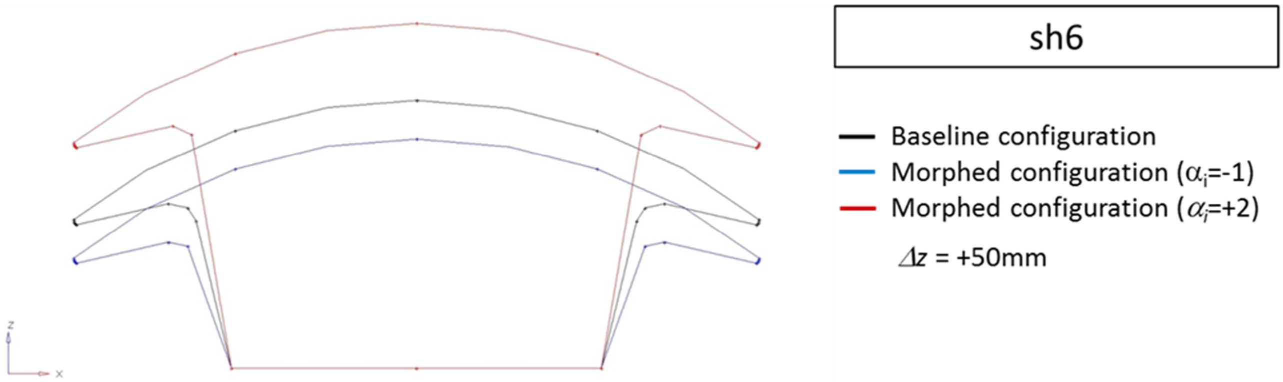

**Figure 4.18: Outline of the parametric shape *sh6* applied to the beanie with a scaling factor -1≤$\alpha_6$≤2.**

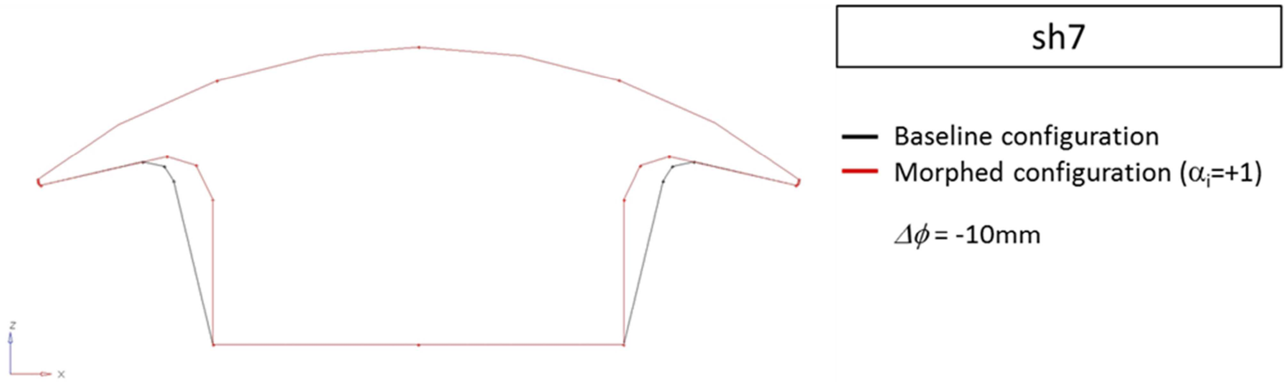

**Figure 4.19: Outline of the parametric shape *sh7* applied to the beanie with a scaling factor $\alpha_7$=+1.**

The selected variability ranges for the $\alpha_i$ factors in the current work are summarised in Table 4.7. It is worth noting that a scaling factor equal to zero means that the morphed geometry is identical to the baseline one. A scaling factor equal to the variable upper bound produces the maximum allowed displacement for the pertinent shape. A scaling factor equal to the variable lower bound produces the maximum allowed displacement for the pertinent shape but in the opposite direction with respect to the original definition of the shape modification.

| $\alpha_i$ | range |
|---|---|
| **1** | [-5; 6] |
| **2** | [0; 1.1] |
| **3** | [-1; 1] |
| **4** | [0; 1] |

| $\alpha_i$ | range |
|---|---|
| **5** | [0; 1] |
| **6** | [-1; 2] |
| **7** | [0; 1] |

**Table 4.7: The variability ranges of the beanie design parameters.**

### 4.5.2 Geometrical constraints

Geometrical constraints are a key factor that needs to be taken into account during an optimization process, since they limit the research space and thus the range in which the design variables can be varied. Therefore, it is important to automatically exclude from the analysis those geometries that do not fulfil the geometrical constraints (since they are not of any practical industrial interest) in order to save time and computational resources.

In the present work, the beanie overall dimensions were limited by the kinematics of the rotor blade hinge fairings and in particular by the blade flap motion. In order to facilitate the identification of a research domain compliant with the geometrical constraints, a box enveloping the movements (pinch, flap and lead-lag) of all the blades around the hub cap was built in CATIA ® v.5. This analysis resulted in the constraint surface depicted in Figure 4.20, which clearly identifies the feasible research domain.

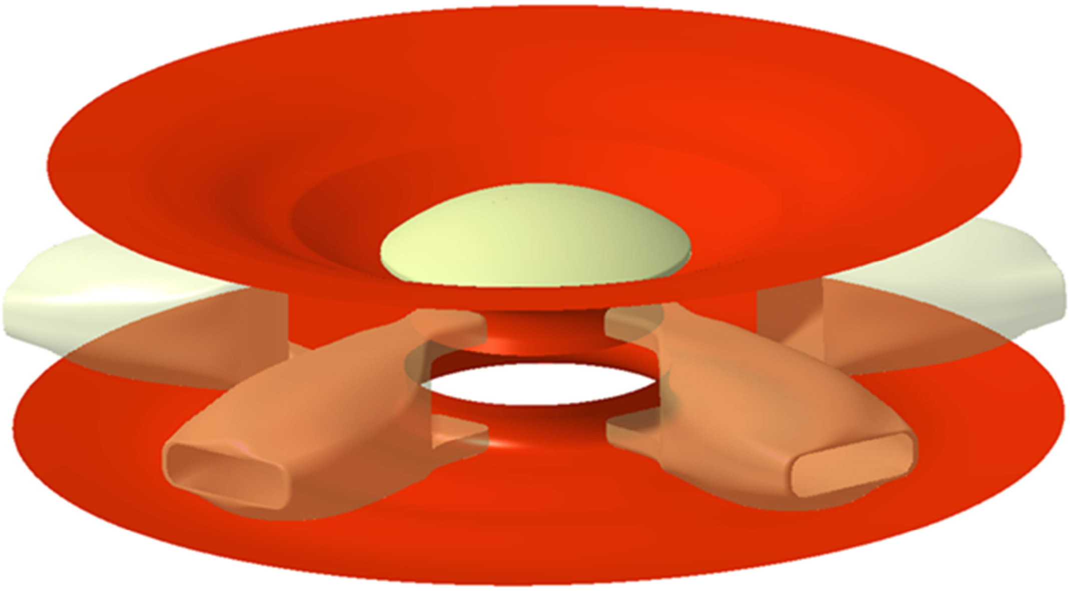

**Figure 4.20: The surfaces that envelope the blade hinge fairing motions.**

The constraint surface had to be expressed using a mathematical function that could be easily implemented in the optimization process. To this purpose, a section on the x-z plane of the afore-mentioned axis-symmetric surface was derived. Then, the curve was offset by 5 mm for two practical reasons: (1) a certain gap between the beanie and the constraint surface was necessary, in order for the involved components (i.e. the hub cap and the blade hinges fairings) not to collapse into each other; (2) the constraint curve was approximated with a six-degrees polynomial, hence the offset has the additional function of overcoming any interpolation problem. In Figure 4.21, the original constraint curve, the offset curve and the polynomial approximation are illustrated.

The beanie was parameterized using seven independent variables, therefore the geometrical constraint can be expressed as follows:

$$\boldsymbol{x} < f(\boldsymbol{z}) \qquad \textbf{Eq. 11}$$

where:

$$f(\boldsymbol{z}) = \sum_{i=0}^{6} a_i \boldsymbol{z}^i \qquad \textbf{Eq. 12}$$

$$x = f_1(sh2, sh5, sh7)$$ **Eq. 13**

$$z = f_2(sh2, sh5, sh6)$$ **Eq. 14**

In particular, $f_1$ and $f_2$ are two linear functions that associate the design variables (together with their scaling factors) with some beanie geometrical characteristics such as the hub cap height and longitudinal position with respect to the global reference system, the hub cap diameter, etc. The dot in Figure 4.21 represents the edge position of the original AW101 beanie calculated by means of the equations reported above: as apparent, the original AW101 geometry is compliant with the geometrical constraints.

As far as the automatic optimization process was concerned, equations 11, 12, 13, and 14 were implemented into a MATLAB® function. Using this function, each individual of a given population was checked for compliance with constraints: individuals that did not fulfil the constraint equation were then replaced by new, randomly generated, constraint-compliant individuals.

In addition, a structural constraint had to be taken into account: the new hub cap model will be manufactured using composite materials (Kevlar for the beanie and carbon fibre for the support): therefore, some constraints on both the thickness and the minimum internal curvature radius ($r_{min}^{int}$) need to be respected. Specifically, the usual thickness for the hub cap surfaces is 1.5mm and the minimum acceptable internal radius is 3 mm.

This structural constraint could not be easily controlled during the optimization process, since the model was discretized in a triangular based linear type mesh, whose mean size was much larger than 4 mm. Nonetheless, particular attention was paid in the model parameterization in order to avoid the possibility of generating geometries with low internal curvature radius.

The final control on this structural constraint could only be carried out during the reverse engineering process that leads to the definition of the CAD surfaces. In fact, within CATIA® the user may smooth and round off the sharp edges and control that the limits on the internal curvature radii are fulfilled, in order to obtain a final geometry suitable for industrial purposes.

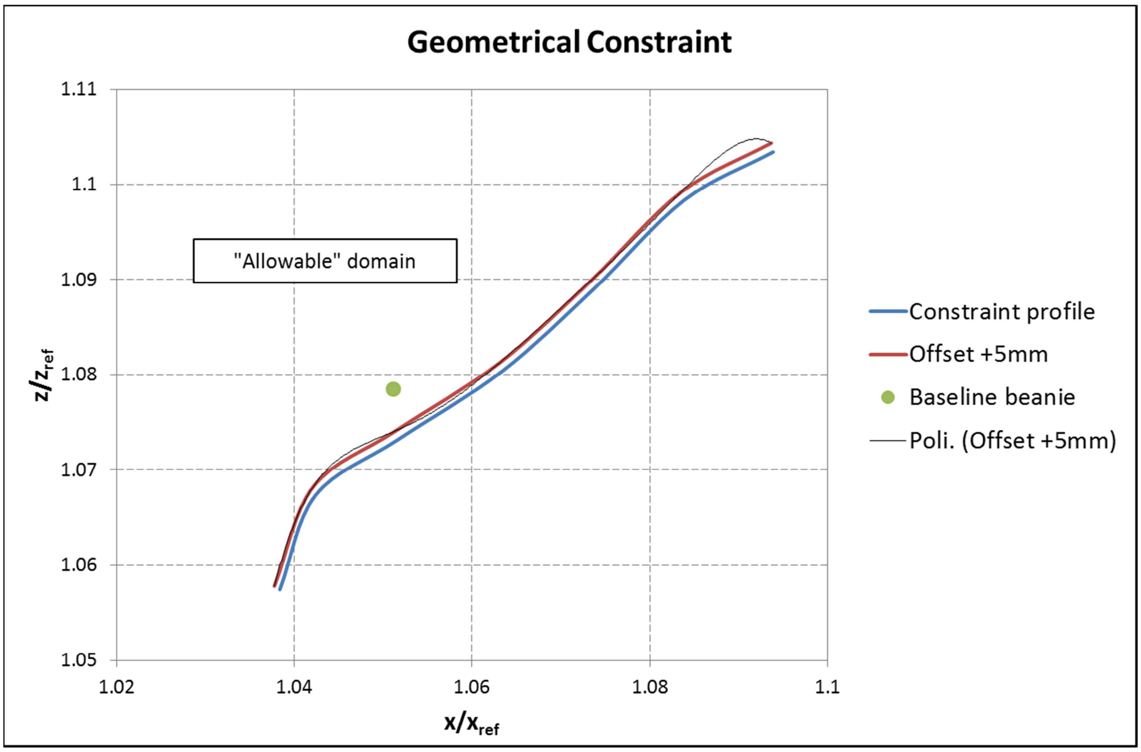

**Figure 4.21: Representation of the curves desribing the geometrical constraint and the point representing the baseline beanie edge.**

## 4.6 Beanie preliminary parametric analysis.

A parametric analysis was carried out before the optimization in order to identify the proper lateral position for the wake rake to be used during the optimization process for determination of the wake deflection. Moreover, these tests were useful to better understand the effects of the selected variables on the beanie performance.

A number of new beanie geometries were created following the parameter matrix reported in Table 4.8. The meshes were obtained applying the morphing technique described in §4.5 and the CFD simulations were carried out using the settings discussed in §4.3 for the baseline model. Results were compared to the baseline geometry in terms of both global forces acting on the beanie and total pressure losses at the beanie wake rake.

The two dimensional curves of total pressure losses over the wake rake placed near the helicopter tail fin were obtained for each case and are reported in Figure 4.22. The wakes of the different beanies were always symmetrical with respect to the longitudinal plane y=0. Moreover, the maximum displacement, as well as the maximum total pressure loss, were observed exactly at y=0.

Therefore, it is possible to conclude that the most suitable lateral position for the wake rake positioning is y=0.

Table 4.9 summarizes the aerodynamic beanie loads and the ordinate z corresponding to the maximum total pressure loss over the longitudinal symmetry plane (y=0). As apparent, the reduction of both the beanie height (sh6) and diameter (sh1) along with the increase of the beanie upper surface curvature (sh3) have positive effects on both the beanie lift and drag and on its wake deflection capabilities. By lowering the beanie edge (sh2), a remarkable increase in lift was achieved with respect to the baseline (Case#1), together with a negligible increase in drag and wake deflection. Furthermore, the flattening of the beanie lower surface (sh5) led to a decrease in both the lift and drag, and a lower wake deflection along the z axis.

| Case # | sh1 | sh2 | sh3 | sh4 | sh5 | sh6 | sh7 |
|---|---|---|---|---|---|---|---|
| **0 (baseline)** | 0 | 0 | 0 | 0 | 0 | 0 | 0 |
| **1** | 0 | 1 | 0 | 0 | 0 | 0 | 0 |
| **2** | 0 | 0 | 0 | 0 | 1 | 0 | 0 |
| **3** | 0 | 0 | 1 | 0 | 1 | 0.6 | 0 |
| **4** | -5 | 0 | 0 | 1 | 0 | 0.5 | 0 |
| **5** | -5 | 1 | 1 | 1 | 1 | 2 | 1 |
| **6** | 6 | 0 | -1 | 0 | 0 | -0.85 | 0 |

**Table 4.8: Beanie parametric study test matrix.**

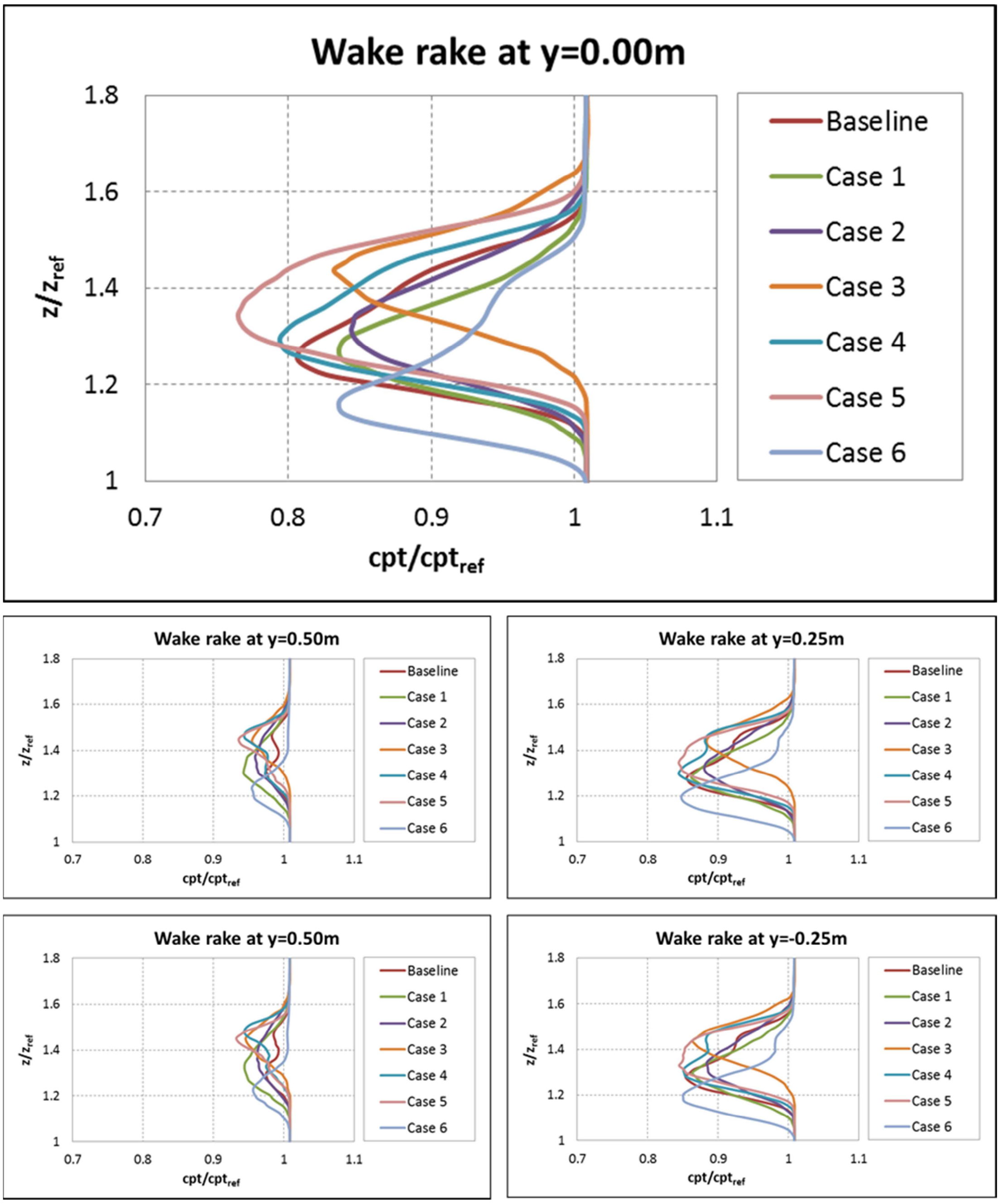

**Figure 4.22: Two dimensional total pressure losses plots at different lateral position over a transversal section downstream of the beanie centre along the x direction near the tail fin**

Finally, it is worth noting that there is quite a good correlation between the beanie lift and the wake deflection: as expected, the larger the lift, the higher the wake deflection downwards. On the other hand, the original AW101 beanie featured good wake deflection capabilities (-6% compared to $z_{baseline}$) combined with a lower lift (-5% compared to the baseline lift) and a higher drag (+20% compared to the baseline drag).

| **Case #** | **$L/L_0$**<br>*Δ%* | **$D/D_0$**<br>*Δ%* | **$z/z_0$**<br>*Δ%* |
|---|---|---|---|
| **0 (baseline)** | - | - | - |
| 1 | 26.3 | 4.9 | 0.25 |
| 2 | -3 | -3 | 3.96 |
| 3 | -61.9 | -15.5 | 13.86 |
| 4 | -12.5 | 19.2 | 2.72 |
| 5 | -15.1 | 27.8 | 6.44 |
| 6 | 41.7 | -5.7 | -8.42 |

**Table 4.9: Summary of the parametric analysis.**

## *4.7 Formulation of the optimization problem.*

Once the CFD analysis and the parameterization of the baseline model were carried out, the successive step consisted in the GeDEA-driven optimization.

The two main objectives of the optimization process were (1) the reduction of the beanie drag and (2) the improvement of its capabilities of deflecting the wake downwards. It is worth remembering that the wake deflection is measured with the z location of the maximum total pressure losses over a wake rake located on the longitudinal symmetry plane (y=0m), at a given position downstream of the beanie centre. Therefore, the second objective of the optimization problem may be expressed as the reduction of the above mentioned z-ordinate value.

Since the GeDEA was programmed for carrying out the maximization of the objective functions, the actual optimization problem could be stated as follows:

$$Maximize[\boldsymbol{F}(\boldsymbol{sh})] \qquad \textbf{Eq. 15}$$

where:

$$\boldsymbol{F}(\boldsymbol{sh}) = [-D;\ -z] \qquad \textbf{Eq. 16}$$

$$\boldsymbol{sh} = [\alpha_1, \alpha_2, \alpha_3, \alpha_4, \alpha_5, \alpha_6, \alpha_7] \qquad \textbf{Eq. 17}$$

being $\alpha_i$ the $i^{th}$ shape scaling factors, whose ranges are reported in Table 4.7.

Thanks to its multi-objective formulation, the optimization algorithm seeks for solutions featuring improved performance in terms of both drag and wake deflection.

The number of individuals per generation was set to 15, while the overall number of generations was set to 12.

## 4.8 Discussion of the results.

The final Pareto front is illustrated in Figure 4.23, while the overall set of investigated geometries is depicted in Figure 4.24. As apparent, a remarkable drag reduction is achieved for the individuals over the final front with respect to both the optimization baseline and the original AW101 beanie. In addition, also an improvement in the beanie capabilities of deflecting downwards the oncoming air flow was observed with respect to the baseline model.

Table 4.10 reports the design variables and objectives function values for each of the individuals belonging the final Pareto front. From the achieved results, the following considerations can be drawn:

- all the configurations over the Pareto front feature a drag reduction of around 20% with respect to the baseline;
- the improvement in the beanie wake deflection is less pronounced; specifically, some individuals on the front feature a maximum pressure loss in the wake at a higher z coordinate than the baseline. However, a maximum wake deflection improvement of around 10% is achieved for the individual at one bound of the Pareto front with respect to the baseline;
- it is apparent that a reduction of the beanie diameter is strongly recommended in order to achieve a better performance: in fact, the scaling factor of sh1 variable has a positive value for all the individuals over the front and features values close to the upper bound of its allowed variability range;
- a smaller height of the beanie support has positive effects on the wake deflection, since the individuals belonging to the Pareto front are characterized by a negative scaling factor of sh6 variable;
- an increase in the beanie convexity (variable sh3) has positive effects on the wake deflection: in fact, it causes an increase of the beanie lift, even though a larger drag is found as well;
- finally, a decrease of the scaling factors of sh2, sh4, sh5 and sh7 variables causes an improvement in the beanie capabilities of deflecting the wake, though it leads to an increase in drag as well.

| **sh1** | **sh2** | **sh3** | **sh4** | **sh5** | **sh6** | **sh7** | **Objectives** | |
|---|---|---|---|---|---|---|---|---|
| | | | | | | | **ΔD%** | **Δz%** |
| 4.8164 | 0.1720 | 0.7110 | 0.6448 | 0.3763 | -0.4272 | 0.4283 | **-23.5** | **2.0** |
| 6.0000 | 0.0000 | -1.0000 | 0.0000 | 0.0000 | -0.8500 | 0.0000 | **-6.5** | **-9.2** |
| 5.1779 | 0.2317 | 0.5347 | 0.5440 | 0.3518 | -0.4043 | 0.4037 | **-21.1** | **0.0** |
| 5.8569 | 0.1619 | -0.1173 | 0.2481 | 0.1583 | -0.6782 | 0.1770 | **-18.2** | **-5.4** |
| 5.6351 | 0.2528 | 0.4174 | 0.4962 | 0.3269 | -0.4275 | 0.3964 | **-20.3** | **-1.0** |
| 5.8250 | 0.2043 | 0.1244 | 0.3639 | 0.2549 | -0.5896 | 0.2886 | **-19.7** | **-3.2** |
| 5.0886 | 0.1319 | -0.4333 | 0.1929 | 0.1302 | -0.6240 | 0.1752 | **-9.5** | **-6.4** |

**Table 4.10: Scaling factor values for the shape functions of the individuals belonging to the final Pareto front and pertinent objective values compared to the baseline.**

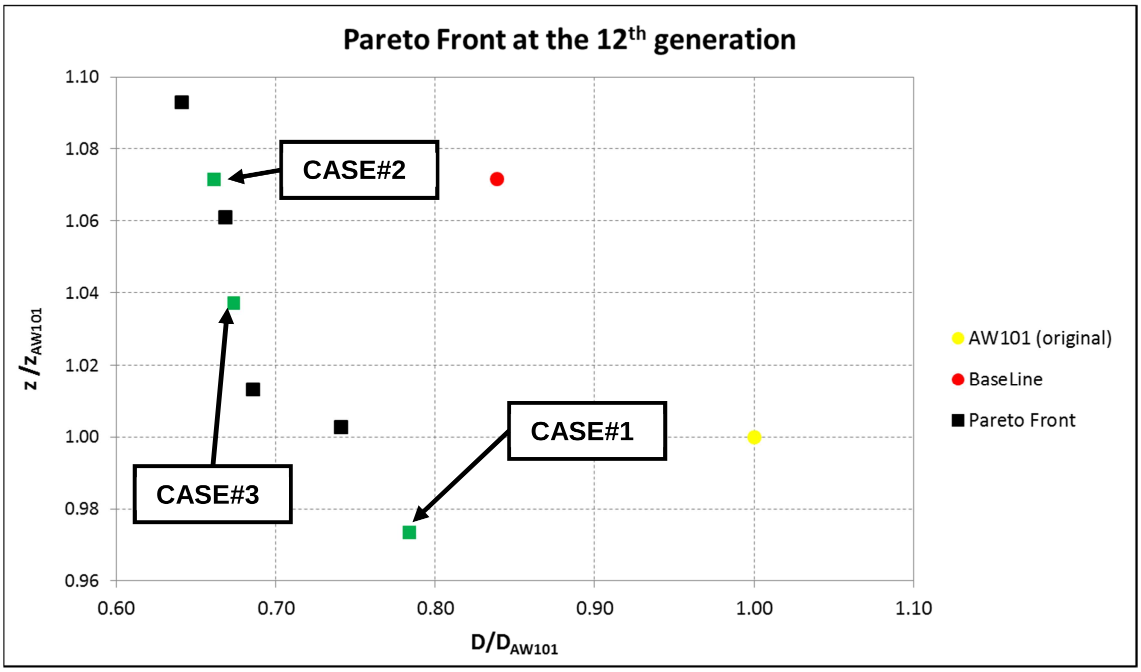

**Figure 4.23: Final Pareto front after 12 generations.**

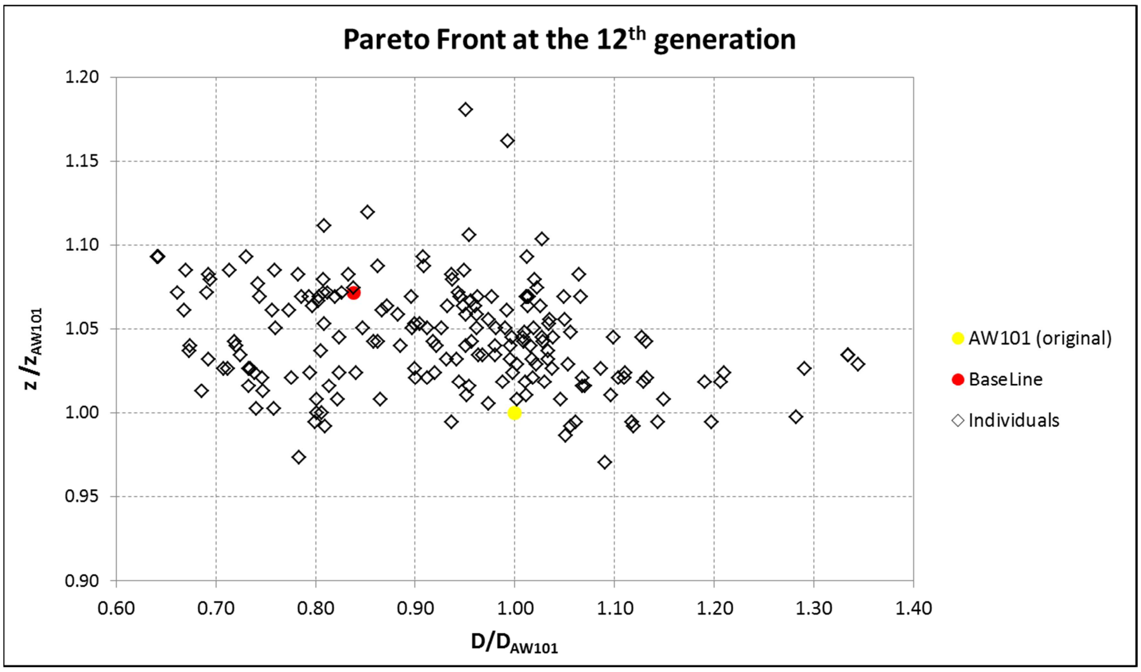

Figure 4.24: The entire set of individuals simulated during the optimization run.

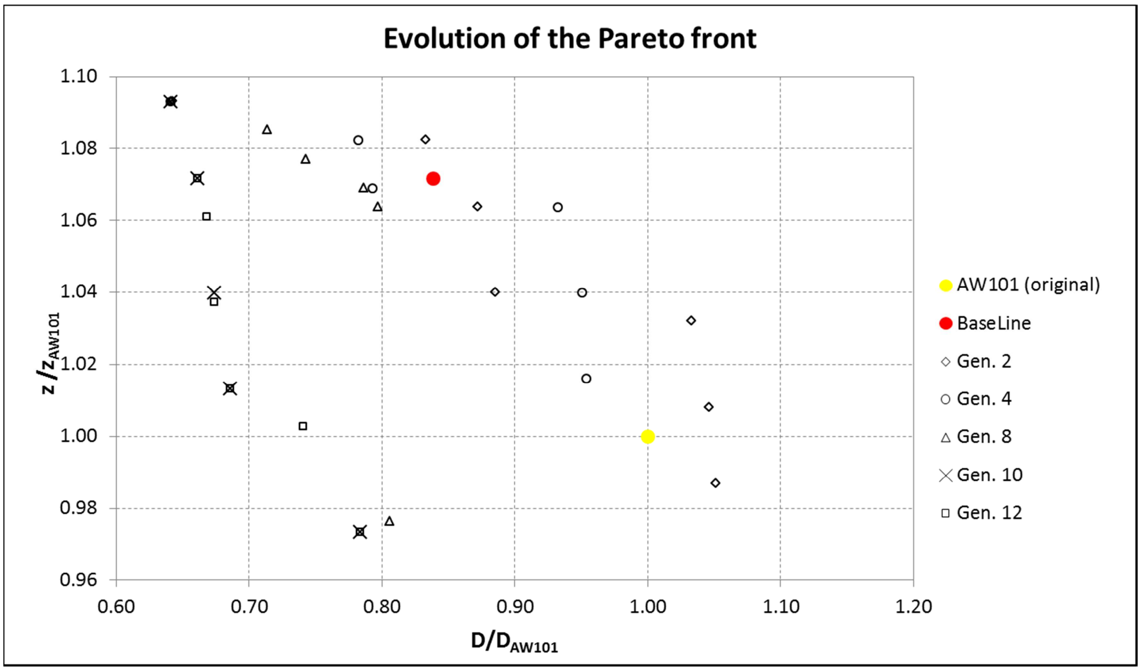

Figure 4.25: Evolution of the Pareto front.

Three individuals belonging to the Pareto front are selected as the final solutions and compared to the baseline model: they are represented by the green square points in Figure 4.23. Specifically:

- CASE#1: it is the individual having the highest drag value in the front and the maximum capabilities in wake deflection;
- CASE#2: it has the same value of the z ordinate of the baseline, though the drag is much lower;
- CASE#3: it is a compromise between CASE#1 and CASE#2.

The design variables of the optimized solutions are reported in Table 4.10, while their geometrical configuration is illustrated in Figure 4.26, Figure 4.27 and Figure 4.28, where the differences with the baseline and the constraint surface are evidenced as well. Moreover, the three selected optimized geometries are superimposed in Figure 4.29 at the proper shaft tilt angle, together with the original AW101 beanie and the constraint surface for a direct comparison. As apparent, the CASE#1 geometry is characterized by a higher convexity, a lower support (with an increased opening cone angle) and a reduced diameter compared to the baseline; CASE#2 is smaller than the baseline model both in terms of diameter and beanie height; in addition, the upper surface is inflected over its central portion; CASE#3 is clearly a compromise solution between the other two cases. Figure 4.30, Figure 4.31 and Figure 4.32 illustrate the CAD models of the CASE#1, CASE#2 and CASE#3 optimized beanies respectively.

The mesh post-processing of the optimized solutions was then carried out using CATIA®: this made it possible to verify that the optimized solutions were compliant with both the structural and the geometrical constraints described above. However, it is worth noting that the optimized configurations lie quite close to the curve representing the constraint surface (described in §4.5.1), as apparent from Figure 4.33.

In Figure 4.34, the static pressure coefficient distribution over the optimized beanie surfaces is reported and compared with the baseline. As far as the upper surfaces are concerned, a wide area of low Cp can be observed in CASE#1, while the effects of the surface inflexion on the Cp distribution are apparent in both CASE#2 and CASE#3. On the beanie lower surfaces, an area of low Cp appears in the fore portion of both the baseline and the CASE#2 beanies, whereas this feature is less pronounced in CASE#1 and CASE#3.

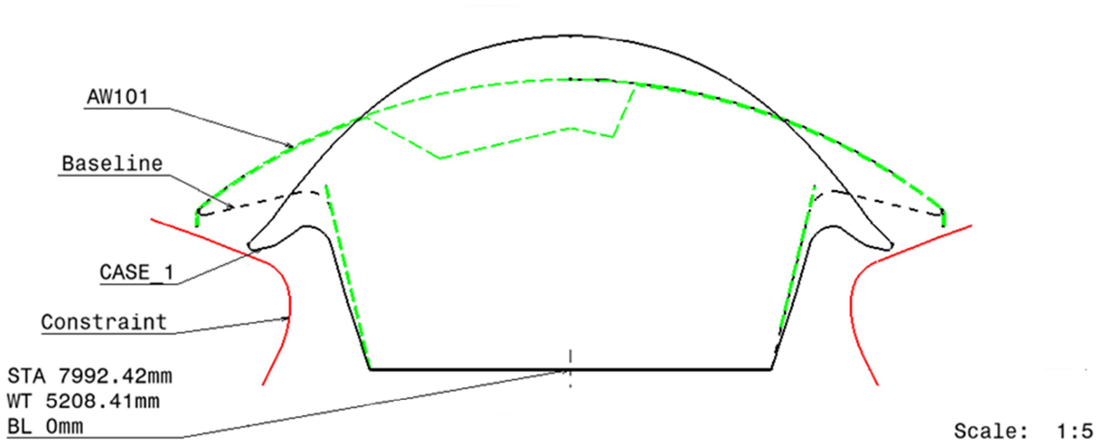

Figure 4.26: CASE#1 main geometrical characteristics (solid line), compared to the baseline.

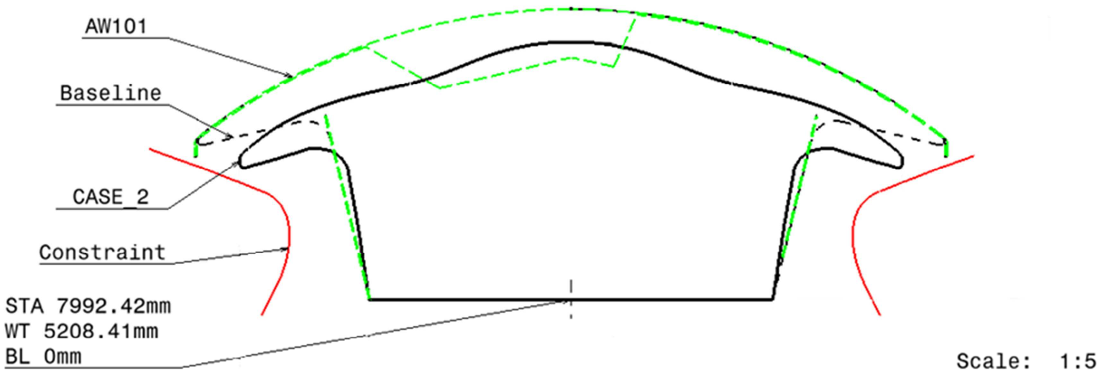

Figure 4.27: CASE#2 main geometrical characteristics (solid line), compared to the baseline.

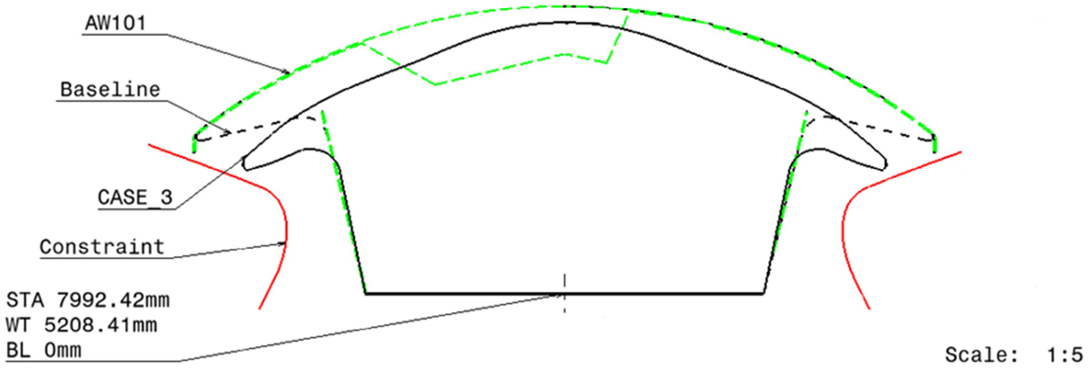

Figure 4.28: CASE#3 main geometrical characteristics (solid line), compared to the baseline.

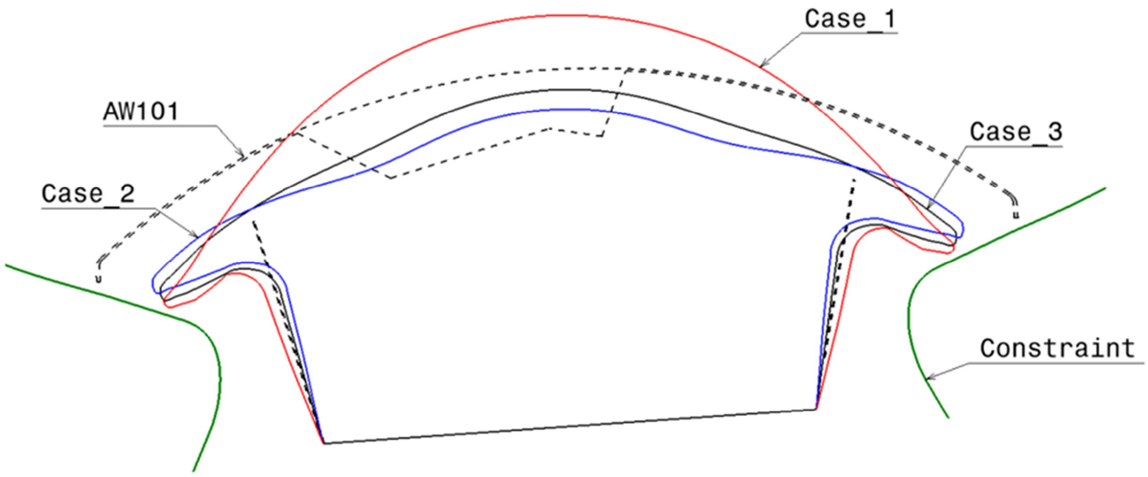

**Figure 4.29: Direct comparison of the three selected optimized configurations at the proper shaft tilt angle: constraints are represented as well.**

The comparison of the optimized beanie wake characteristics with the baseline (Figure 4.36) shows the improved capabilities of the optimized solutions (when compared with the baseline) in deflecting downwards the oncoming air flow; moreover, the improvement is apparent not only at the midsection, but also at various lateral positions. Furthermore, it is worth noting that CASE#1 configuration causes the lowest total pressure losses over the midsection and the highest ones on the lateral positions, especially for y=±0.5m. Figure 4.35 the contour plots of the non-dimensionalized total pressure coefficient over the helicopter midsection, for all the analyzed configurations.

Finally, Table 22 summarizes the values of the aerodynamic forces and moments of the optimized solutions compared to the baseline. All the optimized solutions feature a drag drop with respect to both the baseline and the original AW101 (up to 21% with respect to the baseline and 34% with respect to the AW101) and a lift increase; moreover, a reduction in the absolute values of the moments was observed as well. In particular, the pitching moment coefficient becomes positive for the CASE#1 geometry, probably because of the increased beanie convexity and the reduction of the support height with respect to the baseline. Regarding the wake deflection, while the optimized solutions are better than the baseline, they feature a reduced wake deflection capability if compared to the original AW101, exception given for CASE#1.

Figure 4.30: CASE#1 beanie CAD model

Figure 4.31: CASE#2 beanie CAD model

Figure 4.32: CASE#3 beanie CAD model

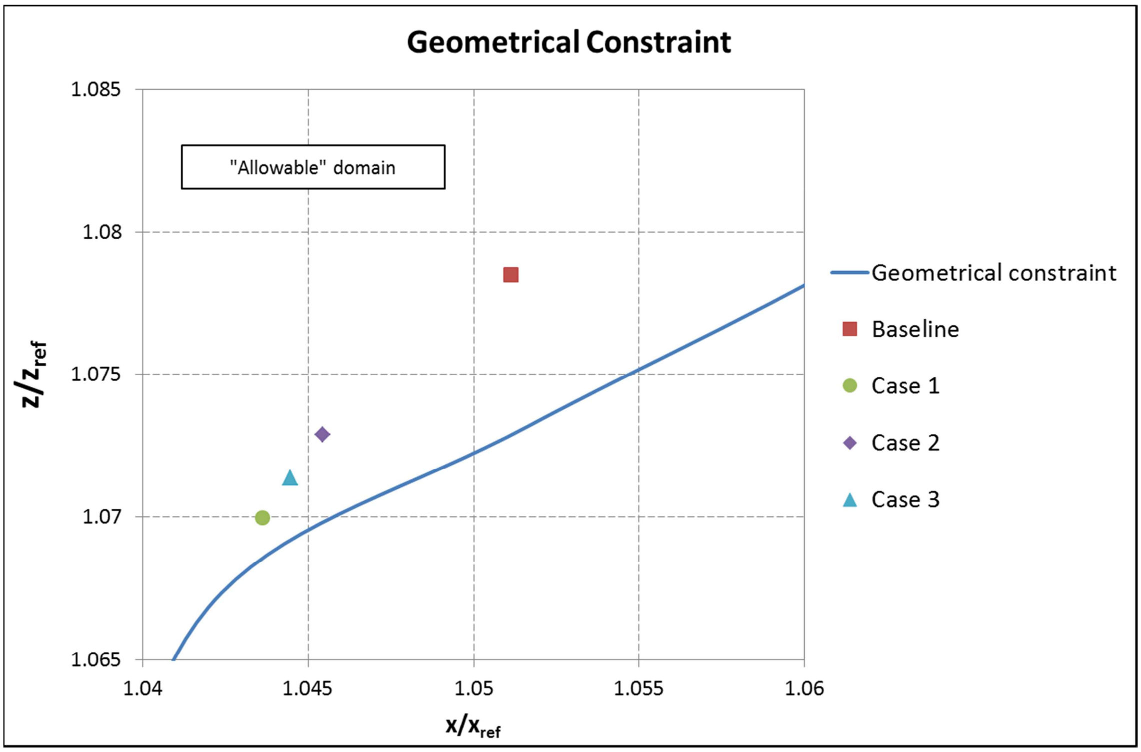

Figure 4.33: The optimized beanie edge location with respect to the constraint surface

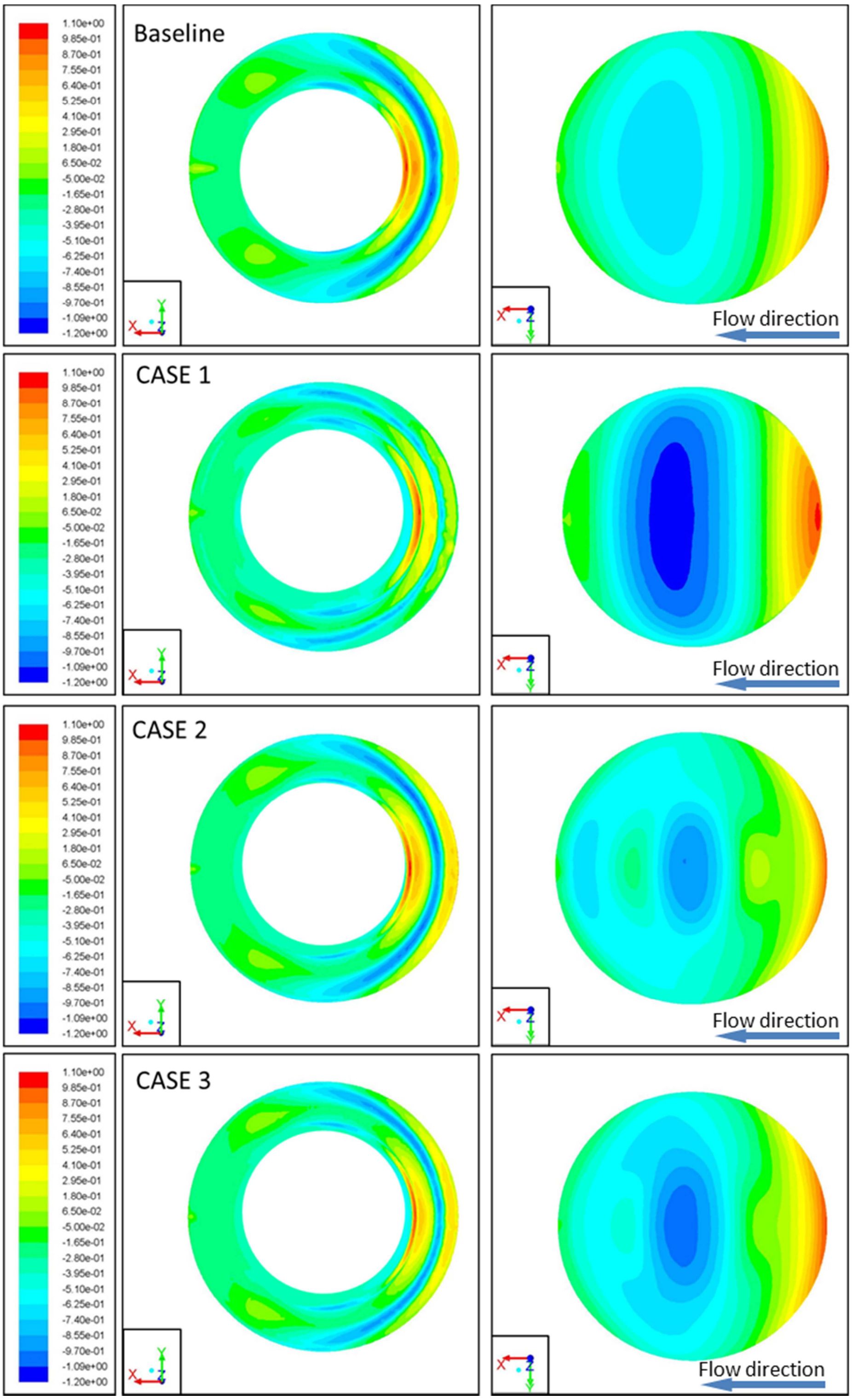

**Figure 4.34: Static pressure coefficient distribution over the optimized beanie surfaces and the baseline**

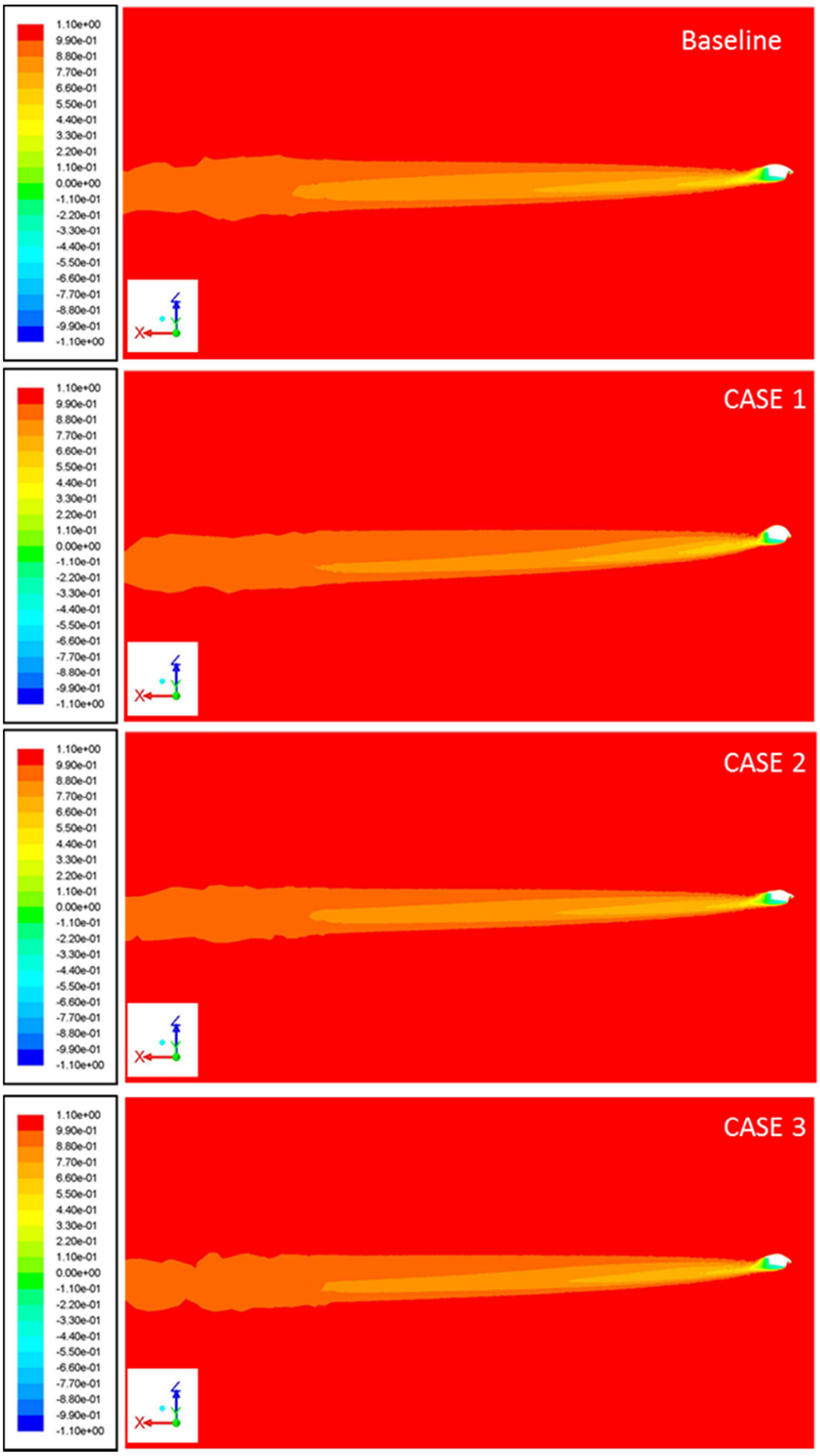

**Figure 4.35: Contour plots of the total pressure coefficient over the helicopter midsection for the optimized beanie configurations and baseline**

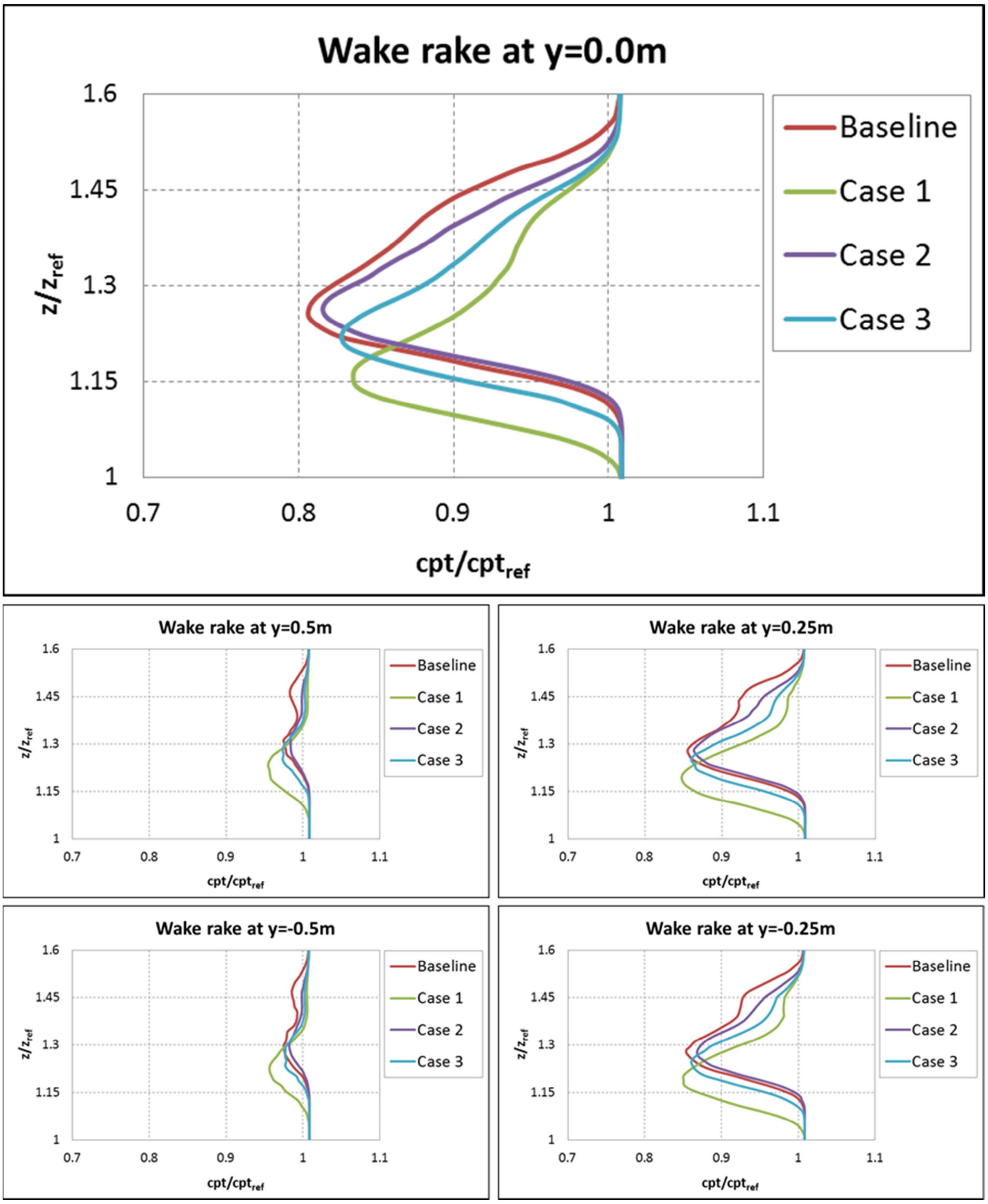

**Figure 4.36: Two dimensional total pressure losses at the different lateral position for the three optimized beanies and the baseline.**

| | **Baseline** | **Optimized** | | |
|---|---|---|---|---|
| | | CASE#1 | CASE#2 | CASE#3 |
| **$L/L_{AW101}$** | 1.06 | 1.52 | 1.06 | 1.23 |
| **$D/D_{AW101}$** | 0.84 | 0.78 | 0.66 | 0.67 |
| **$Mx/Mx_{AW101}$** | 0.38 | -0.13 | -0.27 | -0.12 |
| **$My/Mx_{AW101}$** | 0.70 | -0.69 | 0.50 | 0.23 |
| **$Mz/Mz_{AW101}$** | -0.24 | -0.01 | 0.09 | -0.01 |
| **$z/z_{AW101}$** | 1.07 | 0.98 | 1.07 | 1.04 |

**Table 4.11: Comparison of the Optimized and baseline beanies aerodynamic forces, moments with respect to the original AW101 geometry values.**

# 5. NEW BEANIE CONCEPT DESIGN FOR FUTURE APPLICATIONS

## *5.1 The new beanie model*

This chapter deals with the creation and the analysis of a new beanie concept-design, developed for future application on AW101 helicopters. This study aims at identifying new geometrical solutions, which could not be investigated within an automatic optimization tool, that can lead to an improvement in the beanie capabilities of deflecting the upcoming flow, reducing the aerodynamic drag with respect to the original model at the same time.

The beanie optimization activity thoroughly described in Chapter 4 led to the selection of three new beanie geometries featured a lower drag with respect to both the baseline model and the original AW101 beanie. Moreover, one of these new models (CASE#1) was also characterized by a larger wake deflection than the AW101 beanie. The optimization results made it possible to highlight the most influential shape parameters for the selected objective functions. In particular, a decreased beanie diameter, an increased upper surface convexity and a lower support height were strongly recommended in order to reduce the beanie aerodynamic drag and improve its capabilities in the deflection of the oncoming flow.

From all the analyses carried out on the AW101 beanie, it seems that the original model is characterized by a good downward deflection of its the wake, even with respect to the new optimized solutions. Regardless the drag, the reason of this aerodynamic behaviour is probably due to the beanie peculiar hollow geometry. Therefore, a new hollow beanie model (HBM) based on the original AW101 and composed of a disk supported by three arms mounted on a base, was created and then analysed via CFD in order to study its aerodynamic performances. In particular, the numerical simulations were carried out following the criteria developed during the AW101 optimization activity. Once the baseline analysis was carried out, the HBM was parameterized and some of the most important variables describing the main HBM geometrical characteristics, were defined. Finally a parametric study, preliminary to the future optimization, was carried out in order to analyse the aerodynamic behaviour of this new beanie model, and to better understand the effects of the selected design variables on the HBM overall aerodynamic performances.

## 5.2 The HBM hub cap geometrical characteristics.

As already mentioned in Chapter 4, the AW101 beanie has a complex structure characterized by many cavities and sharp edges, but it is anyhow capable of a remarkable downward deflection of the oncoming flow. The new HBM was created using CATIA v5 starting from the original AW101 geometry and it was made up of:

- A disk similar to the original AW101 spherical cap. Some changes were applied to the convexity of the upper surface, which was increased, and to the external edge which was smoothed in order to make it possible to realize the final beanie geometry in composite materials.
- A base. It was directly obtained from a section of the original beanie truncated-cone support. The base was closed by a semi-spherical upper surface
- The base and the disk are connected by three arms, which are smoothed in order remove the sharp edges and carefully linked to the other components using a 60mm fillet radii.

The superficial area of the HBM beanie is increased by the 23% with respect to the beanie MODEL_4 described in §4.2 and it is decreased by the 27% with respect to the AW101 beanie original model. Finally, the geometrical characteristics of the HBM hub cap are reported in Figure 5.1, and Figure 5.2

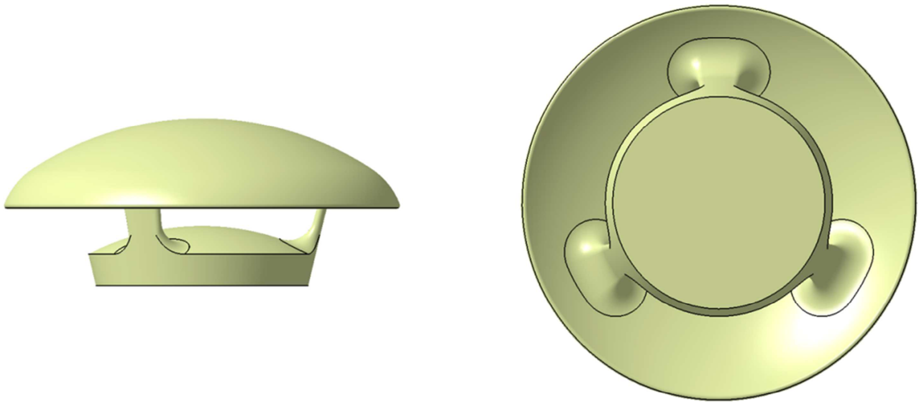

**Figure 5.1: Side view (on the left) and bottom wiew (on the right) of the new HMB model.**

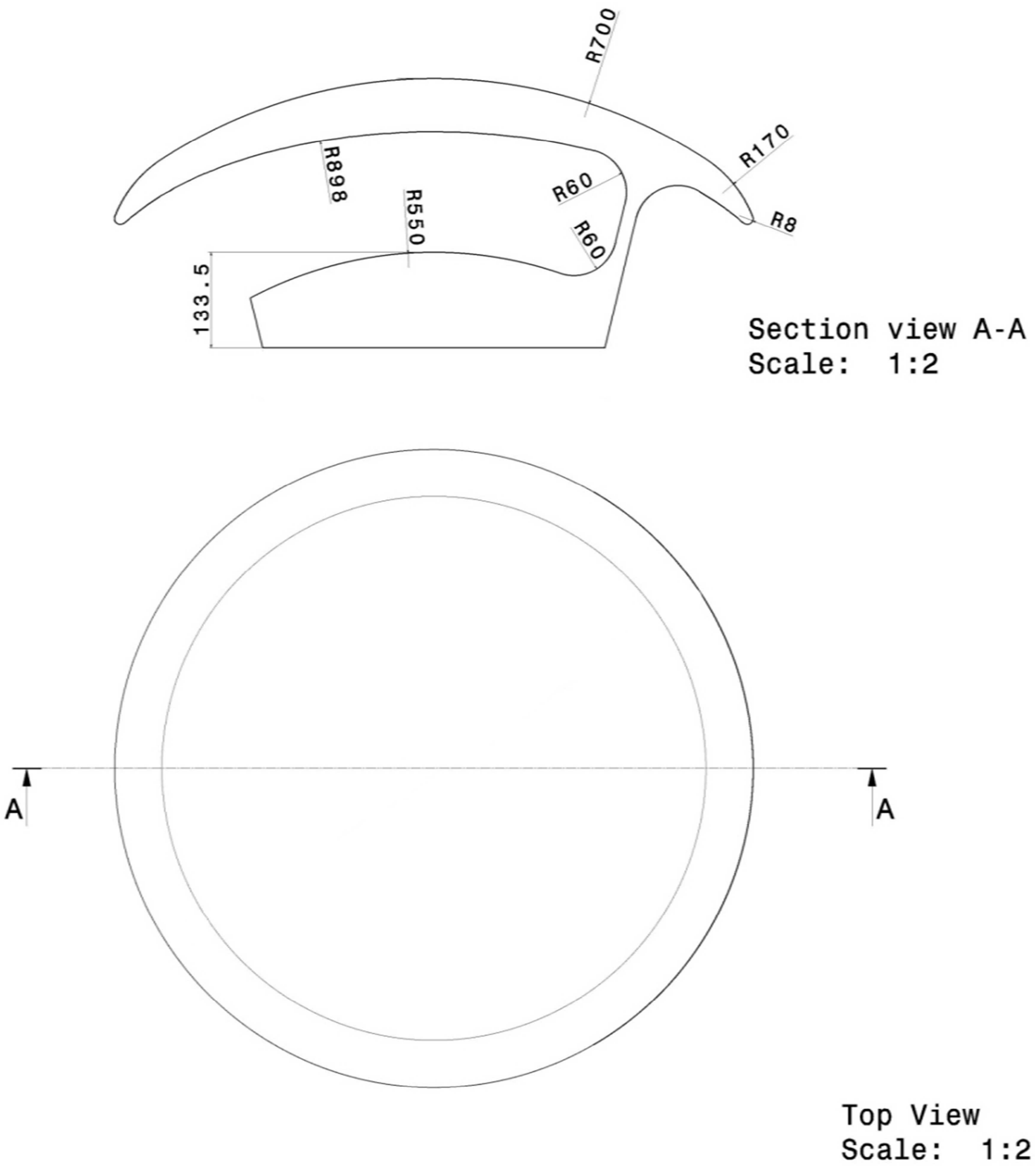

**Figure 5.2:Main geometrical characteristics of the HBM beanie.**

## *5.3 The CFD numerical model*

The numerical model of the newly generated beanie was set-up following the criteria already illustrated in Chapter 4. A dedicated tool of CATIA® V5 was used to generate the superficial girds made of triangular based, linear type surface elements. The quality parameters (skewness and aspect ratio) were carefully kept within the recommended ranges for a reliable CFD simulation. As far as the virtual wind tunnel box is concerned, the grid used in the beanie optimization activity was retained and used also for the analysis of the HBM beanie.

The meshes were uploaded within ANSYS Tgrid® for the volume mesh generation. The pitch attitude of the fuselage was given negative angel of incidence angle equal to -4.38 degrees, according to the chosen operating conditions, hence the resulting beanie angle of attack was equal to -8.38 degrees, as a consequence of the components relative position. As for the other analyses, this specific configuration was obtained by rotating the virtual wind tunnel by an angle equal and opposite to the prescribed one, in order to simplify the measurement of the downward deflection of the beanie wake during the post processing of CFD results.

The mesh was unstructured with structured elements over the beanie surfaces, in order to better simulate the boundary layer. The grow rate, the number of layers and the first layer thickness were selected following the criteria already presented in Chapter 2, which were proven to guarantee for the present case that the non-dimensional mesh thickness at the beanie surfaces (y+) fell well within the range that it is suggested for the wall function implemented in the conventional turbulence models to work properly. The volumetric mesh around the HMB hub cap is represented in Figure 5.3.

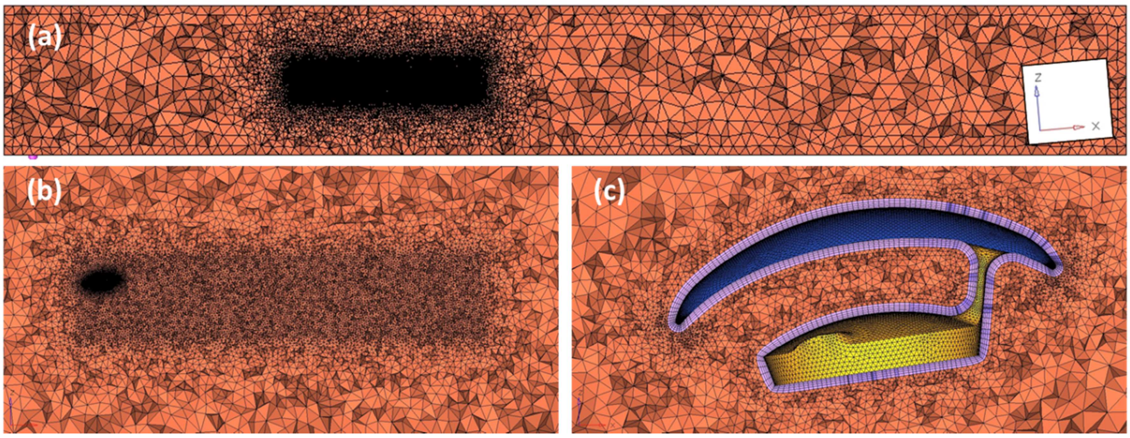

**Figure 5.3: Volumetric mesh over the HBM benaie: (a) global longitudinal view, (b) a close-up of the volume mesh grid refinement, and (c) a close-up of the beanie prismatic layers.**

The preliminary steady CFD simulations were carried out by means of ANAYS Fluent® v.14 adopting a pressure-based type approach with a velocity formulations. Moreover, the k-ω SST model was selected for the turbulence treatment. The air was treated as an ideal gas, which automatically enabled the energy equation resolution. Finally, the pre-defined three-coefficient Sutherland low was used to model the fluid viscosity.

Following the indication drawn in Chapter 4, a COUPLED scheme was preferred to the SIMPLE, since it was proven to decrease the number of the required iterations and the overall time to reach a goof convergence. The selected scheme solves the pressure and the momentum equations simultaneously and normally entails an increase in the required computational resources. The Courant number was set to 20, and the explicit relaxation factors were decreased from 0.75 to 0.5, in order to get a steep and stable solution convergence. On the contrary, the under-relaxation factors were left unchanged.

To achieve the desired solution accuracy, the highest order of the discretization scheme available within ANSYS Fluent® were chosen, despite the increase of both the computational time and the normalized RSM residuals.

The boundary conditions were set according the indications presented in Chapter 2. In this case, the total pressure and total temperature were calculated based on the new operating conditions prescribed for the optimization. Table 5.1 shows the final CFD boundary condition settings that were for the analyses concerning the HMB hub cap.

For the preliminary simulation, the solution was initialized by applying the fluid values of the inlet section over the fluid domain using an absolute reference frame. Then, the results of this converged CFD simulation were used to create an interpolation file containing the values of pressure, temperature, velocity, $k$ and $\omega$, which was used to initialized the solution in the case of the morphed HMB beanies. Owing to this different approach, the required computational time for each CFD analysis was considerably reduced.

For each simulation, the convergence criterion was established when the normalized REM residuals were less than $1*10^{-4}$. Furthermore, the global aerodynamic coefficients were monitored, in order to be sure they reached stabilized value at the end of each simulation.

| | | | | |
|---|---|---|---|---|
| **Viscous Model** | k–ω SST | | | |
| **Fluid** | Air | Ideal Gas | | |
| | | Sutherland low for viscosity | | |
| **Boundary Conditions** | Pressure Inlet | Gauge Total Pressure= 2,219.02 Pa | | |
| | | Total Temperature= 286.09 K | | |
| | Pressure Outlet | Gauge pressure= 0 Pa | | |
| | | Backflow Total temperature= 284.19K | | |
| | Symmetry | All lateral surfaces | | |
| | Wall | No-slip wall | | |
| **Operating Conditions** | Pressure | 94,210 Pa | x | 62 (m) |
| | | | y | 4.9 (m) |
| | | | z | 9.5 (m) |
| | Gravity | Deactivated | | |

**Table 5.1: CFD boundary conditions settings used in the baseline simulation and in the whole optimization process.**

## 5.4 Results of the CFD preliminary analysis

The results of the CFD simulation on the HBM beanie were compared to the data available for the AW101 original hub cap and for the baseline model described in §4.3 in terms of:

i. total pressure losses at the beanie wake;
ii. Wake deflection downstream of the beanie;
iii. global aerodynamic coefficients.

The characteristics of the wake downstream of the beanie were analysed by measuring the total pressure losses at specific section located near the AW101 helicopter tail fin downstream of the beanie. Specifically, a series of wake rakes were placed at various lateral positions and the results are depicted in Figure 5.4. As apparent, the wake was centred in y=0 for all the examined configurations. The AW101 original beanie is clearly characterized by more intense wake than the other two models, especially at the two extreme lateral positions (y=±0.5). The HMB model has a more regular wake which was less intense at y=0 than the baseline beanie used in the optimization activity.

Moreover, it is clear by looking at Table 5.2 that the AW101 model still presents the best wake deflection capabilities among the three analysed configurations. The baseline and the HBM featured a larger lift than the original beanie and always a lower drag. Finally an noticeably increase in the pitching moment (2.5 times the respective value of the original AW101) was observed in the case of the HBM hub cap.

| | **Baseline** | **HBM** |
|---|---|---|
| **$L/L_{AW101}$** | 1.06 | 1.27 |
| **$D/D_{AW101}$** | 0.84 | 0.79 |
| **$Z/Z_{AW101}$** | 1.07 | 1.06 |
| **$My/My_{AW101}$** | 0.69 | 2.49 |

**Table 5.2: Global aerodynamic coefficients and moments acting on the baseline and HBM models with respect to the original AW101 values.**

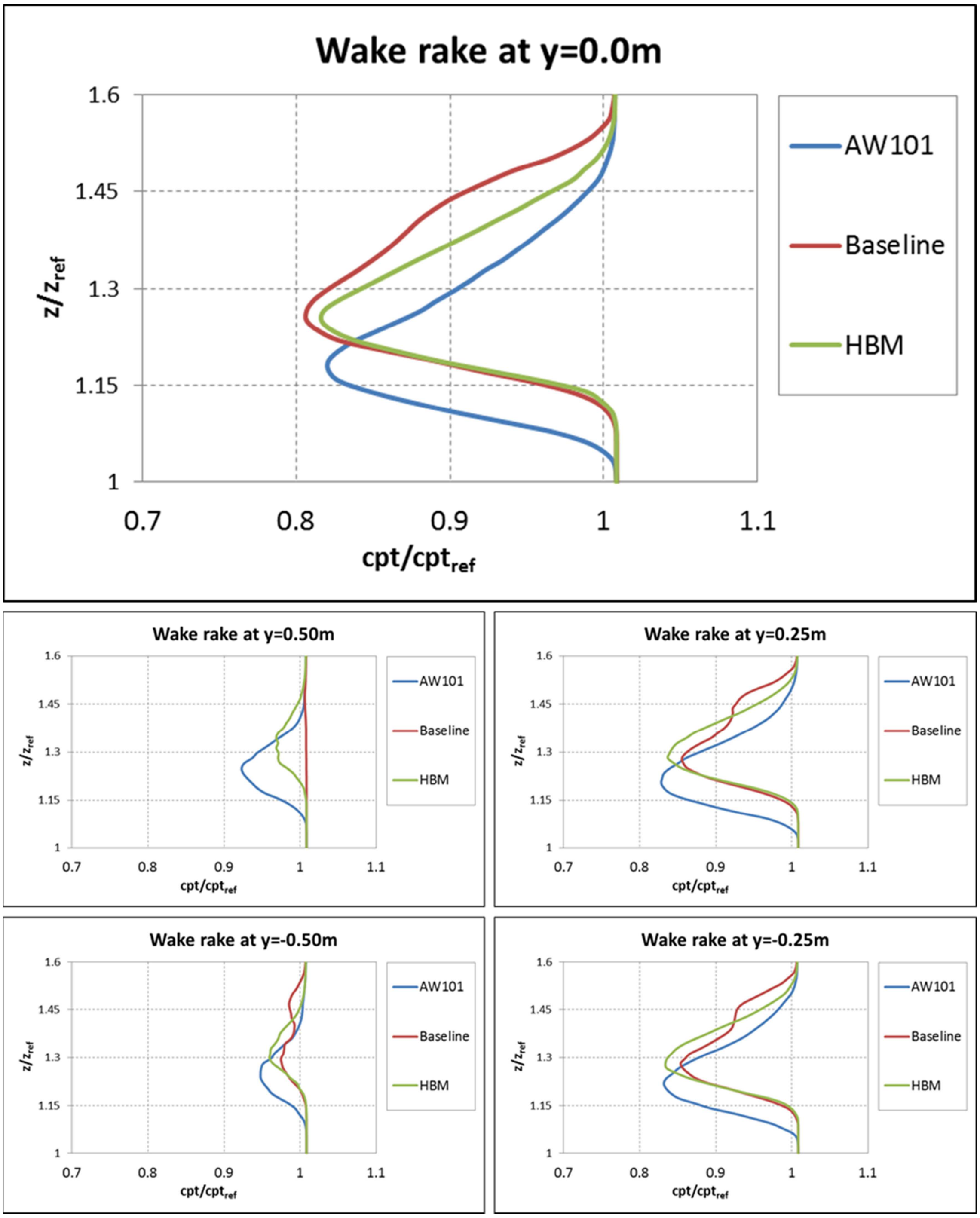

**Figure 5.4: Two dimensional total pressure losses at different lateral positions over the transversal section located near the tail fin downstream of the beanie.**

## 5.5 *The model parameterization*

The HBM beanie described in the previous paragraph was parameterized using the domain/handle morphing technique already presented in §4.5. Only five design variables describing some beanie specific geometrical characteristic were selected. In particular:

- **Sh1**: this shape is directly connected to the base height. The assigned deformation range is equal to [-15mm;+30mm] (Figure 5.5);
- **Sh2**: this shapes governs the beanie upper surface convexity by translating a single handle placed at the surface centre along the z direction (Figure 5.6);
- **Sh3**: this variable changes the convexity o the disk lower surface using the same approach described for sh2 (Figure 5.7);
- **Sh4**: this shape is connected to the beanie diameter. The deformation range assigned to this variable is equal to [-25mm;+50mm] (Figure 5.8);
- **Sh5**: is connected to the beanie edge characteristics. In particular, when the sh5 is applied to the mesh a different beanie angle of attack is obtained (Figure 5.9).

It is worth remembering that this analysis aims at assessing the effects of the hollow structure on the beanie overall aerodynamic characteristics. Therefore, the selection of a high number of variables or the application of wide deformations would have unnecessarily complicated the preliminary study of the new beanie concept-design.

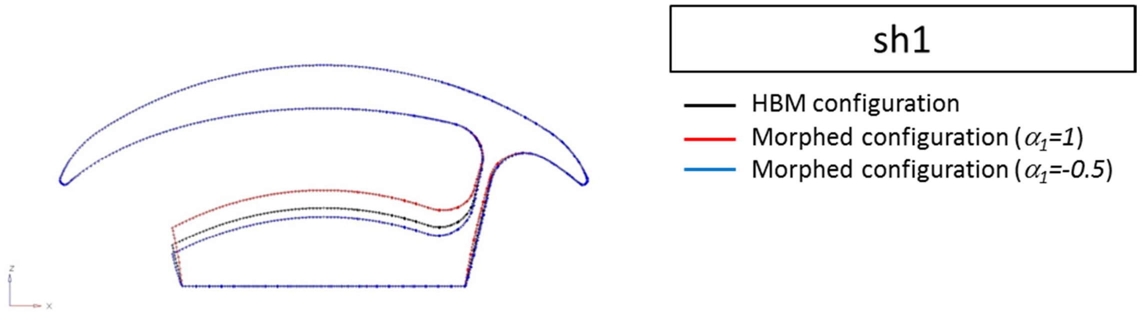

**Figure 5.5: Outline of the parametric shape *sh1* applied to the beanie with a scaling factor $-0.5\leq \alpha_1 \leq 1$.**

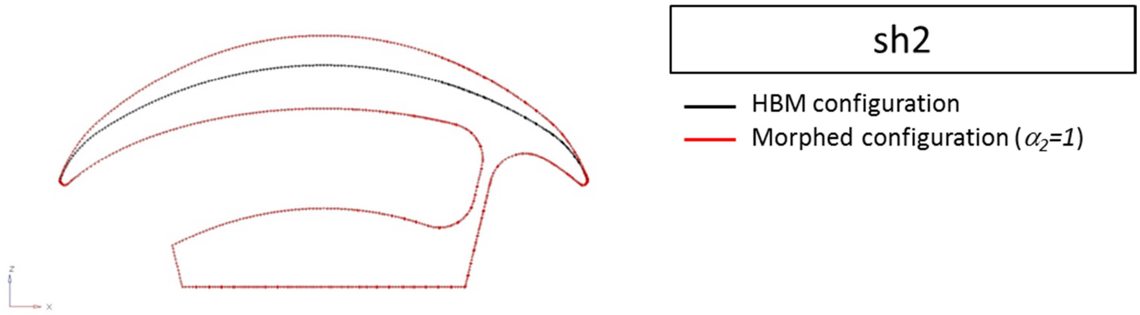

**Figure 5.6: Outline of the parametric shape *sh2* applied to the beanie with a scaling factor $\alpha_2 \leq 1$.**

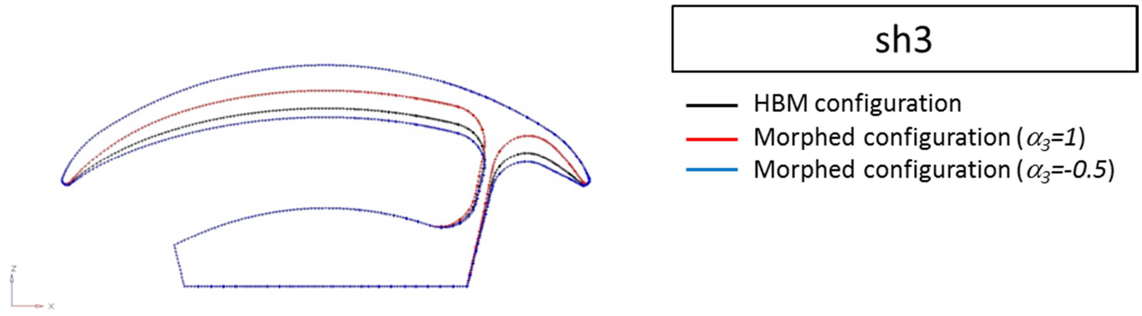

**Figure 5.7: Outline of the parametric shape *sh3* applied to the beanie with a scaling factor -0.5≤ $\alpha_3$≤1.**

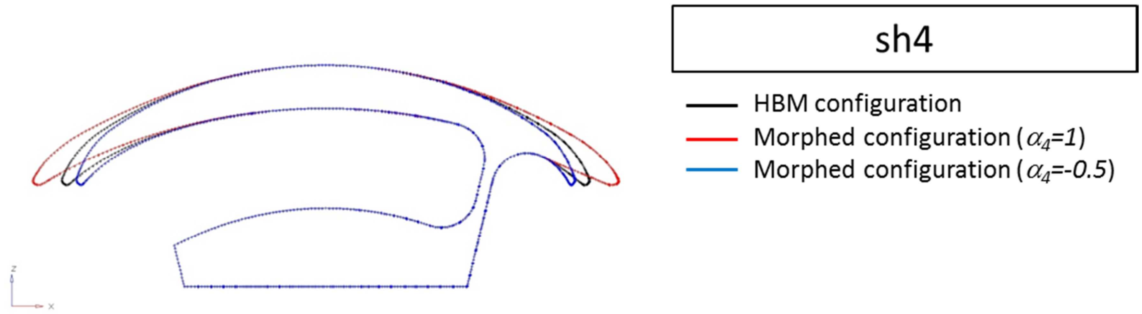

**Figure 5.8: Outline of the parametric shape *sh4* applied to the beanie with a scaling factor -0.5≤ $\alpha_4$≤1.**

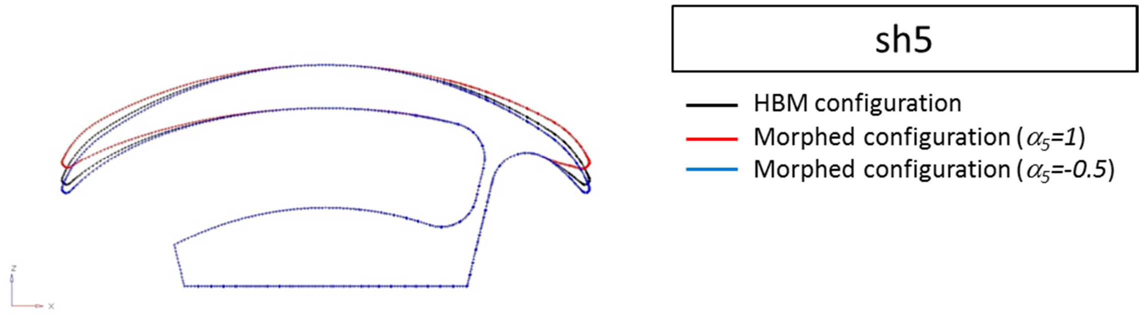

**Figure 5.9: Outline of the parametric shape *sh5* applied to the beanie with a scaling factor -0.5≤ $\alpha_5$≤1.**

## 5.6 HBM Beanie Parametric analysis

The parametric analysis was carried out in §4.6 mainly to identify the proper lateral position for the wake rake to be used during the optimization. In this case, the parametric study aim at determining the effects of the selected variables on the beanie aerodynamic performances. It is worth noting that the all the analysed configurations respect the geometrical constrained described in §4.5.2.

Table 5.3: Beanie parametric study test matrix. reports the parameter matrix followed for the creation of five different beanie geometries. The meshes were obtained following the technique already described in §4.2.2 and the CFD simulations were carried out using the settings defined for the beanie optimization. Results were then compared to the AW101 and the HBM original hub cap geometries in terms of both total pressure losses at the beanie wake and global aerodynamic forces acting on this beanie.

| CASE# | sh1 | sh2 | sh3 | sh4 | sh5 |
|---|---|---|---|---|---|
| **0 (HBM)** | 0 | 0 | 0 | 0 | 0 |
| **1** | 1 | 0 | 0 | 0 | 0 |
| **2** | 0 | 1 | 0 | 0 | 0 |
| **3** | 0 | 0 | -0.5 | 0 | 0 |
| **4** | 0 | 0 | 0 | -0.5 | 0 |
| **5** | 0 | 0 | 0 | 0 | -0.5 |

**Table 5.3: Beanie parametric study test matrix.**

The two dimensional curves of total pressure losses over the wake rake placed near the helicopter tail fin were obtained for each case and are reported in Figure 5.10. The wakes of the different beanies were always symmetrical with respect to the longitudinal plane as already observed in §4.6. All the geometries were characterized by similar wakes though the displacement in the CASE#1 and CASE#2 was clearly more pronounced as it also can be deduced by Table 5.4 were the coordinate z of the maximum total pressure loss is reported with respect to the AW101 reference value. Figure 5.11 shows the contour plots of the non-dimensionalized total pressure coefficient distribution over the helicopter midsection, for all the analysed configurations.

The increase of both the base height and the convexity of the upper surface had remarkable effects on both the beanie lift and drag and on its deflection capabilities, while the other design variables had modest effects on the beanie overall aerodynamic behaviour with respect the original HBM. However, the decrease of the beanie diameter led to reduction of the pitching moment with respect to the HBM with only negligible effects on lift, drag and wake deflection. Finally it is worth noting that, even though the new HBM model is characterized by a more complex structure than the beanie analysed in the optimization, the aerodynamic drag was still lower than the original AW101 hub cap.

A comparison between the HBM_CASE#1 model and the CASE#1 beanie model obtained by means of the optimization process described in Chapter 4 revealed that the new hollow geometry is characterized by a higher drag (20%) and a lower capability of wake deflection (2.4%). However, HBM_CASE#1 was obtained thanks to the variation of only one parameter, hence it can be expected that the performance of the HBM beanies can be improved even further through a real and complete optimization process.

| | **HBM** | **CASE#1** | **CASE#2** | **CASE#3** | **CASE#4** | **CASE#5** |
|---|---|---|---|---|---|---|
| **$L/L_{AW101}$** | 1.27 | 1.48 | 1.50 | 1.22 | 1.30 | 1.35 |
| **$D/D_{AW101}$** | 0.79 | 0.94 | 0.90 | 0.77 | 0.79 | 0.77 |
| **$Z/Z_{AW101}$** | 1.06 | 0.99 | 1.01 | 1.08 | 1.06 | 1.04 |
| **$My/My_{AW101}$** | 2.49 | 3.17 | 1.60 | 2.91 | 1.50 | 2.05 |

**Table 5.4: Summary of the paraemtric CFD analyses.**

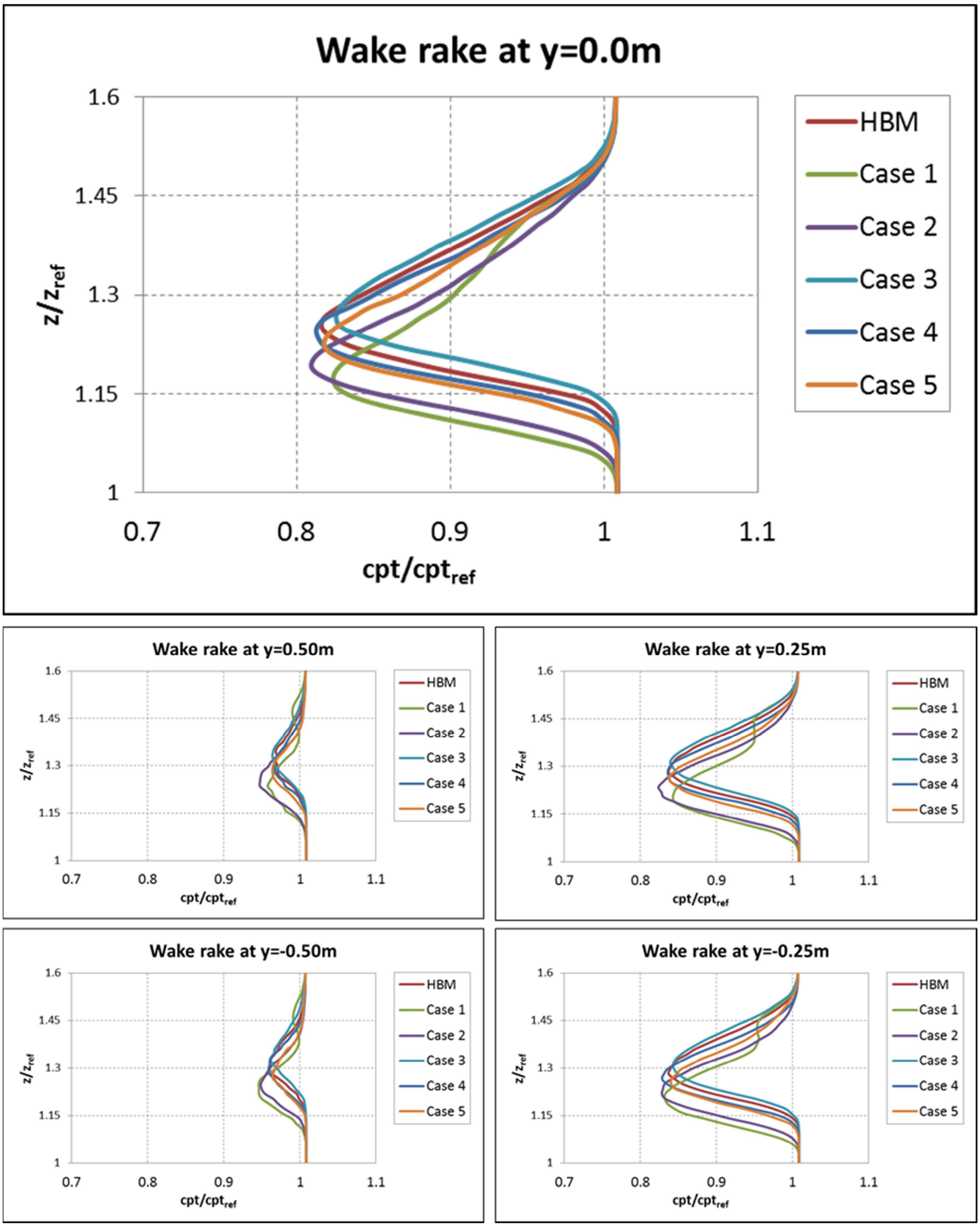

**Figure 5.10:Two dimensional total pressure losses at different lateral position in the parametric analyses.**

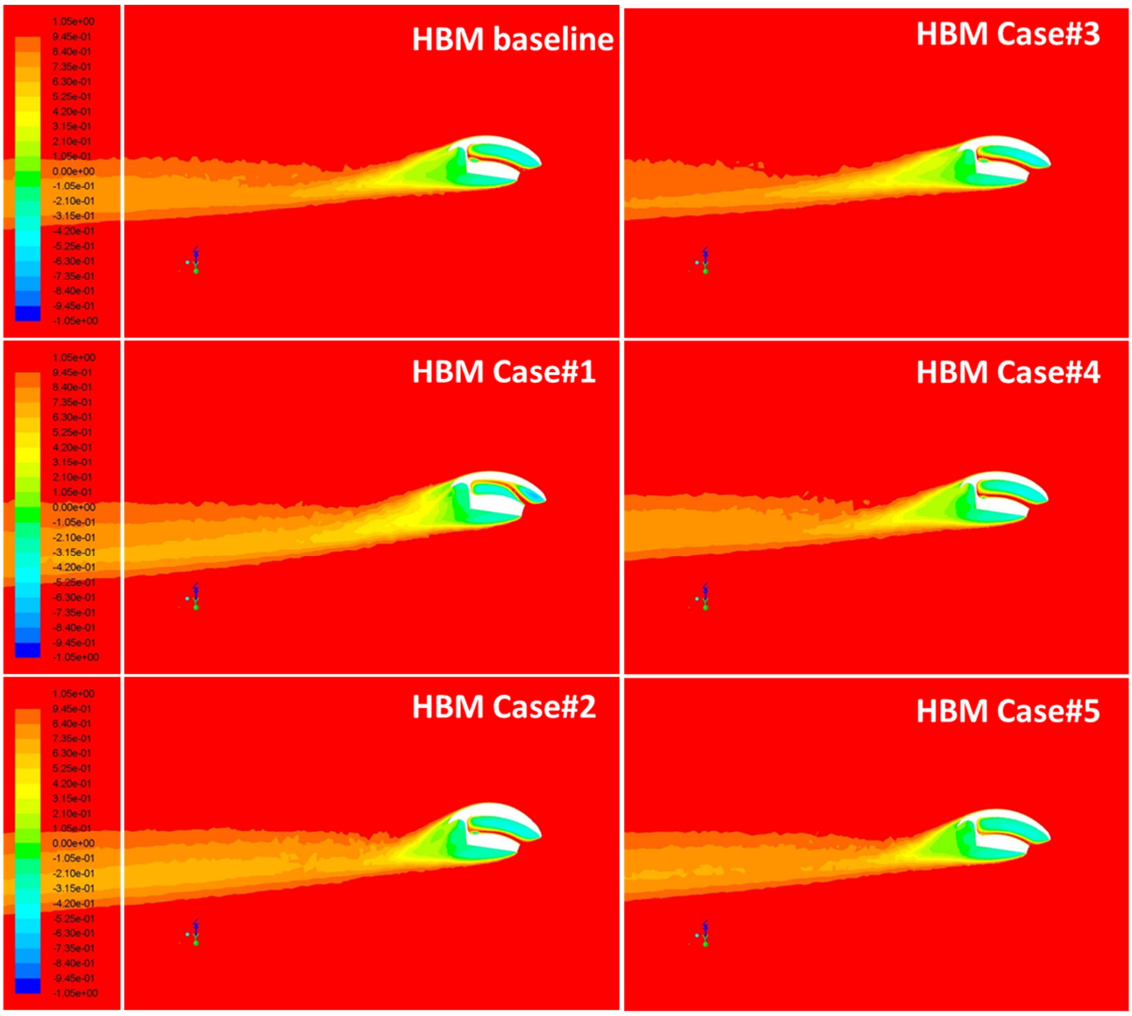

**Figure 5.11: Contour plots of the non-dimensionalized total pressure coefficient distribution over the helicopter mid-section for all the analysed configurations**

# 6. CONCLUSIONS

The first objective of this thesis was to characterize the aerodynamic behaviour of different types of beanie models that are mounted over the main rotor hub of different *AgustaWestland* helicopters. This aerodynamic component is probably one of the most important devices that help in the reduction of the tail shake phenomenon. In fact, the beanie induces a downward deflection of the wake generated by all the components near the rotor hub, thus modifying the way this wake interacts with the helicopter tail fin.

Since the beanie aerodynamic behaviour was not well known, the validation a CFD numerical model was the first step toward the aerodynamic characterization of such a component. To this purpose, the data of two specific wind tunnel test campaigns carried out on the AW139 and AW109 beanies were used to determine a series of grid parameters which allowed the achievement of a good match between the CFD predicted aerodynamic coefficients and the experimental data. In particular, the comparisons between numerical results and wind tunnel test acquisitions were made in terms of static pressure distribution over the beanie surfaces (both for the AW139 and AW109 models),of total pressure distribution at the beanie wake (only for the AW139 model), and of global forces acting on the beanie (only for the AW139).

Once the numerical model was proven to be sufficiently robust, it had been possible to test and evaluate the beanie performances at different operating conditions and in different configurations. In particular, an extensive CFD test campaign was carried out on the AW101 beanie model, over which no experimental data were available. Hence, the numerical model of this component was created following the criteria developed in the AW139 and AW109 hub cap validation and aerodynamic characterization activities. Part of the engine fairing of the AW101 helicopter was included in the simulations in order to quantify its effects on the flow deflection induced by the beanie. Specifically, the engine upper deck led to a decrease of the incidence angle of the oncoming flow over the beanie, which in turn produced some significant changes of its global forces and moments compared to the isolated beanie. Moreover, the beanie was tested both in rotating and non-rotating configurations. In general, the rotational speed was shown to lead both to a different distribution of the static pressure over the beanie surfaces, and to a lateral deviation of the wake, which lost its longitudinal symmetry with respect to the flow deflection. These results were evidenced regardless the presence of the upper deck.

The introduction of a robust numerical model was essential also for the development of the new procedure for the determination of the beanie limit loads to be used for structural and design purposes, that has replaced the old *AgustaWestland* guidelines, which relied only on a semi-empirical approach based on the strip theory. To develop this new procedure, two other methodologies were analysed and compared to the semi-empirical model: the experimental and the CFD methods. From all the analysis that were carried out, it was clear that the CFD simulations could be judged a reliable method for the determination of the beanie airloads, and that they could replace the wind tunnel test campaigns, which are much more expensive. Moreover, by investigating the effects of the presence of the engine upper deck on the beanie performances, it was possible to state that the determination of the design loads could be carried out on the isolated beanie configuration, since the airloads at stall were highly conservative with respect to those of the beanie installed on the engine fairing. Furthermore, even the effects of the rotation on both lift and drag were proven to be negligible. This enables to ignore the beanie rotation in the CFD simulations for the estimation of the limit loads, thus allowing a further simplification of the numerical model to be implemented.

The second objective of this thesis was to carry out an aerodynamic optimization of the AW101 beanie model, by means of computer procedure based on the advanced multi-objective evolutionary algorithm developed by the University of Padova. The final aim was the investigation of new beanie geometries to be installed on the AW101 helicopter that simultaneously manifested a lower drag and improved flow deflection capabilities with respect to the original hub cap model. However, the investigation carried out on the original AW101 beanie evidenced some of the component’s drawbacks (e.g. large drag), mainly related to its complex shape. Therefore, a series of new beanie geometries were created first starting from the original one: specifically, the beanie lower surface was greatly modified, since it was proven to be the most important source of aerodynamic drag.

Then, one of the new beanie models was chosen as the starting point for the optimization process. This model, called “baseline”, was analysed via CFD in order to investigate its aerodynamic performance at the specific operating conditions to be used for optimization.

Once the baseline analysis was carried out, the most important parameters describing the new beanie model were identified and they were translated into design variables during the parameterization phase.

Before starting the optimization, an analysis of the geometrical and structural constraints to be compliant with was carried out. In fact, due to the beanie location, the feasible design space was limited by the presence of the blade hinge fairings. Moreover, the blade motions (i.e. pitching, lead-lag, and above all flapping) limited this space even further. To this purpose, a surface describing the feasible design space was created and expressed in a mathematical from, so that it could be easily implemented in the main optimization algorithm. As a result, each generated individual throughout the optimization process that did not fulfil the geometrical constraints was automatically replaced by another individual randomly generated.

A beanie parametric analysis was carried out before the optimization in order to highlight the effects of the selected parameters on the beanie performance and to assess the most suitable procedure for the evaluation of the objective functions. Moreover, the effects of some of the design variables on the overall beanie performance were assessed.

Then, the bi-objective optimization was run. The achieved results were satisfactory, since a meaningful reduction in drag (up to 20% with respect to the baseline and up to 34% with respect to the original AW101). Moreover, an increase in the beanie capabilities of deflecting the oncoming flow downwards was obtained when comparing them with the baseline, while this does not holds true for the original AW101 beanie: actually, only CASE#1 features a larger wake deflection than the original AW101. Moreover, the optimization results made it possible to highlight the most influential shape parameters for the selected objective functions. In particular, a decreased beanie diameter, an increased upper surface convexity and a lower support height are strongly recommended in order to reduce the beanie aerodynamic drag and improve its capabilities in the deflection of the oncoming air flow. Three different solutions were selected from the Pareto front, and they were analysed and compared to the baseline in terms of (1) static pressure coefficient over the upper and lower surfaces, (2) total pressure coefficient at the beanie wake, and (3) global aerodynamic forces and moments. The final geometries of the optimized beanies were then obtained and compliance with both the geometrical and structural constraints was verified, though it was observed that the edge of optimized models was quite close to the geometrical constraint surface limit. These three new main rotor hub caps were submitted to *AgustaWestland*, which had created the full scale models that are going to be tested in the wind tunnel during 2013.

Finally, a new beanie concept-design was presented. This particular main rotor hub cap was characterized by an hollow structure which had never been tested before. The aerodynamic behaviour of this component was analysed in an initial CFD test camping carried out at the conditions used for the optimization activity, and the results were compared to those of both the optimization baseline model and the original AW101 beanie. The HBM was characterized by lower drag, and higher lift and pitching moment coefficient with respect to the other test cases. Form the analysis of the total pressure losses, it was apparent that the wake was less extended along the transversal (y) direction. However, the hollow geometry seemed not to have enhanced the beanie wake deflection capabilities, though a slight improvement with respect the optimization baseline model was observed.

In order to better understand the effects of some design variables on the HBM aerodynamic behaviour, a parametric study was assessed. Five different parameters were identified and changed using a mesh morphing technique. The models were tested via CFD and the results were compared to the HBM initial simulation and to the outcomes of the optimization activity. Although this was only a preliminary study, it was apparent that there were two specific parameters that affected the beanie wake deflection capabilities: the base height and the disk upper surface convexity. For instance, an increase in the former lead to an improvement in the wake deflection by the 6%. The other design variables were less incisive, though they seemed to help in the reduction of the pitching moment which was higher than the respective value of the original AW101 beanie.

The results obtained from the parametric analyses of the new HBM are encouraging, though a more detailed CFD study is strongly recommend before a complete optimization process can be carried out. In fact, the number or the design variables that can be selected (and the respective range of variation) is extremely high, and the effects of them on the beanie aerodynamic performances are not predictable at the moment. Moreover, a CFD test campaign both in steady and unsteady conditions should also be performed in order to assess the effects that the three-arms connection structure can have on the wake characteristics both in the case of a rotating and non-rotating beanie.

To conclude, it is worth noting that the beanie optimization was carried out considering only aerodynamic constraints, without taking into account any structural aspect due to the fact that the classic beanie models can be easily designed and manufactured. However, the new advanced HBM beanie presents some particular geometrical characteristics that may suggest the introduction of specific structural constraints. In particular, a limit to the local loads should be imposed at the base of each arms, since they have to withstand all the centrifugal and pulsating forces that act on the beanie. To this purpose, a simple structural model may be included within the CFD optimization procedure in order to take into account these additional constraints.

.

# 7. REFERENCES

[1] Waad, P. G., and Trouvé, M., “Tail Shake Vibration: Objective Comparison of Aerodynamic Configurations in a Subjective Environment,” NLR, 55th American Helicopter Society Annual Forum, Montreal, Candada, 1999.

[2] Roesch, P., Dequin, A. M., “Experimental Research on Helicopter Fuselage and Rotor Hub Wake Turbulence,” American Helicopter Society 39th Annual Forum, St. Louis, Missouri, May 1983.

[3] Mian, B. J., Mussi, F., “EH101 – Development Status Report,” 16th European Rotorcraft and Powered Lift Forum, September 1990.

[4] Mazzucchelli, C., Wilson, F.T., “The Achievement of Aerodynamic Goals on the EH101 Project through the ‘Single Site’ Concept,” 17th European Rotorcraft Forum, 1991

[5] Eglin, P., “Aerodynamic Design for Improved Aerodynamic Stability on Recent Aerospatiale Helicopters,” American Helicopter Society 37th Annual Forum, New Orleans, May 1981.

[6] Hermans, C, et. al., “Overview of the NH90 Wind Tunnel Test Activities and Benefits to the Helicopter Developments,” American Helicopter Society 53rd Annual Forum, Virginia Beach, Virginia, April 1997.

[7] De Giorgio, F., “Flow field characterization and interactional aerodynamics analysis of a complete helicopter,” Aerospace Science and Technology, No. 19, pp. 19–36, 2012

[8] Borie, S., Mosca, J., Sudre, L., Benoit, C., and, Péron, S., ”Influence of rotor wakes on helicopter aerodynamic behavior,” 35th European Rotorcraft Forum 2009, v. 2, p 648-660, 2009.

[9] Vogel, F., Breitsamter, C., and Adams, N.A., “Aerodynamic investigations on a helicopter fuselage with rotor hub,” 34th European Rotorcraft Forum 2008, v 3, p 2093-2121, 2008.

[10] Dal Mas, L., and Benini, E., “Clean Sky GRC2 - CFD Analysis Validation in Support of beanie Optimization,” Technical Report MULG0000K006, June 2010.

[11] Dal Mas, L., and Benini, E., “Clean Sky GRC2 - CFD Analysis of the AW109 main rotor hub beanie,” Technical Report MULG6200K002, Rev. A, December 2010.

[12] Dal Mas, L., and Benini, E., “Clean Sky GRC2 - CFD Analysis of the AW101 main rotor hub beanie,” Technical Report MULG6200K001, Rev. A, November 2010.

[13] Andreoli, P., Saporiti, A., Caramaschi, V., and Monti, G.,“AB139 - Aerodynamic Characterization of the Full Scale Beanie. Weight and Pressure Trials,” Technical Report 139G6220K001 Rev. A, June 2003.

[14] Pisoni, A., Saporiti, A., Caramaschi, V., and Monti, G., “AB139 - Aerodynamic Characterization of the Full Scale Beanie. Data analysis,” Techincal Report 139G6220K002 Rev. A, June 2003.

[15] Andreoli, P., Saporiti, A., Caramaschi, V., and Arra, M., “AW109 - Aerodynamic Characterization of the Full Scale Beanie. Pressure Trials,” Technical Report 109G6220K001 Rev. A, July 2004.

[16] Dal Mas, L., and Saporiti, A., “Clean Sky GRC2 – Rationale for the evaluation of beanie aerodynamic limit loads,” Technical Report MULG6200K005, May 2011.

[17] Mazzucchelli, C., “Aerodynamic Loads on the EH101 beanie”, Technical Note AER-101-45, Rev. A, 25/02/94

[18] Saporiti, A., “AB139 Airframe airloads”, Technical Report 139G0000K002/10 Rev.A, August 2002.

[19] Hoerner, S. G., and Borst, H. V., “Fluid-Dynamic Lift”, Hoerner Editions, Brick Town, 1958.

[20] Hoerner, S. G., “Fluid-Dynamic Drag”, Hoerner Editions, Brick Town, 1965.

[21] “AB139 Aerodynamic Data Comprehensive Report”, Report 139G0000P004 Rev. A.

[22] Saporiti, A., “AB139 Airframe airloads”, Technical Report 139G0000K002/10 Rev.B, July 2003.

[23] Andreoli, A. , “AW139. Main rotor hub loads from wind tunnel tests on the 1/3.5 scale model”, Technical Report 139G6200K011 Rev.A , August 2009.

[24] Dal Mas, L., and Benini, E., “Clean Sky GRC2 – summary and main outcomes of the CFD analysis carried out on the AW139, AW101 and AW109 beanies”, Report MULG6200K004 Rev.A, January 2011.

[25] Garavello, A., “Optimization software user manual” Document number CD/TT/HIT09/WP1.2/1/A.

[26] Toffolo, A., and Benini, E., “Genetic diversity as an objective in multi-objective evolutionary algorithms.”, *Evolutionary Computation*, Massachusetts Institute of Technology, Vol. 11, No 2, pp. 151-167, 2003.

[27] Garavello, A., “CODETilt Deliverable D1 part II: Release of the optimization Software user package”, Document number CD/CT/HIT09/WP1.2/1/A.

[28] Comis Da Ronco, C., “Program name: GeDEA 1.0. Theoretical and validation report.” AgustaWestland report number 800-91-066, 2010.

[29] Dal Mas, L., and Benini, E., “Clean Sky GRC2: AW101 Aerodynamic Optimization of Main Rotor Hub Beanie,” Technical Report No. 4800274706, December 2011